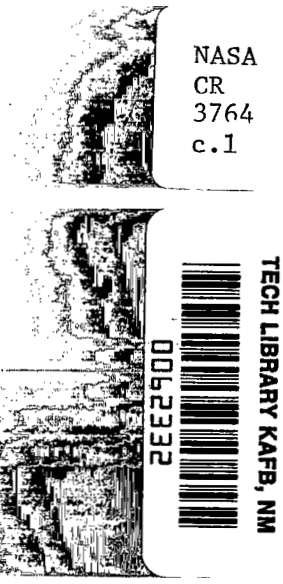

NASA Contractor Report 3764

A Study of Prediction Methods for the High Angle-of-Attack Aerodynamics of Straight Wings and Fighter Aircraft

O. J. McMillan, M. R. Mendenhall,
and S. C. Perkins, Jr.

CONTRACT NAS1-17026
JANUARY 1984

NASA

NASA Contractor Report 3764

A Study of Prediction Methods for the High Angle-of-Attack Aerodynamics of Straight Wings and Fighter Aircraft

O. J. McMillan, M. R. Mendenhall,
and S. C. Perkins, Jr.
Nielsen Engineering & Research, Inc.
Mountain View, California

Prepared for
Langley Research Center
under Contract NAS1-17026

NASA
National Aeronautics
and Space Administration

**Scientific and Technical
Information Office**

1984

TABLE OF CONTENTS

TABLE OF CONTENTS (Concluded)

SYMBOLS

AS	aspect ratio, b^2/S
b	wing span
c	local wing chord
$\bar{c}$	mean aerodynamic chord
c_ℓ	section lift coefficient
c_n	section normal-force coefficient, $\int_0^1 (C_{p_\ell} - C_{p_u}) d(\frac{x}{c})$
C_L	lift coefficient, lift/$q_\infty S$
C_ℓ	body-axis rolling moment coefficient, positive right wing down, rolling moment/$q_\infty Sb$
C_m	body-axis pitching moment coefficient, positive nose up, pitching moment/$q_\infty S\bar{c}$
C_N	normal force coefficient, normal force/$q_\infty S$
C_n	body-axis yawing moment coefficient, positive nose right, yawing moment/$q_\infty Sb$
C_p	pressure coefficient, $(p - p_\infty)/q_\infty$
C_y	body-axis side force coefficient, positive right, side force/$q_\infty S$
h	modified shape factor, $\delta^* - \theta/\delta^*$
K_v^*	vortex-lift reduction factor, equation 3
M	Mach number
N, N_a	nodal points in distribution of skin friction lines, figure 11
p	static pressure
q_∞	free-stream dynamic pressure
Re	Reynolds numbers, $V_\infty \bar{c}/\nu$
s	wing semispan, b/2
S	wing reference area
t	time

V_∞	free-stream velocity
V_u, V_ℓ	velocities above and under shear layer, fig. 6
x,y,z	cartesian coordinates, figures 6, 8, and 23
x_s, z_s	wing-section coordinates
$\bar{x}$	aerodynamic coordinate, $\bar{x} = x \cos \alpha + z \sin \alpha$
$\bar{z}$	aerodynamic coordinate in plane of constant $\bar{x}$, $\bar{z} = z/\cos$
α	angle of attack
β	angle of sideslip, positive nose left
Γ	vortex strength
δ^*	boundary-layer displacement thickness
θ	boundary-layer momentum thickness
Λ	leading-edge sweep angle
λ	ratio of tip chord to root chord
ν	kinematic viscosity
$\bar{\xi}$	dimensionless aerodynamic coordinate, $\bar{\xi} = \frac{\bar{x}}{c_r \cos \alpha}$

Subscripts

BSW	body-strake-wing configuration
BSWT	body-strake-wing-tail configuration
ℓ	lower
ℓ_e	leading edge
p	potential
r	value at the wing root
ref	reference
se	side edge
sep	separation
tail	component of load on tail

u	upper
va	contribution from augmentation term, eq. (2)
vℓe	contribution from leading-edge vortex, eq. (2)
vse	contribution from side-edge vortex, eq. (2)
wp	outer wing panel
2	quantity measured using strake balance, fig. 24
∞	free-stream value

SUMMARY

Work is described dealing with two areas which are dominated by the nonlinear effects of vortex flows. The first area concerns the stall/spin characteristics of a general aviation wing with a modified leading edge. The second area concerns the high-angle-of-attack characteristics of a high-performance military aircraft. For each area, the governing phenomena are described as identified with the aid of existing experimental data. Existing analytical methods are reviewed, and the most promising method for each area used to perform some preliminary calculations. Based on these results, the strengths and weaknesses of the methods are defined, and research programs recommended to improve the methods as a result of better understanding of the flow mechanisms involved.

For the general aviation wing, the most promising approach involves coupling boundary-layer theory with an inviscid representation of the flow field. The inviscid representation accounts for attached areas of the wing with a surface-singularity distribution and the separated wake using a free vortex sheet. An iterative calculation is required, wherein the wake shape is relaxed so that the vortex sheet is a stream surface in the converged three-dimensional flow field and a consistent separation line is predicted. Because only the unseparated version of the inviscid model is currently available, many important aspects of the coupling have not yet been investigated. The recommended research program includes study of these aspects as well as work to determine the best available boundary-layer method to be included and the appropriate separation criterion to be used. Additionally, study is recommended of the role in a prediction of the discrete vortex which has been

observed in flow visualization experiments in the region of the break in the leading edge.

With respect to the fighter aircraft, it is shown that good results for overall loads result from the use of a vortex-lattice method incorporating the Polhamus suction analogy as extended for side-edge and edge-vortex-lift-reduction effects, and by inclusion of the augmented-vortex-lift concept. The loads on the nose and the effects of the vortical field shed by the nose are included. Additional work is required to allow satisfactory calculation of the trajectories of the nose and separation vortices as they pass over the configuration. The angle-of-attack range of the method can be extended by inclusion of the effects of vortex bursting. Existing methods to be incorporated for the trajectory calculations and for the effects of bursting are identified.

INTRODUCTION

The NASA Langley Research Center is currently engaged in stall/spin research programs on both general aviation and military airplane configurations. These programs seek to advance the state of the art in high-angle-of-attack, stall/spin technology for improved safety of flight and for improved airplane flight performance. The stall/spin characteristics of both types of aircraft in the high-angle-of-attack flight regime have a large effect on their operational usage. The primary interest in this flight regime for general aviation aircraft concerns safety of flight, and emphasis has been placed on the alleviation of undesirable stall/spin characteristics. For military aircraft, improved high-angle-of-attack characteristics have produced greater maneuverability and tactical effectiveness, and recent emphasis has been placed on stall/spin prevention by means of

airframe design and control methods. In both cases, it is important for the designer to have access to prediction methods which are applicable in the nonlinear aerodynamic flight regimes. It is desirable that these methods provide rapid and accurate predictions of the aerodynamic characteristics of specific aircraft designs under a wide range of flow conditions.

Current efforts in the development of high-angle-of-attack aerodynamic prediction methods involve the combination of both experimental and analytical information to produce a rational model to represent the flow phenomena present. These methods have application in the high-angle-of-attack range where non-linear aerodynamc effects may dominate the flight characteristics. It is important that the chosen flow models correctly represent the physics of the flow, not only to enhance the accuracy of the prediction method, but also for increased understanding of the actual flow characteristics. Recent work on flow modeling has produced analytical and empirical prediction methods which have application to the prediction of lateral-directional aerodynamic characteristics of aircraft at high angles of attack.

Two separate problem areas involving similar flow phenomena are of interest in the present work. The first area of interest concerns the stall/spin characteristics of a general aviation wing with a modified leading edge. An extensive data base including forces and moments, pressure distributions, and flow visualizations is available for this configuration. This data base shows that appropriate modifications can control local stall progression and minimize loss of damping in roll at the stall. Significantly improved lateral stability characteristics at the stall, spin resistance, and developed spin characteristics result.

Analytical models to predict the separated aerodynamic characteristics of such a configuration are not available at this time. As a consequence, it is impossible to extrapolate the effect of the droop-leading-edge modification on this wing to any other wing and predict the modified stability characteristics. Such an analytic capability would greatly reduce the time and cost associated with the development of similar modifications for other wings. Analysis of the existing data can provide a means to understand the flow phenomena, develop flow models, and identify the needed theoretical approach.

The second area of interest concerns the high-angle-of-attack characteristics of high-performance military aircraft. Tests indicate that some modern fighter aircraft experience serious stability and control problems during high-angle-of-attack maneuvers. These tests have shown that directional and lateral stability characteristics change with geometric modifications in the configuration. For example, wing position (high, low, or mid), strakes, single or twin vertical tails, and fuselage nose cross section can all have an effect on the stability characteristics either singly or in combination. An extensive data base on a NASA generalized research fighter configuration is available for use in understanding the flow phenomena and directing the selection of a theoretical model.

The prediction capability for the total aircraft in the high-angle-of-attack regime near stall is not yet available; however, various methods are available for predicting characteristics of components of the configurations. These could be combined into a unified method for the complete aircraft. Such a preliminary design method will be very useful in predicting stability characteristics of various configurations for purposes of reducing the total number of configurations required for wind-tunnel testing.

In this report, investigations are documented which were designed to enhance physical understanding of and computational capability for both of these problem areas. In Parts 1 and 2, respectively, work is discussed on the general aviation wing with a modified leading edge, and on a generic high-performance military aircraft. These studies, though separate, employed the same general approach. In each, relevant experimental data were analyzed to allow identification of the governing phenomena, existing analytical methods were reviewed to identify the most promising, some preliminary calculations were carried out to define the strengths and weaknesses of existing methods, and a course of action was recommended for developing a comprehensive prediction method. Each of the two parts of the report is organized to reflect the specific implementation of this general approach to the problem at hand.

PART 1. A GENERAL AVIATION WING WITH A MODIFIED LEADING EDGE

APPROACH

The flow phenomena responsible for the improved stall-departure and spin-resistance characteristics of a general aviation airplane with an outboard-droop wing modification have been the subject of intense scrutiny in recent years. Model- and full-scale flight tests, sub- and full-scale wind-tunnel tests, and extensive flow-visualization studies have resulted in the following description of the mechanisms involved (refs. 1-4).

With the basic wing, as angle of attack is gradually increased, there is a conventional progression of trailing-edge stall which starts at the wing-fuselage junction and progresses forward and outboard. Above an angle of attack of about 12°, however, the outboard portion of the wing undergoes apparently random separation and reattachment which persists until $\alpha \approx 30^{\circ}$, at which point the wing is essentially fully stalled. The measured time-average lift curve for the airplane with the basic wing (tails off) is shown in figure 1 (the points representing a calculation are discussed later).

If a glove is installed over the forward part of the outer wing resulting in a discontinuity in the wing leading edge, as shown in figure 2, the lift-curve behavior changes substantially

for $\alpha \geq 20^{\circ}$ (fig. 1). As shown in figure 2, the glove provides a 3-percent chord extension and a droop which increases the leading-edge camber and radius (the wing with this modification will hereafter be referred to as having "outboard droop"). The lift curve for this modified wing exhibits the "flat top" which has been correlated with improved spin resistance after stall, and which results from the flow staying attached to the outer portions of the wing until very high angles of attack. Detailed visualization of the flow associated with the outboard-droop configuration indicates that the effectiveness of this modification in maintaining attached flow at the wing tips is the result of a vortex flow generated at the discontinuity in the leading edge. This vortex flow apparently acts as an aerodynamic fence "to stop the spanwise progression of the separated flow region toward the wing tips such that the tips continue to generate lift to high angles of attack" (ref. 1).

Further investigation has shown that this favorable behavior is quite sensitive to geometrical detail. For example, elimination of the leading-edge discontinuity (and presumably the vortex generated there) by addition of a fairing reintroduces the destabilizing negative slope of the lift curve after stall. Measurements using a wing-tip balance show that with the fairing, the stall behavior of the outer wing panel is similar to that of the basic wing, although delayed until a somewhat higher angle of attack. Additionally, if the position of the leading-edge discontinuity is varied outside a certain band, or if the entire wing is modified with the leading-edge droop, almost all of the spin resistance after stall exhibited by the outboard-droop configuration is lost. In each of these cases, this is due to the tip regions no longer maintaining attached flow at high α.

In order to allow prediction of the static longitudinal aerodynamic characteristics of a particular wing geometry at high angle of attack, the strong interaction between the viscous separated region and the inviscid flow must be accounted for. In this situation, the pressure distribution is not determined by the inviscid flow as is assumed in the standard aerodynamic perturbation procedure where boundary-layer theory is used to account for small viscous effects. Instead, the viscous region of the flow controls the pressure distribution. But short of abandoning all hope for an iterative inviscid-viscous scheme and retreating directly to a full Navier-Stokes solution, in this work we suppose that a modification of the classical procedure may be successful and should be examined, for reasons of computational economy if nothing else. This modified scheme should proceed as follows:

1. An inviscid (fully attached) calculation is made for the wing, resulting in an inviscid pressure distribution.

2. A boundary-layer analysis is applied to this pressure distribution to produce a predicted detachment line and a distribution of displacement thickness in the attached region.

3. The inviscid analysis is repeated, this time allowing for the boundary-layer displacement effects in the attached regions and the effects of the separated wake downstream of the detachment line. The existence of a vortex at any discontinuity in the leading edge must be predicted, and its effects allowed for in the inviscid calculation. A new inviscid pressure distribution results.

4. Steps 2 and 3 are repeated until the solution converges: i.e., until subsequent iterations yield changes in the location of the detachment line and the calculated pressure distribution which are less than some acceptable tolerance. At this point, a consistent representation of the separated flow has been determined, and the loads on the wing may be calculated.

While it is possible to broadly specify in this way the elements and the interactions likely to be required in a predictive scheme, it is not possible to specify with complete confidence a priori what physical effects must be included, and a comprehensive integrated method suitable for application to this problem does not currently exist. Furthermore, it is not clear if adequate methods exist for each step in this scheme, and if so, the best approach for a given step. In constructing an integrated method, the ever-present need to balance accuracy and representation of the important physical effects against computational cost must be considered.

With this as background, the effort which is the subject of this portion of this report can be discussed. The tasks were to examine existing data and methods which are relevant to this problem, to select the method which appears most satisfactory for application to each step of the scheme outlined above, to evaluate possible inadequacies in these methods through the performance of some preliminary calculations, and to identify a rational approach to the development of the complete method. In the following sections, the existing methods which are applicable to this problem are reviewed and a preliminary selection of methods to be pursued is made. Results are presented of some preliminary calculations made using these methods (thereby illustrating some of their capabilities and shortcomings), and necessary improvements and a process which

will result in a complete predictive capability are recommended. Because of the need to limit the scope of this work, attention is focused on the inviscid portion of the analysis. While the viscous analysis required is important (indeed pivotal) to the success of the overall scheme, there have been several recent state-of-the-art review conferences on this subject (described later) which provide input adequate for the present purposes. Inferences are drawn from these reviews relevant to the current application.

REVIEW OF EXISTING INVISCID METHODS FOR WINGS WITH MASSIVE SEPARATION

A review of existing methods which deal with the related, but considerably simpler, problem of calculating the loads on a stalled airfoil is given in Appendix A. Study of these two-dimensional methods reveals that they fall into two broad categories, differing primarily in the nature of the treatment of the separated region. In one of these categories, the flow is analyzed using the notion that the streamlines leaving the upper and lower surfaces, when combined with the forward unseparated portion of the body, define an "equivalent inviscid body" (see sketch). External to this "body", the flow is analyzed using conventional inviscid methods. Within the body, the separated region is treated either as having constant pressure at a level determined by some preset criterion, or a more detailed model is constructed to attempt to describe the governing phenomena. The latter include reverse flow and the mixing of the bounding shear layers with the accompanying recompression to the free-stream value of pressure. In this approach, the trajectories and points of origin of the separation streamlines which form part of the boundary of the equivalent inviscid body are calculated in an iterative

procedure. In the second category, the solid airfoil surfaces are represented by singularity distributions, and the free shear layers bounding the separated-wake-flow region are represented by vortex sheets. Each point of these sheets is convected by the velocity induced by all the other singularities in the model in an iterative calculation, and at convergence the pressure distribution is known over the entire airfoil, including the separated region.

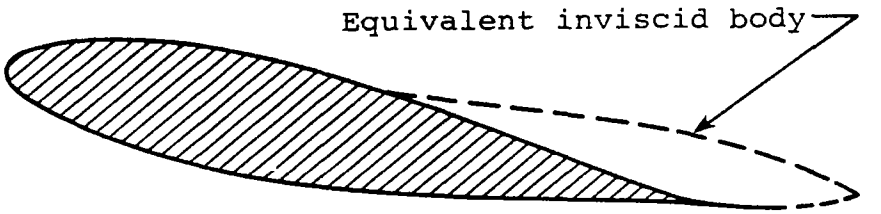

Methods which, conceptually at least, are applicable to the problem of a finite wing with large regions of separated flow, unsurprisingly, are extensions of prior analyses of the two-dimensional stalled-airfoil problem. In this section, four such methods are discussed, two from each of the categories discussed above.

The first method (ref. 5) uses the notion of an equivalent inviscid body. The solid surface is paneled with a source distribution, and an internal vortex lattice along the mean chord of the lifting surface provides circulation to the flow. The surface of the equivalent inviscid body in the separated region is the dividing stream surface between the external flow and the flow emanating from the sources on the actual body surface in the separated region. In reference 5, the source distribution in this region was adjusted until the pressure distribution on the unseparated (upstream) portion of the body matched experimental data. The resulting pressure distribution

in the separated region was not physically realistic, and it had to be replaced with a constant value assumed equal to the pressure at the separation point, again in approximate accord with existing data. Because it is not known how to specify the source distribution in the separated region in the absence of experimental data, and because it was stated in reference 5 that there was considerable development necessary before the method could be coupled with a boundary-layer analysis allowing prediction of the separation line, this method is not considered further here.

In reference 6, an attempt is made to model accurately the flow inside the separated region, with emphasis on the "recompression zone" where the pressure relaxes from the constant value in the forward portion of the separated region to the free-stream value. Separate zonal models are used for the free-shear layers, the backflow, and the rear stagnation region which interact to cause the pressure rise. The separation streamline which forms a part of the boundary of the equivalent inviscid body is used in the recompression model. Its position is calculated at each iteration step by a mixed-boundary-condition potential flow procedure, as discussed for the two-dimensional case in Appendix A. The solution procedure of reference 6 is as follows: an initial pressure distribution in the separated region is assumed, the mixed-boundary-condition potential method is applied resulting in an updated pressure distribution on the unseparated region and a new location for the separation streamline, and the separation streamline is input into the separation model, resulting in an updated pressure distribution in the separated region. This process is repeated (including application of integral boundary-layer methods to model the displacement effects in the attached region and to predict the separation location) until convergence is achieved; four or five iterations are typically required.

Results calculated using this method for the "controlled partial span stall" wing (fig. 3) are compared to data in figures 4 and 5 for an angle of attack of 19° and a Reynolds number of 1.1×10^{6}. Poor agreement with the wing span-load data is shown in figure 4. The pressure distributions of figure 5 indicate that agreement with measurements on the suction side of the wing is generally lacking, particularly in the leading-edge region. This is so in portions of the wing both with and without slats. The author of reference 6 notes that in the leading edge region, the resolution available from the paneling method may be inadequate.

Presumably, the strong point of this method is its detailed treatment of the flow in the separated region. When the recompression process occurs over the wing, as is sometimes possible, it would seem to be important to model this phenomenon. However, it is shown in Appendix A that in a case where this does occur (a 63_1-012 airfoil section at 15° angle of attack), the two-dimensional precursor to the method of reference 6 fails to reflect this behavior and the recompression is predicted downstream of the airfoil. Furthermore, the lift curve at high angle of attack for this airfoil is poorly predicted using this method.

Moving to the free-vortex-sheet category of methods, the first method we discuss is that of reference 7. Guided by the observation that, beyond stall, time-periodic flow patterns are observed, the analysis is unsteady with the wing considered to be moving in a stationary reference frame. The model shown in figure 6 (from ref. 7) is based on experimental observations of cellular type three-dimensional turbulent separation where the cell shape depends on wing aspect ratio or (in the current application) leading-edge treatment. As shown in figure 6, the wing is represented by a vortex lattice and the separated wake by vortex

rings shed at each time step at the separation locations, which are assumed known in this model. The bound and free vortex strengths are determined by the imposition of the following conditions at each time step: (1) there is no flow through the wing surface; (2) the strength of the vortex ring shed at the current time step is calculated at the forward separation point (fig. 6(b)) using the shear velocity relation

$$\frac{d\Gamma}{dt} \approx c_1(V_u^2 - V_\ell^2)/2 \tag{1}$$

where c_1 is an empirical factor with a value of 0.6 and V_u and V_ℓ are calculated about 0.2-0.4c above the separated wake and at the separated-panel collocation point, respectively. The vortex ring shed at each time step is located with its upstream spanwise leg at the midpoint of the path covered by the leading edge of the panel on which separation is specified during the latest time step; this filament is connected to the downstream spanwise leg which is located at the midpoint of the path covered by the wing trailing edge (the specified downstream separation point) during the same time interval. During each time step, all of the vortex rings previously shed are convected by the three-dimensional wing-wake induced velocity field. The large-scale vortex lattice shown in figure 6 is not suited to calculating the details of wake roll-up, so only the time-asymptotic average wing loads are obtained. The wing is started from rest, and the time required until the steady-state condition is reached is claimed to vary with wing planform and aspect ratio. Typical run times are less than a minute on a CDC 7600 computer. Loads are calculated from integrated pressures obtained using the unsteady Bernoulli equation.

An example of the results obtained using this technique is shown in figure 7 (from ref. 7). The planform analyzed is shown in the inset of this figure. The droop leading-edge modification consisted of a glove which increased the wing chord and camber. Up to three vortex rings were shed at each time step, using the experimental separation locations shown in figure 7(b). In spite of the use of a rather coarse paneling distribution (4 chordwise by 13 spanwise panels were used with 3 spanwise panels in the gap), the use of the observed separation locations gives very good results (see fig. 7(a)). The method requires extension to include interaction with a boundary-layer analysis to allow prediction of the separation line. However, it is doubtful that the pressure distribution generated by the vortex lattice would be adequate for an accurate prediction of the separation line, no matter what boundary-layer analysis was used, so this extension is viewed as a difficult one.

The last method to be discussed also falls in the category of free-vortex-sheet methods. This method, implemented in a computer program known as VSAERO (for Vortex Separation AEROdynamics), is currently under development (refs. 8 and 9). It is a low-order surface-paneling procedure wherein the wing surface is represented by a set of flat quadrilateral panels, each with a constant doublet and source strength. When the method is fully implemented, the free-shear layers bounding the separated region will also be represented by doublet panels, the strengths of which are asssumed to vary linearly in the downstream direction. The doublet distribution is the unknown in this procedure, with the source distribution set in each iteration by the Neumann boundary condition on the wing external surface. In the unseparated region, the velocity normal to the wing surface is zero, or is the transpiration velocity given by a boundary-layer procedure to account for the displacement effect. In the separated region, the normal velocity is set

equal to zero. A unique solution to the inviscid problem is generated by imposing the internal Dirichlet boundary condition of zero perturbation potential inside the wing.

When the inviscid procedure is coupled to a boundary-layer analysis, a solution is obtained by the convergence of a double-iteration loop:

1. An initial wake shape is specified and zero normal velocity is assumed on the wing surface.

2. A solution for the doublet distribution is obtained.

3. The wake is repositioned using as many iterations as desired so that the streamwise edges of the wake panels are aligned with the local calculated flow directions; for each wake position, a new doublet distribution is calculated.

4. The boundary-layer calculation is made, and updated estimates are made for the transpiration-velocity distribution in the unseparated region and the location of the separation line.

5. A new solution for the doublet distribution is obtained using the last wake position, i.e., return to step 2 and continue the loop.

As stated previously, this method is being developed and is not currently available in a form which provides the full capability just described. In particular, the ability to deal with "massive separation" is not presently fully implemented. However, results have been obtained for a wing with a large separated

region using a precursor of the VSAERO code (refs. 10 and 11) which allow for preliminary evaluation of this approach.

As described in these references, the precursor code had the main features just listed, but the wake-relaxation and viscous/potential iteration cycles had not been automated. The separation model used is schematically illustrated in figure 8 (from ref. 10), where it is seen that the shear layers from the forward and rearward separation lines are assumed to meet and coalesce into a zero-thickness free wake. This closure of the separation region is a feature of the precursor code and is not carried over into VSAERO.

The model was applied to a constant-chord wing of aspect ratio 6 with a NACA 0012 profile and a sweep angle of 10°. The separation line was prescribed from experimental measurements, and the wake was prescribed to leave the wing at $\alpha/2$ in accord with earlier experience. The wake remained fixed in this position throughout the computation. Calculated pressure distributions from this model and for assumed fully attached flow are shown at 60% and 90% semispan locations for $\alpha = 21.38^{\circ}$ in figures 9(a) and (b), respectively, again taken from reference 10. Excellent agreement of the separated flow model with the data is evident in these figures, indicating that the inviscid portion of VSAERO holds promise for being applicable to finite wings with large regions of separation. As an aside, it is pointed out in reference 10 that the data points that appear anomalous in figure 9 are actually indicative of unsteady separation. It appears that the bulk of the measurements were made under separated conditions, but a few pressures were measured when the flow was attached.

VSAERO was developed from the two-dimensional method known as CLMAX (ref. 12). In Appendix A, it is shown that CLMAX is quite successful in modeling the flow over airfoils at angles of incidence beyond that for maximum lift, angles where an extensive region of separated flow exerts an important influence on the load distribution on the airfoil. The example just presented indicates that the inviscid modeling capability of CLMAX as extended to the three-dimensional case may be successful as well. Furthermore, because VSAERO is a surface-paneling technique, it holds the promise of being able to predict pressure distributions with sufficient accuracy to allow coupling with boundary-layer analysis and thus allow prediction of the separation line. For these reasons, and because VSAERO is being provided with a convenient and powerful automated procedure for geometrical input, it is chosen from among the methods discussed in this section for further examination relative to the general-aviation-wing problem. Because the version of VSAERO currently available does not allow for the treatment of large separated regions, the extent of this examination is limited. Nevertheless, some conclusions can be drawn and these are presented after a few remarks about the boundary-layer analysis which must be coupled to whichever inviscid technique is ultimately applied to this problem.

SOME REMARKS ON BOUNDARY-LAYER ANALYSIS

The overall analytical framework proposed for application to this problem supposes that at each iteration step the inviscid analysis is done accounting for the separated region (e.g., in VSAERO by a doublet sheet) and thus the pressure distribution available for use in the boundary-layer-analysis step reflects the downstream separation. As stated earlier, it is postulated that the iterative process will lead

eventually to a consistent representation in which boundary-layer separation is predicted along the line from which the doublet sheet emerges. In this context, what has been loosely termed "boundary-layer analysis" must be formulated in such a way that the upstream influence of the separated region is properly accounted for. This is discussed further below.

On each streamline, the boundary layer on the finite wing will start as a laminar layer at the stagnation point and proceed in one of several ways. In the current application, all of these possibilities ultimately result in a turbulent boundary layer which proceeds back over the wing surface; it is the separation of this turbulent layer that is our main interest in the remainder of this section. The transition from the initial laminar flow to the turbulent one can occur: (a) smoothly, with no intervening separation, (b) after laminar separation and reattachment, resulting in a small laminar "bubble", or (c) after laminar separation, in the free shear layer, and the reattachment is turbulent, again resulting in a small separation bubble on the front portion of the wing. For purposes of the present discussion, it is assumed that the approximate methods (see, for example, the review in ref. 6) which exist for the small regions of laminar and transitional flow are adequate, and attention is focused on the turbulent boundary layer.

First, the fact must be dealt with that the flow field at high angle of attack over the finite wing of interest here is undeniably three-dimensional. Flow-visualization studies (e.g., refs. 13-15) have demonstrated the existence of "mushroom-shaped" stall cells on finite wings at high alpha, a tentative sketch of which is shown in figure 10 (from ref. 14). A formal topological analysis has been applied to flows of this type, and a conjectured pattern of skin-friction lines drawn (figure 11, from ref. 16). This pattern features a number of

nodes (N) and saddle points (S) which have been found to follow certain rules which hold generally in three-dimensional separated flows. With the addition of outboard droop, the mushroom-shaped stall cell doesn't extend spanwise over the entire wing but instead is terminated at its outboard end by a vortical flow emanating at the leading-edge break (refs. 13 and 15). A sketch of the surface oil-flow patterns on such a wing attached to a fuselage is shown in figure 12 (from ref. 13).

Given this evidence, the application of three-dimensional boundary-layer theory is suggested immediately. However, the prospects for predicting separation in this flow field in this way do not seem particularly bright. In the so-called "Trondheim trials" (ref. 17), a meeting devoted to validating three-dimensional methods by comparison with experiment, a series of quasi-three-dimensional flows were calculated. These are flows in which two spatial coordinates are sufficient to describe the flow locally (an example is the flow over an infinite swept wing), and most of the test cases involved only the region well upstream of separation. In an included separating case, however, all available boundary-layer methods showed remarkably poor agreement with data (ref. 18). A central difficulty seems to involve the treatment of the essential non-isotropy of the eddy viscosity, or its equivalent, in these methods. In a more recent review, reference 19, the situation seems no more encouraging.

It is therefore appropriate to see what can be done with two-dimensional methods in the current application. Although such a study is beyond the scope of the present work (except for a brief examination of perhaps the simplest such approach, use of the Stratford criterion, described later), some comments can be made and a more detailed study of this matter is recommended for the next phase of work.

In a certain class of strictly two-dimensional flows, the ability to predict separation is reasonably well established. This ability requires a properly formulated boundary-layer method and the use of an appropriate separation criterion. Each of these topics will now be briefly discussed.

It is well known that the usual two-dimensional boundary-layer equations exhibit singular behavior at the point of zero skin friction when the pressure is prescribed. This is a manifestation of the physics of the situation. An arbitrary specification of the pressure distribution near and downstream of separation is not compatible with the elliptic nature of the problem: the pressure distribution in fact adjusts itself to the separated region. Furthermore, use of the experimentally measured pressure distribution for a separated flow in a solution of the boundary-layer equations often leads to calculated behavior that erroneously suggests that the flow is attached (refs. 20 and 21). Fortunately, however, there are several well-known techniques that allow for the removal of the "separation singularity" through a proper choice of the dependent variables (e.g., refs. 22 and 23). With the proper formulation, the calculation using one of these methods can successfully proceed downstream through the separation point.

Using one of the techniques from reference 22 or 23 to predict the location of separation requires some care, however. Turbulent separation is an inherently unsteady process, and correlation of detachment locations inferred from surface flow visualization with the time-average quantities available from a boundary-layer calculation has been accompanied by some confusion. This has led to the use of several separation criteria in the past (e.g., skin friction = 0, or shape factor more than some limiting value). Recently, an analysis was published (ref. 24) that eliminates much of this confusion and

proposes a detachment correlation valid for two-dimensional flows as long as the wall curvature or body forces such as are found in rotating systems are not too strong, and as long as there is no boundary-layer suction or blowing. The correlation is in terms of the modified shape factor $h = \delta^* - \theta/\delta^*$; it is shown that a value of $h_{sep} = 0.63 \pm 0.06$ is associated with "incipient detachment," a condition with from 5% to 20% of time-averaged backflow at a location where the displacement thickness begins to increase rapidly. It is also shown in reference 24 that the incipient-detachment location is the location indicated by conventional visualization methods.

Thus in many two-dimensional flows, the prediction of separation using a properly formulated boundary-layer method and the detachment correlation of reference 24 can be accomplished with some confidence. Application of these techniques to the finite wing of interest here will probably require some further development*. While these techniques could be applied chordwise on the wing in the spirit of strip theory, less violence is done to the two-dimensional basis of these methods if they were to be applied along streamlines of the external flow. Furthermore, because the fundamental natures of flow detachment in two-dimensional and three-dimensional flows are different, a "calibration" of the detachment criterion will probably be required. The resulting method, although approximate and ad hoc in some respects, will nevertheless allow some progress to be made on this problem without resorting to the much larger task of developing an adequate three-dimensional boundary-layer method.

*Note that an integral boundary-layer analysis and a separation criterion (not that of ref. 24) are included in VSAERO (ref. 8). Because the focus of the current work on the general aviation wing is on the inviscid portion of the overall analysis, these specific techniques have not been evaluated.

PRELIMINARY CALCULATIONS WITH VSAERO

Because the version of VSAERO available for use does not have the capability to model separated wakes, the calculations performed were restricted to step 1 in the overall procedure outlined in the Approach section. This is obviously a serious limitation, but by examining the fully attached solutions at various angles of attack for the basic wing and comparing them with the corresponding solutions for the wing with outboard droop, some understanding of the phenomena involved can be gained. For example, while the flow visualization studies previously mentioned have provided considerable information on whether or not the flow is attached at a particular location on these wings, comparing details of the pressure distributions from the calculations with the measurements provides further insight into this matter. Furthermore, at sections where the flow is known to be attached, the extent of the disagreement of the present calculations with the measurements is an indication of the importance of the phenomena not included in the calculations: boundary-layer displacement effects in attached regions, the effects of the separated wake, and the effects revealed in the flow-visualization studies of the vortical flow emanating from the break in the planform of the drooped wing.

To begin, the geometry of the two wings investigated and the paneling layouts used for the calculations are described. The wings modeled are described in detail in reference 1 and are shown in figure 2. The wing with outboard droop is designated "Modification B" in reference 1. The basic airfoil section is a modified 64_2 - 415; the drooped section provides a 3-percent chord extension to this section which results in increased leading-edge camber and radius. The coordinates presented in reference 1 for the basic and drooped sections were used here.

The fuselage shown in figure 2 was not modeled; instead, the wing was extended to the configuration centerline. The basic wing has an aspect ratio of 6.10, constant chord, 5 degrees of dihedral, no twist, and is set at 3.5° incidence with respect to the reference line for angle of attack used in reference 1 and in this report.

Each wing was analyzed using 40 chordwise surface panels (20 top, 20 bottom) and 10 spanwise panels on the semispan. The spanwise distribution of panels is the same for each wing: panels are concentrated in the location of the break in planform of the wing with outboard droop and near the wing tip using half-cosine and cosine distributions, respectively. The chordwise distributions of panel control points used for most of the calculations are shown in figure 13. A modification of the distribution investigated for the drooped section is discussed later. In figure 13, the triangles are the control points of the surface panels generated by VSAERO at the spanwise location shown, and the circles are the section data from reference 1 (plus some manually interpolated points near the leading edge) which were input at other spanwise locations to define the wing. Plots like figure 13 (with their expanded vertical scale) were used to ensure that the wings' geometries were correctly described.

In the following, results are shown for the basic wing and the wing with outboard droop at three angles of attack, α = 11.2°, 21.6°, and 31.9°. These angles were selected because detailed data are available at these conditions in reference 1, and because they allow illumination of some of the similarities and differences in the performance of the two wings. Referring to figure 1, for the first two of these angles, the overall performance of the two wings is essentially identical. At α = 31.9°, however, the lift of the basic wing

has deteriorated significantly while that for the drooped wing remains on the "flat top" portion of the curve.

Some results from VSAERO for the basic wing are shown in figures 14-18. In figure 14, the calculated lift on the outer wing panel is compared to measurements from reference 1; the two symbols shown representing the calculation at each α are for different trailing wake shapes. The symbol for iteration 2 at each α represents the solution after the wake has been relaxed once by VSAERO from its input location. It is seen that the solution for $\alpha = 21.6^{\circ}$ may not yet be converged in this sense. Agreement with the data is reasonably good, even at $\alpha = 21.6^{\circ}$ (here the pertinent measurements are the "maximum readings" which presumably represent the fully attached state in a fluctuating separation condition). The calculation at $\alpha = 31.9^{\circ}$, discussed further below, is not shown on this figure since the flow is obviously separated at this angle and no correspondence with the fully attached calculation can be expected. Referring back to figure 1, the lift calculated for the entire wing is shown at $\alpha = 11.2^{\circ}$ and 21.6° (only the value for the last iteration is shown). At 11.2°, the overall lift agrees fairly well with data, as does the lift on the outer panel. At $\alpha = 21.6^{\circ}$, the disparity is large, reflecting the fully stalled inner wing region and the intermittent stall on the outer panel which, according to figure 14, dominates the averaged readings.

Comparisons with data at a more detailed level are shown in figure 15. Here the span-loading distribution is shown for three angles of attack: $\alpha = 11.2^{\circ}$ (fig. 15(a)) where the data of reference 1 indicate that the flow is steady and attached to the wing except possibly in a small region near the trailing edge in the inboard sections; $\alpha = 21.6^{\circ}$ (fig. 15(b)) where the inboard portion of the wing is stalled and the outboard portion

is undergoing the random separation and reattachment indicated in figure 14; and $\alpha = 31.9^{\circ}$ (fig. 15(c)) where the data indicate that the wing is fully stalled. Although there is generally room for improvement, presumably through inclusion of boundary-layer displacement effects, agreement of the calculations with data at $\alpha = 11.2^{\circ}$ is reasonably good, except at $y_{\ell e}/s \approx 0.38$. The chordwise distributions discussed below indicate that the discrepancy at this section is due to small errors in the calculated loading over the entire section; the difference is not apparently due to separated flow at this spanwise location. At the higher-alpha conditions, where the time-averaged measurements are heavily weighted towards the stalled state, correlation with the fully attached calculation is poor, except perhaps near the wing tip at $\alpha = 21.6^{\circ}$.

The most detailed data which exist, and for the present purposes the most useful, are chordwise pressure distributions at various spanwise stations. Comparisons of the results from VSAERO with the data are made at those spanwise locations where the panel control points (the locations where the calculated values are known) are within about 2% semispan of the measurement locations. It was not felt necessary, at this stage, to refine these comparisons by interpolating on spanwise location in the calculated results (or the data). Under these ground rules, comparisons are possible with the data taken at 38, 78 and 92% semispan. These comparisons are shown for the basic wing in figures 16 ($\alpha = 11.2^{\circ}$), 17 ($\alpha = 21.6^{\circ}$), and 18 ($\alpha = 31.9^{\circ}$).

In figure 16 ($\alpha = 11.2^{\circ}$), it is seen that the overall favorable agreement between calculation and data previously indicated for the overall lift coefficient and the span load distribution is also present at the detailed pressure-distribution level for this attached-flow case. The basic

behavior of the measured pressure distributions seems to be captured by the calculation, and it is supposed that inclusion of attached-flow boundary-layer effects would further improve the agreement. At $\alpha = 21.6^{\circ}$, it is seen that at $y_{\ell e}/s \approx 0.38$ (fig. 17(a)) the data have the characteristic constant-pressure region associated with separation, while the fully attached calculation, of course, does not. Note that the scale of the ordinate has been changed in going from figure 16 to figure 17. The same apparent discrepancy represents a bigger difference in C_p in figure 17 than in figure 16. The data taken further outboard (figs. 17(b) and (c)) are in the region undergoing intermittent separation, as was discussed in relation to figure 14. Because the measurements were made using a rapid-scanning system with an approximate 0.4-second stepping time from port to port, in this region the pressure distributions may be a mixture of attached and stalled data points, and any conclusions drawn from the comparison with the predictions would be of questionable value. At $\alpha = 31.9^{\circ}$ (figure 18), the data indicate separated flow at all three spanwise locations; from figure 14, it is seen that the stall in this region is steady, not intermittent.

Corresponding detailed results are presented for the wing with outboard droop in figures 19-22. The predicted integrated lift for this wing is shown in figure 1, and span load distributions are shown in figure 19. At $\alpha = 11.2^{\circ}$ (fig. 19(a)), good agreement is shown (again except at $y_{\ell e}/s \approx 0.38$) for this attached-flow case, similar to the results for the basic wing. At $\alpha = 21.6^{\circ}$ (fig. 19(b)), again like the basic wing, agreement with the data is poor inboard but somewhat better outboard, indicating that the wing tip has attached flow; this is confirmed by the chordwise distributions shown below. At the highest angle of attack, $\alpha = 31.9^{\circ}$ (fig. 19(c)), the measured span load is in accord with the observation from the

flow visualization studies that the flow remains attached on the outer sections. The lack of agreement with the attached calculation inboard directly reflects the omission from the calculation of the viscous effects; the discrepancies outboard are likely an indirect manifestation of the lack of a separated wake in the inboard portion.

The chordwise pressure distributions for the wing with outboard droop are shown in figures 20 ($\alpha = 11.2^{\circ}$), 21 ($\alpha = 21.6^{\circ}$), and 22 ($\alpha = 31.9^{\circ}$). Note again that a different scale is used for the ordinate for the low-angle-of-attack case than for the other two. Also, remember that the basic section is used in this wing for $y/s < 57\%$, so the calculated pressure distribution changes shape dramatically at this location, i.e., between parts (a) and (b) of each of these figures. At $\alpha = 11.2^{\circ}$ (fig. 20), corresponding to the situation for the basic wing, essentially good agreement with the data is shown. The behavior at $\alpha = 21.6^{\circ}$ (fig. 21) is also like that for the basic wing with separated flow inboard, attached flow outboard. Where the flow is attached, the differences between the calculated and measured distributions are reasonably small. At $\alpha = 31.9^{\circ}$ (fig. 22), the drooped wing retains attached flow on the outer panel, and in this region (figs. 22(b) and (c)) the present calculations again exhibit the major features of the measured chordwise distributions. However, the differences which do exist in these distributions (which appear somewhat subtle) when integrated over the chord result in the quite-obvious discrepancies in c_n shown in figure 19(c). For example, at $y_{\ell e}/s \approx 0.78$ (fig. 22(b)), discounting the absence of the very localized high suction peak in the data, the measured upper-surface distribution near $x_s/c = 0.05$ is quite different from the prediction, and the difference may represent the effects of the discrete vortex observed by flow visualization. Also, over the last 45% of the wing there is a considerably larger $\Delta C_p = C_{p_\ell} - C_{p_u}$

than is predicted. This latter observation also pertains to $y_{\ell e}/s \approx 0.92$ (fig. 22(c)). In this case, the agreement with measurements in the forward half of the wing is fairly good. If the discrepancy between the predicted and measured integrated load at this section from figure 19(c) is represented by a constant ΔC_p over the last 45% of the section, the cross-hatched band in figure 22(c) results. Comparison of this band with the measured and predicted ΔC_p in this region shows that the underprediction of ΔC_p here is sufficient to account for the discrepancy in integrated load. It remains to be seen, of course, whether modeling the inboard separated flow and allowing for local displacement effects can account for these differences.

It should be mentioned that the calculations for the wing with outboard droop at $\alpha = 31.9^{\circ}$ were made with a slightly modified chordwise paneling distribution than was presented in figure 13(b). The original distribution resulted in irregular behavior near the wing leading edge. When the same number of panels were redistributed in this region, the smoothly varying calculated results shown in figure 22 were obtained.

A PRELIMINARY ATTEMPT AT PREDICTING SEPARATION

While the focus of the present work was on inviscid calculation schemes, it was desirable to determine if anything could be learned from perhaps the simplest procedure currently used to predict separation, that due to Stratford (ref. 25). This procedure predicts separation when a quantity involving the product of the level and streamwise derivative of the potential pressure coefficient exceeds a certain value; for turbulent separation, this value depends on the Reynolds number. This procedure was applied to several of the pressure distributions

calculated using VSAERO. It was found that the extremely high suction peaks calculated near the leading edge of the basic wing profile (see figs. 16-18) result in Stratford-predicted turbulent separation essentially at the leading edge even at $\alpha = 11.2^{\circ}$, in constrast to experimental observations. For the drooped section, at $y_{\ell e}/s = 0.78$ the predicted separation is near 60% chord at $\alpha = 11.2^{\circ}$ and near 45% chord at $\alpha = 21.6^{\circ}$. These locations are perhaps compatible with the physical situation, although precise separation lines have not been defined in the experiment. However, the inability of the Stratford analysis to deal properly with the predicted pressure distributions for the basic wing profile seemingly requires use of a more sophisticated separation analysis.

RECOMMENDED APPROACH TO DEVELOPING A PREDICTION METHOD

The fundamental assumption has been made that the problem of interest, which features strong coupling between the inviscid and viscous flow regimes, can be approximately treated using the iterative scheme presented in the Approach section. For the reader's convenience, the description of this scheme is repeated here:

1. An inviscid (fully attached) calculation is made for the wing, resulting in an inviscid pressure distribution.

2. A boundary-layer analysis is applied to this pressure distribution to result in a predicted detachment line and a distribution of displacement thickness in the attached region. The boundary-layer analysis must be properly formulated to allow calculation through separation.

3. The inviscid analysis is repeated, allowing for boundary-layer displacement effects in the attached region and the effects of the separated wake. The effects of a discrete vortex originating at the break in the leading edge may have to be accounted for.

4. Steps 2 and 3 are repeated until convergence.

Based on the work to this point, it appears that VSAERO is the existing inviscid method most likely to be successfully applied to this problem. In the following, the reasons for this choice are briefly reviewed, drawing on the study of the literature and the calculations which have been made. Then the steps of an investigation are outlined which will lead to the desired method.

While the existing version of VSAERO does not possess all of the features necessary for application to this problem, the literature review suggests it is the best available method. It has three important attributes: (a) it is a surface-singularity method and thus has the potential of generating surface pressures with the accuracy necessary to predict the location of separation; (b) the ability to represent the separated wake with a singularity distribution is being incorporated into the program in a current government-sponsored study; and (c) its solution procedure allows for iteration with a boundary-layer analysis. An integral boundary-layer analysis is included in the version of VSAERO available to NEAR, Inc. for this study, but its suitability for application to this problem has not been evaluated. This topic is discussed further below. A feature that VSAERO does not possess, and which may emerge as important, is the ability to include the effects of a

concentrated vortex springing from the break in the leading edge of the wing with outboard droop. This is also discussed further below.

In a calculation in the literature, using a specified separation line, a frozen separated wake and no boundary-layer displacement effects in the attached region, good agreement was shown with pressure distributions measured at high angle of attack on a simple swept rectangular wing. The present calculations for the basic wing and the wing with outboard droop, done without the effects of a separated wake or boundary-layer displacement effects, show good agreement with data for wholly attached flow. At higher angles of attack, the discrepancies between the calculations and the data illuminate the importance of the unmodeled phenomena to the pressure distribution on the entire wing. In the inboard region, which is fully separated, the effects are, of course, major; in the outboard region, the effects of the separated wake are somewhat more subtle, but crucial to the accurate prediction of separation. Near the planform break in the wing with outboard droop, the effects of a discrete vortex may also be important.

The following suggested program of work addresses the outstanding technical questions in a sequential manner, building in capability as it is shown to be needed:

1. Available integral turbulent boundary-layer methods should be studied and the best one selected for application to this problem. The need to include the ability to treat small regions of laminar separation and transition should be examined and existing approximate methods coupled with the turbulent method, if appropriate. The first applications of the method selected should be along stream-lines in the wholly

attached calculations made for the basic wing and the wing with outboard droop. That is, step 2 in the scheme above should be implemented. The detachment criterion of reference 24 should be applied in conjunction with this analysis. The result of this is the first estimation of the location of the separation line.

2. When VSAERO has the massive-separation option available, it should be applied using the separation line predicted as just described, and the remainder of the iterative procedure pursued to convergence. It may be found during this process that the detachment criterion recommended for use requires adjustment to allow the converged solution for the separation line to agree with data.

3. At this point, all but one of the physical phenomena currently thought to be important will have been at least approximately modeled. The missing element is a discrete vortex at the planform break in the wing with outboard droop. If the pressure distributions and separation behavior in this vicinity are still inadequately treated, this phenomena should be included.

4. The resulting optimal method should be applied to some of the other drooped-wing geometries described in reference 1. These geometries include variations in the location of the inboard end of the outboard droop, a wing where the droop exists over the entire span, segmented-droop configurations, and an outboard- droop configuration with a fillet at the break in the leading edge. These perturbations are known to exert a strong

effect on the performance of the wing, and will allow stringent testing and further development of the prediction method.

Successful pursuit of this research program should result in the best method attainable within the underlying assumptions that the iterative approach and the use of two-dimensional boundary-layer methods are adequate. Improvement of predictive capability beyond this point will likely be expensive and will probably require that these fundamental assumptions be relaxed. That is, further improvement may require that adequate three-dimensional boundary-layer methods be developed and used, or that, ultimately, the problem be treated as an entity with an application of the Navier-Stokes equations. The incremental benefits derived from either of these developments will come at high cost.

PART 2. THE GENERALIZED RESEARCH FIGHTER

APPROACH

One of the distinguishing features of modern high-performance supersonic fighter aircraft is a high degree of maneuverability at subsonic speeds. In this mode, the longitudinal and lateral aerodynamics of the aircraft are dominated by the nonlinear effects of vortical flows, and there has been a large amount of work in recent years devoted to the understanding of these flows. In perfectly logical fashion, most of this work has dealt with only a portion of the entire configuration, e.g., treating the high-angle-of-attack aerodynamics of an isolated wing or of an aircraft forebody. In this portion of the report, results are described of work which aims at building on this foundation in order to establish the ability to predict the longitudinal and lateral performance of the complete configuration.

The configurations of interest are confined to those which consist of a nose (or forebody), a highly swept low-aspect-ratio wing with strakes or leading-edge extensions (all with sharp edges), and a tail assembly. As the angle of attack of such a configuration is increased, it is well known that the flow on the nose eventually separates and rolls up into one or more pairs of symmetric discrete vortices which then proceed aft over the remainder of the configuration. Additionally, a pair of vortices appears over the strakes, fed by the shear layers that

leave the strake leading edges, and possibly (depending on the geometrical details) still another set over the wings, fed by the wing leading and side edges. The nose vortices interact with the strakes and wing, the various vortical systems interact with one another, and the combination interacts with the tail to produce behavior considerably different than that predicted by traditional linear analysis. As angle of attack is increased still further, it is known that the nose vortices spontaneously develop asymmetry, producing side forces and yawing moments even though the configuration is at zero sideslip, and the various vortical systems may break down (or "burst"), usually as a result of the influence of the adverse pressure gradients encountered as they pass over the wing.

Just as is the case for the general aviation wing described in the first half of this report, prediction of this behavior requires satisfactory treatment of the separated flows involved. However, for the strake and wing there is a feature of the present problem which provides for a powerful simplification of the necessary analytical treatment: the location of separation is known to be at the sharp leading or side edge, so no interaction with a viscous analysis to predict the location of the separation line is necessary.* The focus can therefore be on inviscid modeling, wherein the effects of the separated flows are represented via singularities in the usual variety of ways.

---

*The foregoing brief description of the governing phenomena omits mention of the secondary separation vortices which form on the wing (see, for example, ref. 26). The location of the secondary separation is not known a priori; detailed calculation of these vortices would therefore require interaction with a boundary-layer analysis. However, these vortices are relatively weak, and it will be shown that satisfactory predictions can be made without considering them.

In the next section, the prediction methods are briefly reviewed which exist for the portion of the configuration which dominates its overall behavior, the wing. No attempt is made to duplicate the recent comprehensive reviews of references 26-28, but rather the important points made in those surveys are noted and a few methods introduced after their publication are included. Based on this information, an approach is selected for incorporation into the overall analysis of the entire configuration, and the complete analytical scheme is described. At the present time, this scheme is applicable to low subsonic Mach numbers and to angles of attack below those at which the effects of vortex bursting are important. The relaxation of the latter restriction is discussed later. Furthermore, the only vortex asymmetries considered are those due to sideslip; that is, the formation of an asymmetrical nose field at very high angle of attack (but $\beta = 0$) is not considered.

The extensive data base which exists for a generic fighter configuration called the Generalized Research Fighter (GRF) is then reviewed. This data base (together with selected results for simple wing planforms) allows the evaluation of the accuracy of some preliminary calculations made with the integrated analytical scheme, as well as an evaluation of the sensitivity of the predictions to some of the assumptions incorporated in this scheme. These results are presented next. Finally, recommendations are presented for the improvements needed in this scheme, and an approach is identified which will ultimately yield a method capable of accurately and economically predicting the longitudinal and lateral aerodynamics of a complete configuration.

REVIEW OF EXISTING METHODS FOR HIGHLY SWEPT WINGS

In references 26-28, comprehensive reviews are presented of prediction methods which deal with this topic, and a large number of methods are discussed involving varying levels of complexity and computational cost. Varying levels of accuracy are, of course, achieved by the different implementations of the different types of methods, but at each level of detail there is generally some success achieved. It is shown, therefore, that the selection of a computational method for a particular application should depend on the degree of detail desired to be accurately represented by the model (i.e., pressure distributions vs. overall forces), and that an increasing level of detail carries with it increased cost.

In the following, no attempt is made to reproduce these surveys, nor are all the individual implementations of the methods cited therein listed. Rather, the major categories of methods are given together with a brief description of the essential features common to the methods in that category:

1. Methods based on slender-body theory (including conical-flow methods). The fundamental feature here is the simplification of the governing equations accomplished by neglecting any dependence on the longitudinal flow. This simplification is also responsible for the fundamental weakness of this category of methods: because no signals are allowed to propagate upstream, loadings do not fall off correctly as the trailing edge is approached, and overall forces and moments are incorrectly predicted. However, far from this region, reasonable agreement with measured pressure distributions have been obtained.

2. Methods based on the suction analogy of Polhamus (ref. 29). In its simplest form, for a delta wing, the method proceeds as follows. A potential solution is calculated for the attached flow on the wing. The resulting in-plane force (which manifests itself as a suction force normal to the leading edge) is assumed equal in magnitude to the vortex lift which occurs near the leading edge. This model has been extended in a number of ways, as is discussed further below, and is remarkably successful in estimating overall forces and moments at small computer cost. However, it does not provide details of the surface pressure distribution.

3. Methods wherein the vorticity leaving the leading edge is modeled using discrete vortex filaments. This approach is a natural extension of the vortex-lattice method to the case of leading-edge separation. A set of line vortices emanates from the leading edge; each of these vortices is forced, in an iterative solution procedure, to follow a streamline of the converged three-dimensional flow over the wing. It is observed that this technique yields fairly accurate results for overall loads, but that pressure distributions are not well predicted unless very large numbers of vortex elements are used. Furthermore, the strong algebraic singularity associated with the Biot-Savart law leads to convergence difficulties in some cases.

4. Methods wherein the vorticity leaving the leading edge is modeled using a free vortex sheet. This is the most elegant (and the most costly) category of methods reported on; just as the previous category is a logical extension of the vortex-lattice method, this category is a logical extension of a surface-paneling method.

> In this representation, the free sheet is represented by doublet panels whose strength and positions are determined by iteration using the criterion that the sheet be locally force free. There have been a number of implementations of this approach, using both high-order (e.g. refs. 30 and 31) and low-order (e.g., ref. 8) singularity distributions, and good success has been achieved in predicting pressure distributions as well as overall loads.

Based on this description, methods in categories 1 and 3 can be immediately eliminated from further consideration for incorporation into a preliminary-design method suitable for analyzing a complete configuation. The methods of category 1 are too simplified; even overall loads are not predicted accurately. As for the methods of category 3, they offer no more accuracy than those of category 2 unless the number of vortex elements becomes large, and in this case, the computing cost increases dramatically. Under these conditions, the methods of category 4 should be considered.

The real choice, then, is between methods based on the Polhamus analogy (which predict overall loads but not pressure distributions and are economical to use), and free-vortex-sheet methods (which if used with sufficient care can also predict pressure distributions accurately but are complex and more expensive to use). Because a method is sought which is useful during preliminary design (at which stage detailed pressure distributions are not usually required), and because unnecessary complexity is to be avoided as the method is applied to a complete configuration, a procedure based on the Polhamus analogy seems the obvious choice. More detail about the structure of this category of methods is presented next.

As described in reference 27, the basis of the approach is as follows. Wings which have attached flows develop suction forces along their leading edges if the stagnation surface does not lie along that edge. This suction force can be calculated by either integrating the pressure near the leading edge over the edge thickness or taking the product of the square of the induced tangential velocity and the distance to the edge. For a wing of infinitesimal thickness the induced tangential velocity approaches an infinite value; however, the product of its square and the distance to the edge is still finite.

If the flow separates from the wing in going around the leading edge due to its sharpness or thinness, or due to a combination of thickness and angle of attack, the suction force in the chord plane is lost. However, if this separated flow forms into a shed vortex which causes the flow to reattach to the leeward surface of the wing, then the fluid energy re-distributes on the wing upper surface near the leading edge resulting in the development of vortex lift. The suction analogy states that for the separated flow situations, the potential-flow leading-edge suction force becomes reoriented from acting in the chord plane to acting normal to the chord plane (a rotation of 90°) by the local vortex action resulting in an additional normal force. The reasoning is that the force required to maintain the reattached flow in a situation associated with the separation-induced vortex flow is the same as that which had been required to maintain the potential flow around the leading edge. Therefore, the suction-analogy concept provides a link between attached-flow solutions and the effects of this particular type of separated flow.

According to the analogy, the reattachment line or details of the pressure field need not be known in advance in order to determine the reattached-flow force. However, if pitching-

moment estimates are needed, the distribution of the reattached force must be determined. The centroid of the leading-edge suction has been used as the longitudinal location of this force. This assumption does not have provision for angle-of-attack effects on the location of the reattachment line or vortex core; hence the core is assumed to remain stationary near the wing leading edge.

Extension of the suction analogy to the calculation of vortex lift at side edges has been done in reference 32 and several implementations using vortex-lattice methods exist (see, for example, ref. 33). In applications of the method including side-edge vortex lift, need for a further modification has emerged. This modification is termed augmented vortex lift (ref. 34), and it arises from the well-established fact that for many delta wings, the leading-edge vortex generated on the wing persists for a considerable distance downstream and therefore can act on other surfaces, such as the aft part of more generalized planforms. This persistence is not accounted for in the suction analogy because the analogy deals only with the edge forces generated along a particular edge, such as leading-edge vortex lift resulting from the leading-edge suction force. The fully extended method, therefore, calculates the total lift (C_L) on a configuration such as a cropped delta wing according to the relation

$$C_L = C_{L_p} + C_{L_{v\ell e}} + C_{L_{vse}} + C_{L_{va}} \tag{2}$$

where C_{L_p} is the potential contribution, $C_{L_{v\ell e}}$ and $C_{L_{vse}}$ are the Polhamus leading- and side-edge contributions, and $C_{L_{va}}$ is the augmented-vortex-lift term. Procedures for calculating $C_{L_{va}}$ have been developed which depend on the planform, and in some cases, on the angle of attack. This has been done for simple

planforms in reference 34, for double-delta wings in reference 35, and for strake-wing configurations in reference 36. It has been determined that $C_{L_{va}}$ may be negative for particular planforms, such as arrow wings, because the full value of the available vortex lift cannot be achieved due to "lack of complete flow reattachment due to trailing edge notching" (ref. 37).

In an implementation of the Polhamus approach which does not include the augmented-lift term (ref. 33), the need to modulate the amount of the leading-edge suction force converted to vortex lift for delta wings of varying aspect ratio was demonstrated. In this implementation,

$$C_L = C_{L_p} + K_v^* C_{L_{v\ell e}} \tag{3}$$

where K_v^* is a parameter ($0 \leq K_v^* \leq 1$) depending on aspect ratio (or equivalently, leading-edge sweep angle). A correlation for K_v^* was developed in that reference which made use of all known available experimental data. As shall be shown later, in applying the Polhamus analogy to complex planforms, it has been found necessary to use a combination of the ideas embodied in equations (2) and (3), that is, to modulate downward the amount of leading-edge suction converted to vortex lift while still allowing for augmented vortex lift.

A PREDICTION METHOD FOR THE COMPLETE CONFIGURATION

In this section, a summary of the approach used to calculate the forces and moments on a complete configuration is given. The major features of the method are schematically illustrated in figure 23. Further detail is contained in Appendix B.

The loads on the nose (defined as ending at the intersection of the strake leading edge and the body) and the vortex field shed by the nose are calculated using program VTXCLD (ref. 38). This program is applicable to circular and noncircular bodies at angles of attack and roll, and is valid up into the asymmetric shedding regime. Noncircular cross sections are handled by means of analytical or numerical conformal transformation to circular cross sections. The actual three-dimensional steady-flow problem is reduced to a two-dimensional unsteady, separated flow problem for solution. The two-dimensional solution is carried out in the crossflow plane where the flow about a body in the presence of discrete vortices is obtained. At each time step, corresponding to an interval of length on the body, the body cross section is changing, and a new vortex pair is shed into the flow field from the separation points. The discrete vortices forming the wake are allowed to move in the flow field under the influences of the free-stream flow, the body, and the other vortices.

The calculation procedure for the nose is carried out in the following manner. Starting at a crossflow plane near the beginning of the nose, the potential pressure distribution on the body is computed using the full Bernoulli equation, including unsteady terms. The boundary layer in the crossflow plane is examined for separation using modified versions of Stratford's laminar or turbulent separation criteria. At the predicted separation points, vortices are shed into the flow field. The strength of these vortices is determined from the vorticity transport in the boundary layer. The paths taken by these free vortices are calculated by integration of the equations of motion of each vortex in a stepwise fashion using a variable-step-size differential equation solver. In the next downstream crossflow plane, the free vortices are allowed to

influence the body pressure distribution and the motion of other vortices in the field. Thus the shed wake has an influence on the predicted separation points in subsequent crossflow planes and it also influences the local force on the body. This procedure is carried out over the entire length of the nose, and the final vortex field and the integrated loads are written out to a file for later use in program ASYMVL, described next.

In ASYMVL, the remainder of the body with its lifting surfaces is broken into a series of regions, in each of which the calculation is carried out allowing for full mutual interference among the lifting surfaces in that region and the resultant image systems in the fuselage (assumed circular). Each quadrilateral lifting surface (henceforth called a fin) is represented by a chordal-plane vortex lattice. The tail region may include a single vertical tail and/or two horizontal tails. The solution in each region is done by calculating the strengths of the lattice singularities so that at each control point in the lattice, the resultant velocity normal to the actual mean surface (i.e., allowing for camber) is zero. Although the slope of the mean surface is thus accounted for, this tangency condition is applied in the plane of the lattice. Nonlinear vortex-lift effects are included through an application of the Polhamus suction analogy, described earlier. In the current version of ASYMVL, the approach associated with equation (3) is used. That is, there is currently no allowance for an augmented-vortex-lift term; in our application, however, the generalization of equation (3) to allow for vortex lift at a planform side edge is used:

$$C_L = C_{L_p} + K^*_{v_{\ell e}} C_{L_{v\ell e}} + K^*_{v_{se}} C_{L_{vse}} \qquad (4)$$

Values of $K^{*}_{v\ell e}$ and K^{*}_{vse} are specified by the user. This topic will be discussed further in the section describing applications of this method.

The solution in each region of ASYMVL allows for the existence of external vortices as calculated by VTXCLD; furthermore, in aft regions, vorticity shed by lifting surfaces in forward regions is included in the calculation. That is, in any region, vortices generated in a forward region (called "impressed" vortices) affect the loads through being included in the lifting-surface boundary condition. Vortices generated within the region affect the loads only through the Polhamus analogy.

The trajectories of the vortices from VTXCLD through each region are assumed parallel to the fuselage center line (constant y and z, fig. 23). This is known to be a major over-simplification. Improvement in this area can be achieved by applying the methods of reference 33 to the tracking of these vortices in and between the lifting-surface regions, as discussed later.

The loads on each lifting surface are calculated from application of the Kutta-Joukowski law to each element of the vortex lattice. Spanwise distributions of the potential and leading-edge suction loads are calculated and are used to determine the positions of the Polhamus vortices which then become impressed vortices in aft regions. The leading-edge vortex inboard of a break in sweep is assumed to stream back over the remainder of the configuration at the lateral position of the centroid of the leading-edge suction. Within its region of generation, its vertical track is assumed to follow an angle equal to one-half the local flow angle starting at the axial position of the intersection of the strake leading edge with the

body. This assumption is based on experimental observation, as discussed in reference 33.

Downstream of the trailing edge of the region in which it is generated, the leading-edge vortex remains at constant z. If a sufficiently long fuselage section existed between the wing and tail regions, the vortex could be tracked using VTXCLD. For the current study, this is unnecessary. The vortex outboard of a break in sweep, which is obtained by combining the leading-edge and side-edge vortices, is also assumed (in its region of generation) to track at half the local flow angle (starting at the axial position of the break). Its lateral position is at the centroid of the combined leading- and side-edge suction distributions. In aft regions, it also tracks at constant y and z.

The trailing-vortex system from the potential lift for each lifting surface is also available from the loading calculations. The vortex-lattice method results in a trailing-vortex filament from each column of the lattice network, which goes to downstream infinity in the fin chordal plane. The system of trailing vortices for each lifting surface is thus distributed across the span, with the vortices originating in the plane of the lifting surface at the lifting-surface-region trailing edge.

The carryover loads on the fuselage due to the loads on each lifting surface are calculated in the spirit of slender-body theory, and then the entire procedure is repeated for the tail region. From the loadings on the various components of the configuration, the complete configuration normal and side forces are calculated. From calculation of the centers of pressure of the various loadings, the pitching, yawing and rolling moments of the configuration are also computed.

DATA BASE FOR THE GENERALIZED RESEARCH FIGHTER

In a series of reports predominantly from the NASA/Langley Research Center (refs. 39-44), the aerodynamic performance of a generic fighter configuration has been documented in some detail. This configuration, called the Generalized Research Fighter (GRF), consists of a nose, a vertical tail, and a number of strake and wing variations. All of the tests reported have been at a single scale except for references 40 and 44. In reference 40, the model used was 2.4 times larger and in reference 44 it was 50% smaller than in the other studies. In related investigations, the effects of canards, horizontal tails, and multiple vertical tails have been investigated, but these studies are not considered here. One particular implementation of the GRF is shown in figure 24 (from ref. 43), in which the dual-balance system used in some of the testing is indicated. Use of two balances has allowed the determination of the performance of the nose/strake portion of the configuration as well as of the entire vehicle.

The cross section of the nose of the GRF is initially circular but transitions to the slab-sided geometry shown in the end view of figure 24. In side view, the nose is defined as if it were a tangent-ogive of fineness ratio 2.18. The GRF strakes in references 41-44 are flat plates with a reflexed planform and beveled leading and side edges. Those shown in figure 24 are the largest tested ("strake 3" in ref. 43) and are one member of a family of three. The other two members feature the same general planform but progressively smaller span. No strakes (or vertical tail) were included in reference 39, and in reference 40 a simple delta strake was used. The wings in the test series have varying leading-edge sweep, with values of 30°, 40°, 44°, 50° and 60° used in various of these studies. The reference area (1032 cm^2), section (double circular arc), and distribution

of maximum thickness (6% of chord at the root varying linearly to 4% at the tip) remain constant for these wings, as do the span, and the root and tip chords (fig. 24).* The vertical tail has the dimensions shown in that figure, and the same section and thickness distribution as the wing.

The range of data available for the various configurations of the GRF is shown in Table 1. In that table, the numbered strakes are identified as in reference 43; that is, the exposed semispans are 10% (strake 1), 20% (strake 2) and 30% (strake 3) of the wing semispan. The information in this table was used to guide the selection of the configuration to be used for some preliminary calculations using the scheme described in the preceding section. It is seen that the most complete data exists for the wing with a leading-edge sweep angle of 44°, and that the experimental coverage is the same for all of the numbered strakes, except that vortex bursting information exists for strake 3. Because of this additional information and because the effects of the strake increase in magnitude with strake size, we selected strake 3; the configuration to be modeled is thus that shown in figure 24.

---

*Except for references 40 and 44, in which scale factors of 2.4 and 0.5, respectively, were used. A wing sweep of 44° was used in these studies.

PRELIMINARY CALCULATIONS WITH THE OVERALL METHOD

In this section, the calculation method consisting of programs VTXCLD and ASYMVL is applied to the GRF configuration of figure 24, treating body-strake, body-wing, body-strake-wing, and body-strake-wing-tail variations. First, however, it is useful to examine some results obtained from ASYMVL as applied to some simple wings (all flat plates with sharp edges).

Simple Wing Planforms, $\beta = 0^{\circ}$

Calculations are made for two rectangular wings, a cropped arrow, a cropped delta, and a double delta to examine various features of the method without the complications introduced by a body, nose vortices or tail.

The rectangular-wing cases serve to demonstrate that the Polhamus vortex-lift analogy has been properly applied for the side edge as well as for the leading edge. Predictions made using ASYMVL are compared to measurements and to calculations made with another implementation of the Polhamus analogy with a vortex-lattice method, that of Lamar (ref. 45), in figures 25 and 26. Figure 25 is for an aspect ratio (AS) of 0.2, while figure 26 is for AS = 1.0. The differences between the calculations of Lamar and ASYMVL in these figures are very small and are presumably due to the different paneling layouts used (Lamar used 6 chordwise x 25 spanwise panels, ASYMVL used 5 x 10), a subject discussed below. The separate contributions of the potential, leading-edge, and side-edge lift are shown. The sum of these terms agrees quite well with the measurements. The center of pressure of the side-edge contribution, however, is seen to be predicted somewhat too far aft as compared to the data.

In figure 27, the calculations of Lamar and ASYMVL for the potential, leading-edge, and side-edge terms for a cropped arrow are again essentially identical. Here, however, the calculation of Lamar shows the effect of the augmented-vortex-lift term (eq. 2). For this planform, the "augmentation" term is negative, and it is seen that the inclusion of this extra term leads to improved agreement with the measurements.

Figure 28 shows a cropped-delta wing where the augmentation term is positive. In this figure, it is shown that the ASYMVL calculation is in good agreement with Lamar's for the potential term and the combination of the leading- and side-edge terms, but that the individual leading- and side-edge vortex-lift terms are somewhat different in the two methods. This may reflect the way the contribution from the swept bound-leg vorticity is handled in these schemes. It is further noted that inclusion of the augmented-vortex-lift term is again required to achieve good agreement with data.

Returning briefly to the question of paneling layout, the ASYMVL calculations in figure 28 were accomplished using 5 chordwise panels by 14 panels over the wing semispan, and those of Lamar were done using a 6 x 25 layout. Sensitivity of the calculation to this difference is examined in figure 29, where the ASYMVL-calculated potential normal force is shown for various paneling layouts. It is seen that the dependence on the number of chordwise panels is weak (5 seems to be sufficient), but that more than 14 spanwise panels (the current maximum value allowed in ASYMVL, see Appendix B) are required to reach the asymptotic value.

The final wing-alone test calculations were for the double delta with $80^{\circ}/60^{\circ}$ leading-edge sweep angles reported on in reference 46. ASYMVL results were obtained using 7 panels

in the chordwise direction and 14 panels on the wing semispan, 7 inboard and 7 outboard of the leading edge break. In each of the inboard and outboard regions, the panels were spaced using a "1/2-cosine" distribution so that the panels were narrower at the outer edge of the region. Our previous experience with the correlation developed in reference 33 for $K^*_{v\ell e}$ (eq. 4) for simple delta wings suggests that, as long as the planform is not cropped and has no trailing-edge cutouts, the correlation can be used for each segment of the double delta. Accordingly, this correlation was applied for the region inboard ($\Lambda_{\ell e} = 80^\circ$, $K^*_{v\ell e_1} = 0.95$) and outboard ($\Lambda_{\ell e} = 60^\circ$, $K^*_{v\ell e_2} = 0.55$) of the break. The resulting calculations are compared with the measurements from reference 46 in figure 30. Excellent agreement is shown up through the angle of attack at which vortex breakdown was observed in the experiment.

While the overall lift coefficient is calculated quite accurately, some features of leading-edge vortices are not. As described earlier and in more detail in Appendix B, the leading-edge vortex for the region inboard of the break is assumed to lie laterally at the location of the centroid of the leading-edge suction distribution for this portion of the wing, and to track at $\alpha/2$ from the wing apex. The outboard vortex is assumed to lie laterally at the centroid of the leading-edge suction for the portion of the wing outboard of the break, and to follow an $\alpha/2$ trajectory starting at the break location. While these assumed vortex paths have no effect on the wing loads in the current implementation of ASYMVL, they can exert important influences on the loads on aft components, as is shown later in calculations for the GRF. The vortex positions which result from these assumptions are compared to total-pressure contours and velocity-field measurements from reference 46 for $\alpha = 10^\circ$ in figures 31(a) and (b), respectively. These figures show results in a plane normal to the free-stream direction

located about 10% of the wing's root chord downstream of the trailing edge. It is seen in these figures that the actual vortex trajectories are considerably different from the assumptions and reflect a mutual interaction that is not represented in the current version of ASYMVL. Furthermore, the calculated vortex strengths shown in figure 31(a) indicate that the inboard vortex is more than twice as strong as the outer one, whereas the experimental evidence suggests that the outboard vortex is stronger. These discrepancies (and some results for the GRF discussed later) suggests some improvements needed in ASYMVL: calculating the vortex paths (instead of assuming them) allowing for their mutual interaction should improve the former situation; allowing the vortices to enter in the calculation of the loads should help the latter. These possible improvements are discussed further later.

GRF Configuration, $\beta = 0^{o}$

Next are examined the longitudinal aerodynamic coefficients of various components of the GRF at zero sideslip. Calculations are compared with measurements for the body-strake, body-wing, and body-strake-wing configurations.

For the body-strake configuration, a layout of 5 chordwise panels by 14 panels on the semispan was used. Predictions are compared to measurements for normal force and pitching moment in figures 32(a) and (b), respectively. In these figures, two sets of measurements are shown: measurements of the total configuration loads (C_N and C_m), and measurements made with the strake balance indicated in figure 24 (C_{N_2} and C_{m_2}). For this configuration, the differences between these two sets of measurements (significant only for normal force) represent the small loads generated on the portion of the body aft of the

strake trailing edge. Three sets of predictions are shown: (1) calculations made using ASYMVL alone with no allowance made for the nose vortex field calculated by VTXCLD or for the loads on the nose ahead of the strake leading edge; (2) calculations made using ASYMVL including the effects of the nose field but excluding the nose loads; and (3) complete predictions including the effects of the field and the nose loads. Because of the details of the calculational procedure, these complete predictions should fall between the two sets of measurements. It is seen, however, that both normal force and pitching moment are somewhat over predicted. Just as for the simple wings discussed earlier, inclusion of an augmented-vortex-lift term (negative for the strake planform) would improve the agreement with the measurements.

In figure 33, similar calculations are shown for the body-wing configuration. A 5 x 14 panel layout was again used in ASYMVL. For this case, the "strake balance" records the loads on the nose only, and the predictions of VTXCLD can be compared directly with these measurements; good agreement is seen to exist for normal force and pitching moment at the single angle calculated. Calculations at additional angles of attack would be required, of course, to verify fully the accuracy of the prediction for the nose. The data in figures 33(a) and (b) show that without the influence of the strake vortex, the wing stalls at $\alpha \approx 16^{\circ}$. Beyond that point, the ASYMVL predictions obviously will show poor agreement since no attempt is made to represent this phenomenon in the model. For $\alpha \leq 16^{\circ}$, however, it is clear that the use of full leading- and side-edge vortex lift ($K^{*}_{v_{\ell e}} = K^{*}_{v_{se}} = 1$) is somewhat optimistic. This is in spite of the fact that surface oil-flow patterns clearly show the existence of a leading-edge vortex system (ref. 43). Note that if the correlation for $K^{*}_{v_{\ell e}}$ developed for simple delta wings is applied to this wing, we obtain $K^{*}_{v_{\ell e}} = 0$. Use of this value with $K^{*}_{v_{se}} = 1$ in ASYMVL (no nose vortices) results in the improved agreement

shown in figures 34(a) and (b). Inclusion of the nose loads from VTXCLD would further improve the prediction of C_m and leave C_N essentially unchanged. However, use of the delta-wing correlation for other planforms does not always work so well. Referring back to the cropped delta of figure 28, we see that even with $K^*_{v_{\ell e}} = 1$ (the delta-wing correlation gives $K^*_{v_{\ell e}} = 0.73$ for this wing), inclusion of augmented vortex lift is required to achieve agreement with data. Obviously, further work is required to develop the guidelines necessary for appropriate specification of $K^*_{v_{\ell e}}$ and augmented vortex lift, as these quantities vary with the wing planform and leading-edge sweep.

The current geometry package for ASYMVL requires modeling the strake-wing combination as a complex wing planform with multiple breaks in leading-edge sweep. Calculations for the body-strake-wing configuration were therefore done using 7 chordwise panels and 14 panels distributed over the semispan, 7 over the strake portion and 7 over the wing portion. On the basis of paneling convergence tests previously conducted on simple planforms (e.g., see fig. 29), it is expected that this is adequate chordwise resolution but that the number spanwise is probably too small; nonetheless, this is the current maximum allowable. This program constraint can be relaxed, and this modification is among the recommendations made later for improving the prediction method.

In figures 35(a) and (b), various predictions for this configuration made using VTXCLD and ASYMVL are compared to measurements for the normal force and pitching moment coefficients, respectively, assuming full vortex lift on the strake and wing. The data for normal force coefficient show a break in slope at $\alpha \approx 20^\circ$ and an abrupt loss of lift at $\alpha = 28^\circ$. These effects are due to vortex bursting. In reference 44, it is shown that strake-vortex bursting occurs for this configuration at the

axial location of the wing-trailing-edge/body junction at $\alpha \approx 23^{\circ}$, and at $\alpha = 30^{\circ}$, the bursting location has progressed forward to the axial position of the wing-leading-edge/body intersection. While no modeling of the vortex-bursting process is included in our calculations, predictions are made up through the angle at which the abrupt loss of lift occurs. Contributions to the predicted quantities resulting from including the nose field in ASYMVL and including the loads calculated on the nose by VTXCLD are shown. As would be expected from the body-wing calculations shown previously, at high angle of attack the assumption that all the leading-edge suction calculated for the wing is converted to vortex lift is optimistic. The predictions for pitching moment (fig. 35(b)) are particularly affected.

Rather than using the values of $K^{*}_{v_{\ell e}}$ and $K^{*}_{v_{se}}$ that were shown to give satisfactory results for the body-wing configuration in figure 34, these factors are set to zero for the wing portion of the body-strake-wing configuration making use of some additional available information. Based on the surface oil-flow patterns of reference 43, an α-dependent vortex-flow pattern has been deduced in reference 36 for the body-strake-wing configuration as follows: at low angle of attack, the strake and wing vortices are individually distinguishable on the configuration surface and the strake vortex persists over the wing at a spanwise station near the tip of the strake; at high angle of attack ($\alpha \leq 20^{\circ}$), the wing surface flow pattern evidences only one large region of spanwise vortex flow which extends spanwise from the wing-fuselage juncture to roughly 86% of the reference wing span, outboard of which the wing appears to be stalled. Additional evidence at high α suggests further that the wing vortex is displaced away from the wing upper surface by the strake vortex.

These observations led to an α-dependent augmented-vortex-lift model in reference 36: at low α, lift augmentation occurs on the wing due to both the wing and the strake leading-edge vortices; at high α, there is a negative "augmentation" effect for the strake itself because of its trailing-edge notching, but a positive augmentation of the wing lift due to the presence of the strake vortex over the wing. Also at high α, due to the vortex-displacement effect, the wing leading- and side-edge vortex-lift terms are assumed to be zero. Thus, for the wing, $K^{*}_{v_{\ell e}} = K^{*}_{v_{se}} = 0$.

As noted earlier, ASYMVL does not currently include an augmented-vortex-lift model, but use can be made of the observations about the vanishing of the wing leading- and side-edge vortex lift at high angle of attack. Calculations using this information are shown in figures 36(a) and (b). As expected, the predictions for full vortex lift on the wing and no vortex lift on the wing bracket the measurements for normal force (fig. 36(a)) and pitching moment (fig. 36(b)), and inclusion of the augmentation terms would yield closer agreement with the data. Further enhancement could conceivably result if the augmented-vortex-lift model were made to include effects of the forward progression of the strake-vortex bursting location shown in reference 44. The predictions of reference 36, including the augmentation terms but without any allowance for bursting, are shown for pitching moment in figure 36(b), and for lift coefficient in figure 37. For comparison, the ASYMVL calculations shown as C_N in figure 36(a) have been converted to lift coefficient and are also included in figure 37.

GRF Configuration, $\beta = 5^{\circ}$

At $\beta = 5°$, a series of calculations has been made using the baseline version of ASYMVL to identify areas needing improvement. The baseline version incorporates a number of simplifying assumptions, particularly with regard to vortex trajectories (Appendix B), that are expected to need upgrading under conditions of sideslip. For example, the nose vortex cloud as calculated by VTXCLD up to the position of the strake leading edge is assumed thereafter in ASYMVL to follow a trajectory parallel to the body centerline. In a similar fashion, the strake leading-edge suction vortex is assumed to move vertically at an angle of $\alpha/2$ from the strake leading edge, and its horizontal position is set at the centroid of the strake leading-edge suction distribution. Calculations made using these assumptions are shown for the body-strake-wing configuration in figure 38 and the body-strake-wing-tail configuration in figure 39. When the tail is included, it is modeled with 5 chordwise and 14 spanwise panels.

Predictions of the longitudinal characteristics of the body-strake-wing configuration at $\beta = 5°$ (C_N, fig. 38(a) and C_m, fig. 38(b)) follow the same general pattern as the previous results for $\beta = 0°$: the two predictions including the effects of the nose field in ASYMVL and the nose loads from VTXCLD, which vary by the amount of vortex lift on the wing, bracket the data. These predictions are shown by the filled symbols in figure 38. Inclusion of an augmented-vortex-lift model for the strake in conjunction with no wing leading- or side-edge suction lift would result in good agreement, as at $\beta = 0°$.

With respect to the lateral characteristics, the data indicate a dramatic change in behavior at $\alpha \approx 20°$, the angle near which (for $\beta = 0°$) symmetric strake-vortex bursting occurred at the axial location of the wing-trailing-edge/fuselage junction. The large effects on the lateral

aerodynamics at $\beta = 5^{\circ}$ are most likely indicative of asymmetric bursting of the left and right strake vortices. Under positive sideslip, previous studies (see, for example, ref. 47) suggest that the strake vortex over the right wing would burst at a somewhat lower angle of attack than at $\beta = 0^{\circ}$, while the vortex over the left wing would retain its identity to a higher angle. This would result in a loss of lift on the right wing, and a tendency for a right-wing-down (positive) rolling moment, just as in figure 38(c). Under these conditions, attention should be confined to predictions made for $\alpha \leq 20^{\circ}$ (although predictions are shown at $\alpha = 28^{\circ}$), because of the previously cited lack of modeling of vortex-bursting phenomena in ASYMVL.

In figures 38(c)-(e), considering the predictions at $\alpha = 20^{\circ}$ which include the effects of the nose field in ASYMVL and the nose loads from VTXCLD, it is seen that the amount of vortex lift which occurs on the wing (as opposed to on the strake) has very little effect on the lateral characteristics. That is, the predictions shown with the filled symbols differ very little from each other. The predictions of the very small yawing moment (C_n) and side force (C_y) shown by the data are very good at low angles of attack, but C_ℓ improvement at higher angles is needed. The rolling moment, of course, comes about as the difference between two quantities of nearly equal magnitude but opposite sign, so it is a difficult test of a prediction method. It is felt that the discrepancies shown in the lateral characteristics are probably due to the simplified treatment of vortex trajectories discussed above.

When the tail is added (fig. 39), comparison of the measurements in the corresponding parts of figures 38 and 39 reveals that the tail loads dominate C_n and C_y but have very little effect on C_ℓ. The abrupt change in behavior at $\alpha \approx 20^{\circ}$ is amplified in C_n and C_y, and presumably stems from changes in the

tracks of the various vortices as they interact with each other and with the tail. Again focusing on the predictions represented by the filled symbols at $\alpha = 20^{o}$, it is seen that C_{ℓ}, C_n and C_y are slightly over-predicted; here again, it is felt that most of the discrepancies stem from the current over-simplified treatment of the vortex trajectories. This view is supported by the excellent predictions at $\alpha = 4^{o}$, where vortex effects are unimportant.

To investigate the sensitivity of the predicted lateral characteristics of the body-strake-wing-tail configuration to changes in the vortex paths, a number of calculations have been performed. These calculations were all done at $\alpha = 20^{o}$ using full vortex lift on the strake and no vortex lift on the wing. Attention is focused on those lateral coefficients which are dominated by the tail loads, C_n and C_y, and the effects on the tail contributions to these quantities studied as the vortex trajectories are varied from the "baseline" paths currently assumed in ASYMVL. No attempt is made to match the observed values of these coefficients through arbitrary maneuvering of the vortex paths, but rather it is attempted to determine the effect on these coefficients of changing the positions in ways that improve on the current simple assumptions.

The following cases were considered:

Case	Vortex Trajectories
0	The "baseline." Normal ASYMVL assumptions, $\alpha = 20^{o}$.
1	No vortex fields from wing region or nose included in tail loads.

2	Only vortices from potential loads on wing included in tail-load calculation.
3	Path of nose and strake vortices calculated to tail location by slender-body tracking over fuselage (no wing).
4	Strake vortices follow baseline path (case 0), nose vortices follow path of case 3.
5	Nose vortices follow baseline path (case 0), strake-vortex vertical path as in baseline (case 0) and horizontal path from case 3.
6	Nose vortices follow path of case 3, strake-vortex vertical path as in baseline (case 0) and horizontal path from case 3.

The resulting vortex positions in the tail region for cases 0 and 2-6 are shown in figures 40(a)-(f), respectively*. Case 1 has no vortices and is not shown. Remember that for the purposes of calculating the contribution to the loads in a given region of an impressed vortex from an upstream region, ASYMVL assumes the vortex is parallel to the fuselage centerline in the region in which the loads are being calculated. Therefore, to be consistant with this modeling, the vortex paths in the tail region are shown parallel to the centerline in figure 40. In figures 40(a) (case 0) and 40(c)-(f) (cases 3-6), the vortices

---

*The nose field consists of two clouds of vortices, one emanating from the right side of the nose, the other from the left. In figure 40, the centroids and overall strengths of these clouds are shown.

associated with the wing potential loads (case 2, figure 40(b)) are not shown for clarity but were included in the associated load calculations. The tracking for case 3 was performed using VTXCLD. The trajectories of the nose field and the strake vortices were calculated separately, both calculations done modeling the fuselage in the wing region as a circular body (the same circular fuselage as assumed in ASYMVL) with no effects of the wing represented. A tracking calculation involving the nose field and the strake vortices simultaneously could have been done, but in a case like this where there are large disparities in the vortex strengths, special care is required. Techniques necessary for such a calculation have been demonstrated, such as incorporating viscous cores in the strake vortices which dominate the calculation or treating the strake vortices as clouds of vorticity. However, it is felt that the added complexity involved is not warranted for the present purpose, which is to determine the sensitivity of the lateral characteristics to changes in the vortex trajectories. After it is demonstrated that these trajectories exert a strong influence, a suitable tracking calculation involving all of the vorticity and the effects of the fuselage and lifting surfaces can be incorporated in ASYMVL (in future work).

The contributions of the tail to C_y and C_n for these cases, at $\beta = 5^o$, are shown in figures 41 (a) and (b). The contributions of the tail as inferred from the measurements of reference 41 are also included in these figures. These latter contributions were calculated, for example for C_y, as

$$C_{y_{tail}} = C_{y_{BSWT}} - C_{y_{BSW}} \tag{5}$$

where the subscripts BSWT and BSW indicate the body-strake-wing-tail and body-strake-wing configurations, respectively.

Cases 1 (no vortices) and 2 (potential-load vortices only) are included as "limiting" cases, in some sense. Consideration of the remaining cases in figures 40 and 41 reveals that the positions of the powerful strake vortices exert a controlling influence on the tail lateral loads. The positions of the nose vortices are not unimportant, but because these vortices are so much weaker than the strake vortices, their effects are much smaller. For example, if the nose field trajectories and the vertical positions of the strake vortices are left unchanged from their baseline values, but the horizontal position of the strake vortices is changed in accord with slender-body tracking, large favorable influences (improving agreement with experiment) on the lateral coefficients result (compare case 5 with case 0). If the nose field is then moved, there is esentially no further change (compare case 6 with case 5). Additionally, if the strake vortices are retained in their baseline positions but the nose field is allowed to move, much smaller (but still favorable) changes result (compare case 4 with case 0).

It is interesting to observe that the induced lateral loads cannot be used to infer the correct paths. This is so because there is not a unique relationship between the two. Notice that C_n and C_y for cases 0 and 3 are nearly the same, but these cases are for radically different vortex trajectories. We can, however, assert that: (1) the simple assumptions for vortex paths currently included in ASYMVL are not physically correct (recall the comparison of the calculated and measured vortex positions of figure 31 for the $80^\circ/60^\circ$ double delta), and (2) the results of figure 41 show large sensitivity of the lateral coefficients to moderate changes in vortex positions. It seems that improved modeling of the vortex paths and interactions holds promise of considerably improving the predictions shown for the body-strake-wing-tail configuration in figure 39.

RECOMMENDED APPROACH TO IMPROVING THE PREDICTION METHOD

In the preceding sections, the importance of vortical flows to the longitudinal and lateral aerodynamic characteristics of complete configurations like the GRF has been demonstrated. At zero sideslip, it has been shown that, so long as detailed pressure distributions are not required, the important phenomena associated with these vortex flows can be represented by approximate engineering models, allowing for the rapid and inexpensive calculations required in preliminary or conceptual design studies. With sideslip, it has been shown that these approximate calculations are sensitive to the trajectories the various vortical flows take, and certain selected trajectories provide solutions which are in reasonable agreement with experimental results. Until additional verification is completed, it is assumed that vortex trajectories which model the actual physical flow phenomena will probably result in predictions of satisfactory accuracy. It has been shown that programs VTXCLD and ASYMVL provide the basis for a method that can deal with all the aspects of this problem, but certain improvements are required. In this section, the areas in which improvement is needed are identified.

1. Vortex-lattice representation. It has been shown that the current maximum limit for the number of spanwise panels is sometimes too restrictive. This limit should be increased in a minor modification to ASYMVL. It is also desirable to allow for separate paneling of the strake and wing for configurations where both are present. Full mutual interference of these sets of panels should be retained, but the current requirement of treating the strake/ wing combination as a complex wing planform for the purpose of laying out the panels should be relaxed. Finally, certain features of the printout should be improved to

allow for easier checking of the panel layout generated by ASYVML.

2. Carryover loads. The scheme described in Appendix B for calculating the portion of the loads generated on a lifting surface which are carried over onto the body is known to be satisfactory for $\beta = 0^{\circ}$. The extension to the condition of sideslip, also described in that appendix, should be investigated in more detail.

3. Augmented vortex lift. Calculations made for the simple wings and for the GRF have shown the need to include both the notions of augmented vortex lift and the edge-vortex-lift reduction factor K_v^*. The augmented-vortex-lift model accounts for the effects of edge-generated vorticity away from the edge, while the K_v^* factor accounts for the observed fact that under some conditions, not all of the leading- or side-edge suction is converted to vortex lift at the edge. While ASYMVL currently allows for a K_v^* effect on the leading and side edges, correlations for K_v^* need to be established for planforms other than simple delta wings, and an augmented-vortex-lift model should be added. It may furthermore be required to allow the strake vortices to enter in the calculation of wing loads, in order to establish the correct relationship among the vortex strengths. This possibility was suggested by the calculations done for the $80^{\circ}/60^{\circ}$ double-delta wing, and should be studied further.

4. Vortex trajectories. In ASYMVL, the vortex paths are currently assumed. The calculations described for the GRF and for the $80^{\circ}/60^{\circ}$ double delta clearly indicate the need to calculate these trajectories, allowing for mutual interaction of the various vortex systems and for interaction of these systems with the lifting surfaces and the fuselage. This is an area where further data would be advantageous: flow-field surveys

over the GRF configuration of figure 24 would be most helpful. Those flow-field data that do exist (Table 1) are for a GRF configuration with a delta strake; the information for the configuration with the delta strake is far less complete than for the GRF studied here. However, in the absence of flow-field data for the configuration of figure 24, the data for the GRF with the delta strake can be used to develop the required method for calculating vortex trajectories.

5. Vortex bursting. For simple delta wings, a considerable amount of experimental data has been obtained concerning vortex-bursting location as a function of leading-edge sweep angle, angle of attack and angle of sideslip, and some information is available for other simple planforms and a few double-delta wings (see, for example, refs. 47 and 48). Furthermore, reference 44 has information on the strake-vortex bursting behavior of the GRF of figure 24. Use should be made of this information, as a minimum to provide an upper limit on α for calculations which contain no modeling of the bursting process. A better approach, however, is to include the effects of vortex bursting on the characteristics calculated using the Polhamus analogy as extended with the K_v^* and augmented-vortex-lift concepts. In recent work (ref. 49), Lan and Hsu have provided the basis of such an approach. Their method uses correlations of experimental data to predict the angle of attack for vortex breakdown at the trailing edge, the forward progression of the breakdown point for higher angles of attack, and the amount of vortex lift remaining in the region aft of breakdown. Results in reference 49 suggest that their approach is valid for $\beta \neq 0^\circ$ as well as for $\beta = 0°$, and that it can be applied to planforms other than simple deltas. The concepts contained in this approach can be included in ASYMVL, considerably expanding its range of applicability.

Improvement of ASYMVL in these five areas will result in an engineering method capable of providing accurate predictions of low-speed longitudinal and lateral configuration aerodynamics. Undue complexity is avoided through the incorporation of the governing physical mechanisms in the form of rational engineering models, and the associated computational cost is commensurate with the preliminary design process. For example, the total CDC Cyber 760 central-processor execution time required by VTXCLD and ASYMVL for each angle of attack at $\beta \neq 0°$ is approximately 50 seconds. For $\beta = 0°$, where symmetry options can be invoked and the vertical tail does not contribute to the loads, less than half of this time is required.

CONCLUDING REMARKS

In this report, work has been described dealing with two areas which are dominated by the nonlinear effects of vortex flows. For each area, the governing phenomena have been described as identified with the aid of existing experimental data. Existing analytical methods have been reviewed, and the most promising method for each area has been used to perform some preliminary calculations. Based on these results, the strengths and weaknesses of the methods have been defined, and a course of action recommended for improving the understanding of the mechanisms involved and the predictive capability.

The most promising approach for predicting the high-angle-of attack aerodynamics of the general aviation wing with a modified leading edge involves coupling boundary-layer theory with an inviscid representation of the flow field. The inviscid representation accounts for attached areas with a surface-singularity distribution and the separated wake using a free vortex sheet. An iterative calculation is required, wherein

the wake shape is relaxed so that the vortex sheet is a stream surface in the converged three-dimensional flow field and a consistent separation line is predicted. Because the inviscid technique is currently under development, the preliminary calculations done could not explore all aspects of the required coupling, and there are several important questions remaining for the recommended research program.

Predominant among the areas needing exploration are the type of boundary-layer analysis necessary and the nature of the criterion which will allow for accurate prediction of the separation line when used in conjunction with the boundary-layer analysis and the inviscid separated-flow model. Additionally, the structure of the flow in the immediate vicinity of the break in the leading edge is not completely understood, and the role in a predictive calculation of the discrete vortex which has been observed in this region in flow-visualization experiments is not clear. Experiments have demonstrated a high level of sensitivity of the stall characteristics of the wing to geometrical perturbations in this region. This sensitivity makes the development of a comprehensive prediction method a most demanding task, possibly requiring technology beyond that currently available.

With respect to the high-angle-of-attack characteristics of fighter aircraft, the development of an engineering method for the overall loads is simplified by the fact that the locations of the primary separations are known to be at the edges of the lifting surfaces. Coupling with boundary-layer analysis is therefore not required for the analysis of the lifting surfaces and use of the well-known Polhamus suction analogy (suitably extended) has been shown to lead to good results. For the analysis of the forebody, consideration of boundary-layer

behavior is required, but the use of simple methods in this regard has been shown to give good results.

As a result of these factors, the recommended program for future work in this area is more developmental and less exploratory in nature than in the previous case. The work recommended for improving the fighter method includes generalizing the correlations which currently exist for the edge-vortex-lift reduction factor and for the augmented-vortex-lift term, and including the effects of vortex bursting using known techniques. Additionally, existing procedures for calculating vortex trajectories should be implemented, a feature which is particularly important under conditions of sideslip. Accomplishment of these tasks will lead to an engineering method which is inexpensive to use but which is of great utility in preliminary design studies.

TABLE 1.- GRF AERODYNAMIC DATA

	Reference					
	39	40	41	42	43	44
Strakes	None	Delta	1,2,3	1,2,3	1,2,3	3
Wing Leading-Edge Sweep Angle (deg)	44	44	30,44,60	30,40,44 50,60	30,44,60	44
M	0.26	0.2	0.30	0.3 to 0.8	0.3,0.5	0 (water tunnel test)
α (deg)	0 to 24	20,35	-4 to 48	-4 to 48	5 to 30	0 to 40
β (deg)	0	0,10	-5,0,5	0	0	0
Longitudinal Aerodynamics	✓	✓	✓	✓		
Lateral Aerodynamics		✓	✓			
Strake Balance Used			✓	✓		
Wing Pressure Distributions	✓					
Wing Section Lift and Drag Coefficients	✓					
Wing Span Loading	✓					
Flow Field Traverse Data		✓				
Surface Flow Visualization	✓				✓	
Vortex Bursting Characteristics						✓

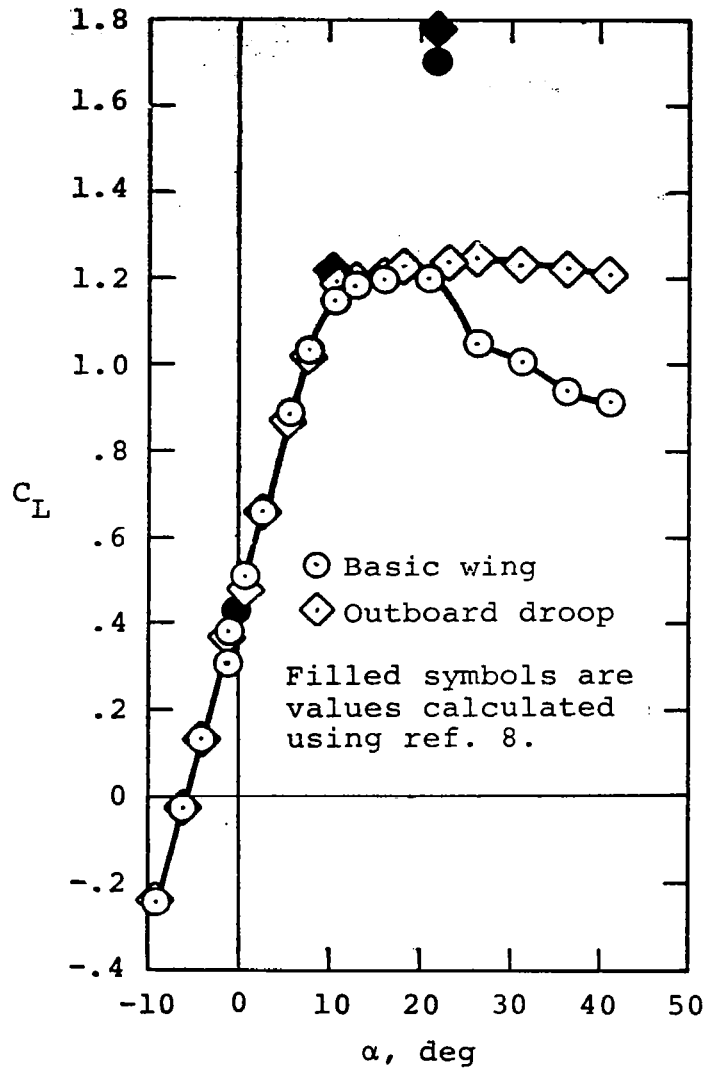

Figure 1.- Lift coefficient of airplane with basic and modified wing (tails off). From reference 1.

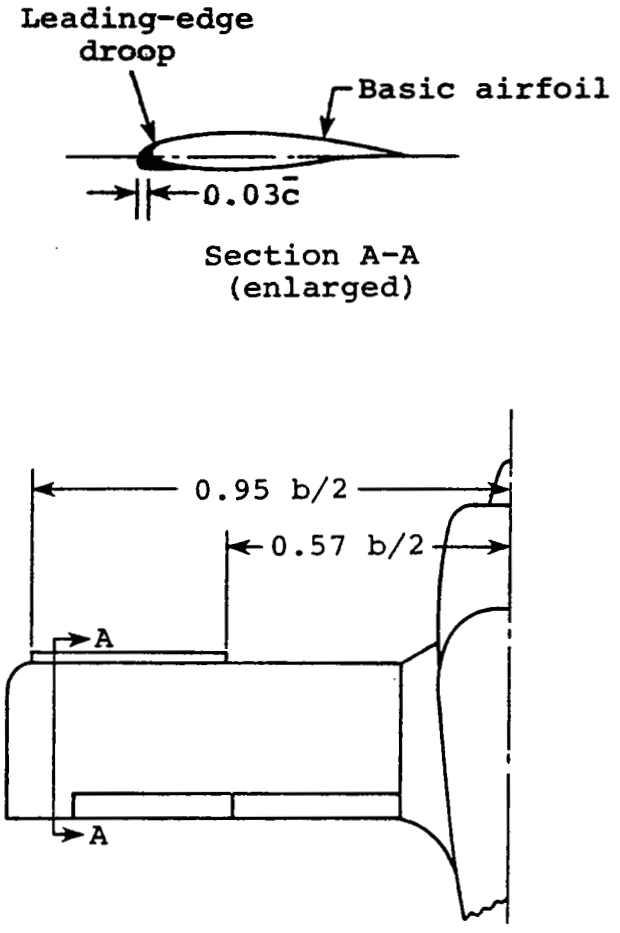

Figure 2.- Outboard-droop configuration. From reference 1.

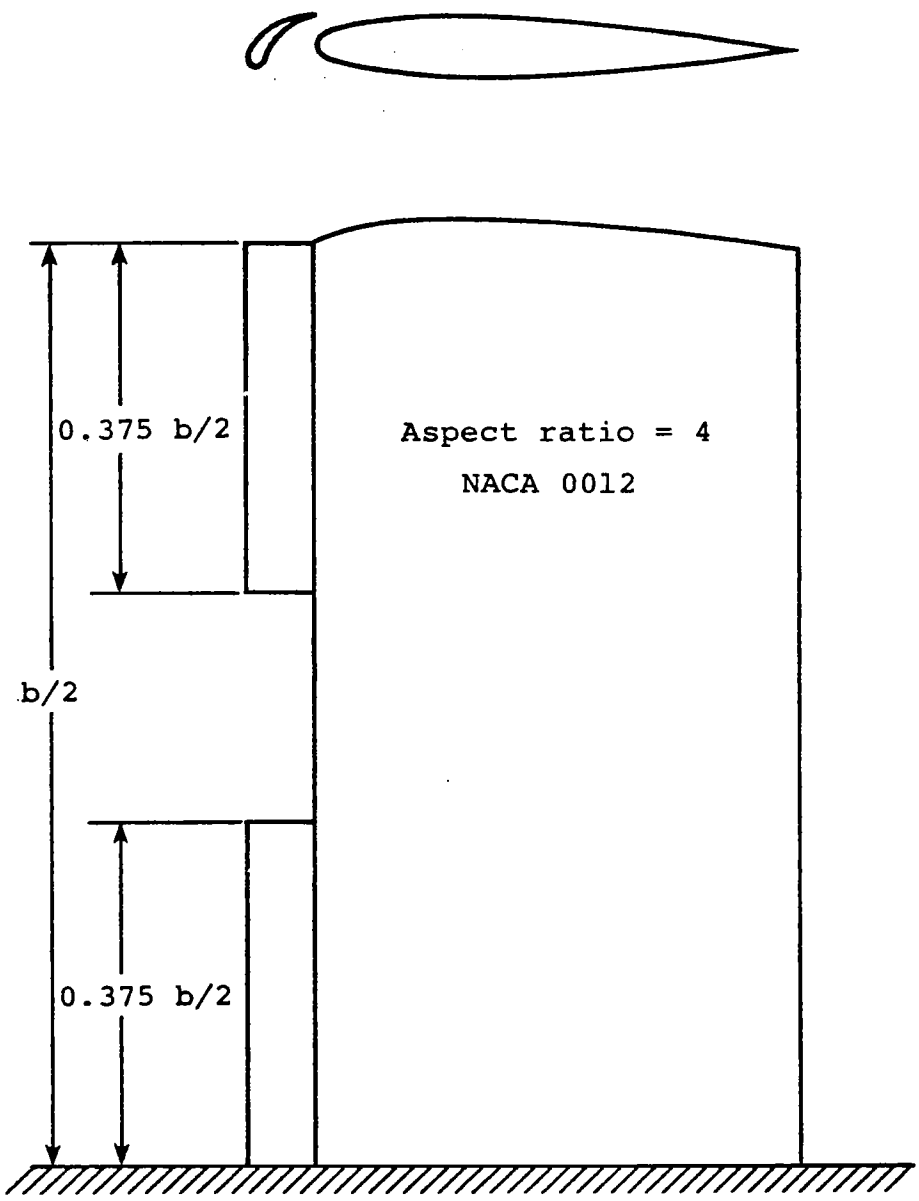

Figure 3.- Controlled partial span stall wing.
From reference 6.

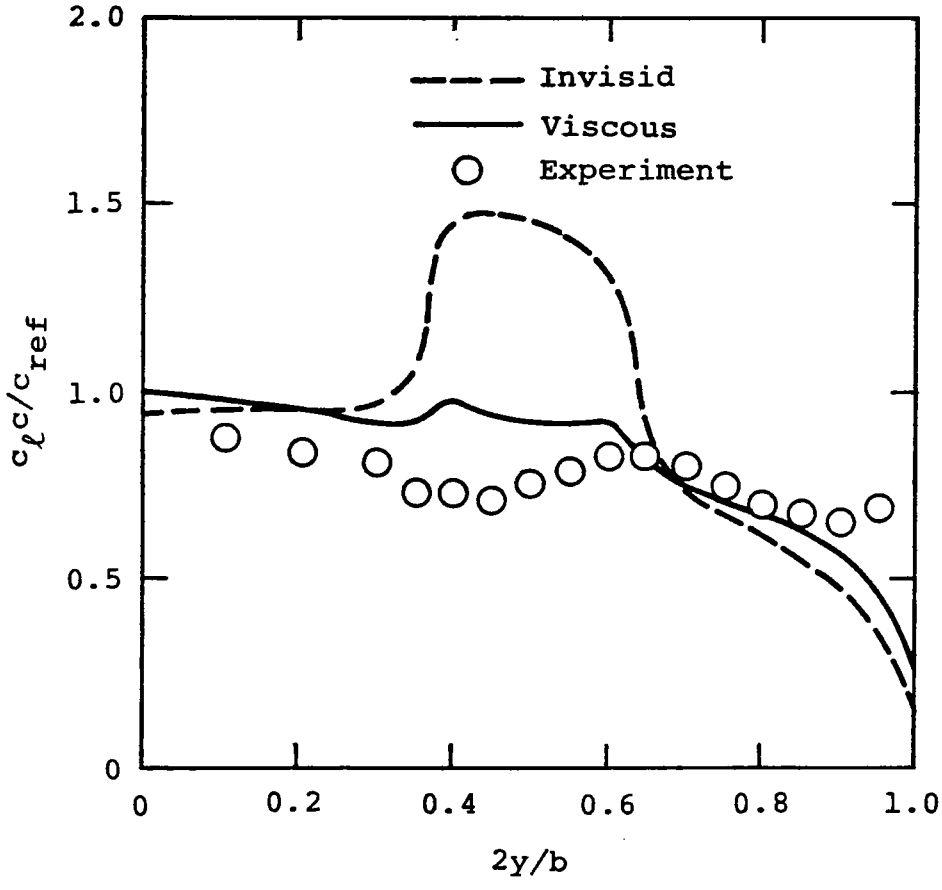

Figure 4.- Comparison with span-load measurements of the method of reference 6 for the controlled partial span stall wing. $\alpha = 19°$, $Re = 1.1 \times 10^6$. From reference 6.

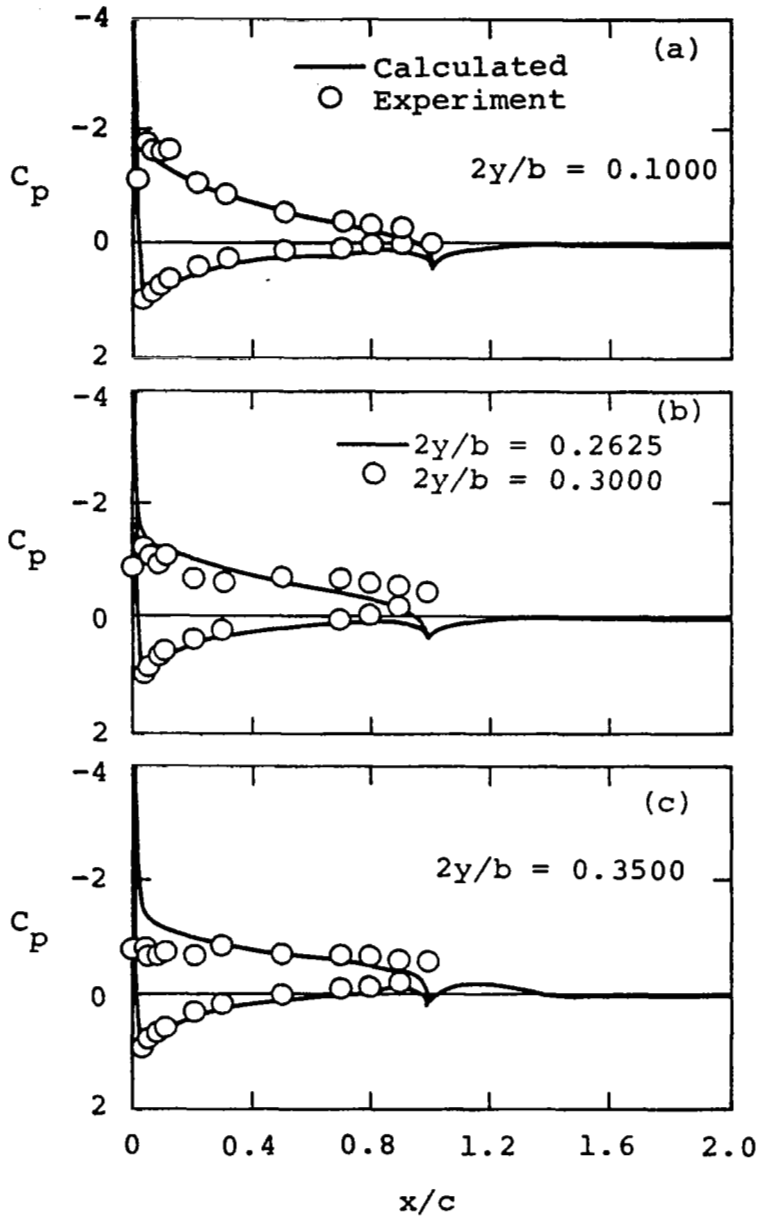

Figure 5.- Comparison with measurements of chordwise pressure distributions calculated using the method of ref. 6 for the controlled partial span stall wing. $\alpha = 19°$, $Re = 1.1 \times 10^6$. From reference 6.

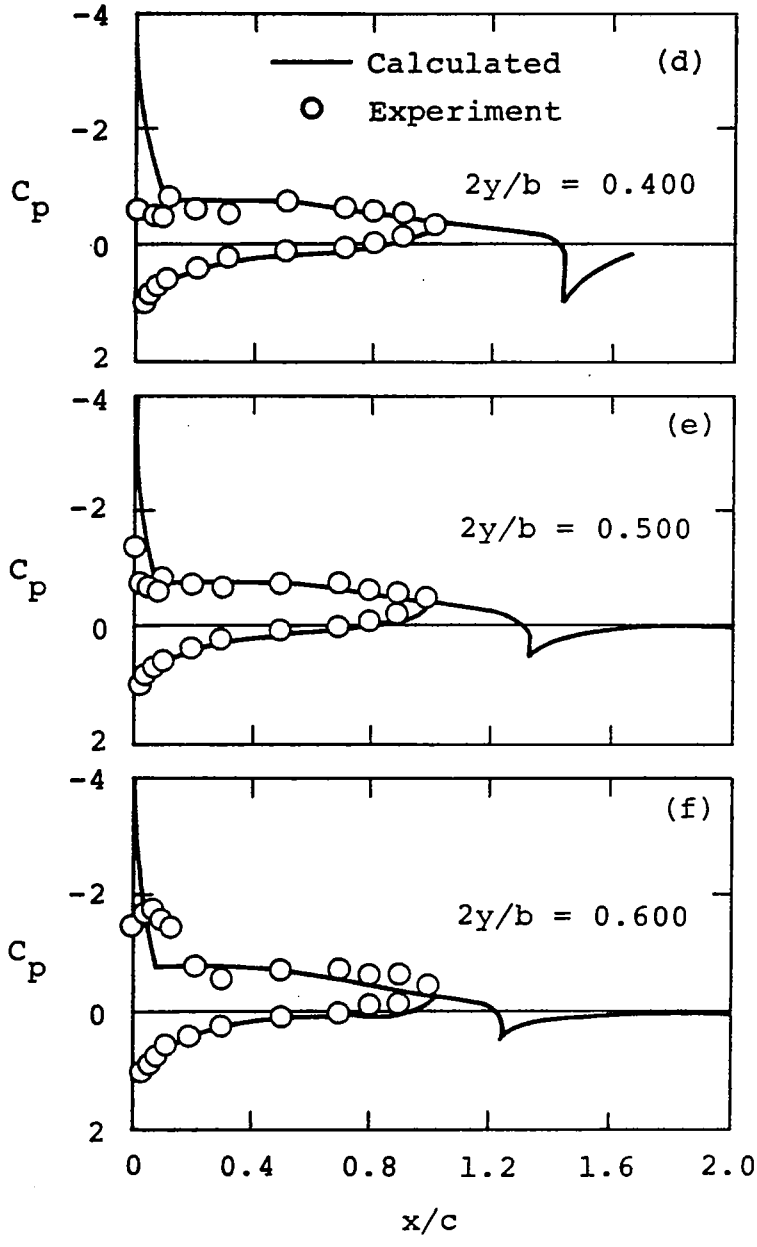

Figure 5.- (continued)

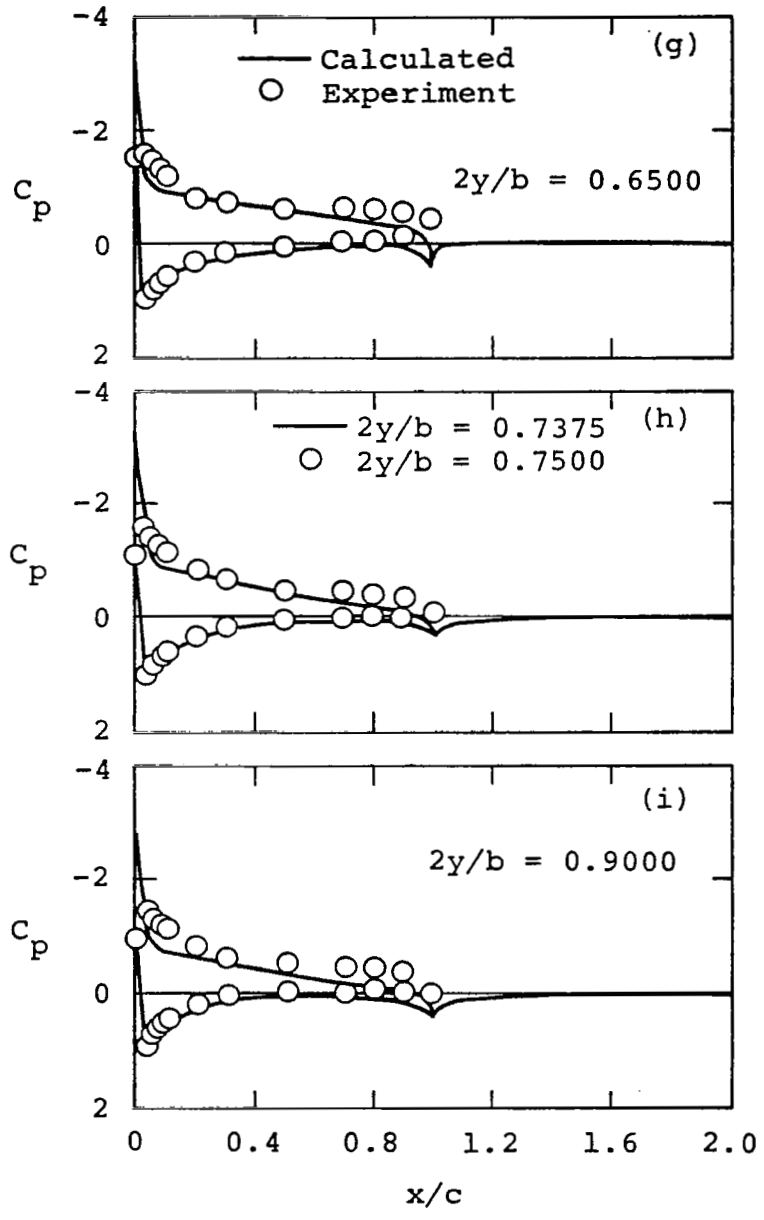

Figure 5.- (Concluded)

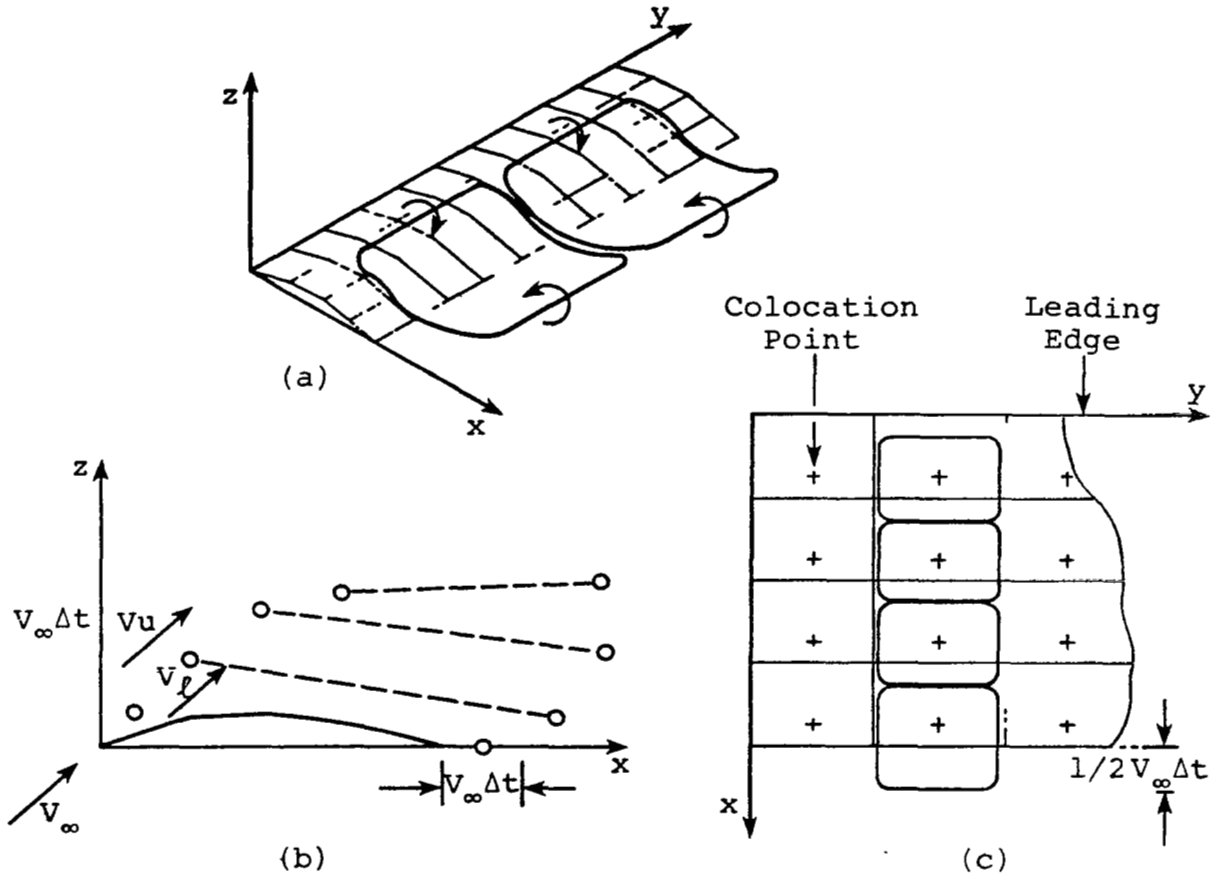

Figure 6.- Vortex-panel and wake geometry of reference 7.

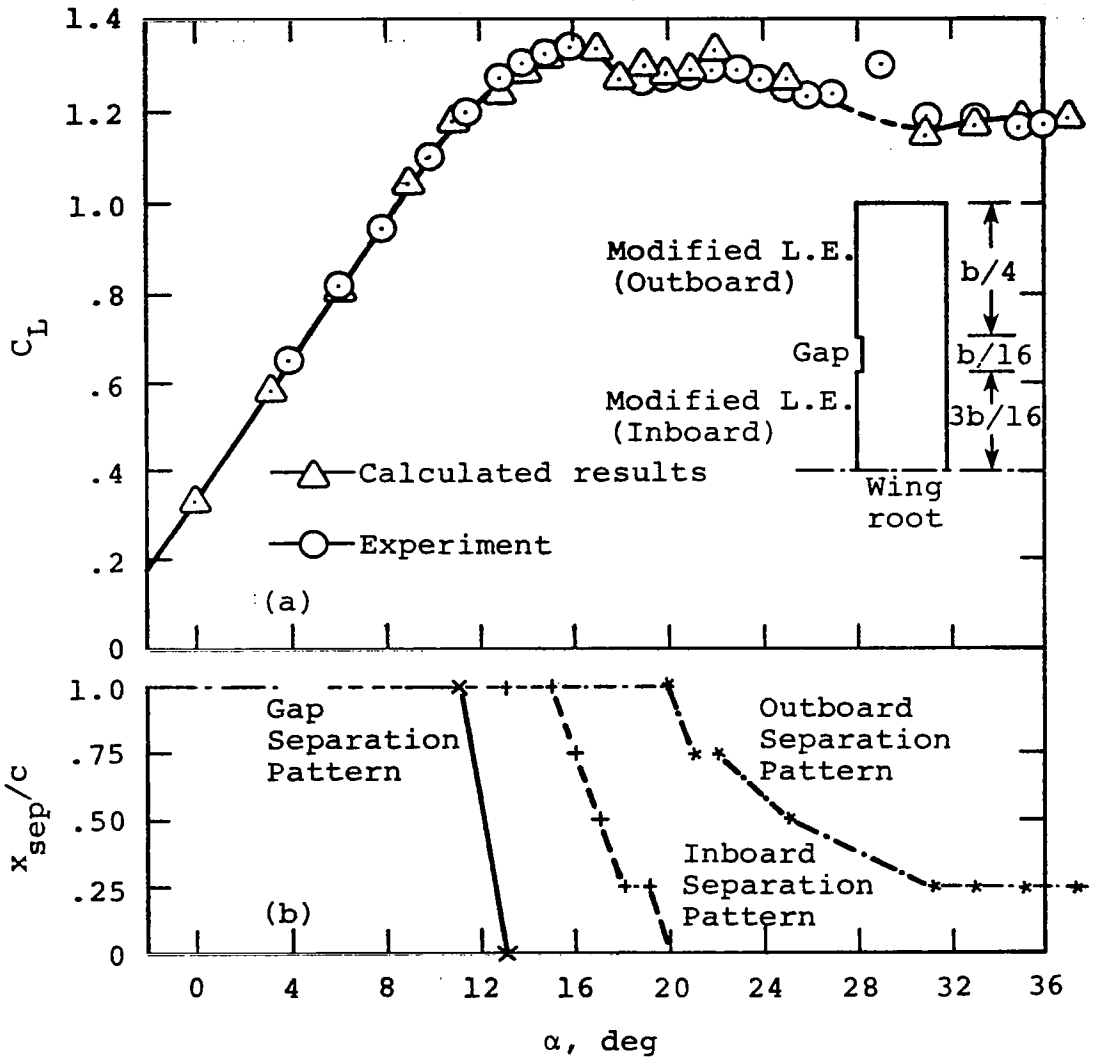

Figure 7.- Comparison of calculated and experimental lift coefficient for a rectangular planform wing of aspect ratio = 7.5 with leading-edge modification (Re = 1.5 x 10^6).
From reference 7.

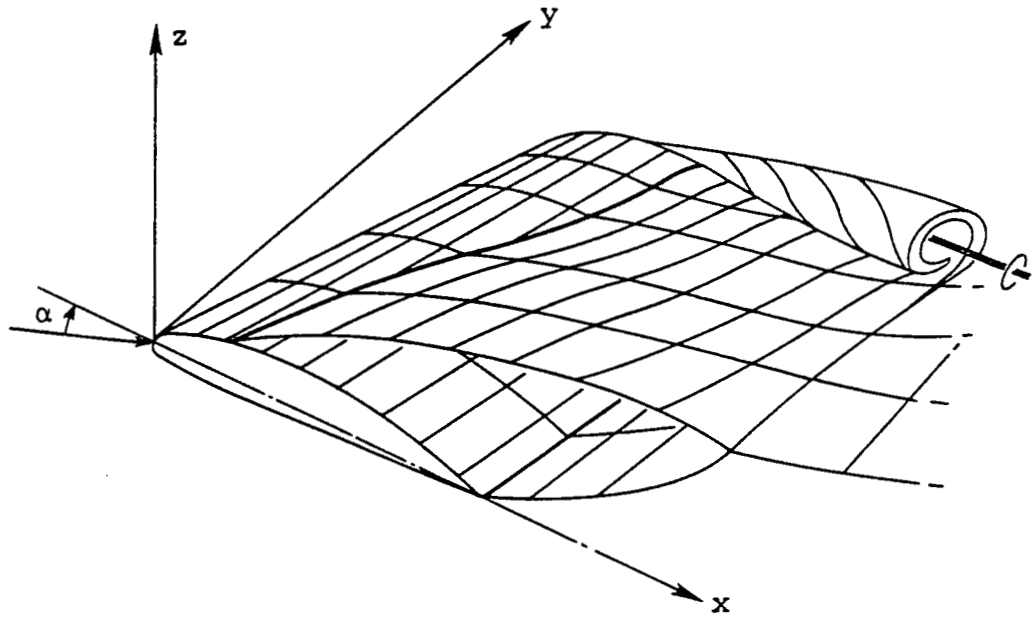

Figure 8.- Schematic representation of the separation model of the precursor code to VSAERO. From reference 10.

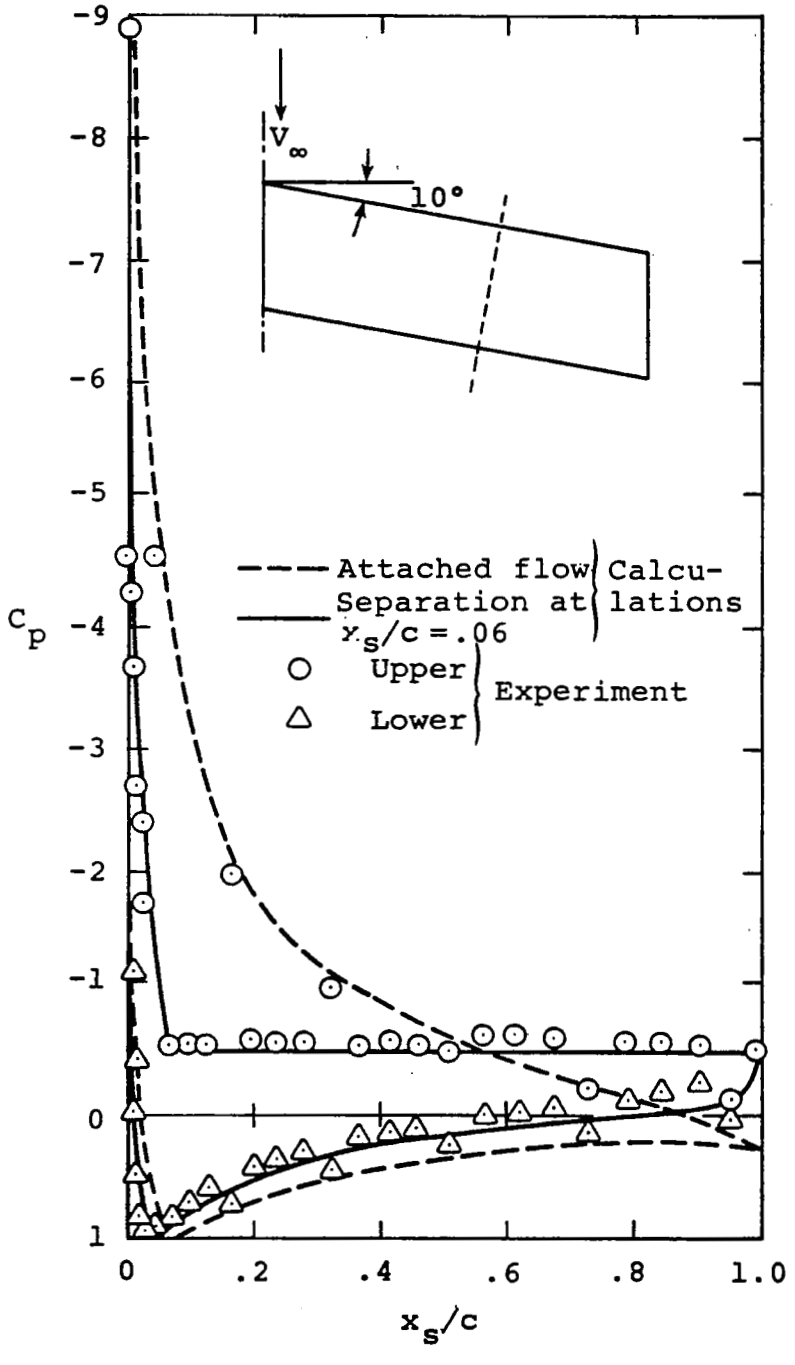

(a) 60% Semispan

Figure 9. - Chordwise pressure distributions for a wing with substantial separation. From reference 10.

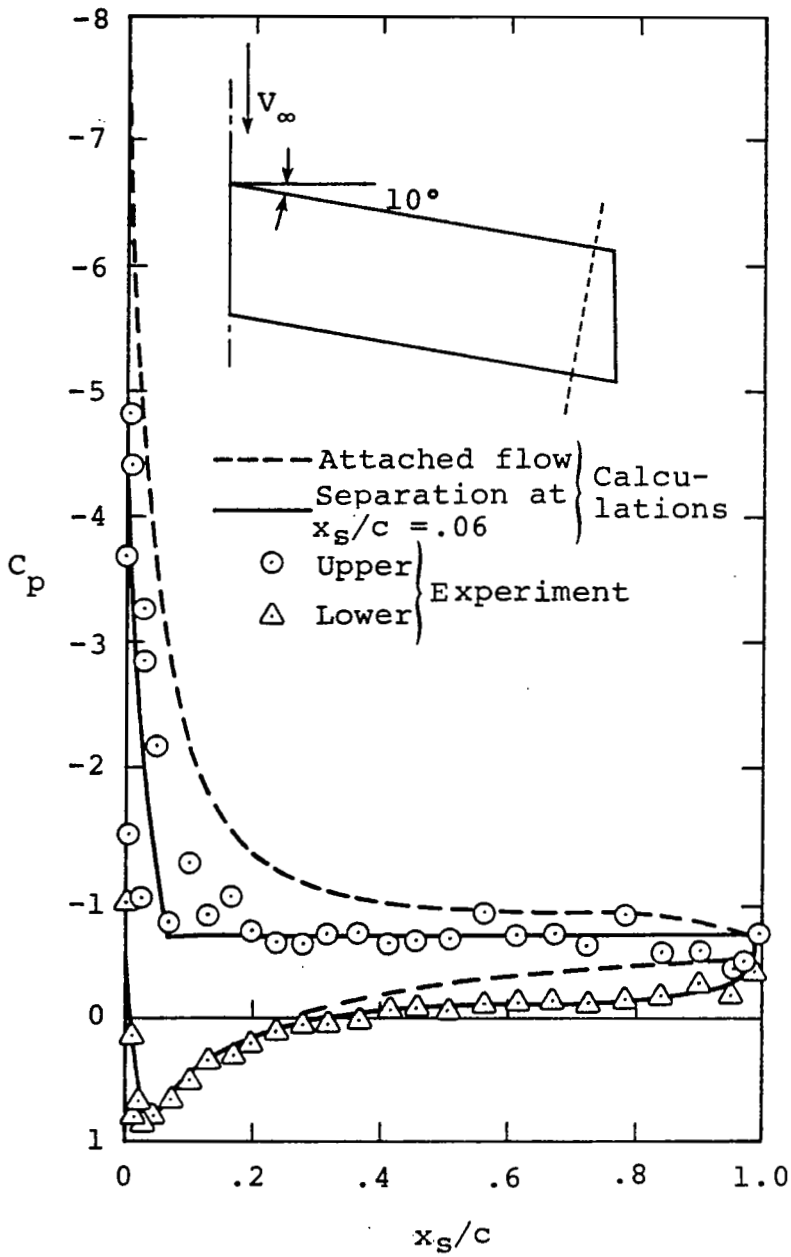

(b) 90% Semispan

Figure 9.- (Concluded).

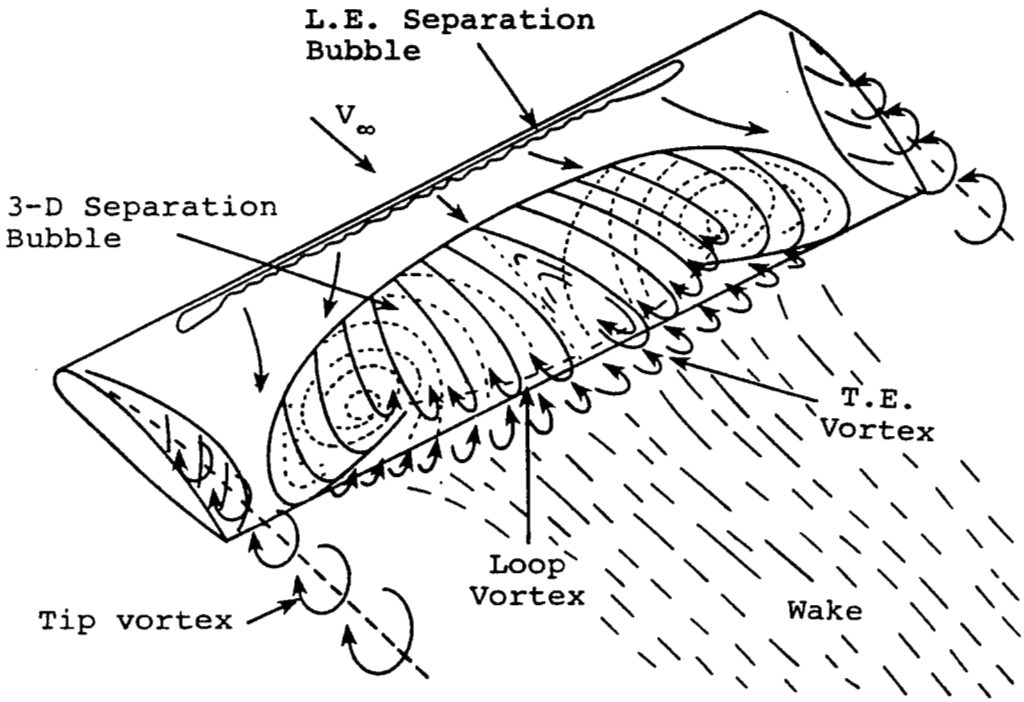

Figure 10.- "Mushroom-shaped" stall cell. From reference 14.

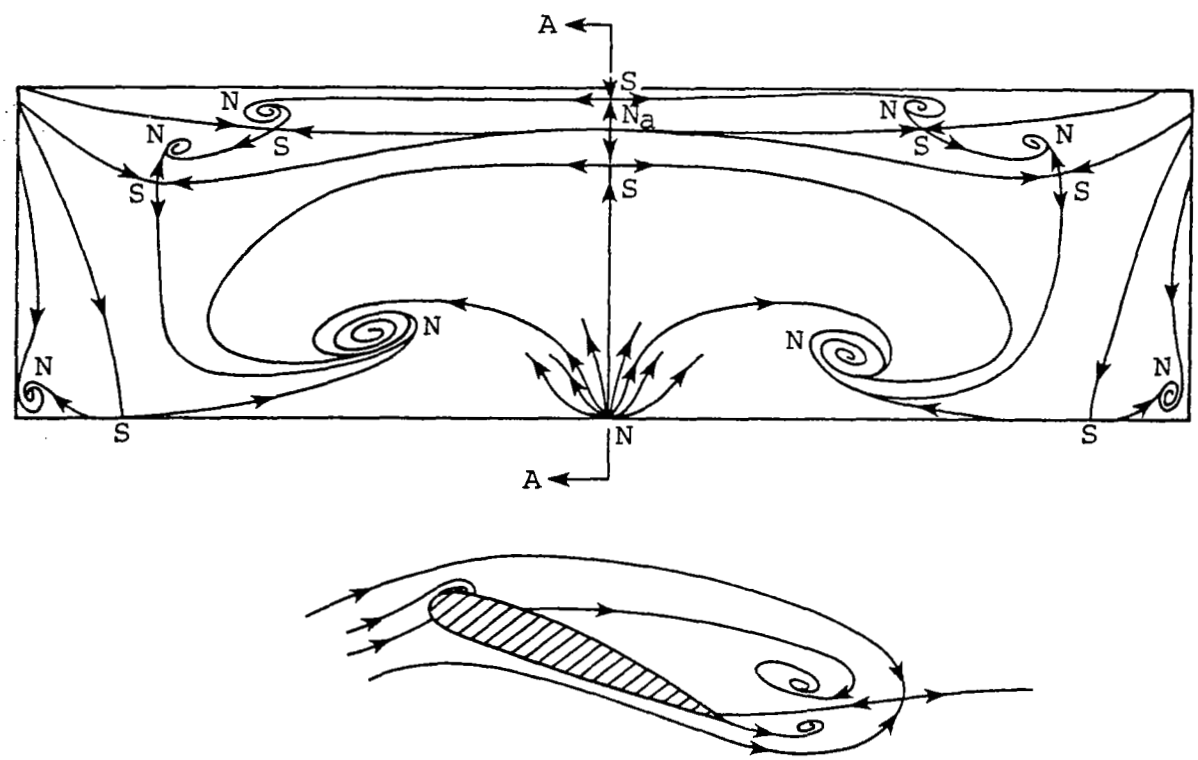

Section AA

Figure 11.- Conjectured pattern of skin-friction lines. From reference 16.

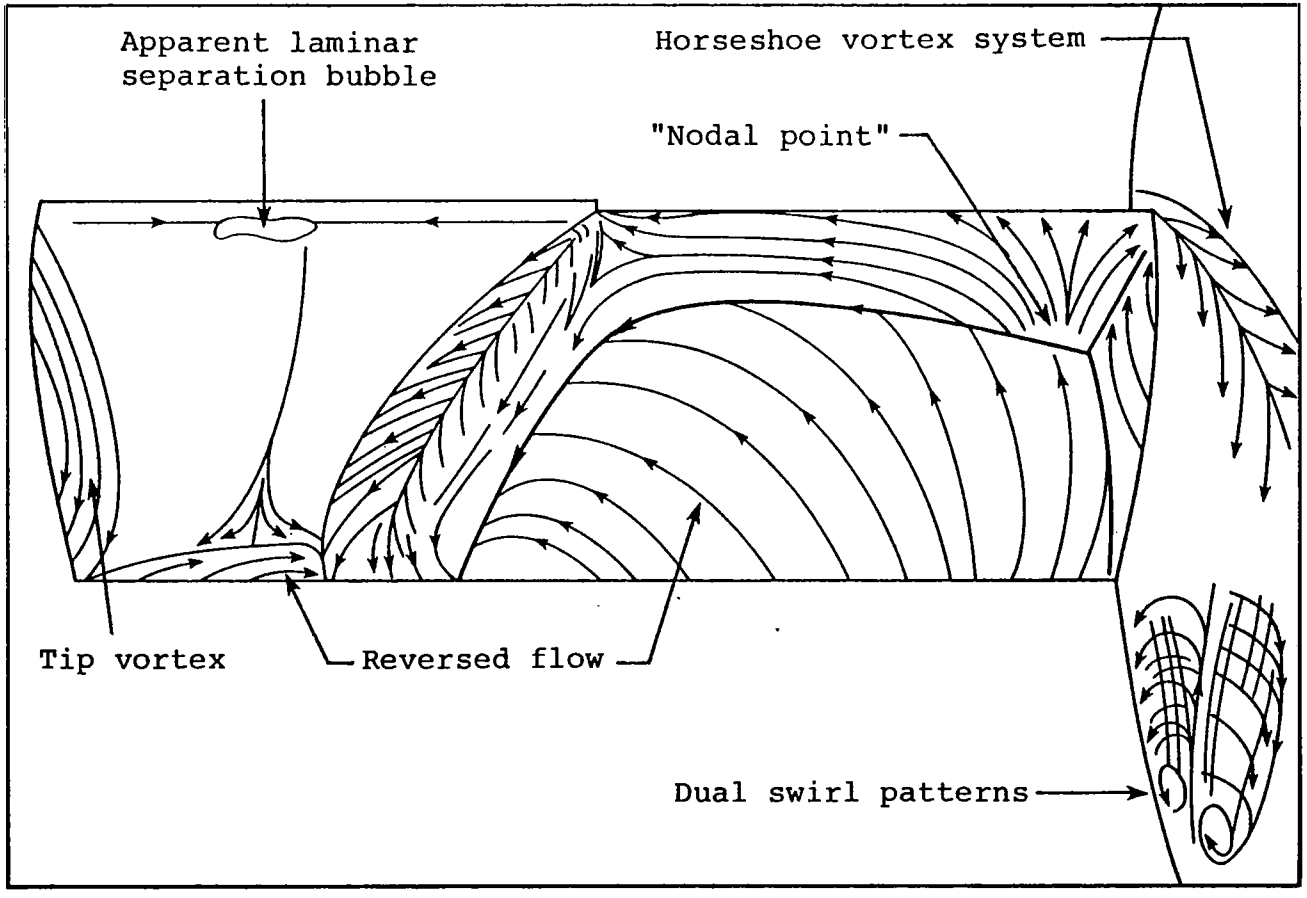

Figure 12.- Surface flow patterns on a wing with outboard droop attached to a fuselage, $\alpha = 25°$. From reference 13.

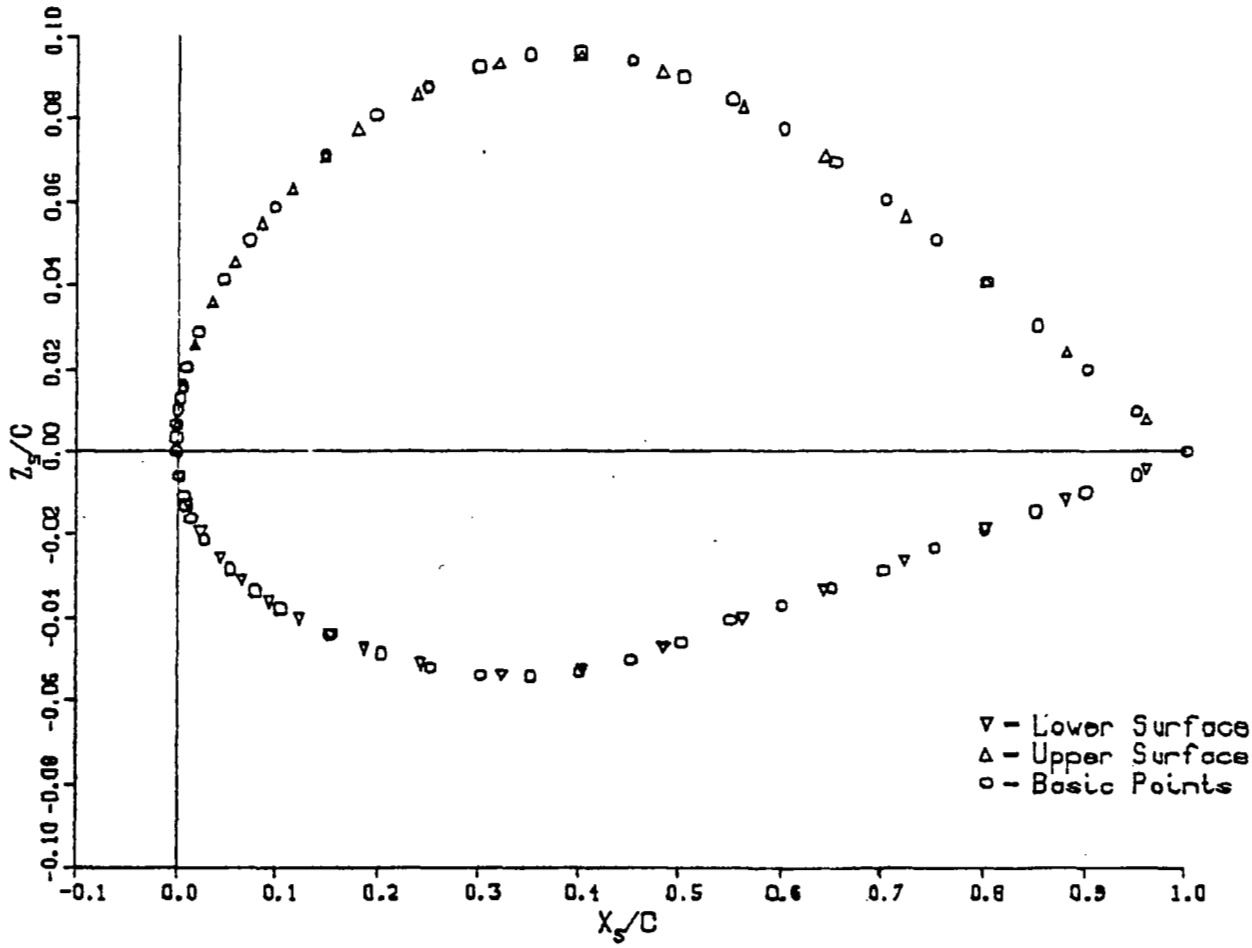

(a) Basic section, $y_{\ell e}/s = 0.4031$

Figure 13.- Chordwise distribution of panel control points.

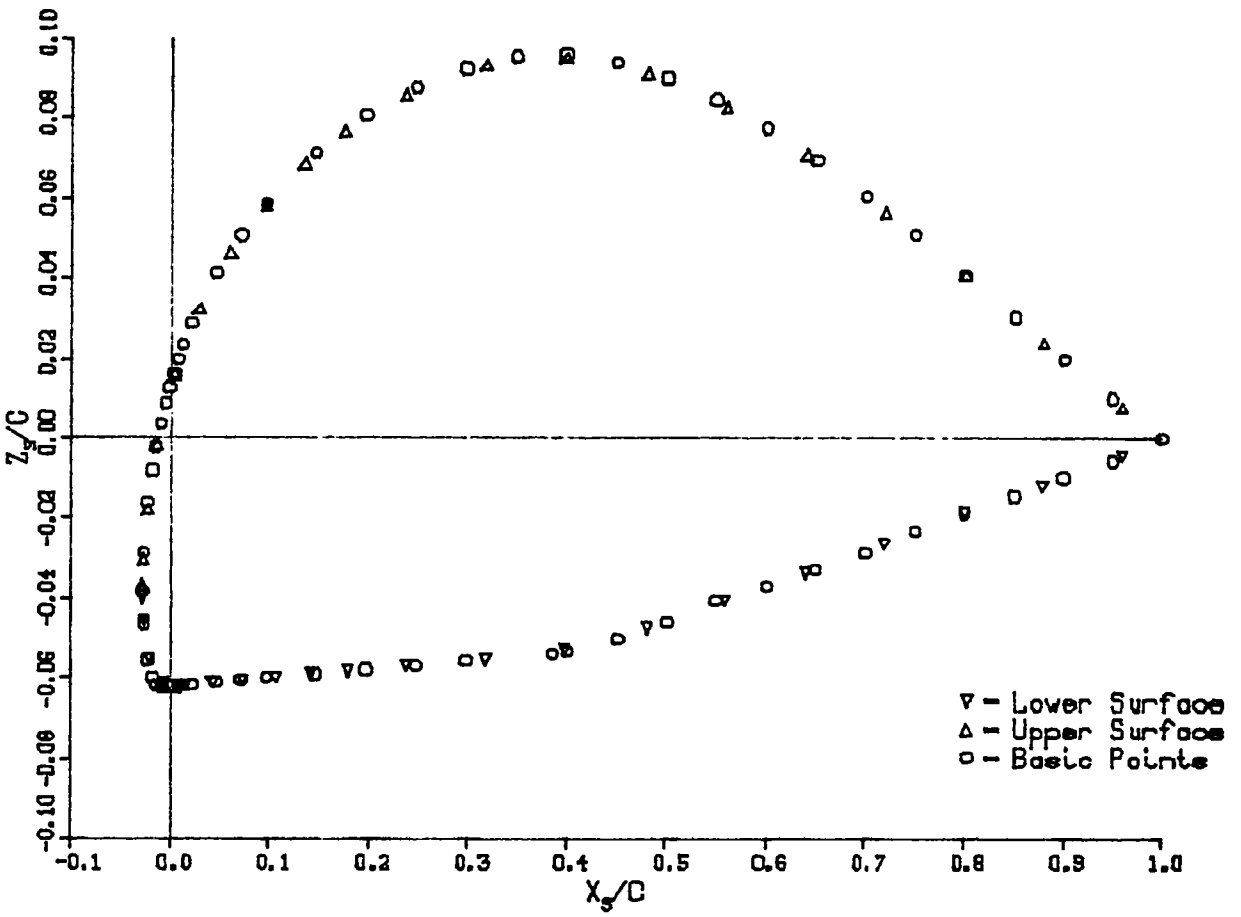

(b) Drooped section, $y_{\ell e}/s = 0.7887$

Figure 13.- Concluded.

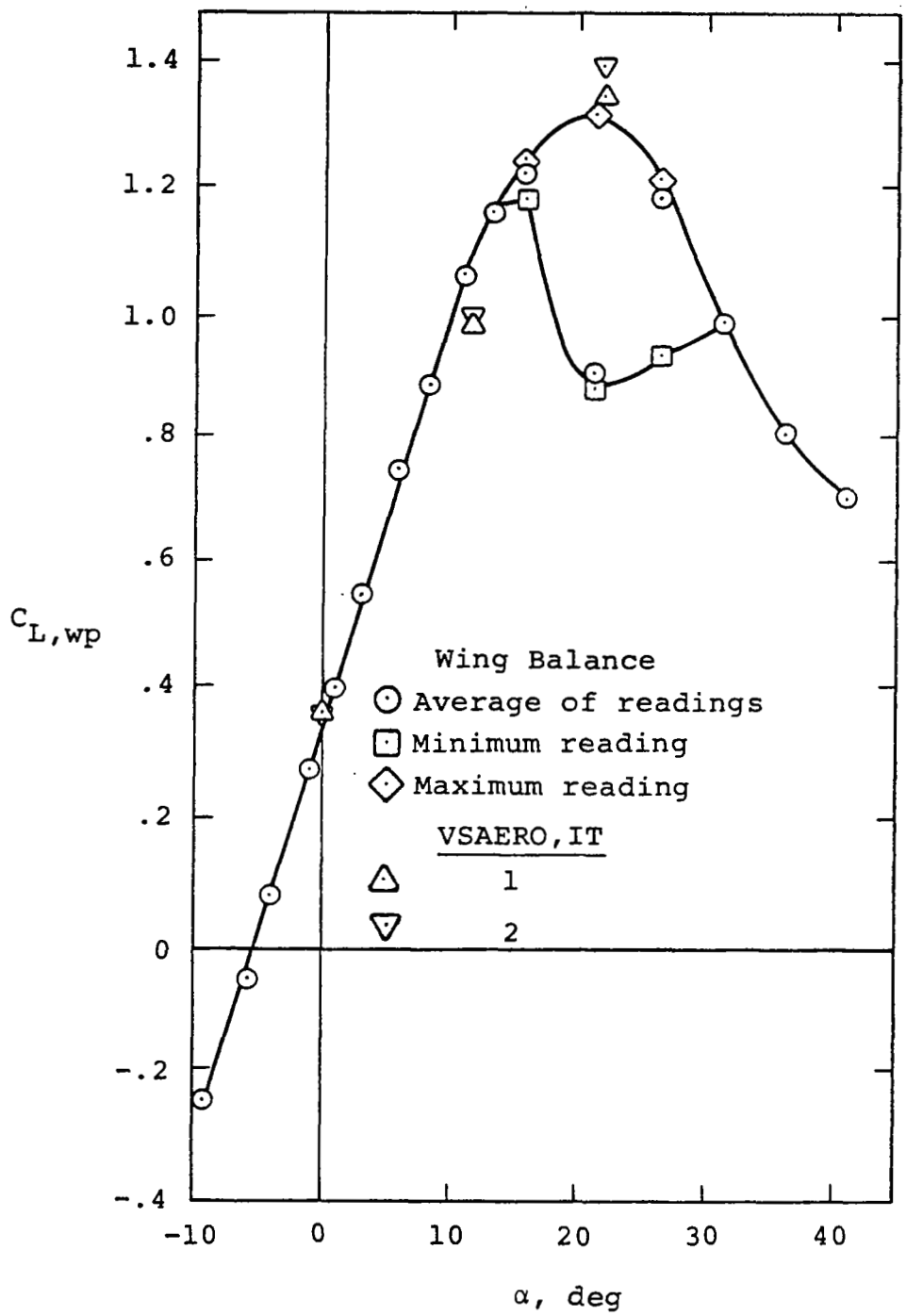

Figure 14.- Lift coefficient on outboard wing panel of basic wing. From reference 1.

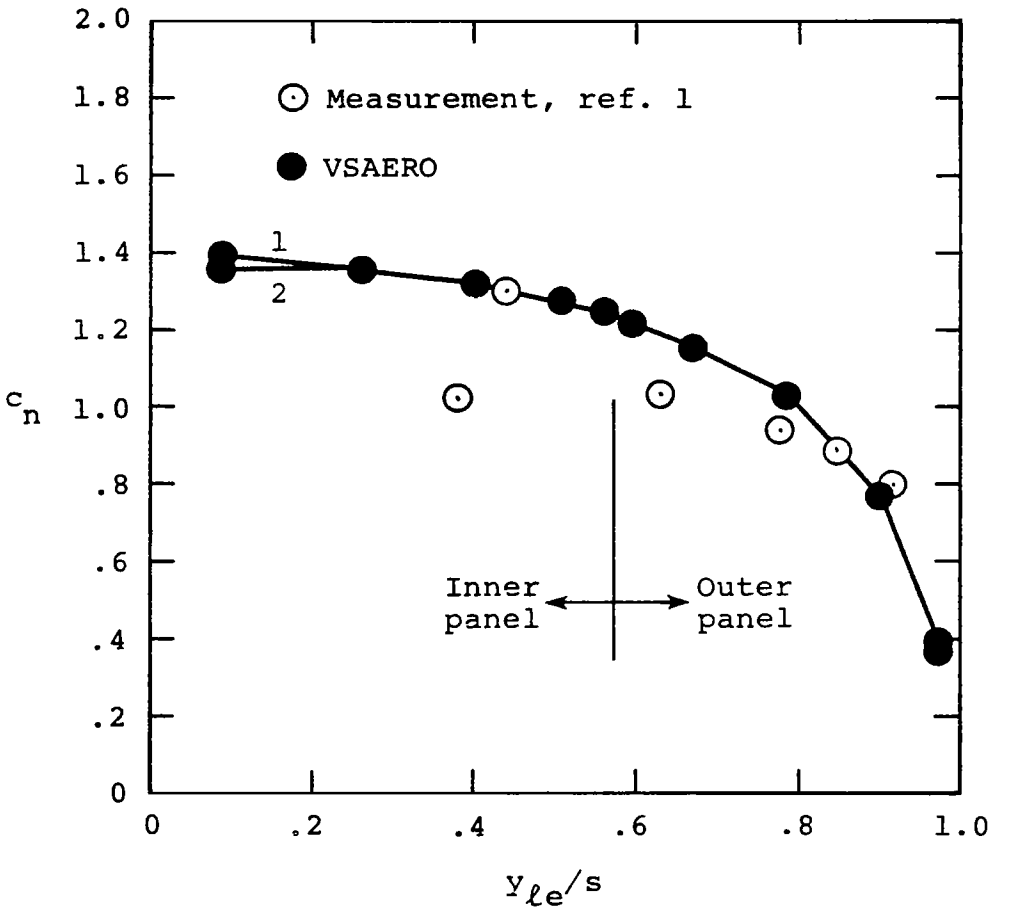

(a) $\alpha = 11.2°$

Figure 15.- Span loading of basic wing.

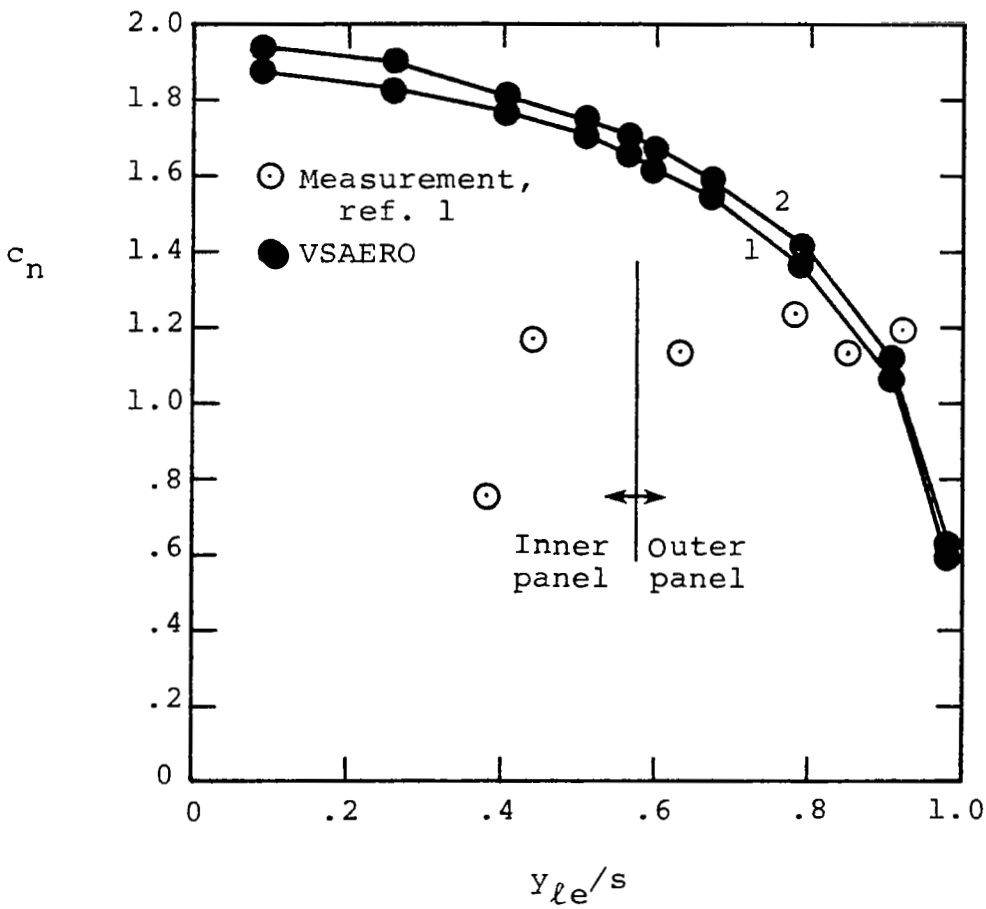

(b) $\alpha = 21.6°$

Figure 15.- (Continued).

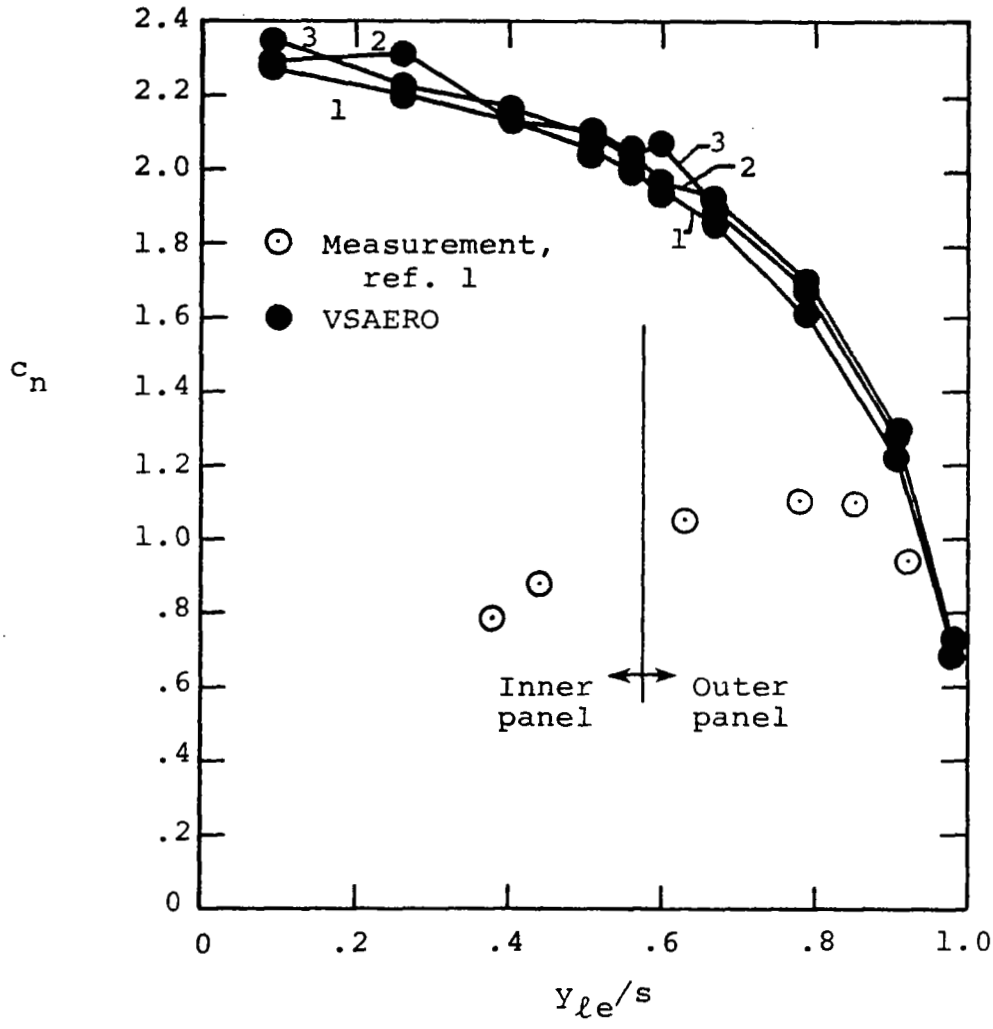

(c) $\alpha = 31.9°$

Figure 15.- (Concluded)

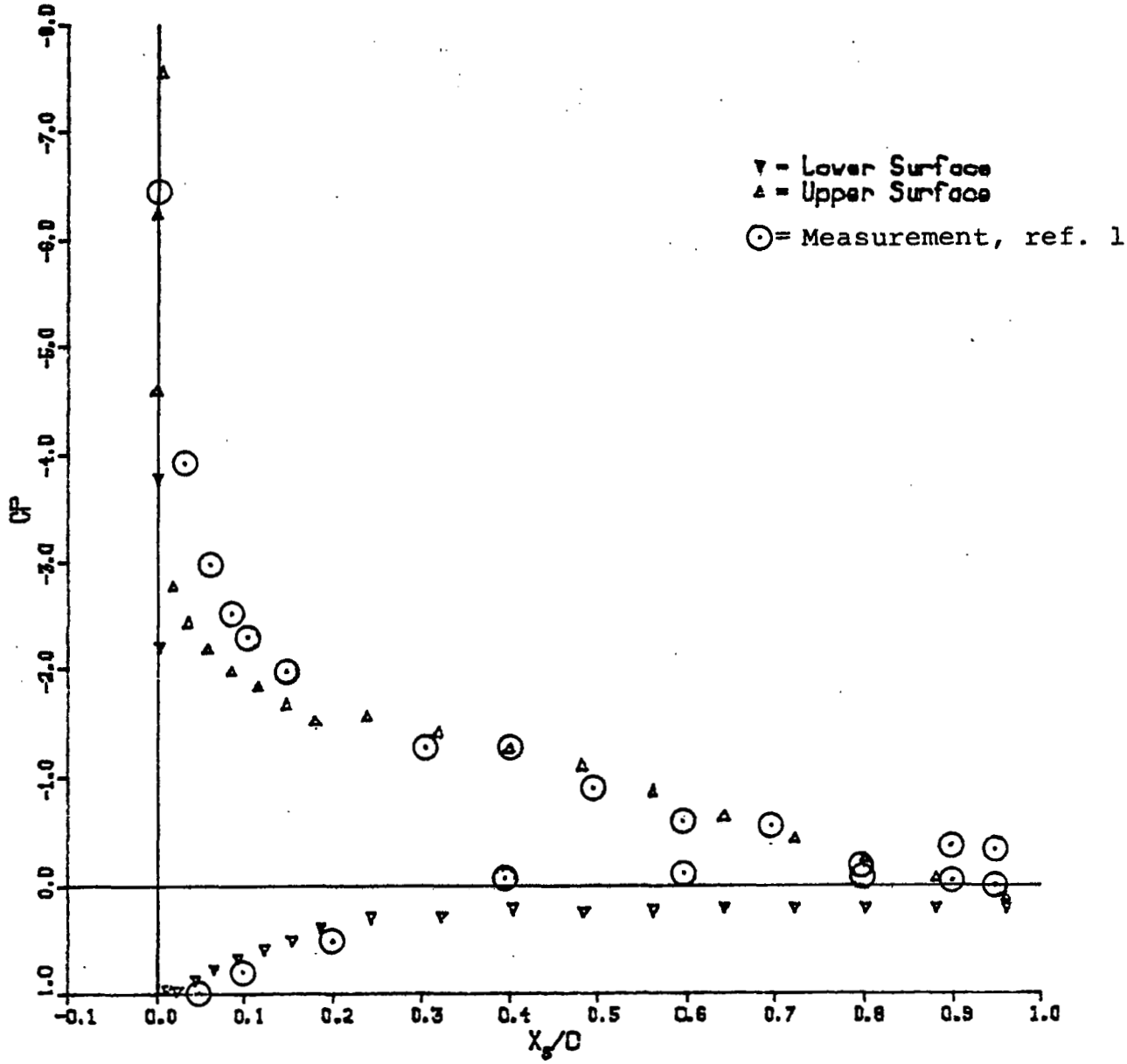

BASIC WING (S X C - 10 X 40) BASICAW1B1A11
Y_s/SSPAN - 0.4031
Iteration 2

(a) $y_{le}/s \approx 0.38$

Figure 16.- Chordwise pressure distribution, basic wing, $\alpha = 11.2°$.

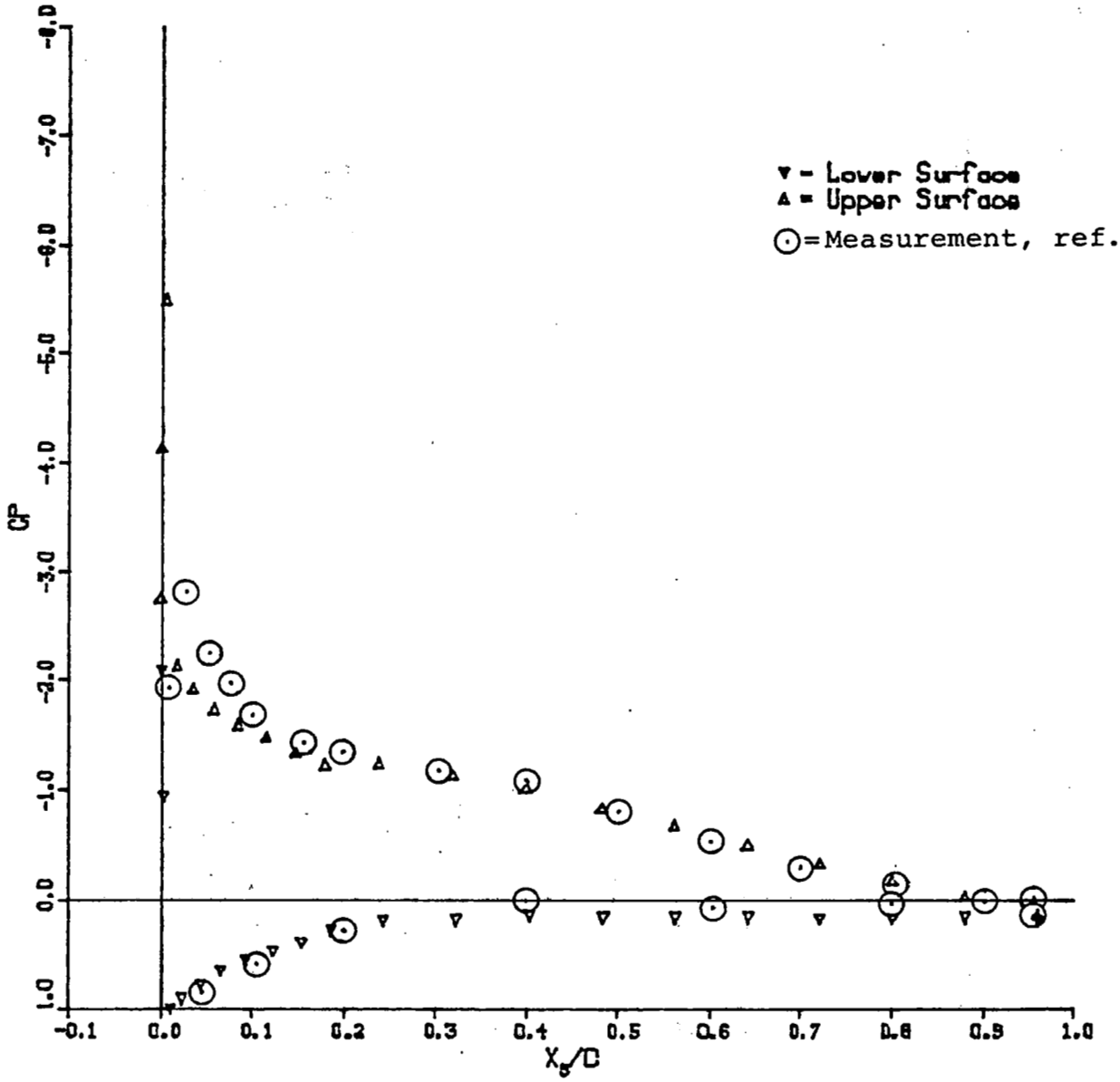

BASIC WING (S X C - 10 X 40) BASICAW1B1A11
Y_s/SSPAN - 0.7887
Iteration 2

(b) $y_{le}/s \approx 0.78$

Figure 16.- (Continued).

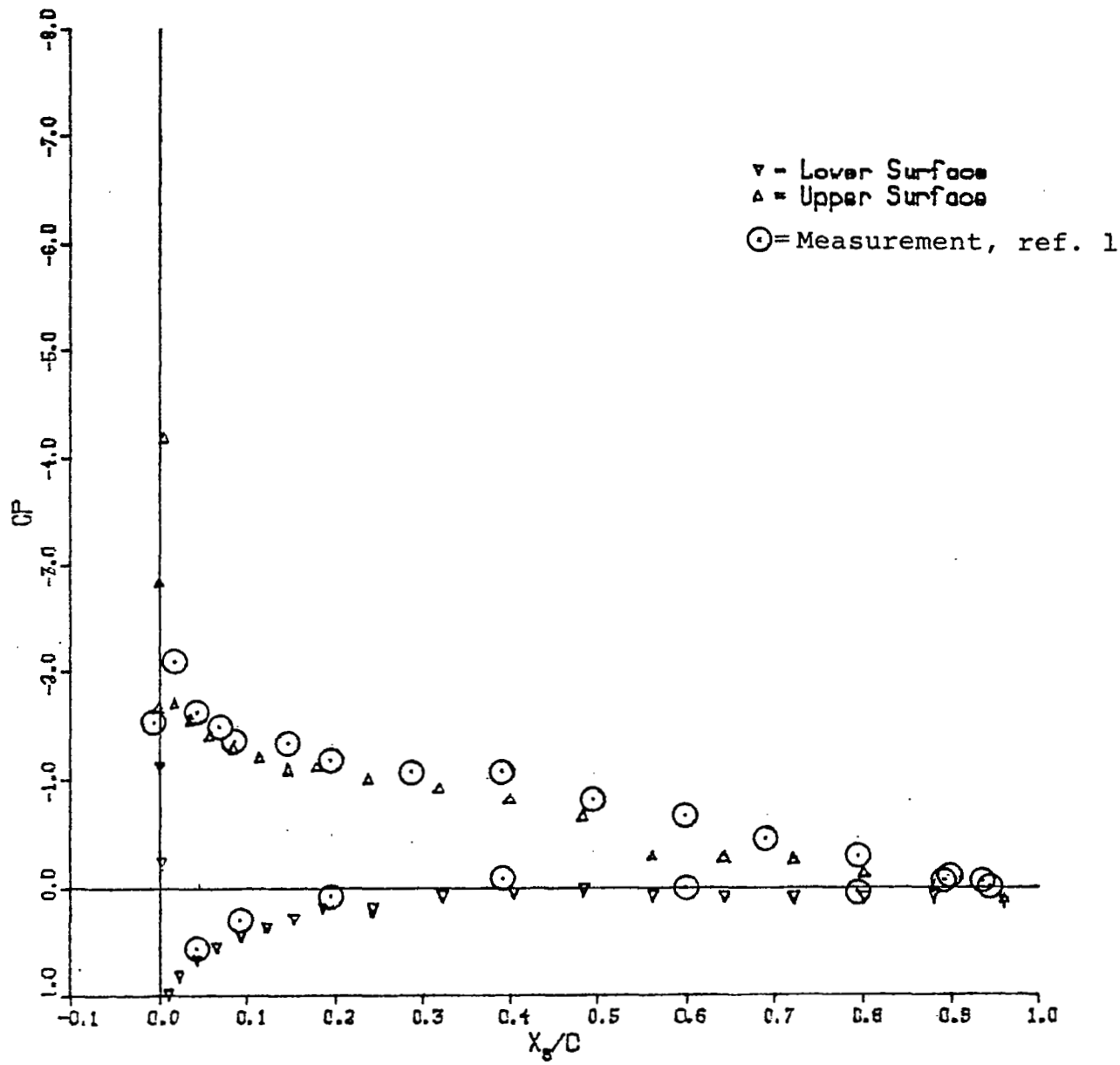

BASIC WING (5 X C - 10 X 40) BASICAW1B1A11
Y_s/SSPAN - 0.9068
Iteration 2

(c) $y_{\ell e}/s \approx 0.92$

Figure 16.- (Concluded).

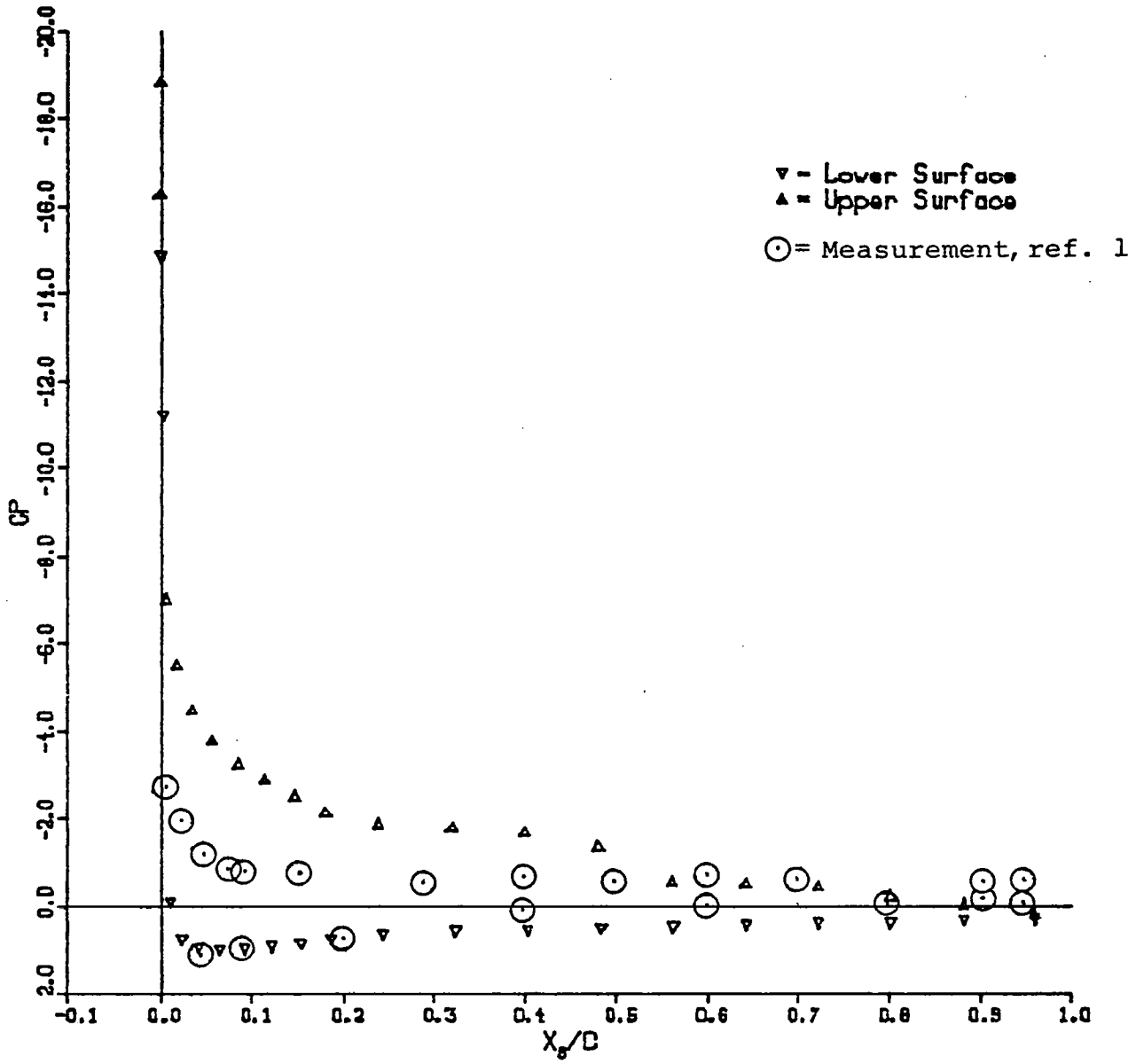

(a) $y_{le}/s \approx 0.38$

Figure 17.- Chordwise pressure distribution, basic wing, $\alpha = 21.6°$

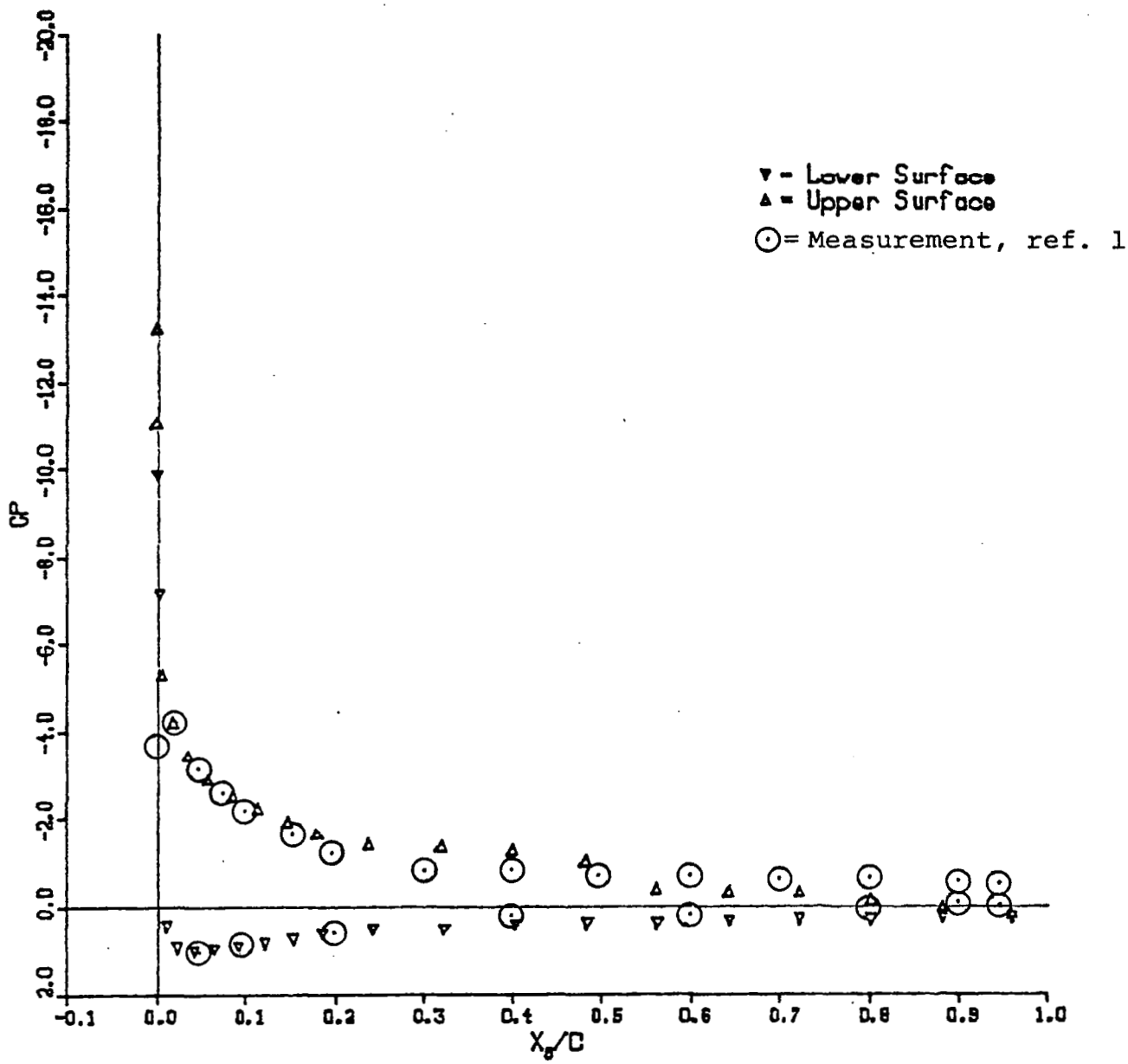

BASIC WING (S X C - 10 X 10) BASICAW1B1A22
$Y_{\ell e}$/SSPAN - 0.7887
Iteration 2

(b) $y_{\ell e}/s \approx 0.78$

Figure 17.- (Continued).

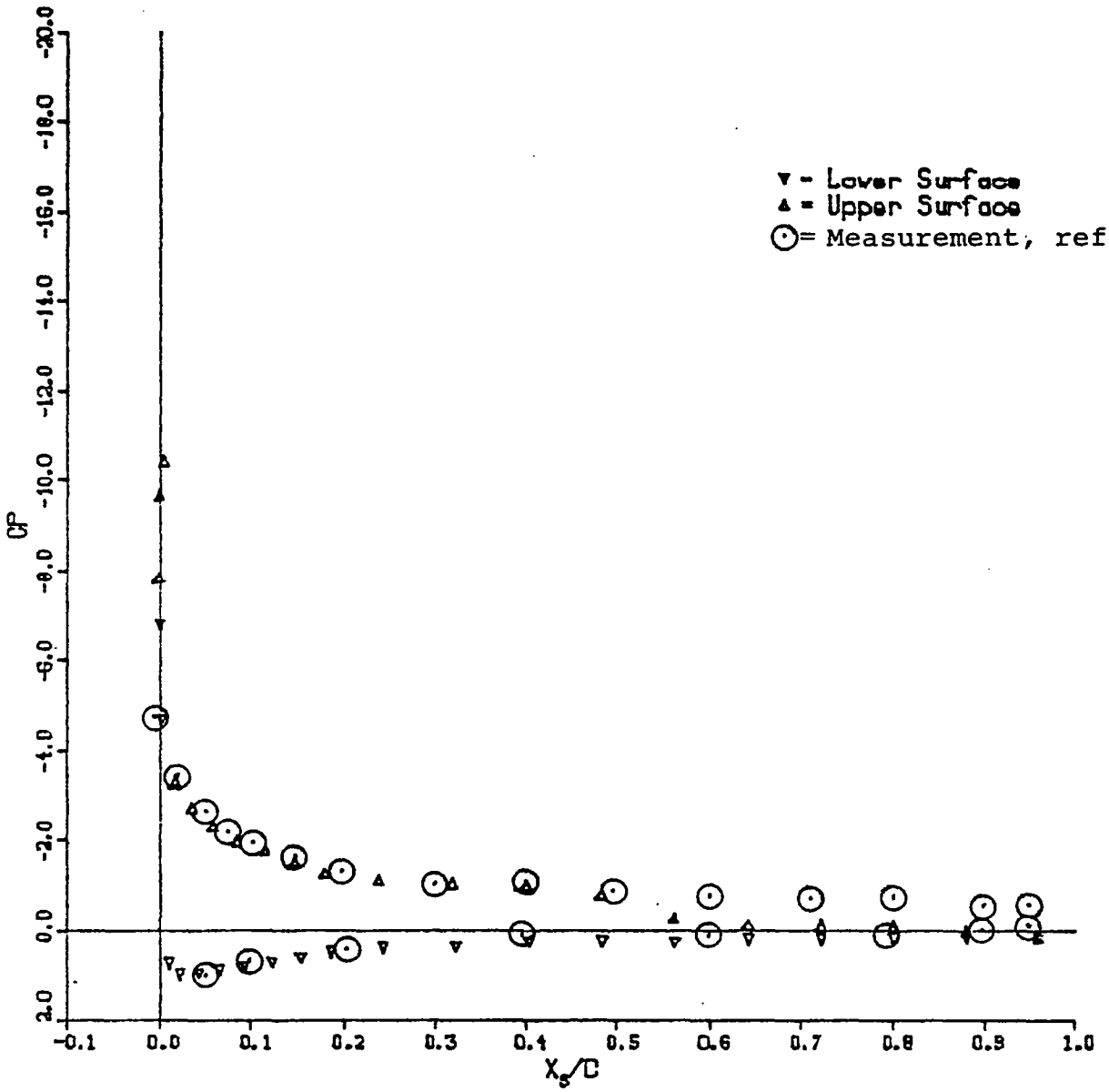

BASIC WING (S X C - 10 X 40) BASICAW1B1A22
Y_s/SSPAN - 0.9068
Iteration 2

(c) $y_{\ell e}/s \approx 0.92$

Figure 17.- (Concluded).

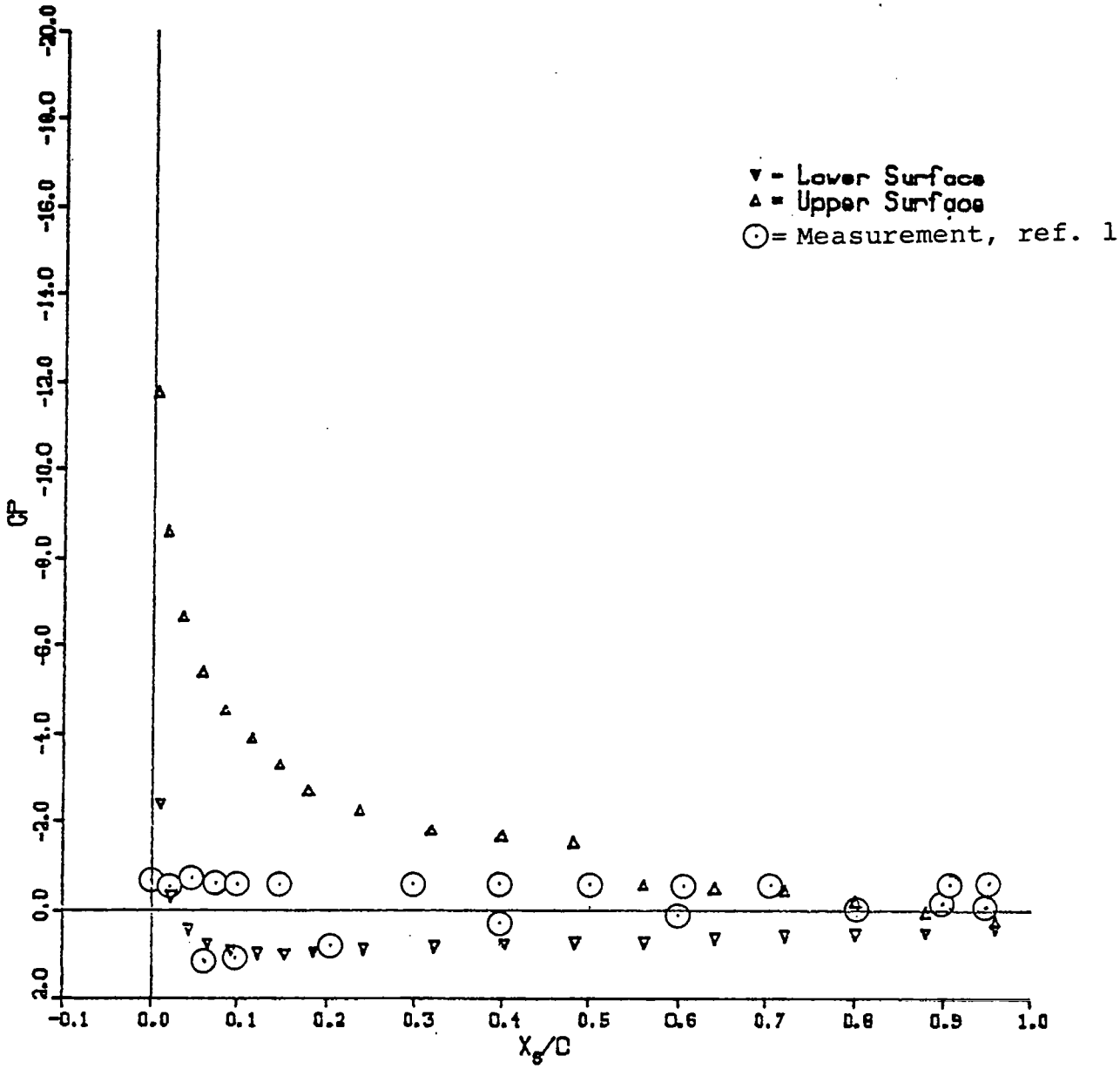

BASIC WING (S X C - 10 X 40) BASICAW2B1A32
Y_s/SSPAN - 0.4031
Iteration 3

(a) $y_{\ell e}/s \approx 0.38$

Figure 18.- Chordwise pressure distribution, basic wing, $\alpha = 31.9°$.

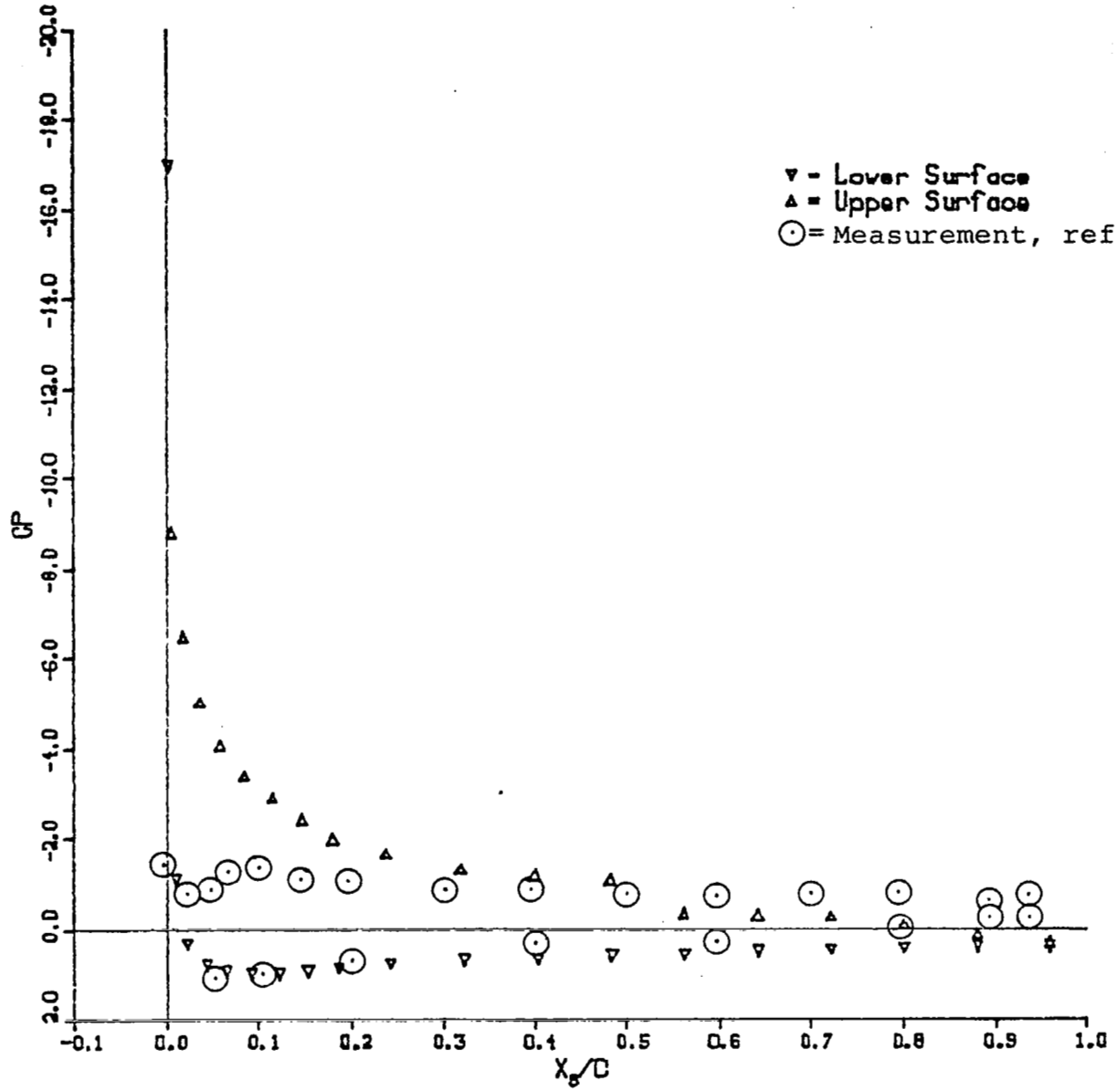

BASIC WING (S X C - 10 X 40) BASICAW2B1A32
Y_p/SSPAN - 0.7887
Iteration 3

(b) $y_{\ell e}/s \simeq 0.78$

Figure 18.- (Continued).

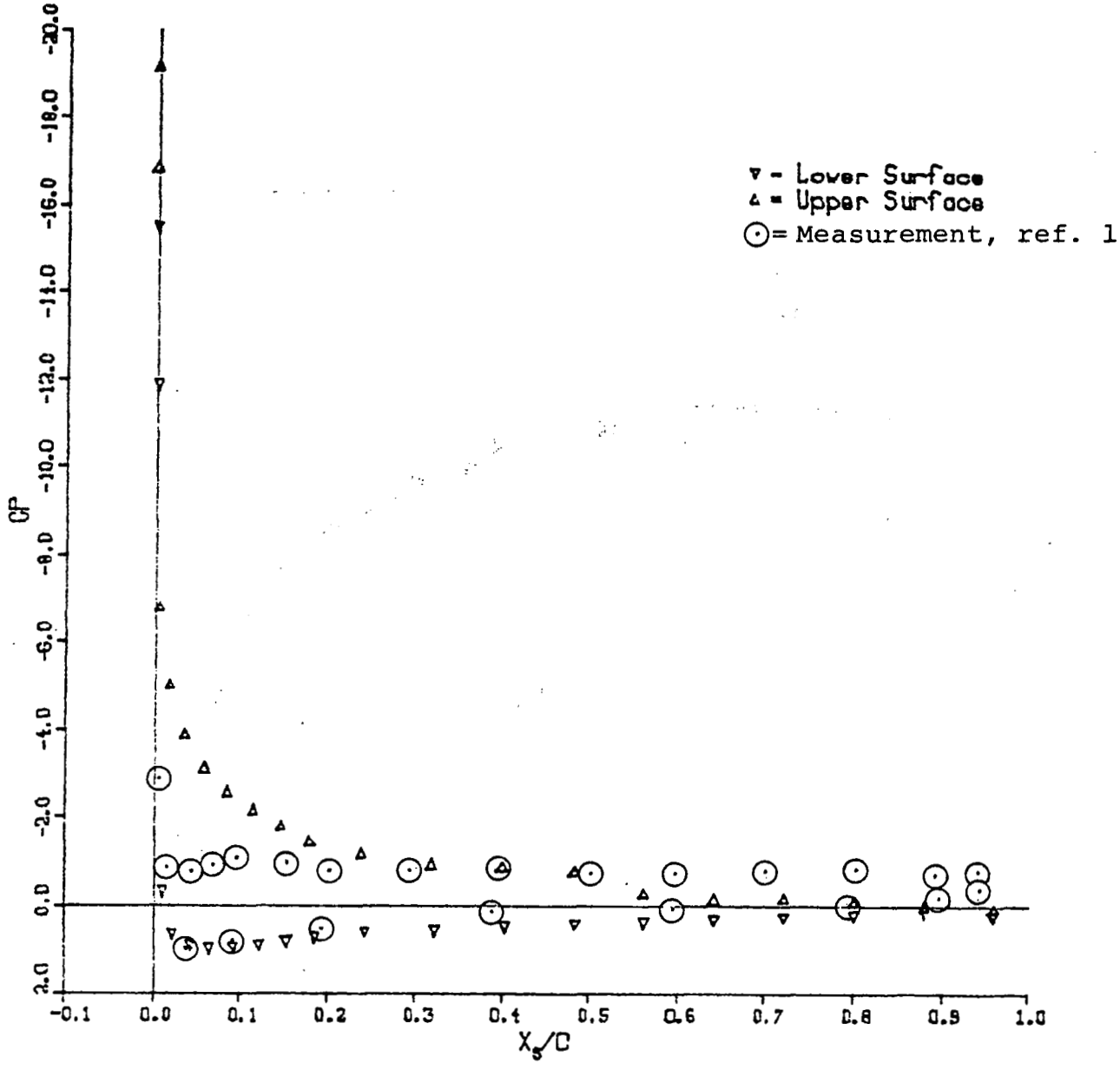

BASIC WING (S X C - 10 X 40) BASICAW2B1A32
Y_p/SSPAN - 0.9068
Iteration 3

(c) $y_{le}/s \simeq 0.92$

Figure 18.- (Concluded).

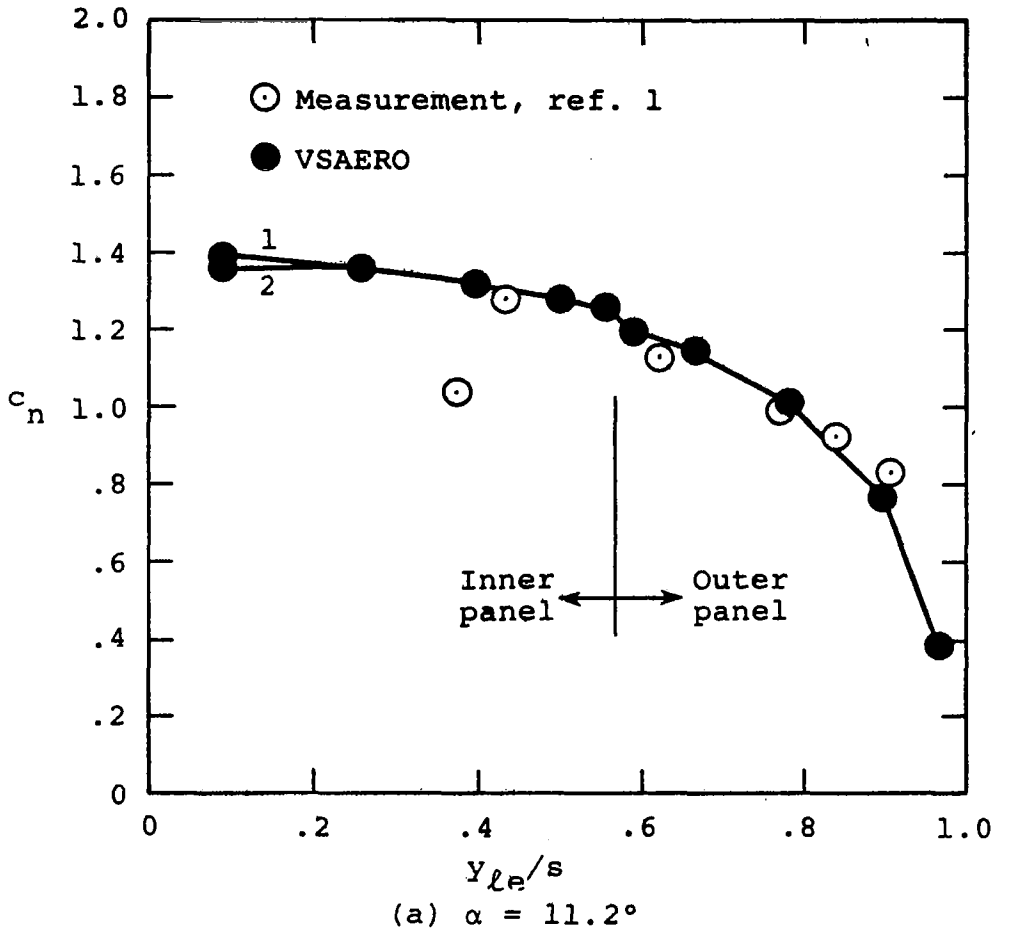

(a) α = 11.2°

Figure 19.- Span loading for wing with outboard droop.

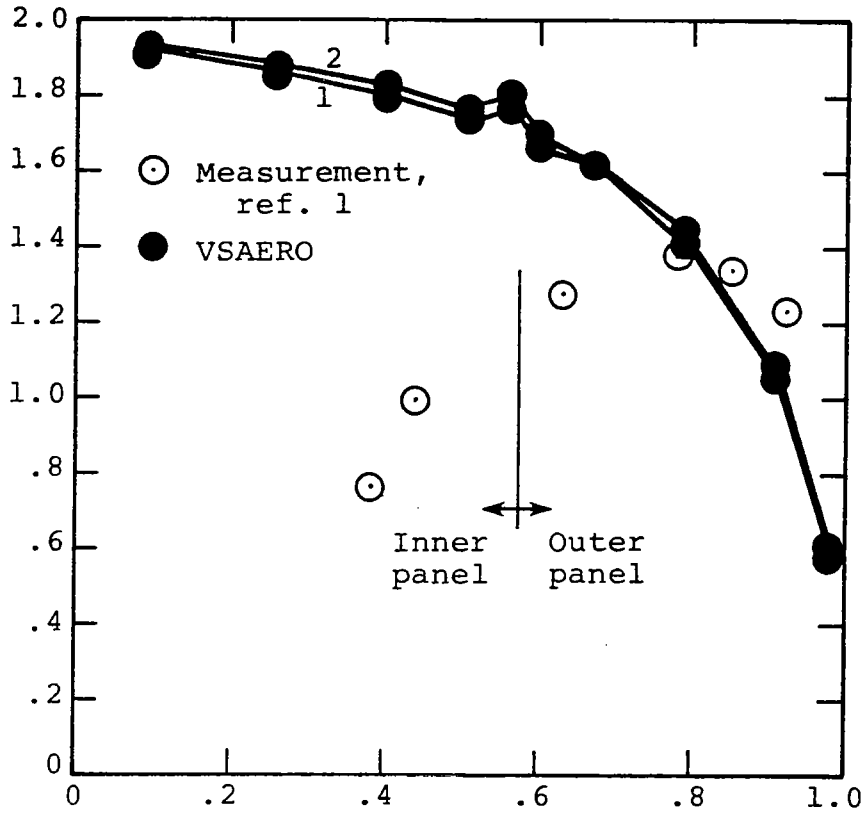

(b) $\alpha = 21.6°$

Figure 19.- (Continued).

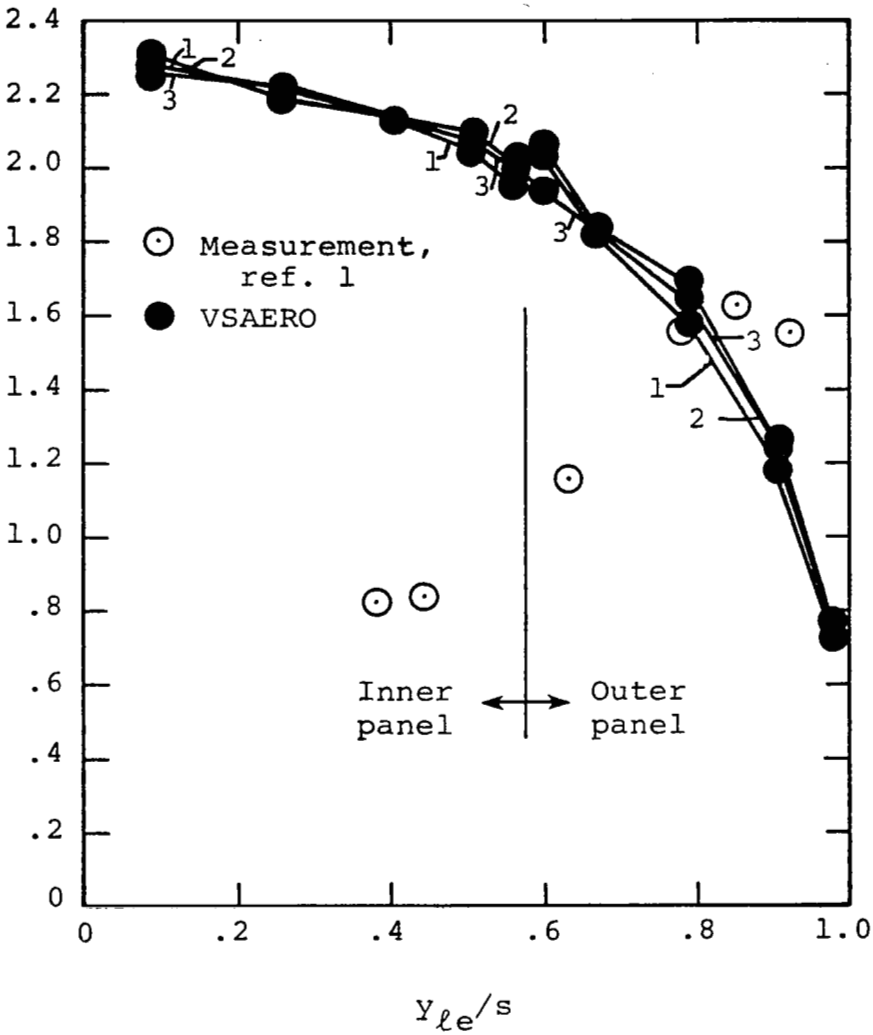

(c) $\alpha = 31.9°$

Figure 19.- (Concluded).

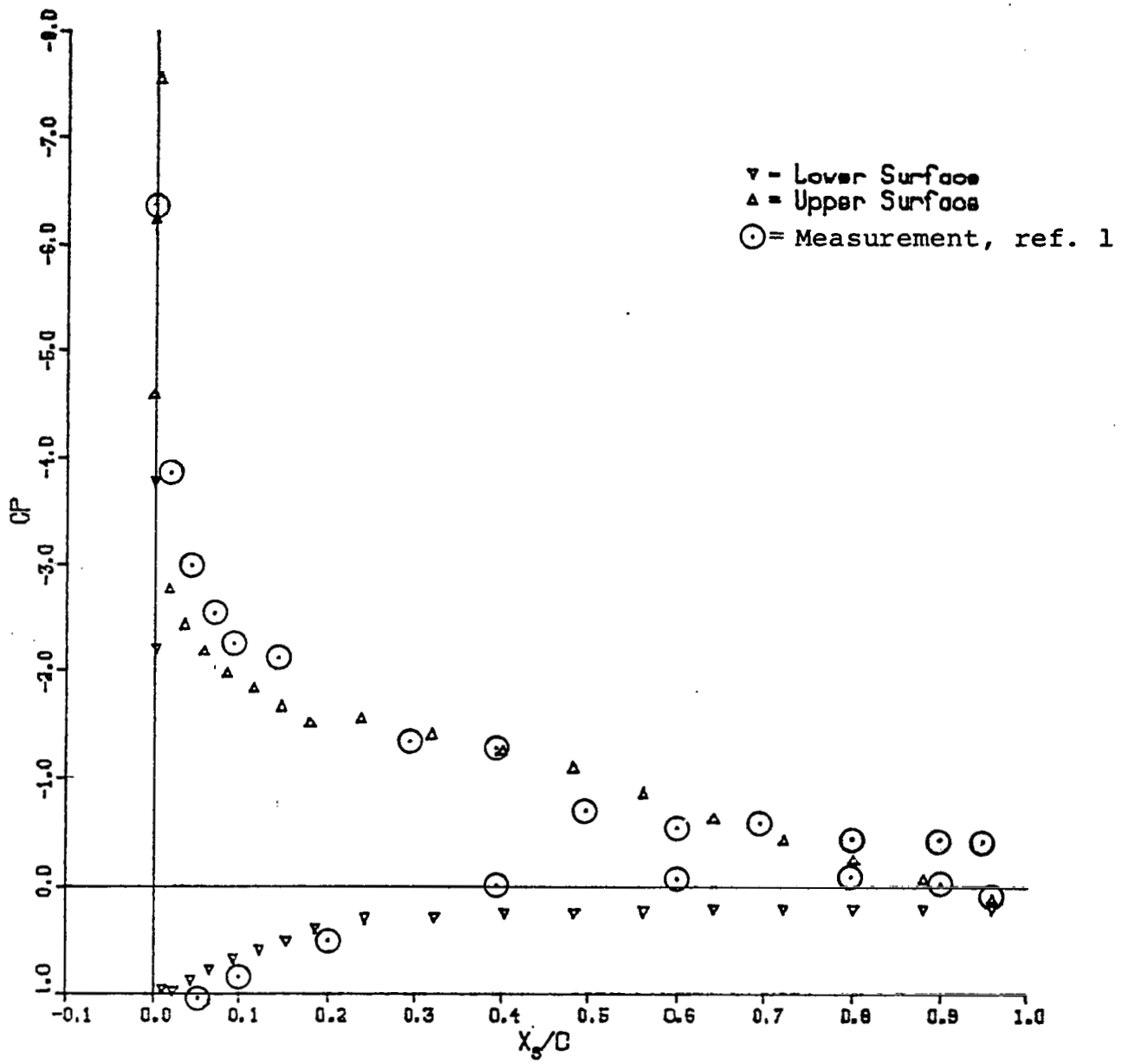

OUTBOARD DROOP (S X C - 10 X 40) DROOPAW1B1A11
$Y_s/SSPAN$ - 0.4031
Iteration 2

(a) $y_{\ell e}/s \approx 0.38$

Figure 20.- Chordwise pressure distribution, wing with outboard droop, $\alpha = 11.2°$

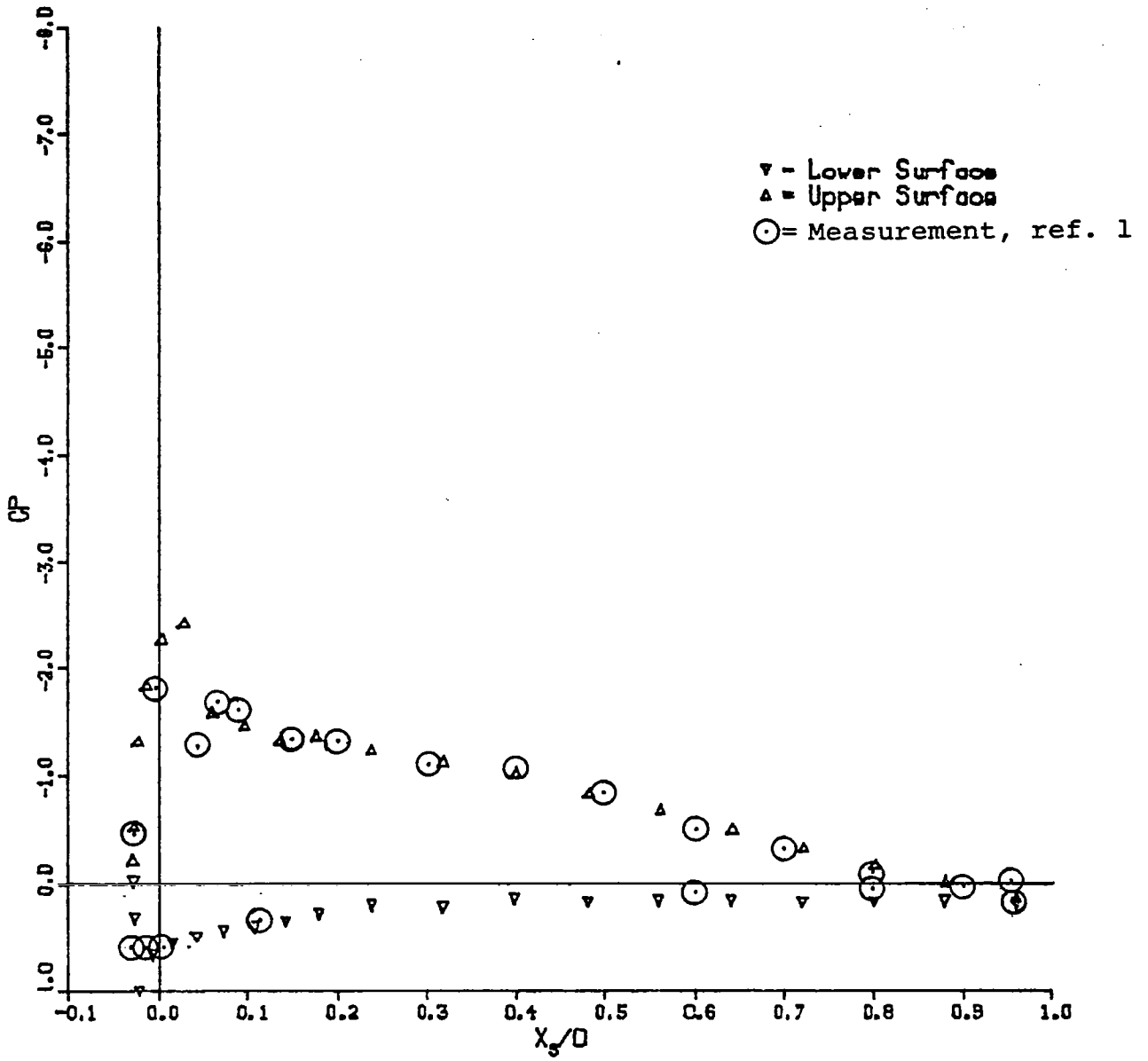

OUTBOARD DROOP (S X C - 10 X 40) DROOPAW1B1A11
Y_s/SSPAN - 0.7887
Iteration 2

(b) $y_{\ell e}/s \approx 0.78$

Figure 20.- (Continued).

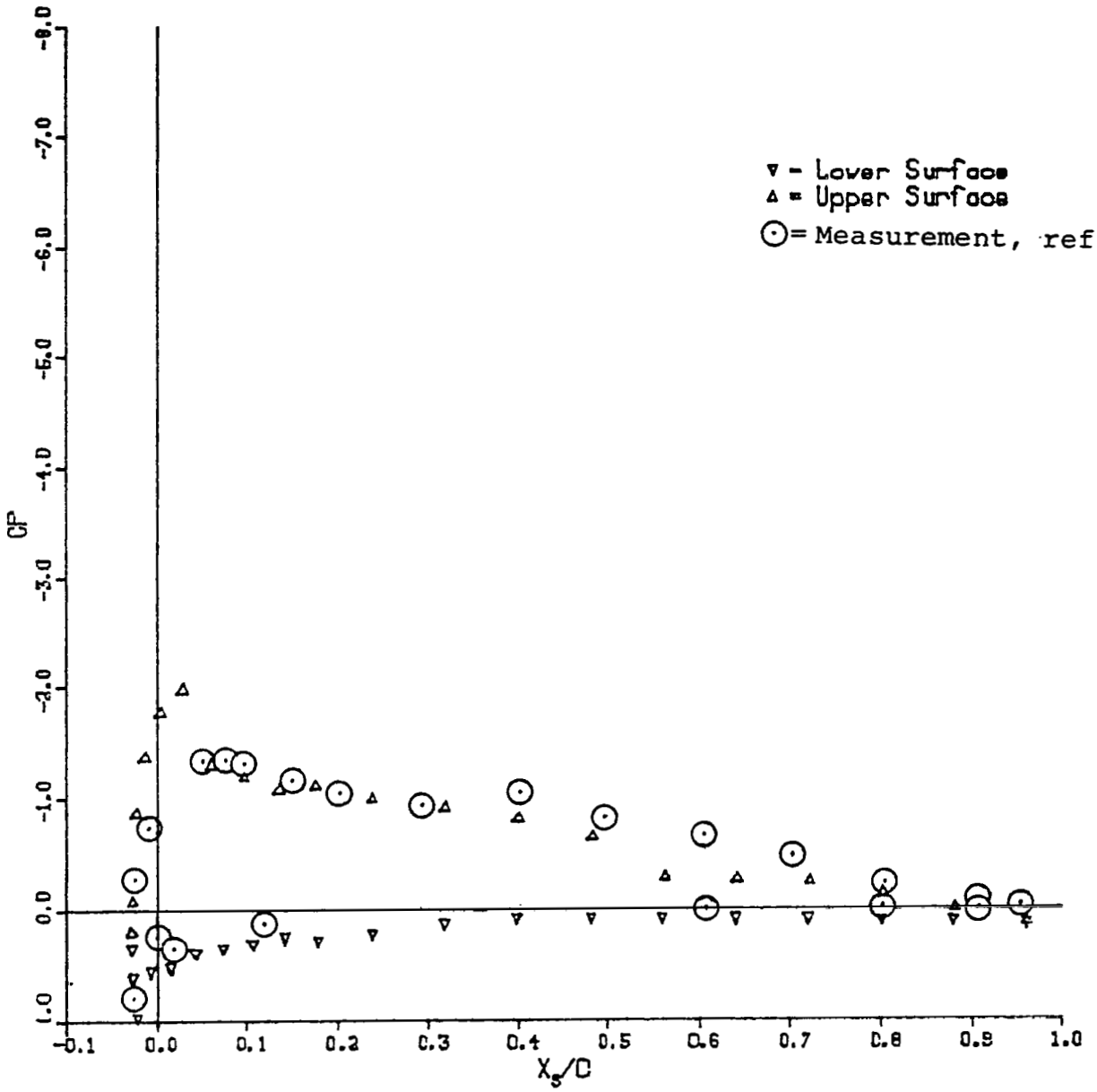

OUTBOARD DROOP (S X C - 10 X 40) DROOPAW1B1A11
Y_s/SSPAN - 0.9068
Iteration 2

(c) $y_{\ell e}/s \simeq 0.92$

Figure 20.- (Concluded).

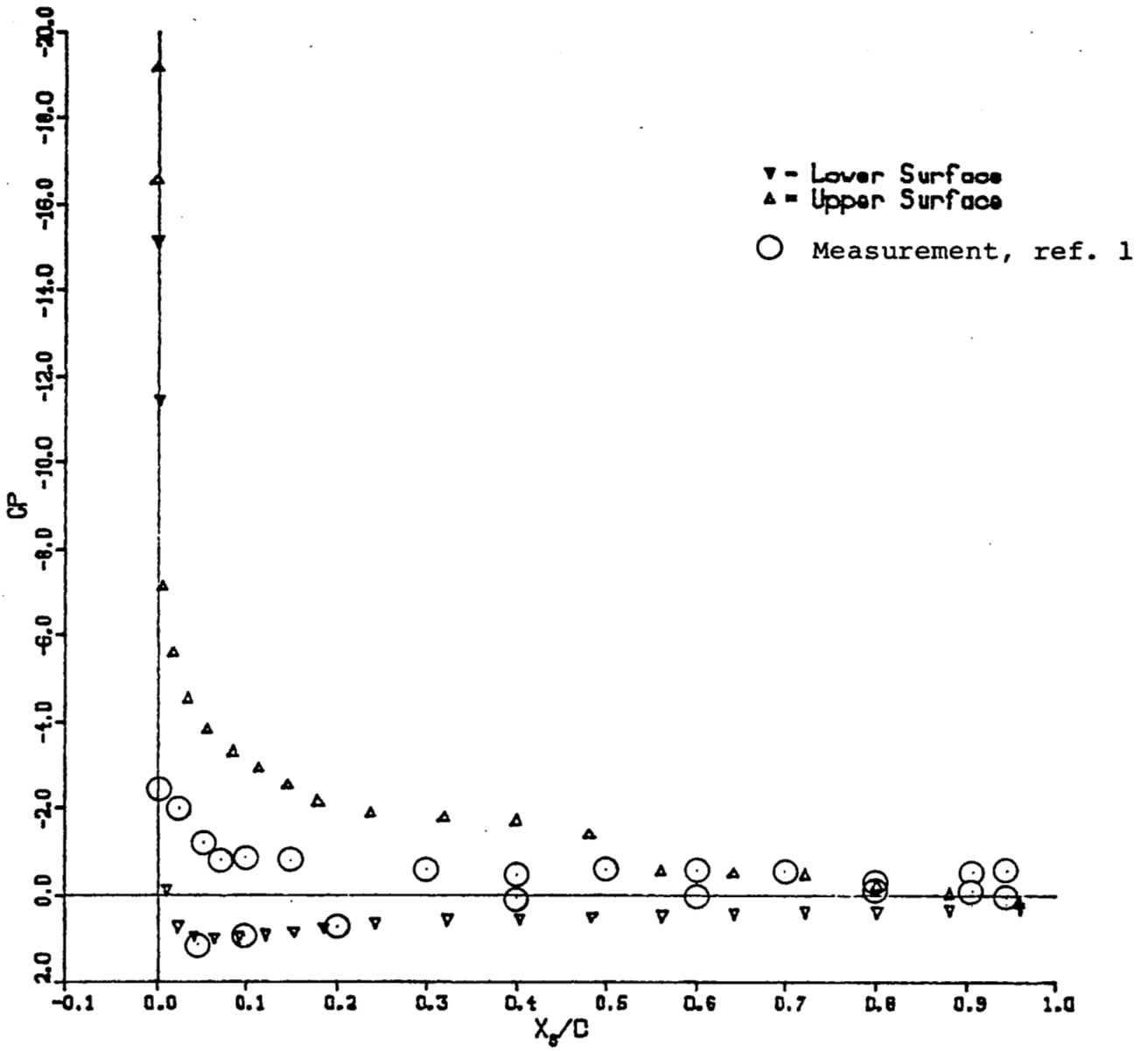

(a) $y_{le}/s \approx 0.38$

Figure 21.- Chordwise pressure distribution, wing with outboard droop, $\alpha = 21.6°$.

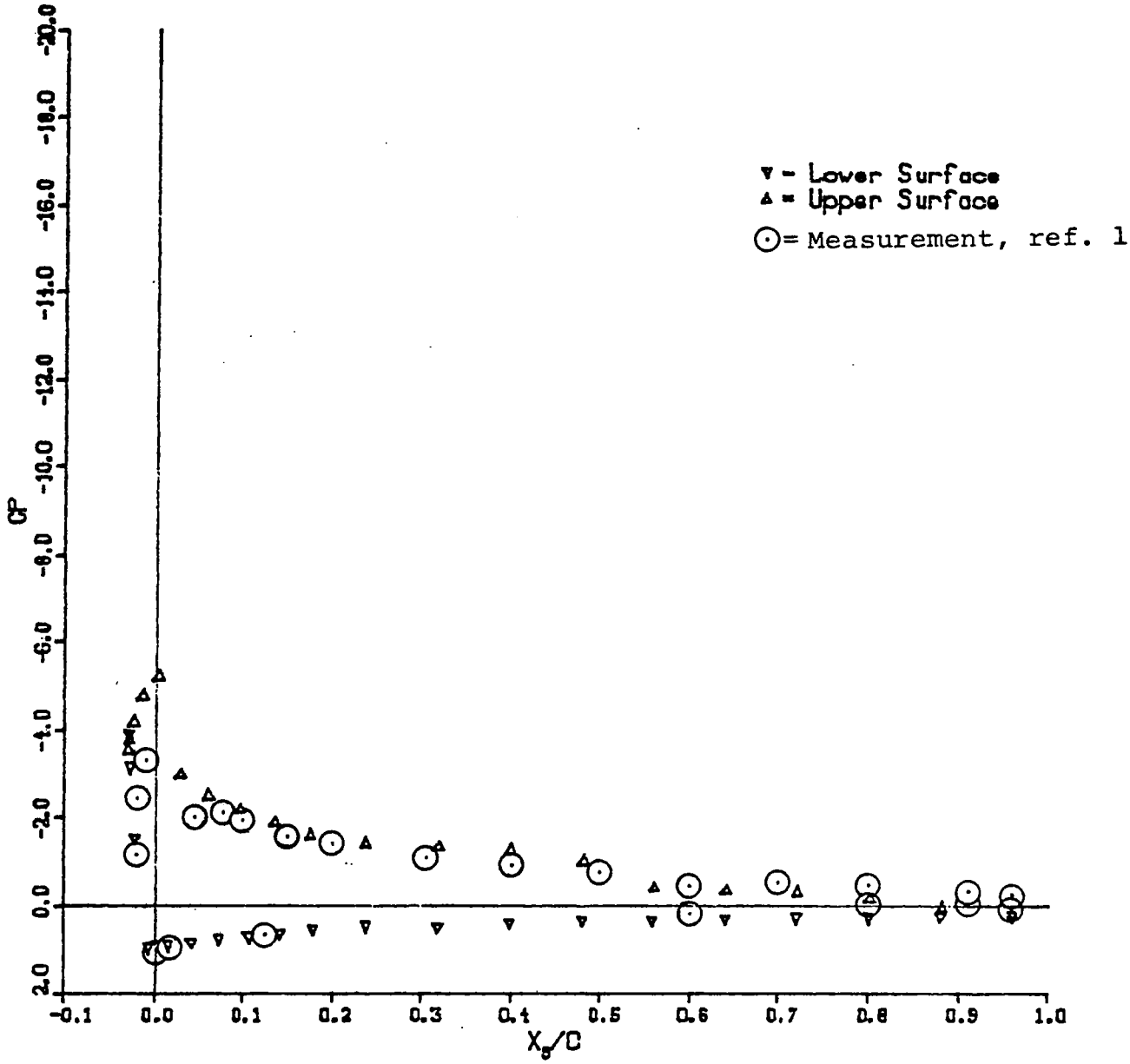

(b) $y_{\ell e}/s \approx 0.78$

Figure 21.- (Continued).

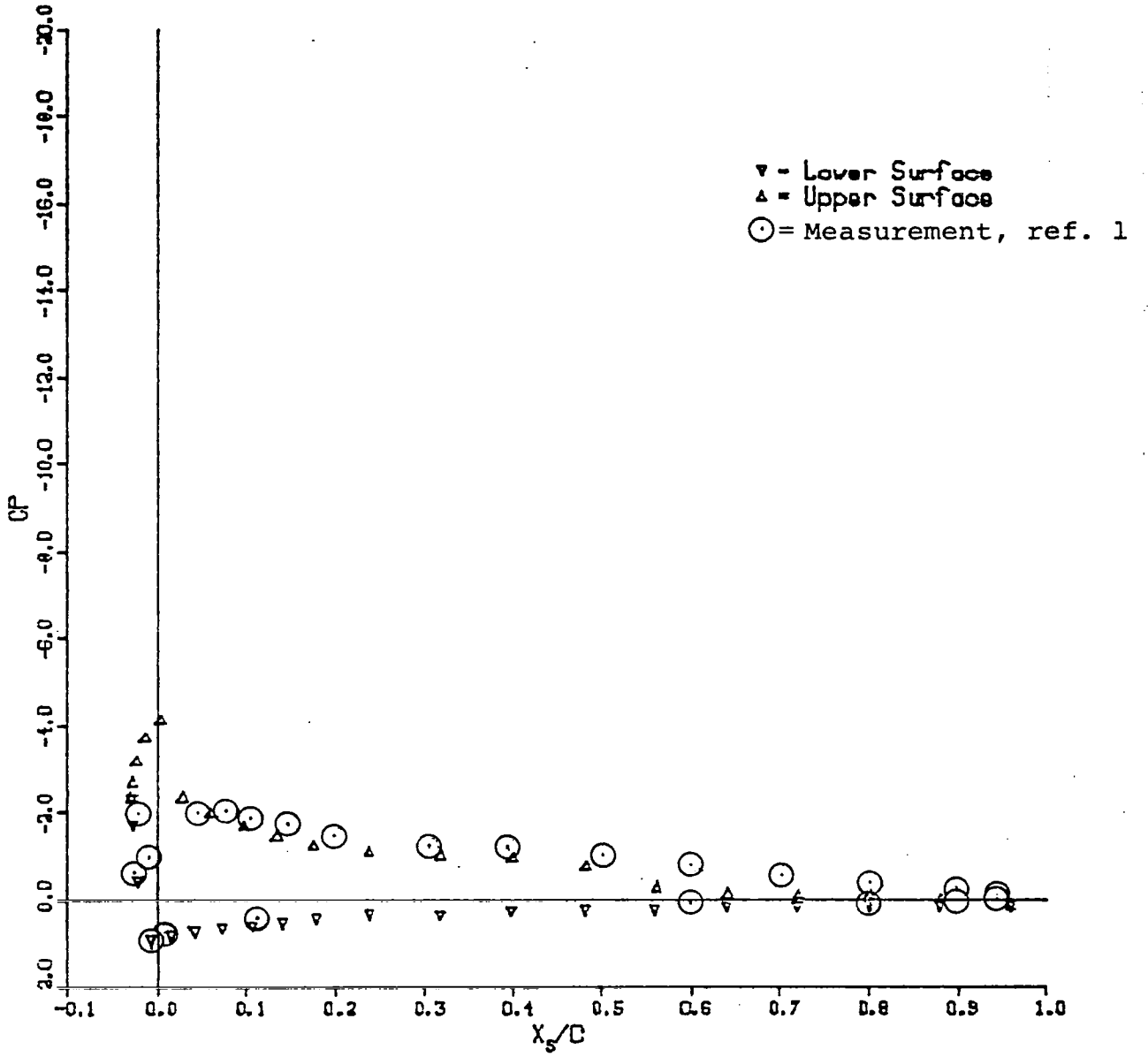

OUTBOARD DROOP (S X C = 10 X 40) DROOPAW1B1A22

$Y_s/SSPAN$ = 0.9068

Iteration 2

(c) $y_{\ell e}/s \approx 0.92$

Figure.- 21 (Concluded).

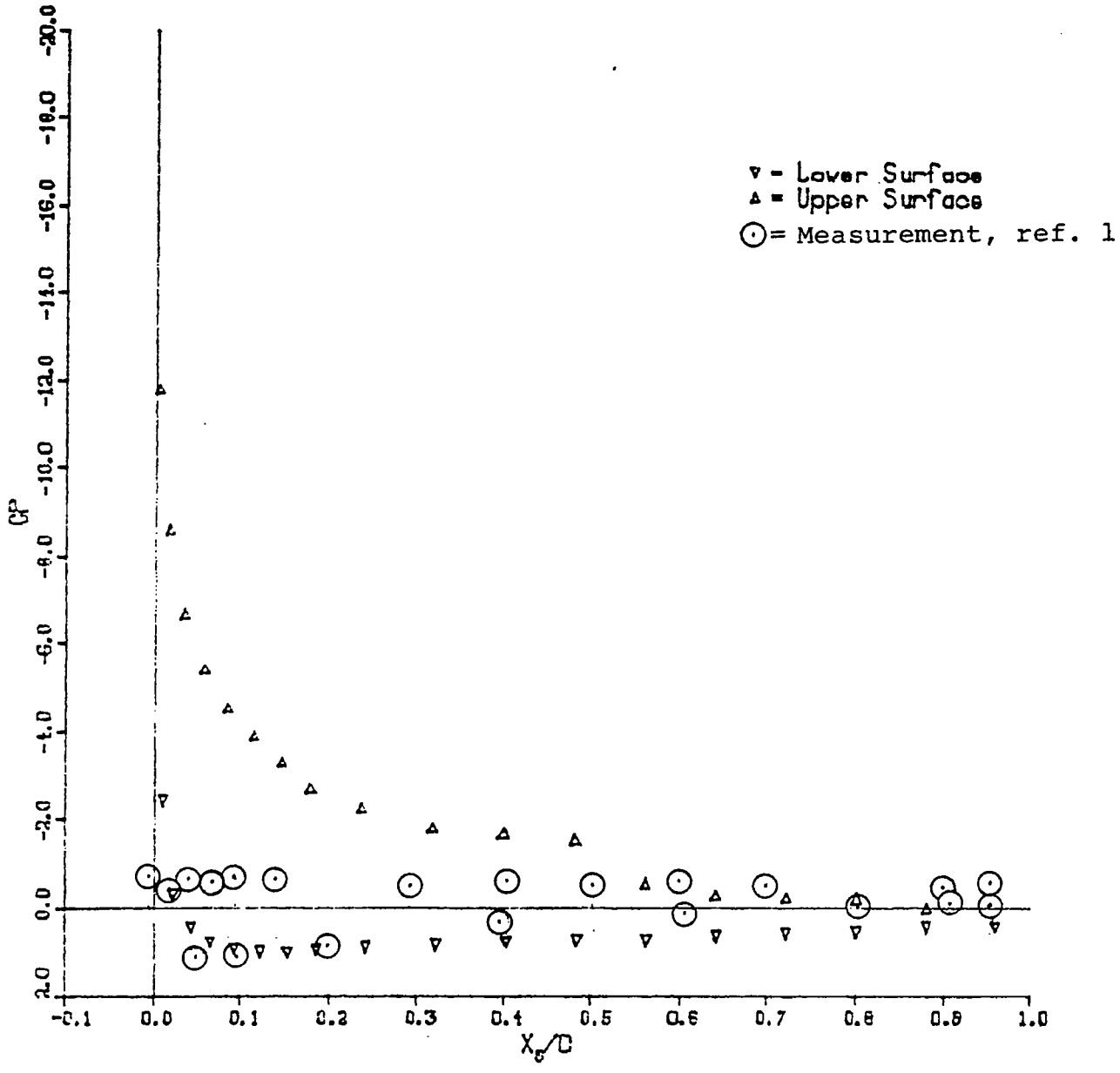

OUTBOARD DROOP IS X C - 10 X 401 DROOPAW2B1A32
Y_p/SSPAN - 0.4031
Iteration 3

(a) $y_{\ell e}/s \approx 0.38$

Figure 22.- Chordwise pressure distribution, wing with outboard droop, $\alpha = 31.9°$.

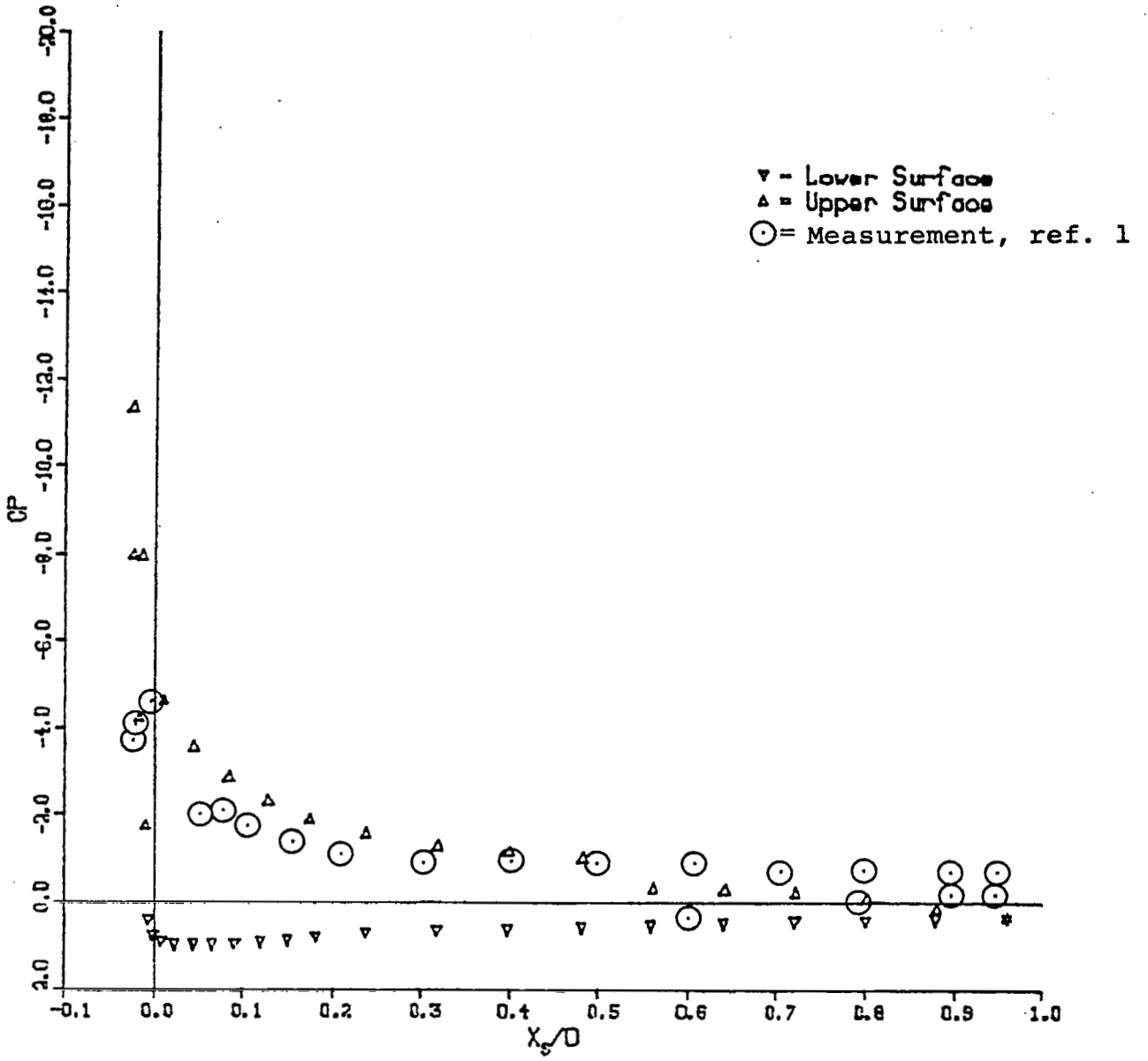

OUTBOARD DROOP (S X C - 10 X 40) DROOPBW2B1A32
Y_e/SSPAN - 0.7687
Iteration 3

(b) $y_{\ell e}/s \approx 0.78$

Figure 22.- (Continued).

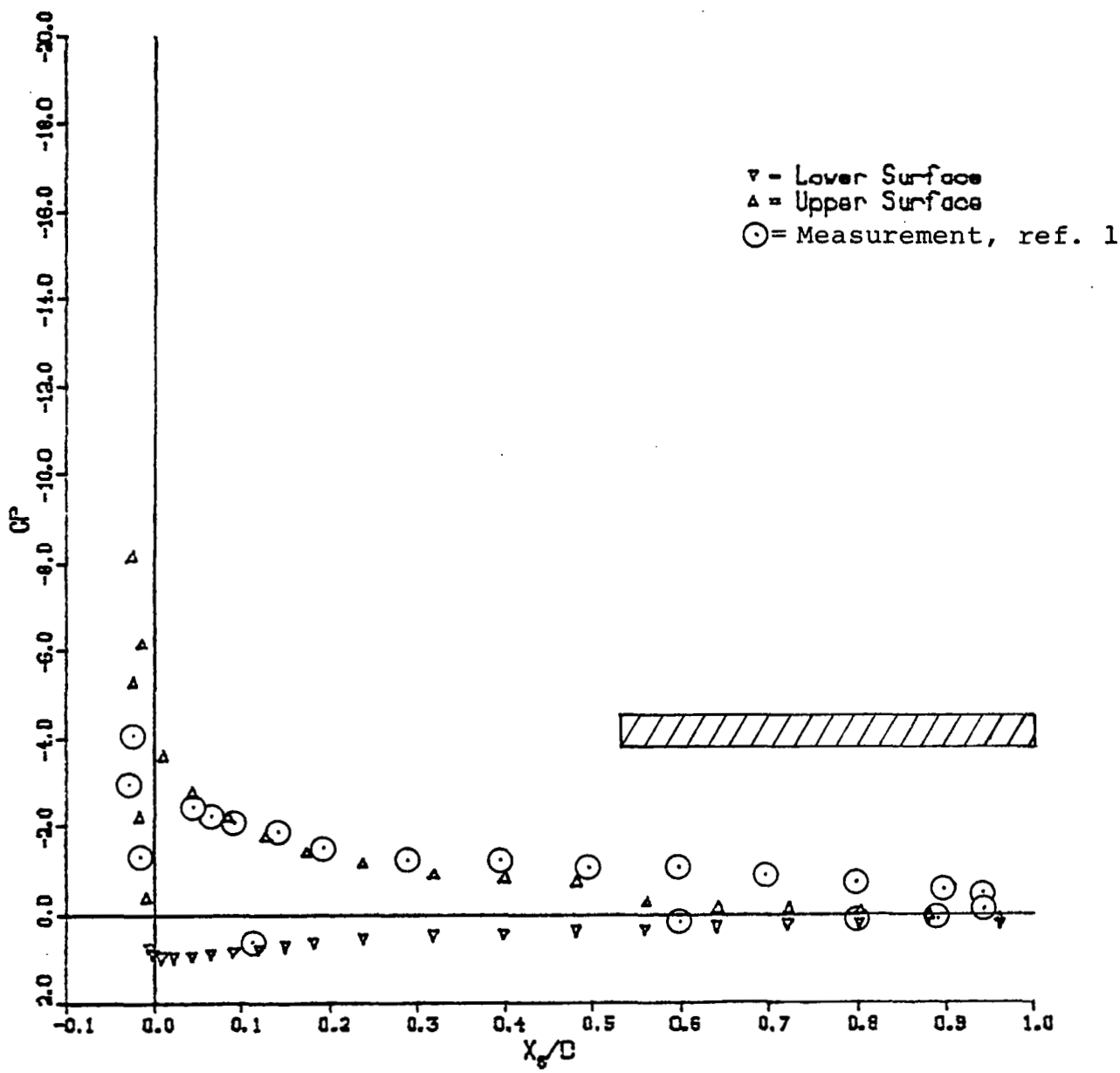

OUTBOARD DROOP (S X C - 10 X 40) DROOPBW2B1A32
Y_s/SSPAN - 0.9068
Iteration 3

(c) $y_{\ell e}/s \approx 0.92$

Figure 22.- Concluded.

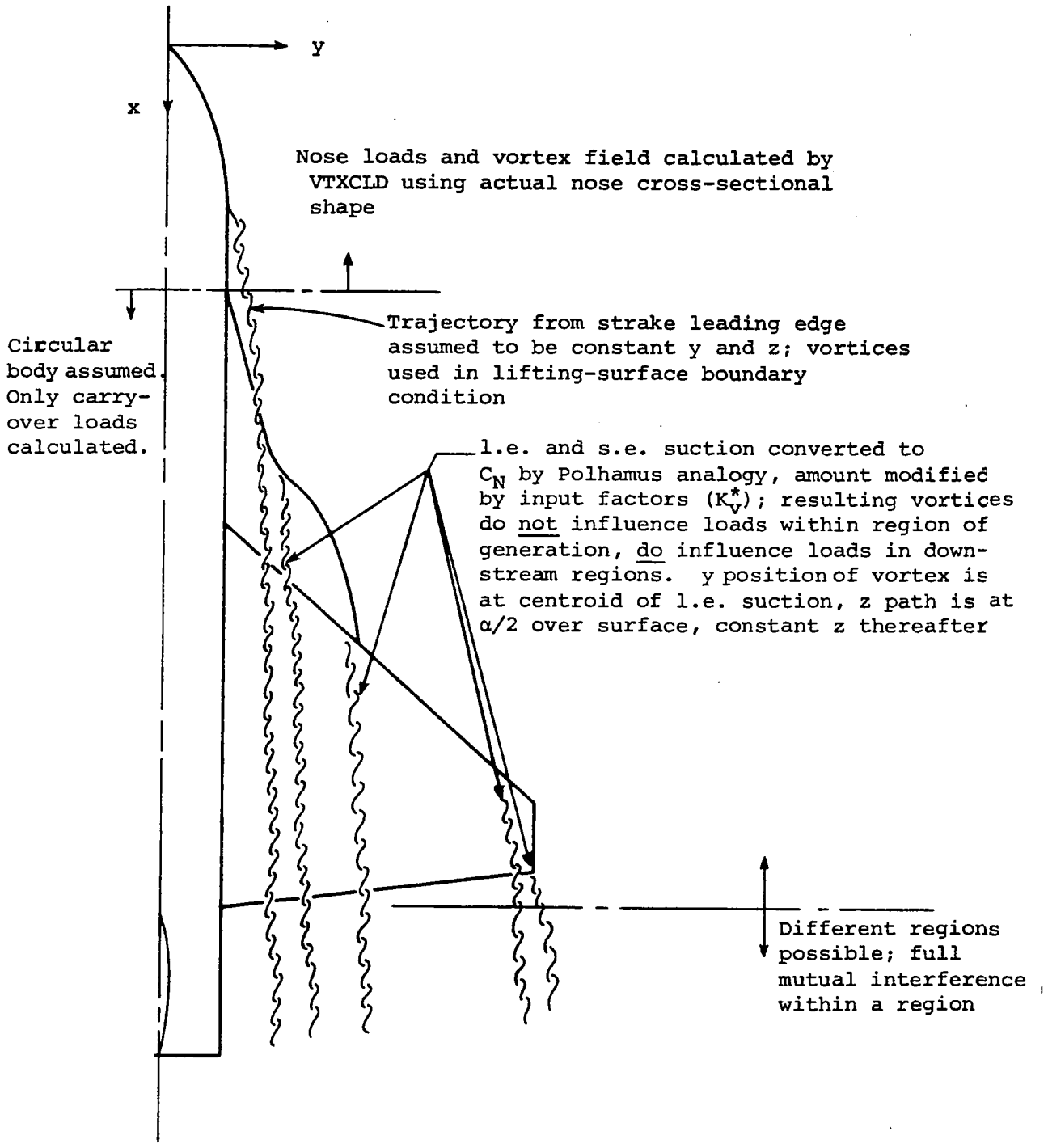

Figure 23.- Major features of the prediction method for a complete fighter configuration.

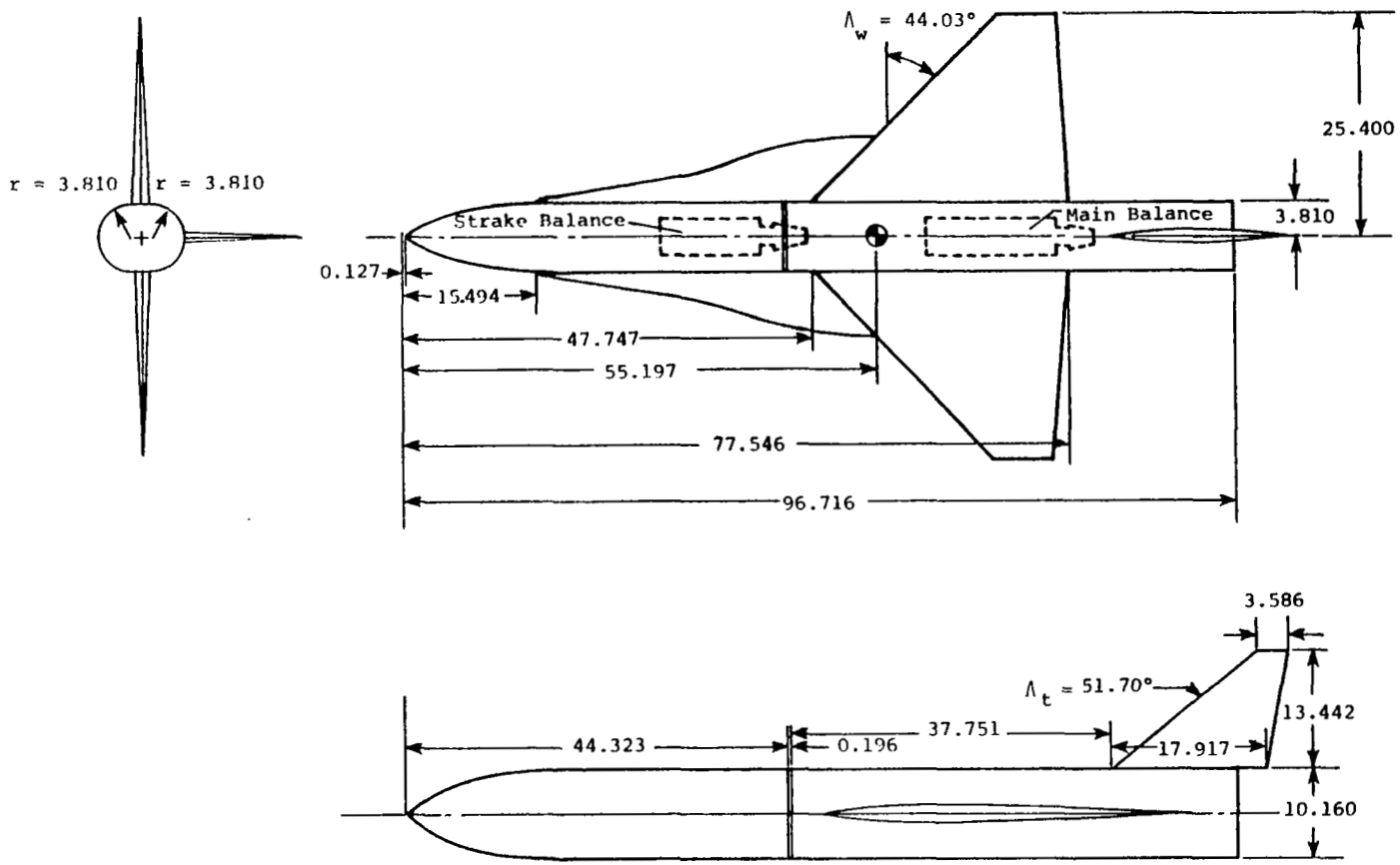

Figure 24.- The Generalized Research Fighter. From reference 43. All linear dimensions are in centimeters.

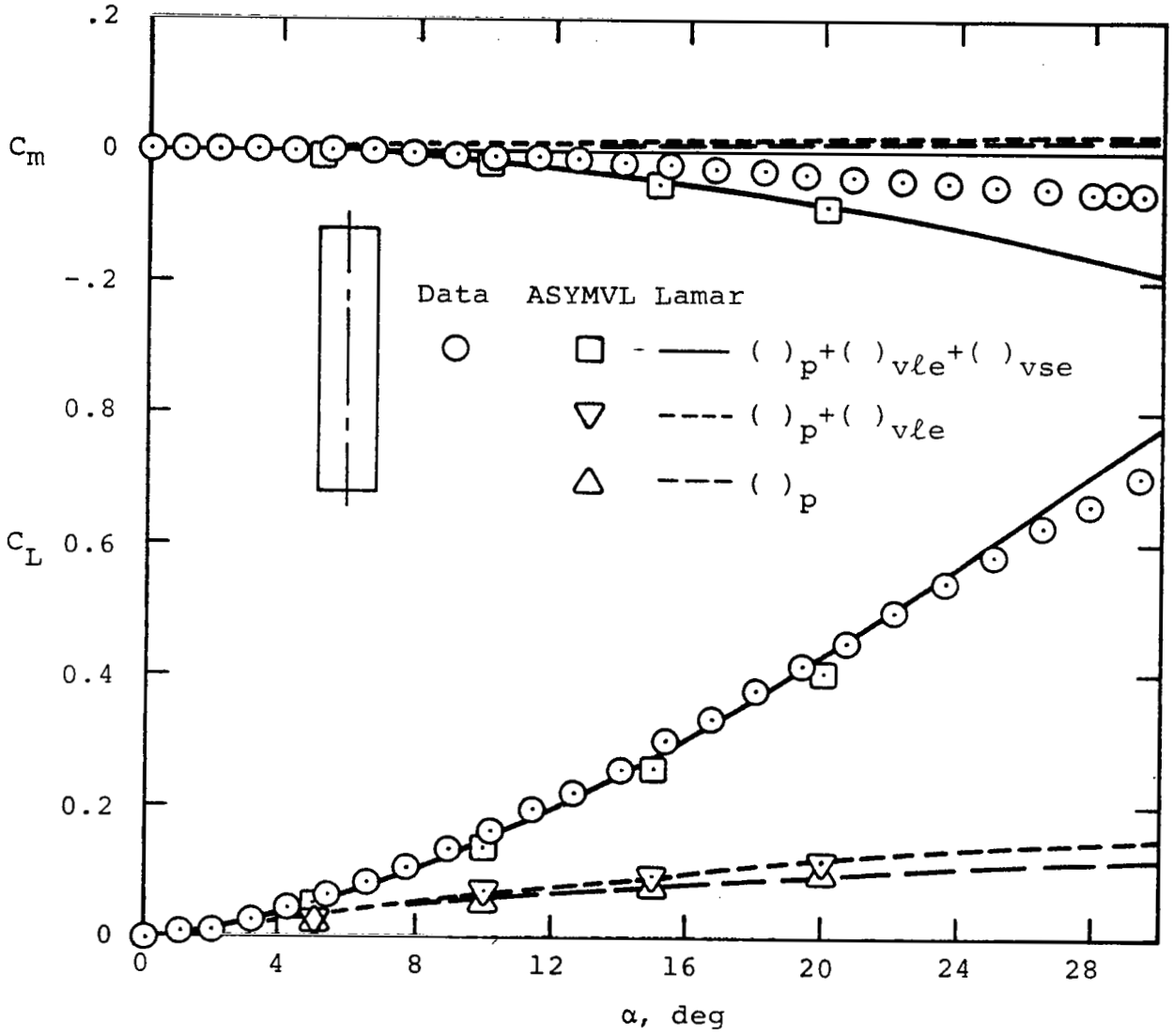

Figure 25.- Calculated and measured results for a flat rectangular wing of AS = 0.2. From reference 45.

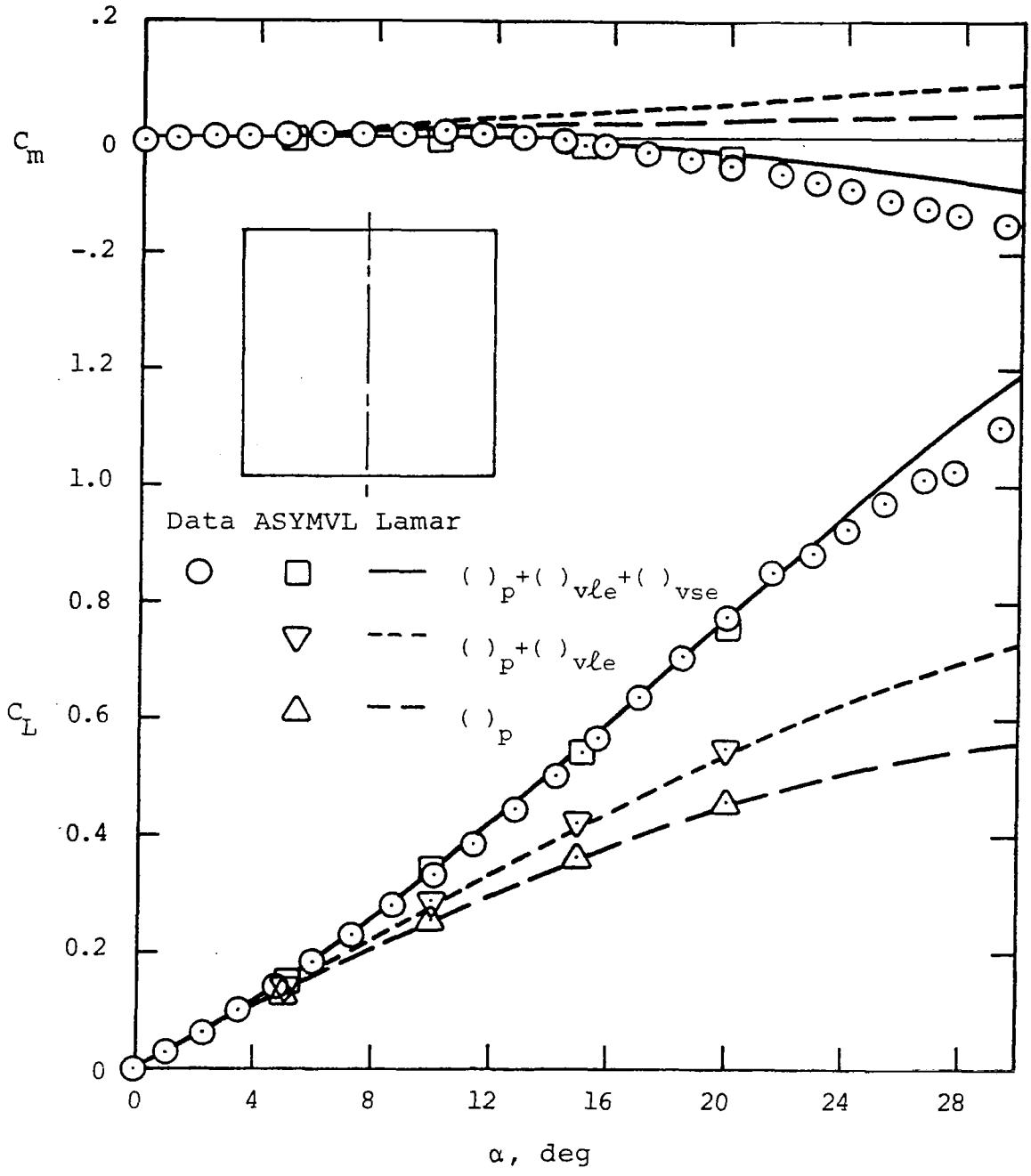

Figure 26.- Calculated and measured results for a flat rectangular wing of AS = 1.0. From reference 45.

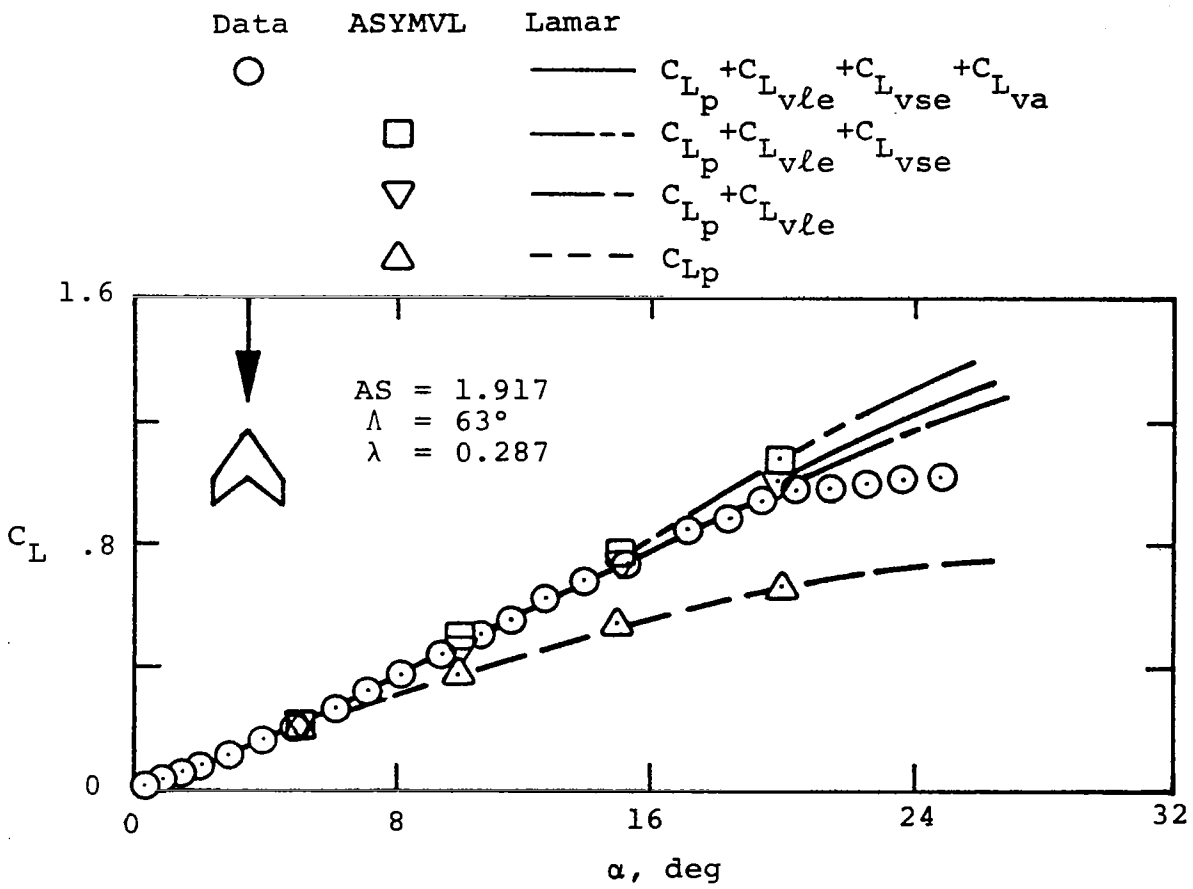

Figure 27.- Calculated and measured lift coefficient for a cropped arrow wing. From reference 34.

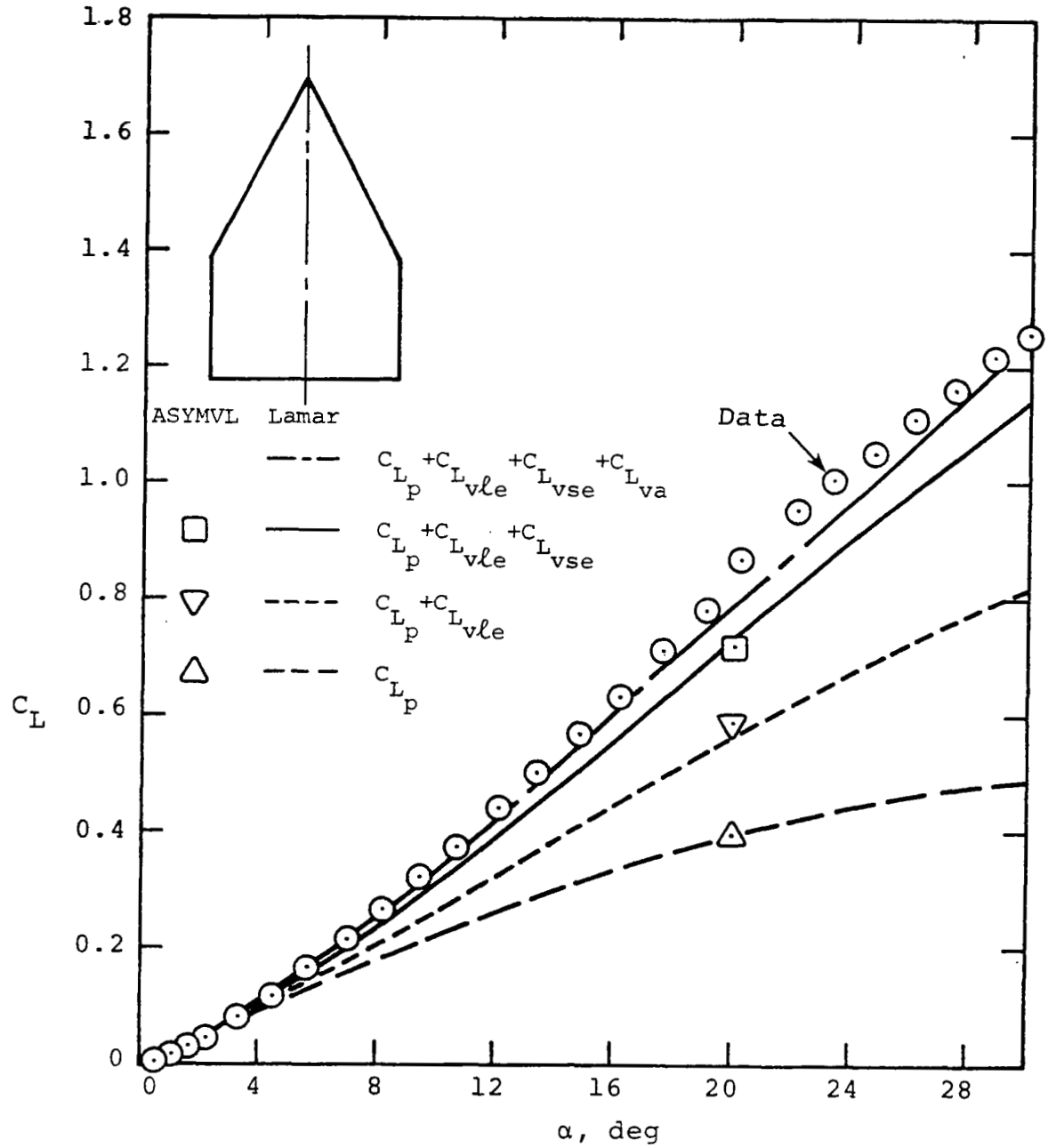

Figure 28.- Calculated and measured lift coefficient for a cropped delta wing of AS = 0.873 (from ref. 45).

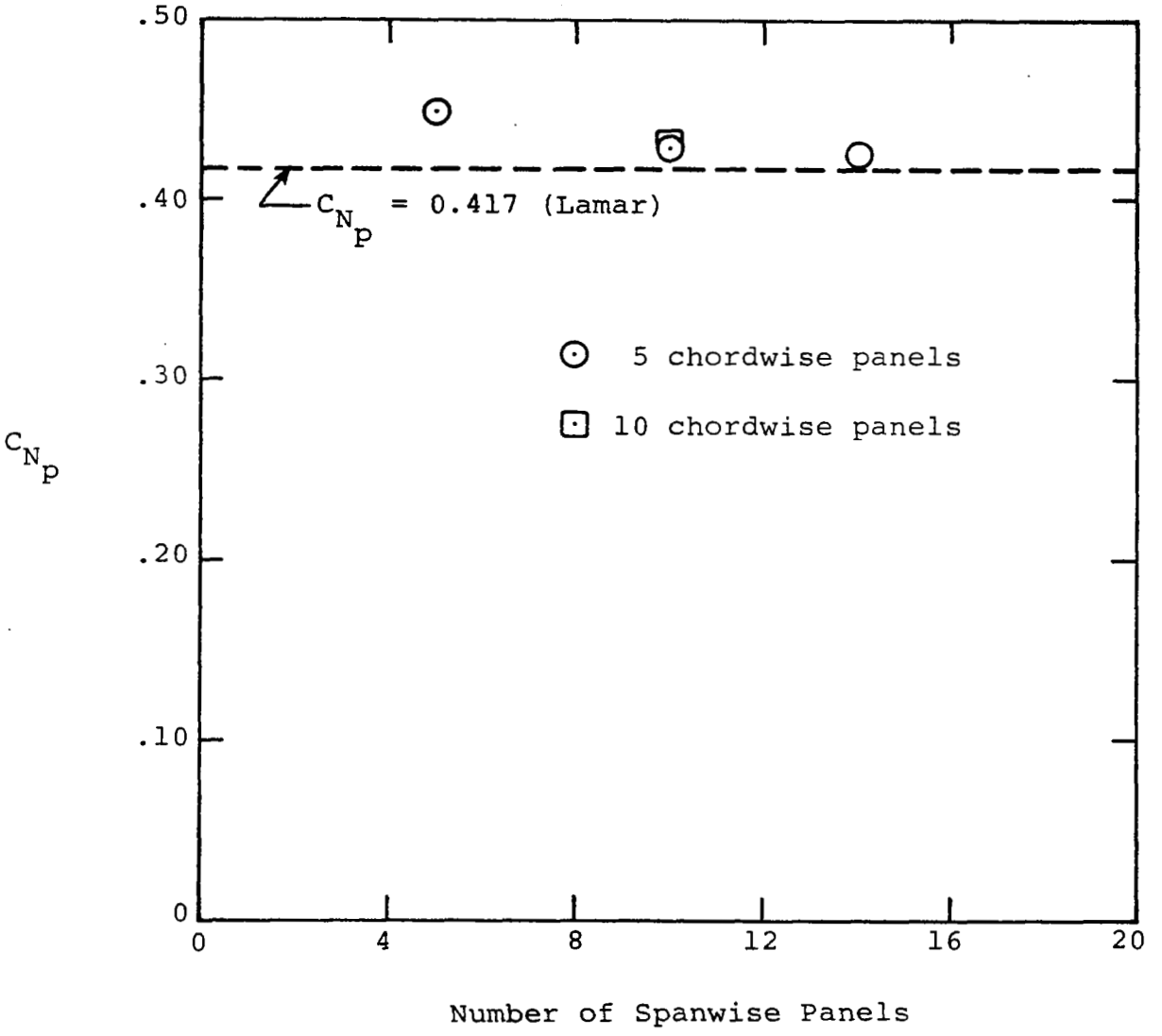

Figure 29.- Sensitivity of ASYMVL-calculated potential normal force to paneling layout, cropped delta wing of AS = 0.873, α = 20°.

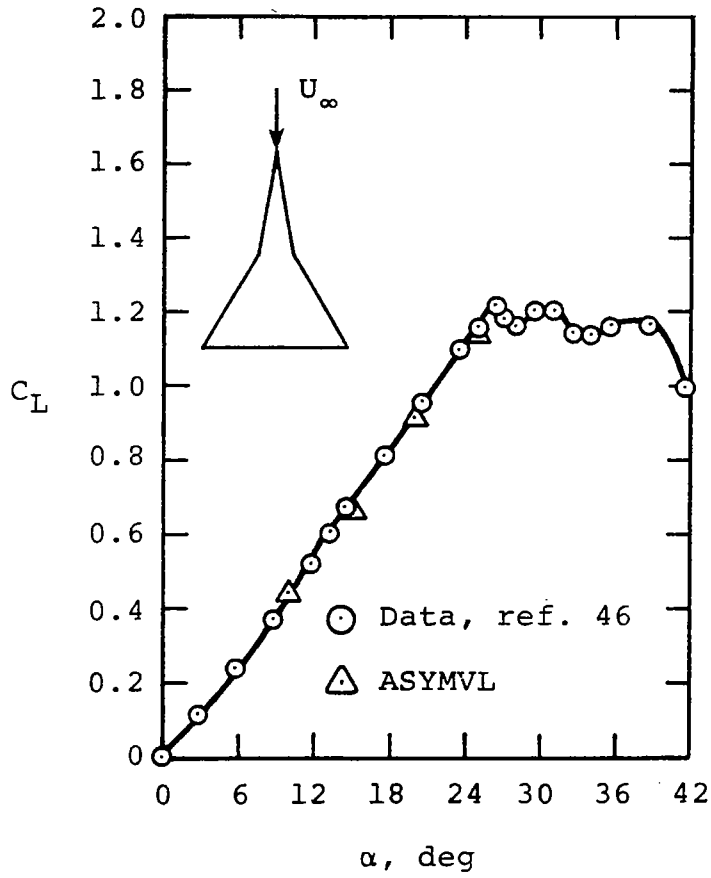

Figure 30.- Calculated and measured lift coefficient for an 80°/60° double delta.

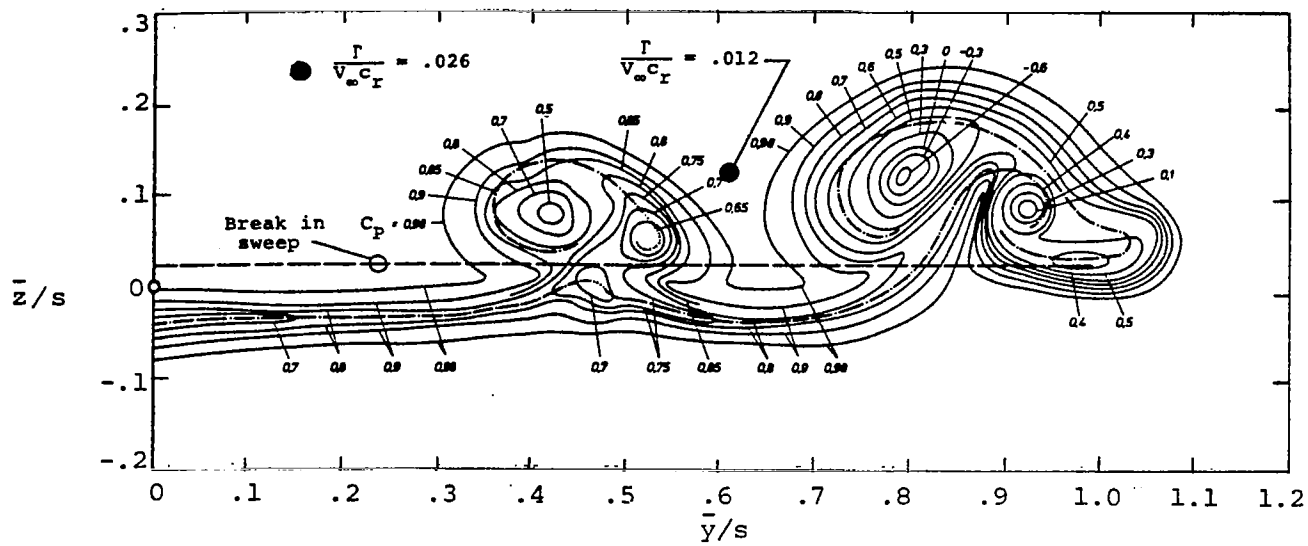

(a) Lines of constant total pressure coefficient

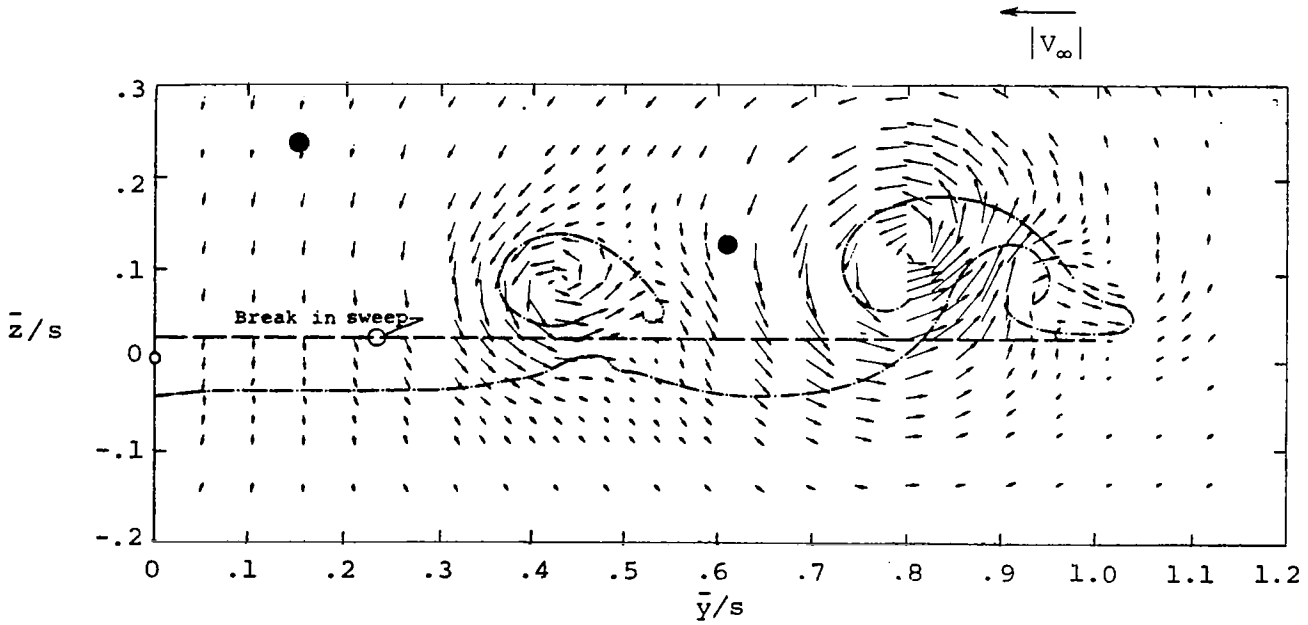

(b) Component of the velocity vector in a plane normal to V_∞

— — — Trailing edge

—·—·— Vortex sheet

● Vortex from ASYMVL

Figure 31.- Vortex formation behind an 80°/60° double delta at α = 10°; the measurements are from reference 46 at $\bar{\xi}$ = 1.10.

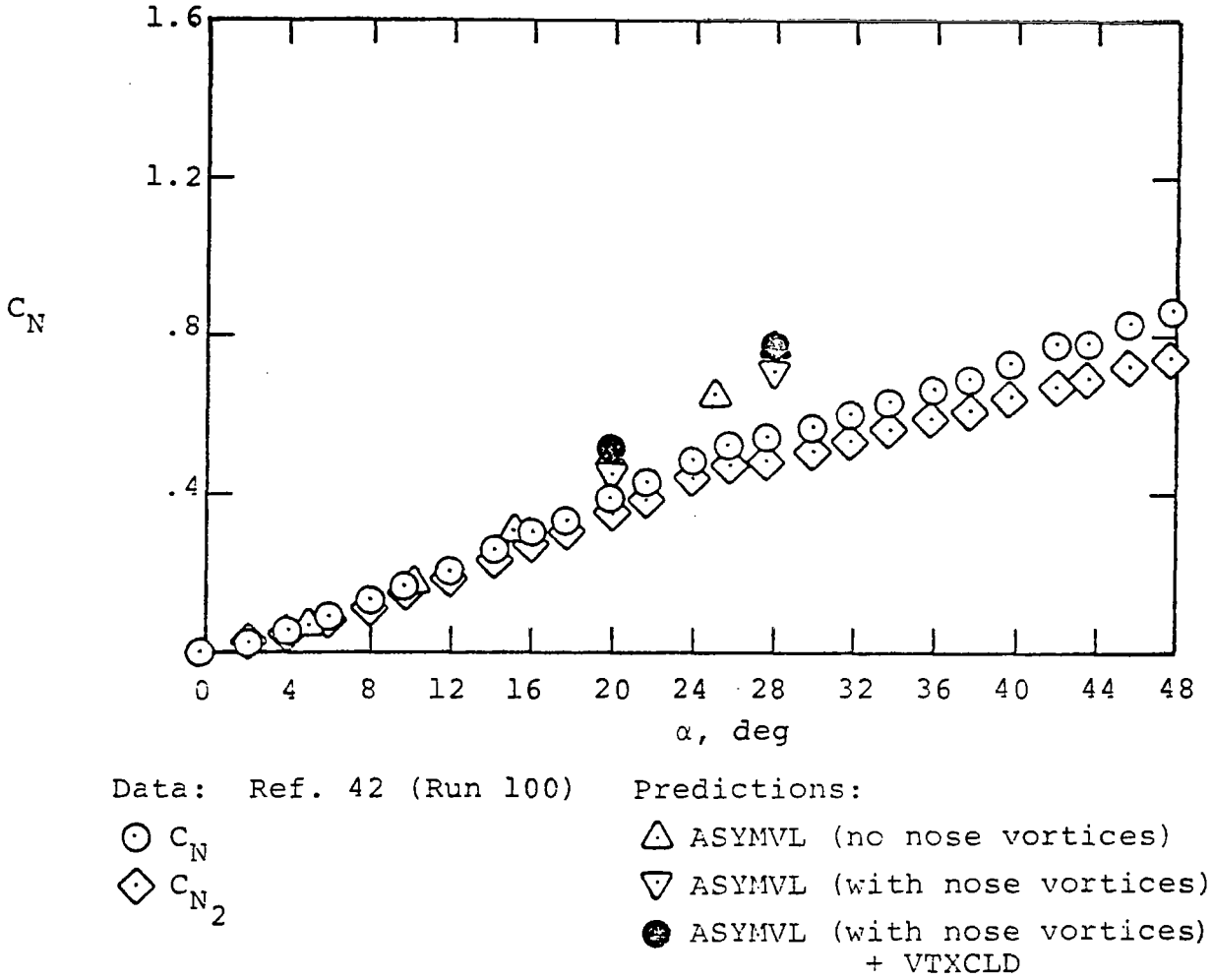

(a) Normal force coefficient

Figure 32.- Longitudinal aerodynamics, body-strake configuration, β = 0. Full vortex lift in calculations.

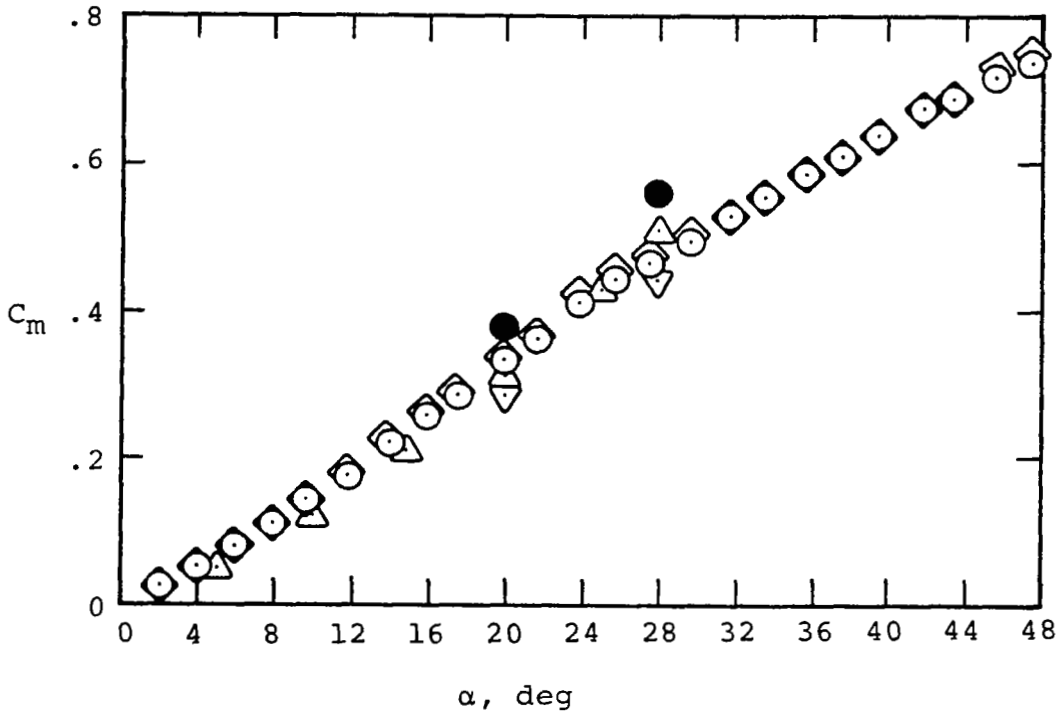

(b) Pitching moment coefficient

Figure 32.- (Concluded). For legend, see part (a).

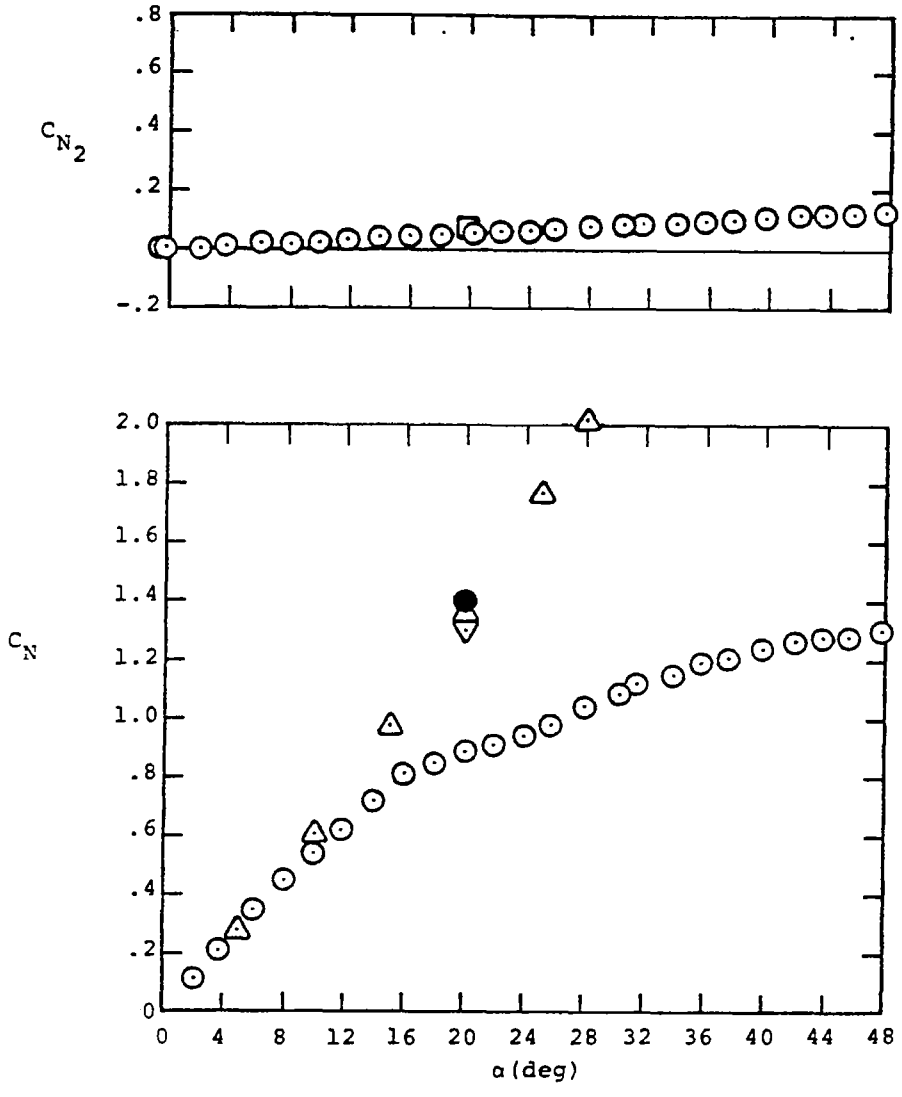

(a) Normal force coefficient

Figure 33.- Longitudinal aerodynamics, body-wing configuration, $\beta = 0$. Full vortex lift in calculations.

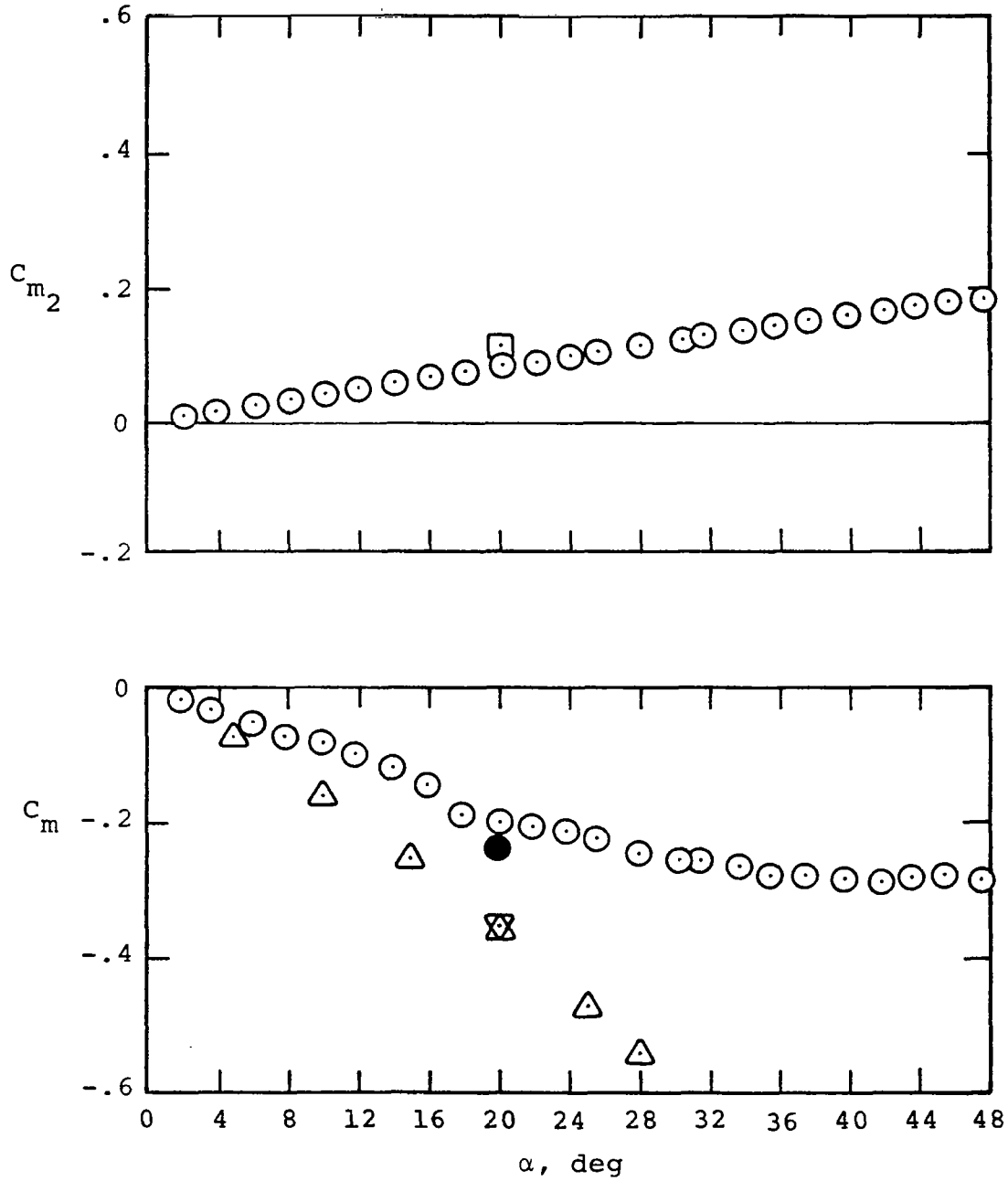

(b) Pitching moment coefficient

Figure 33.- (Concluded) For legend, see part (a).

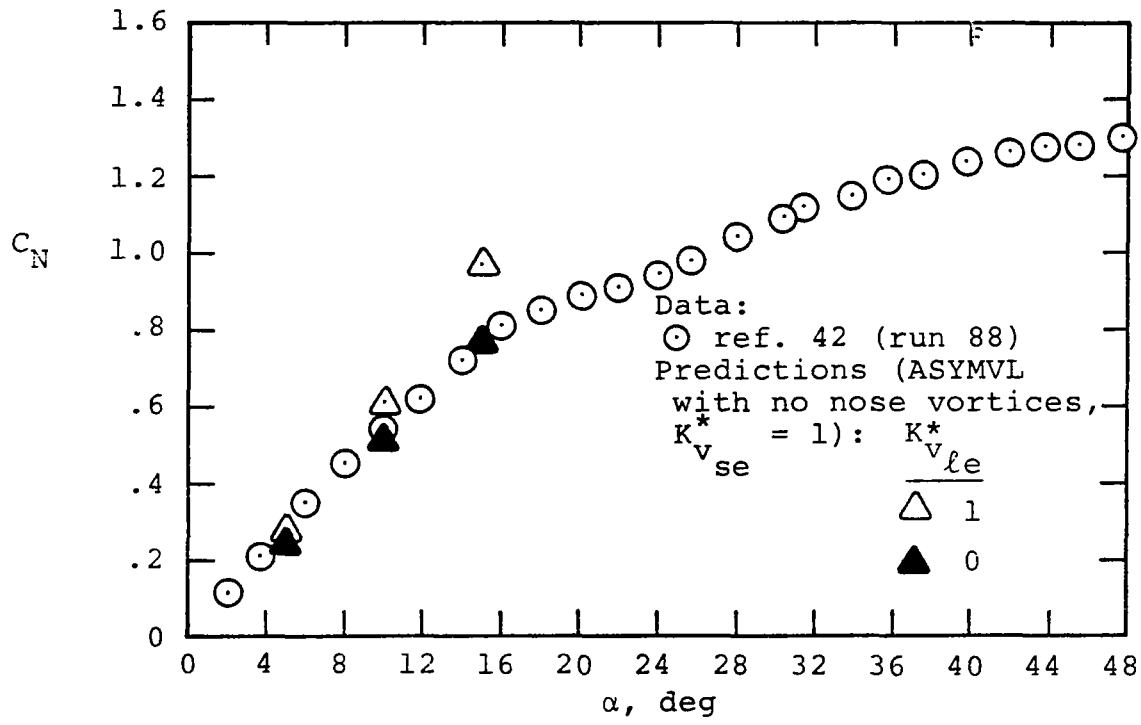

(a) Normal force coefficient

Figure 34.- Effect of $K^*_{v_{\ell e}}$ on longitudinal aerodynamics, body-wing configuration, $\beta = 0$.

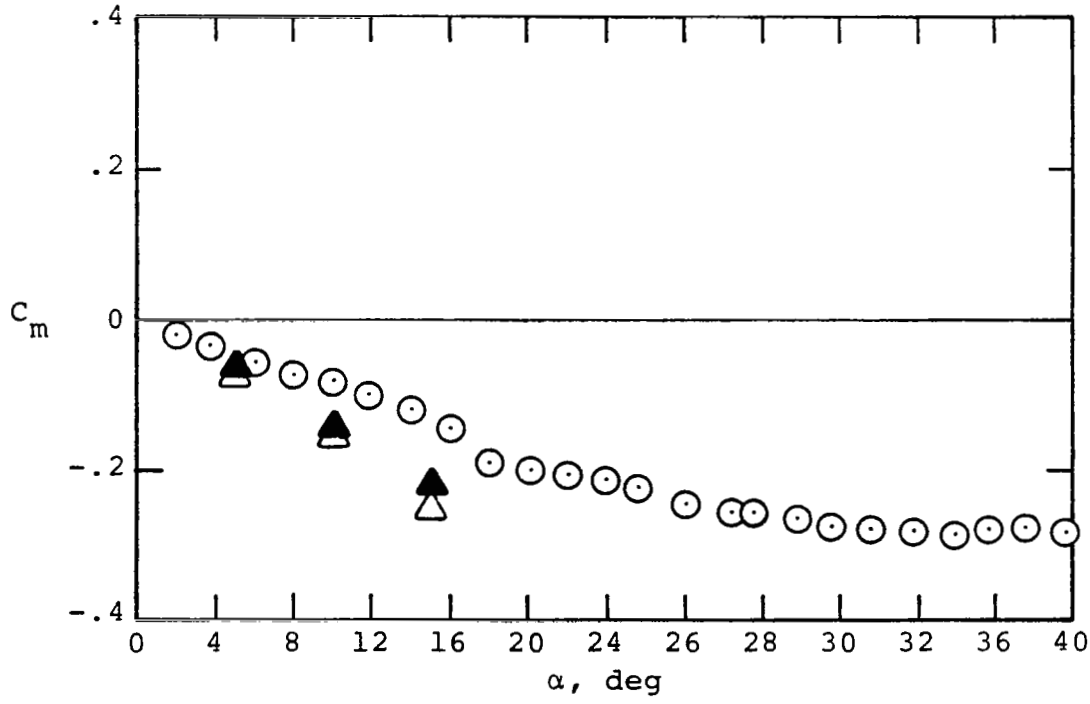

(b) Pitching moment coefficient

Figure 34. - (Concluded)
For legend, see part (a).

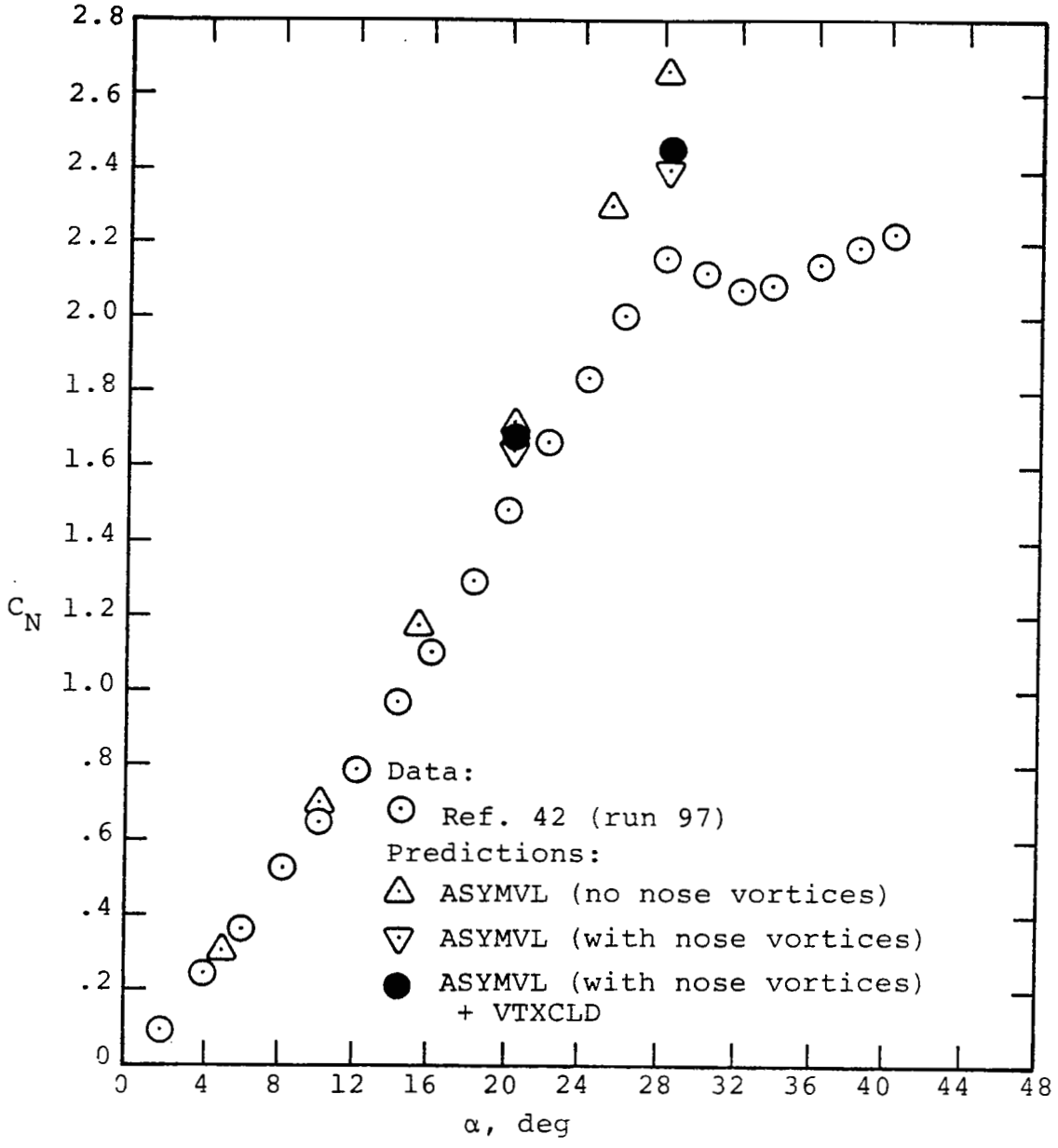

(a) Normal force coefficient

Figure 35.- Longitudinal aerodynamics, body-strake-wing configuration, $\beta = 0$. Full vortex lift in calculations.

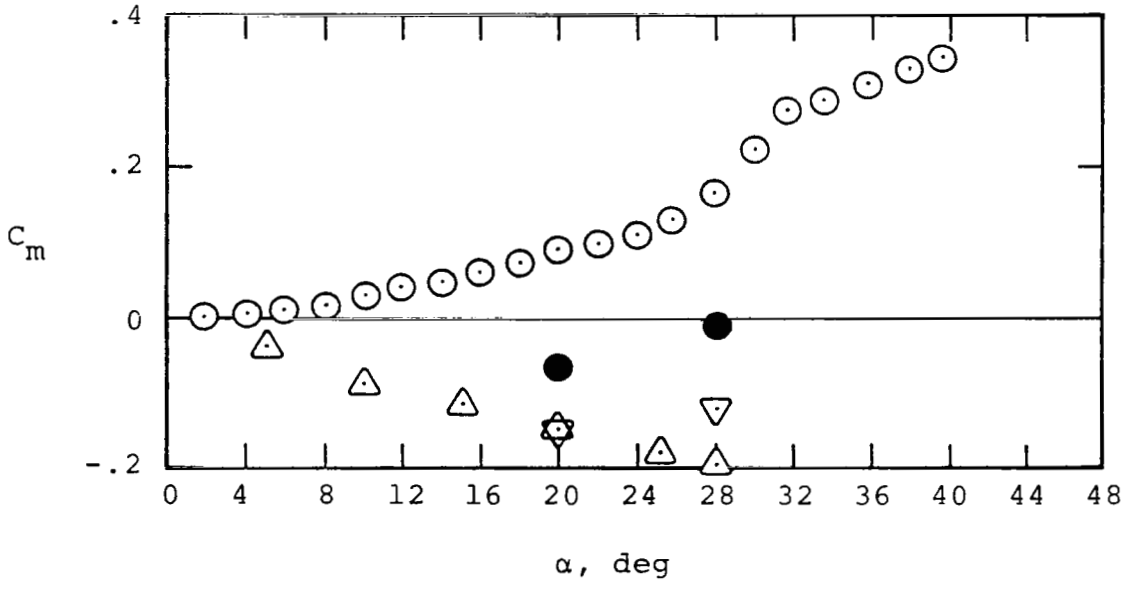

(b) Pitching moment coefficient

Figure 35.- (Concluded). For legend, see part (a).

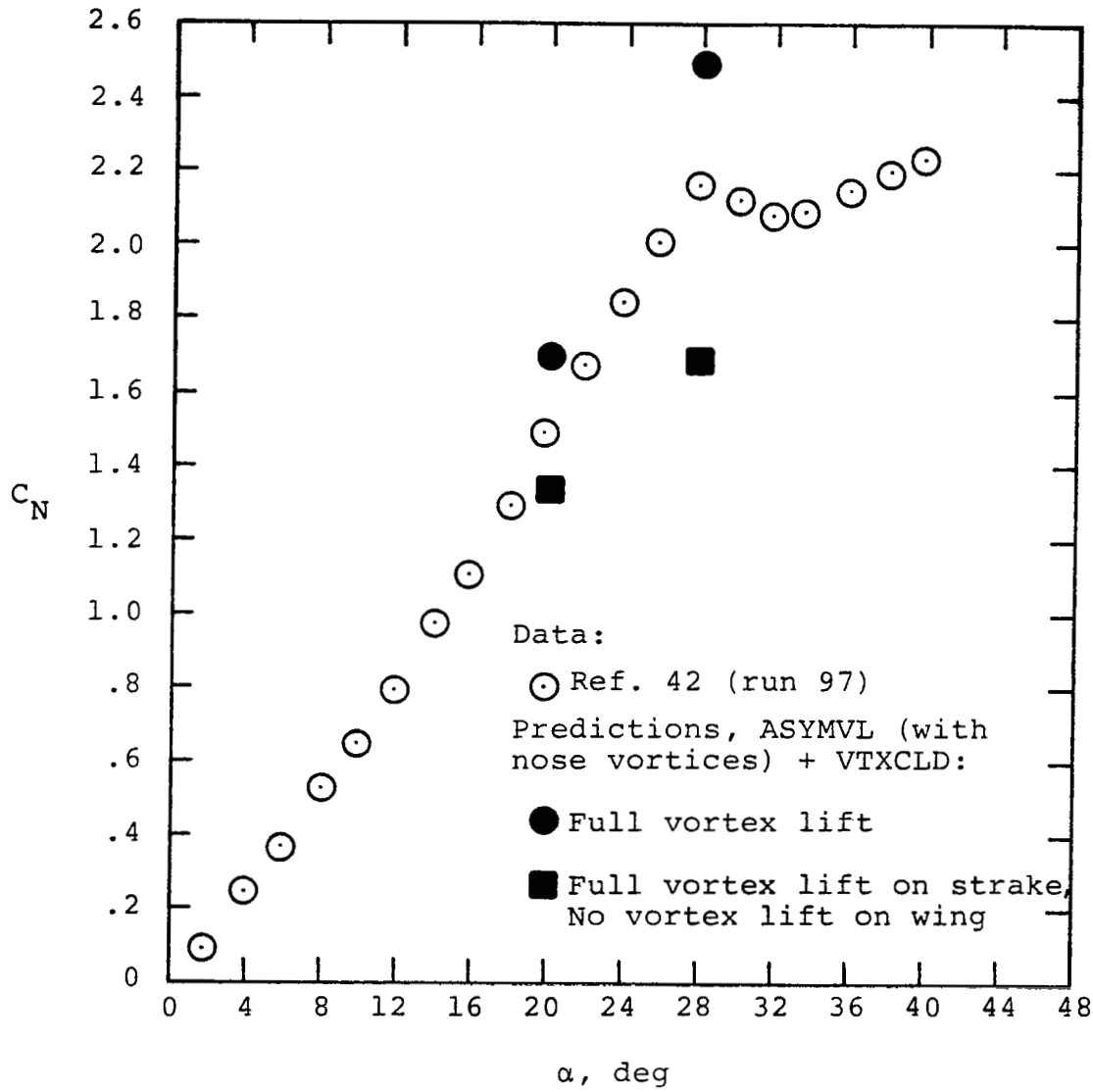

(a) Normal force coefficient

Figure 36.- Effect of vortex lift on the wing, body-strake-wing configuration, $\beta = 0$.

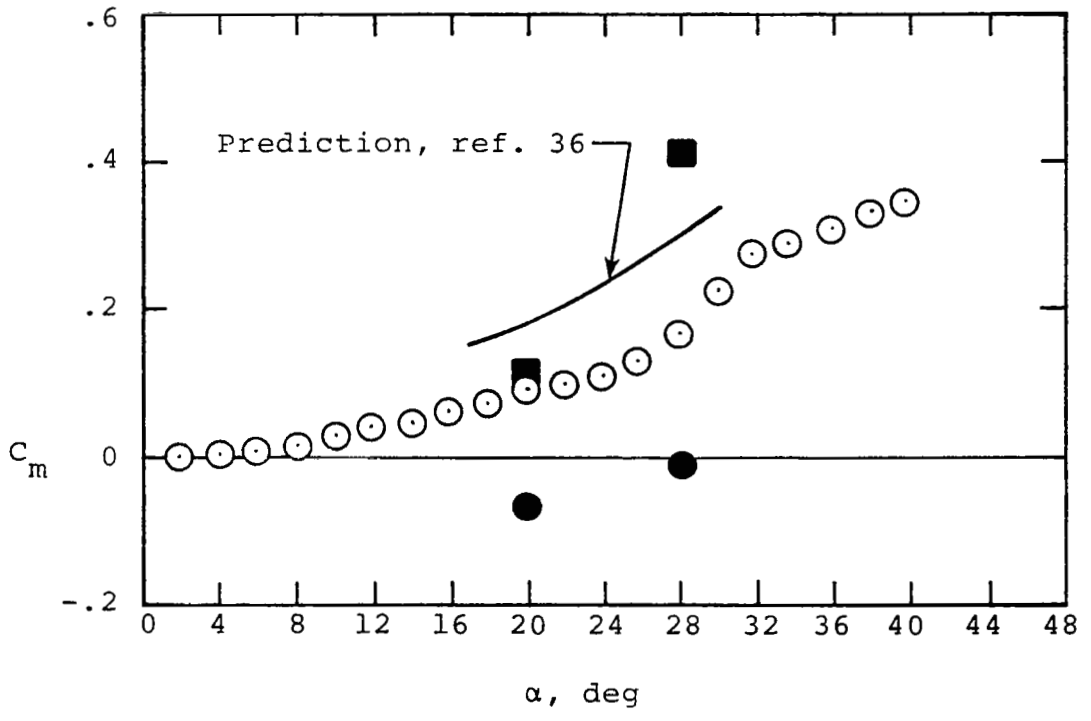

(b) Pitching-moment coefficient

Figure 36.- (Concluded). For legend, see part (a).

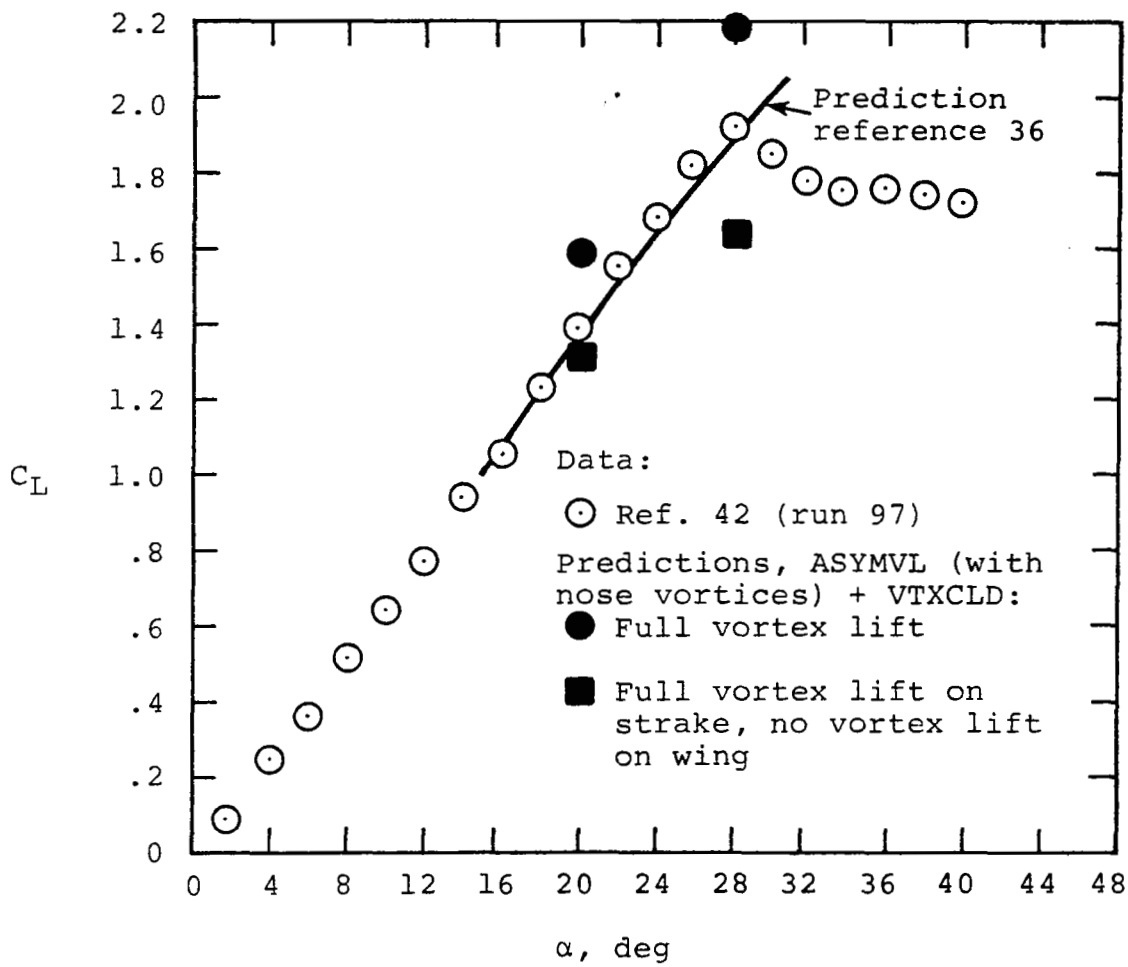

Figure 37.- Lift coefficient vs. α, body-strake-wing configuration, β = 0. Effect of augmented vortex lift.

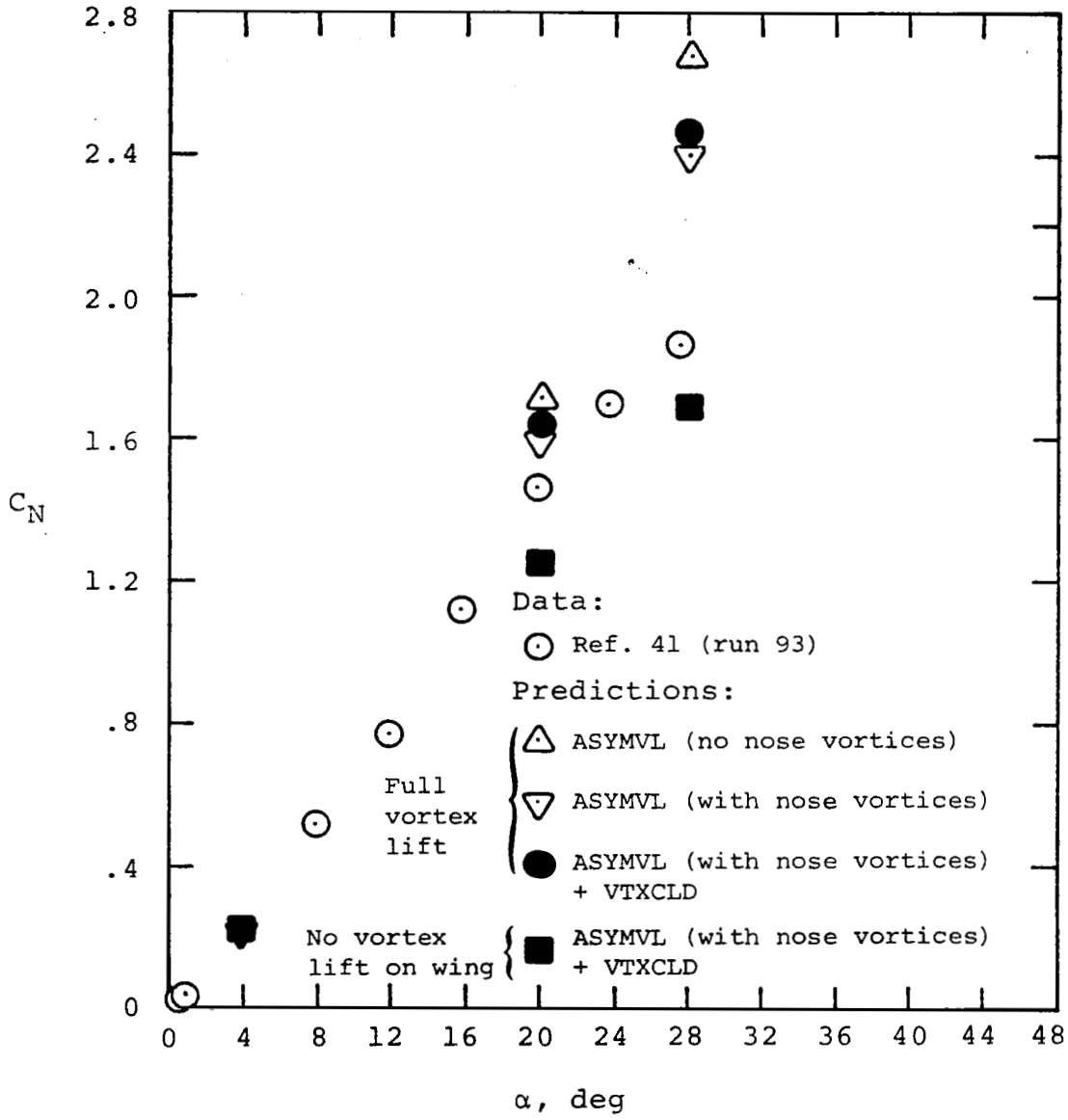

(a) Normal force coefficient

Figure 38.- Body-strake-wing configuration at $\beta = 5°$.

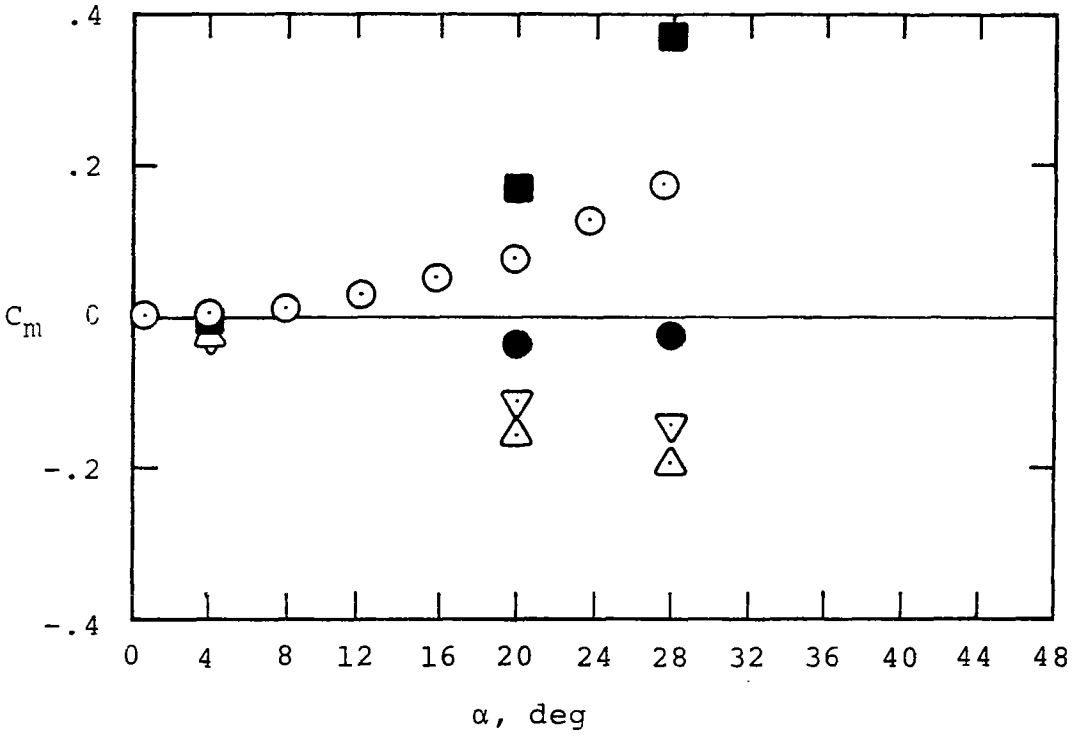

(b) Pitching moment coefficient

Figure 38.- (Continued). For legend, see part (a).

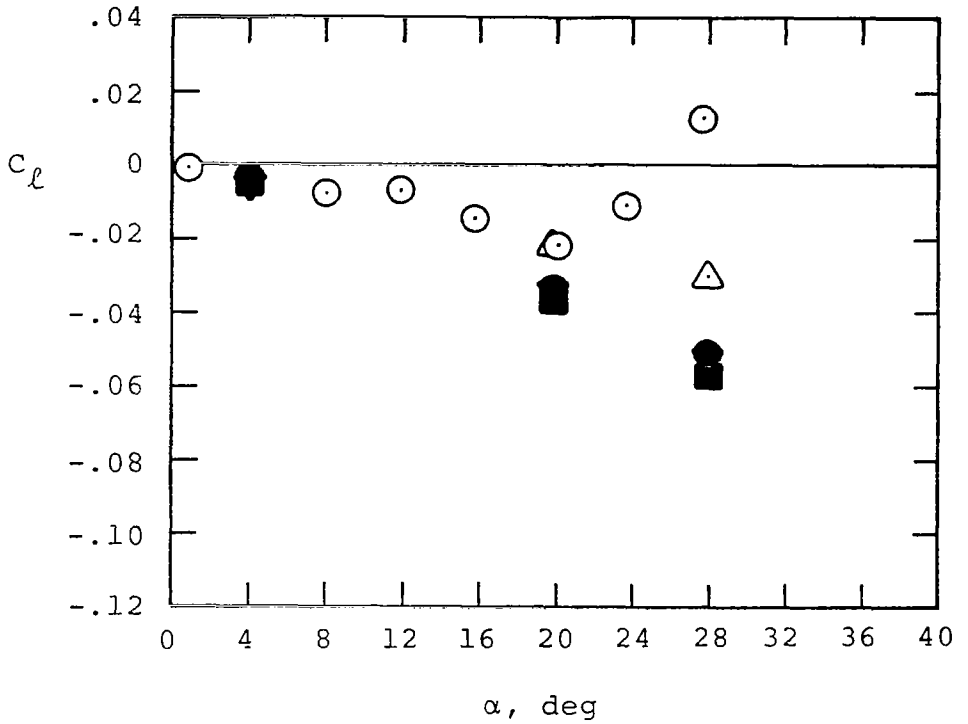

(c) Rolling moment coefficient

Figure 38.- (Continued). For legend, see part (a).

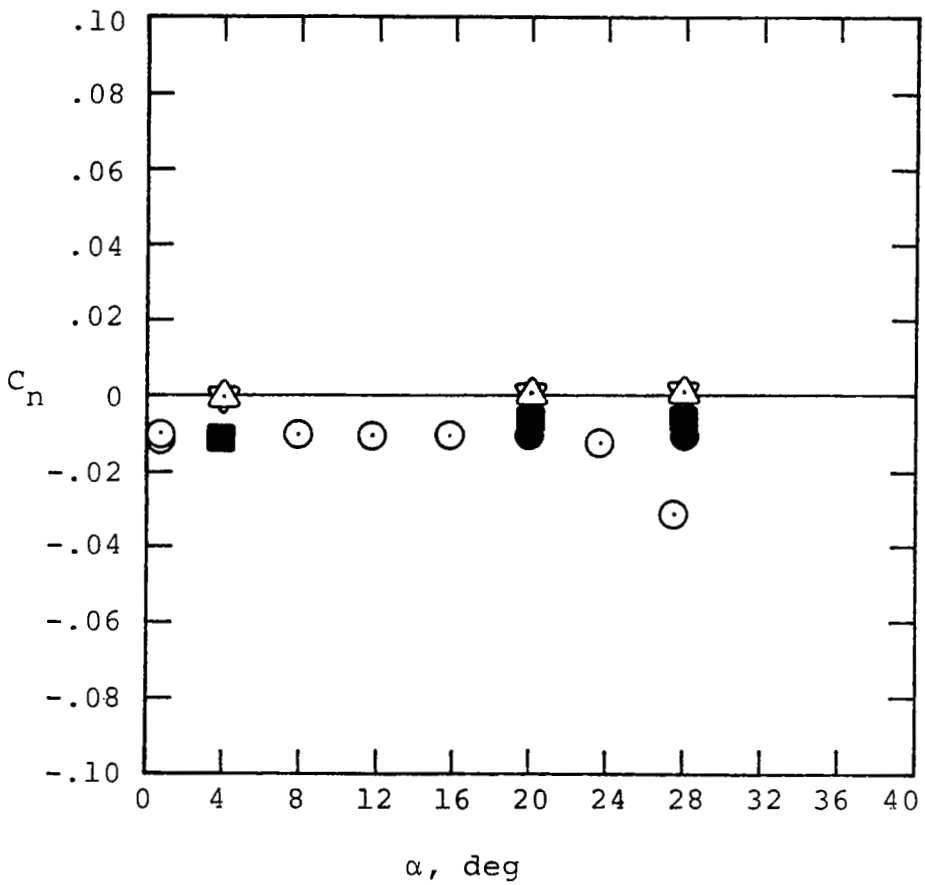

(d) Yawing moment coefficient

Figure 38.- (Continued). For legend, see part (a).

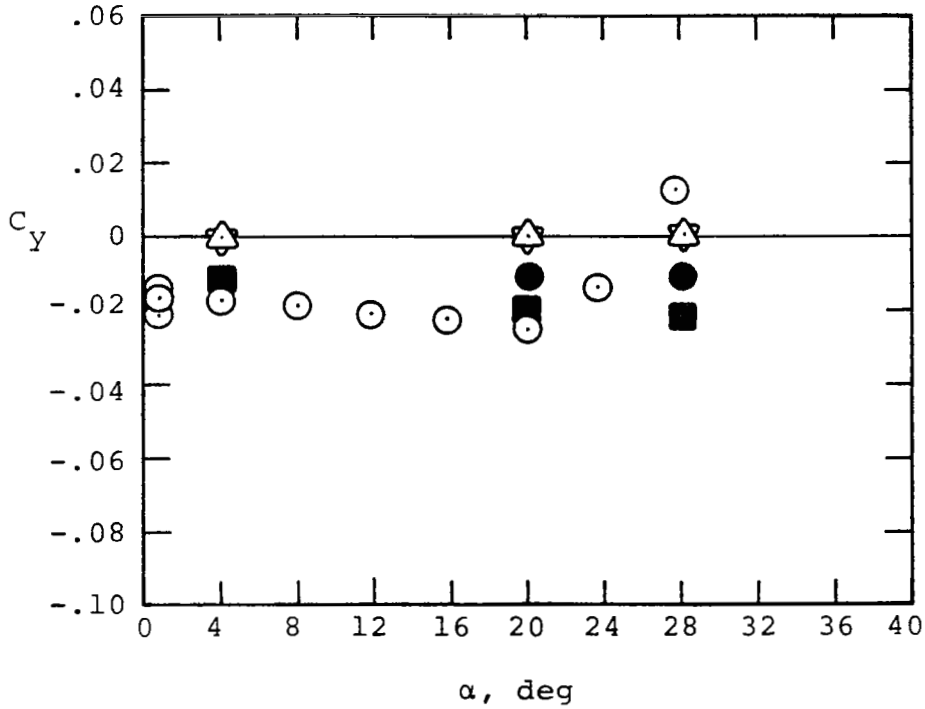

(e) Side force coefficient

Figure 38.- (Concluded). For legend, see part (a).

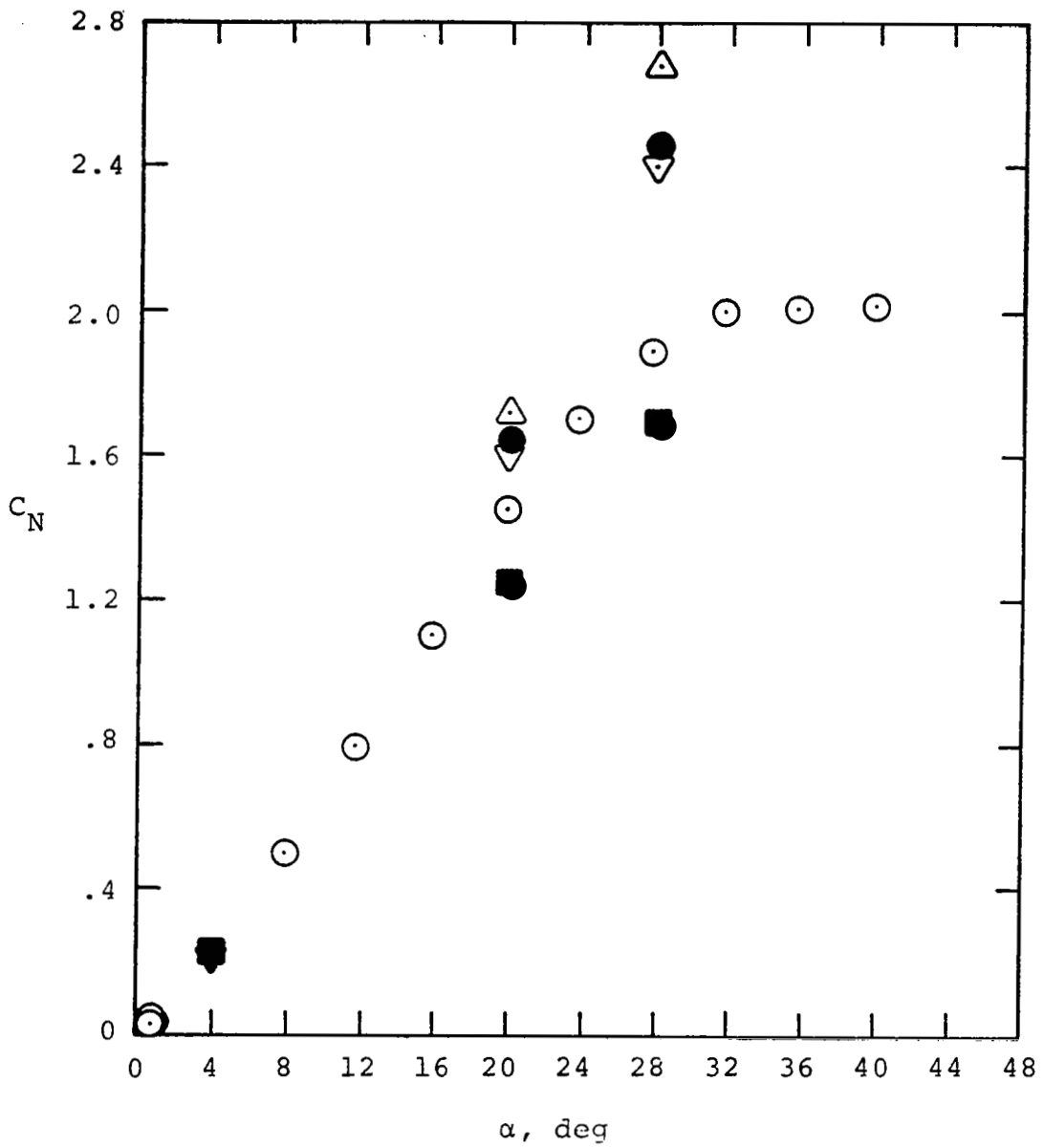

(a) Normal force coefficient

Figure 39.- Body-strake-wing-tail configuration at β = 5°. For legend see figure 38(a).

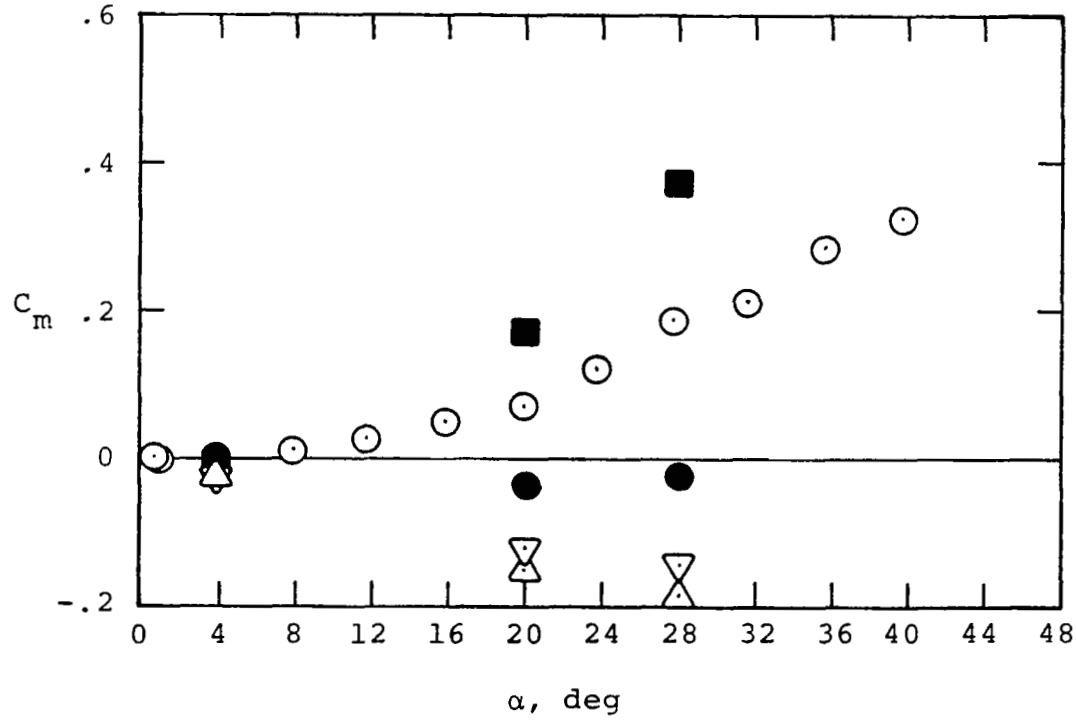

(b) Pitching moment coefficient

Figure 39.- (Continued). For legend, see figure 38(a).

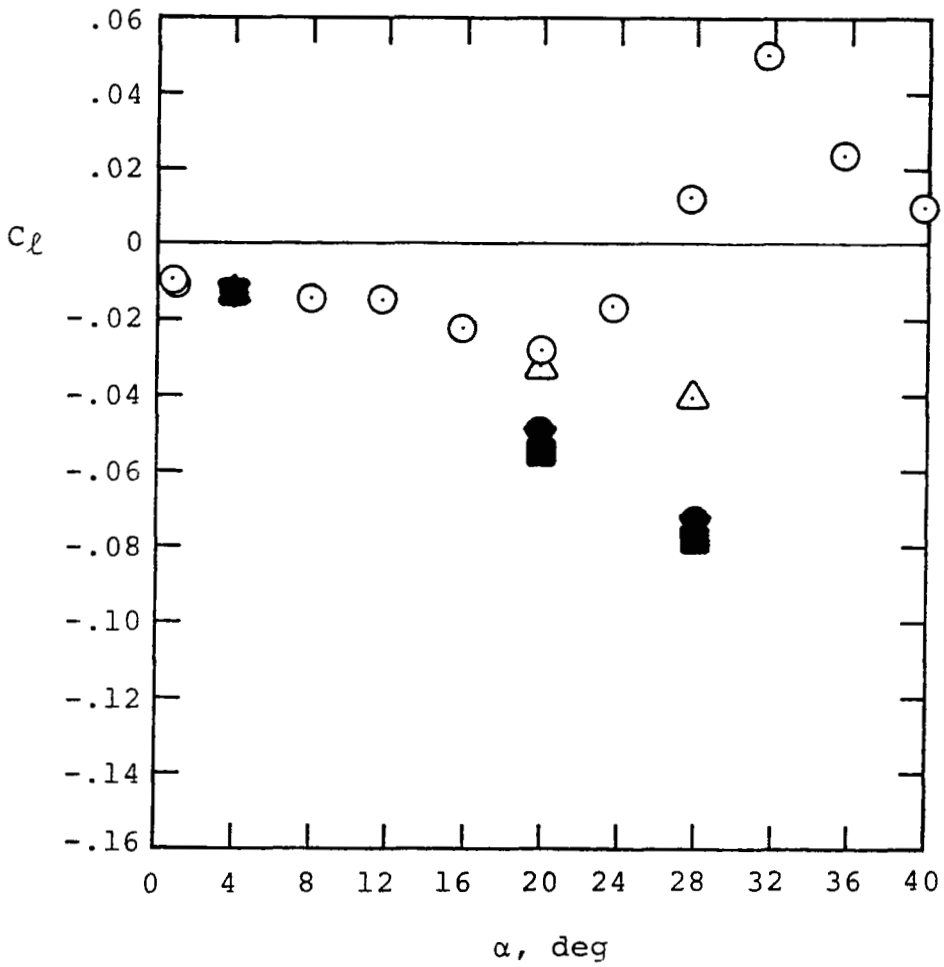

(c) Rolling moment coefficient

Figure 39.- (Continued). For legend, see figure 38(a).

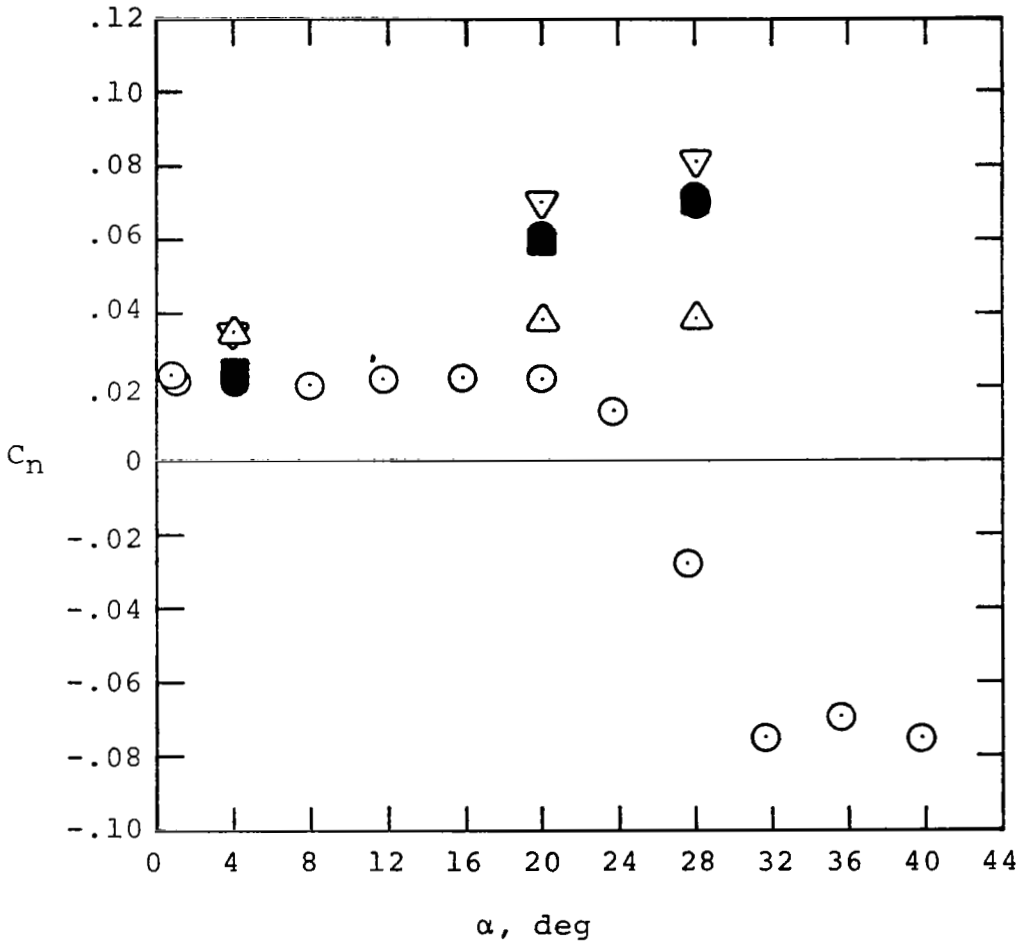

(d) Yawing moment coefficient

Figure 39.- (Continued). For legend, see figure 38(a).

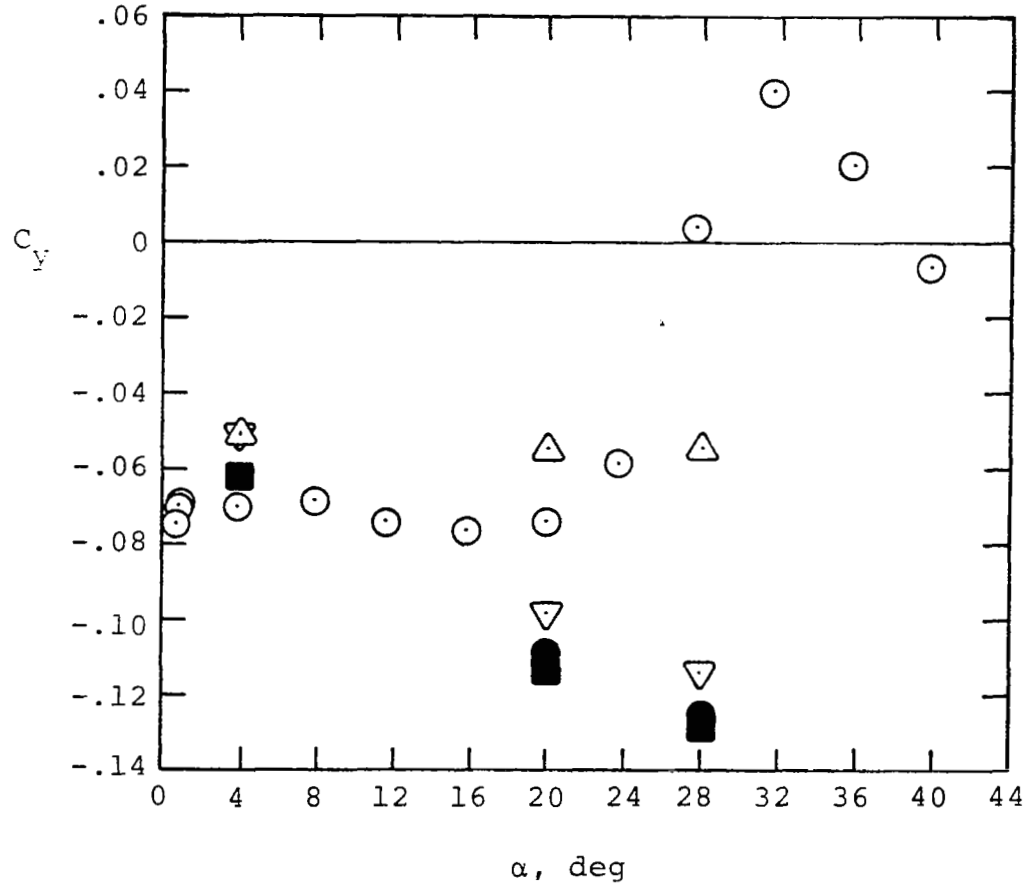

(e) Side force coefficient

Figure 39.- (Concluded). For legend, see figure 38(a).

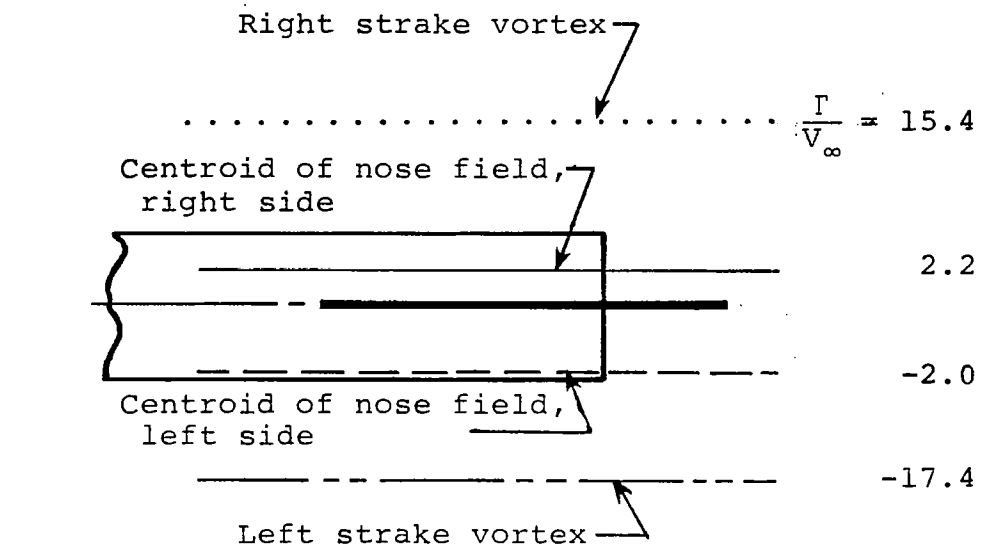

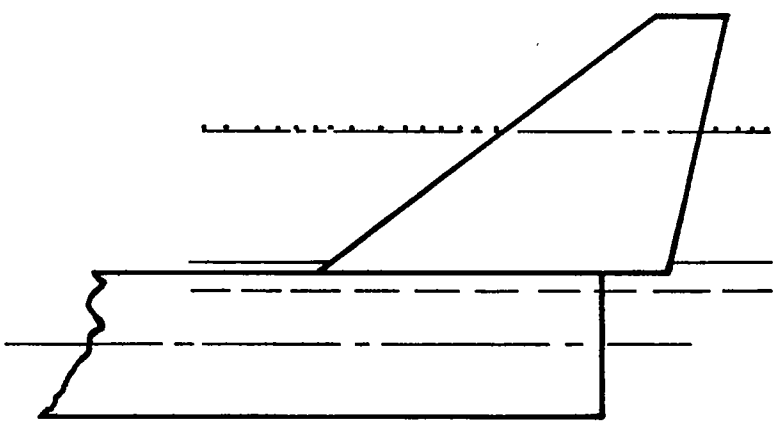

(a) Case 0

Figure 40.- Vortex positions in the tail region, $\alpha = 20°$.

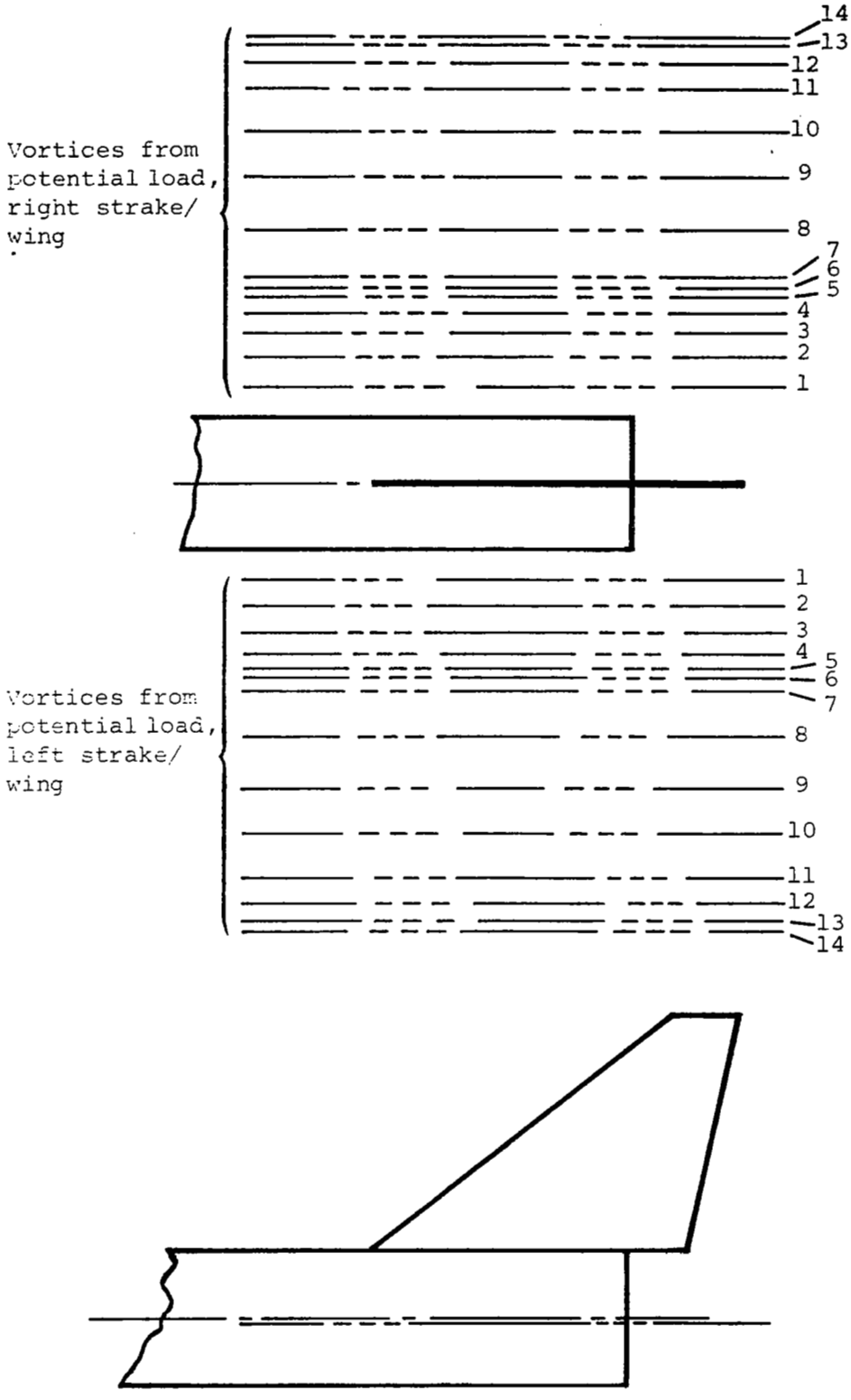

Vortex	Γ/V_∞ Left Wing	Right Wing
1	-.4	.2
2	-.4	.3
3	-.4	.3
4	-.3	.3
5	-.3	.2
6	-.3	.2
7	-.4	.4
8	-1.0	1.0
9	-1.3	1.3
10	-1.5	1.5
11	-1.6	1.6
12	-1.8	1.7
13	-1.7	1.7
14	-2.4	2.4

(b) Case 2

Figure 40.-(Continued).

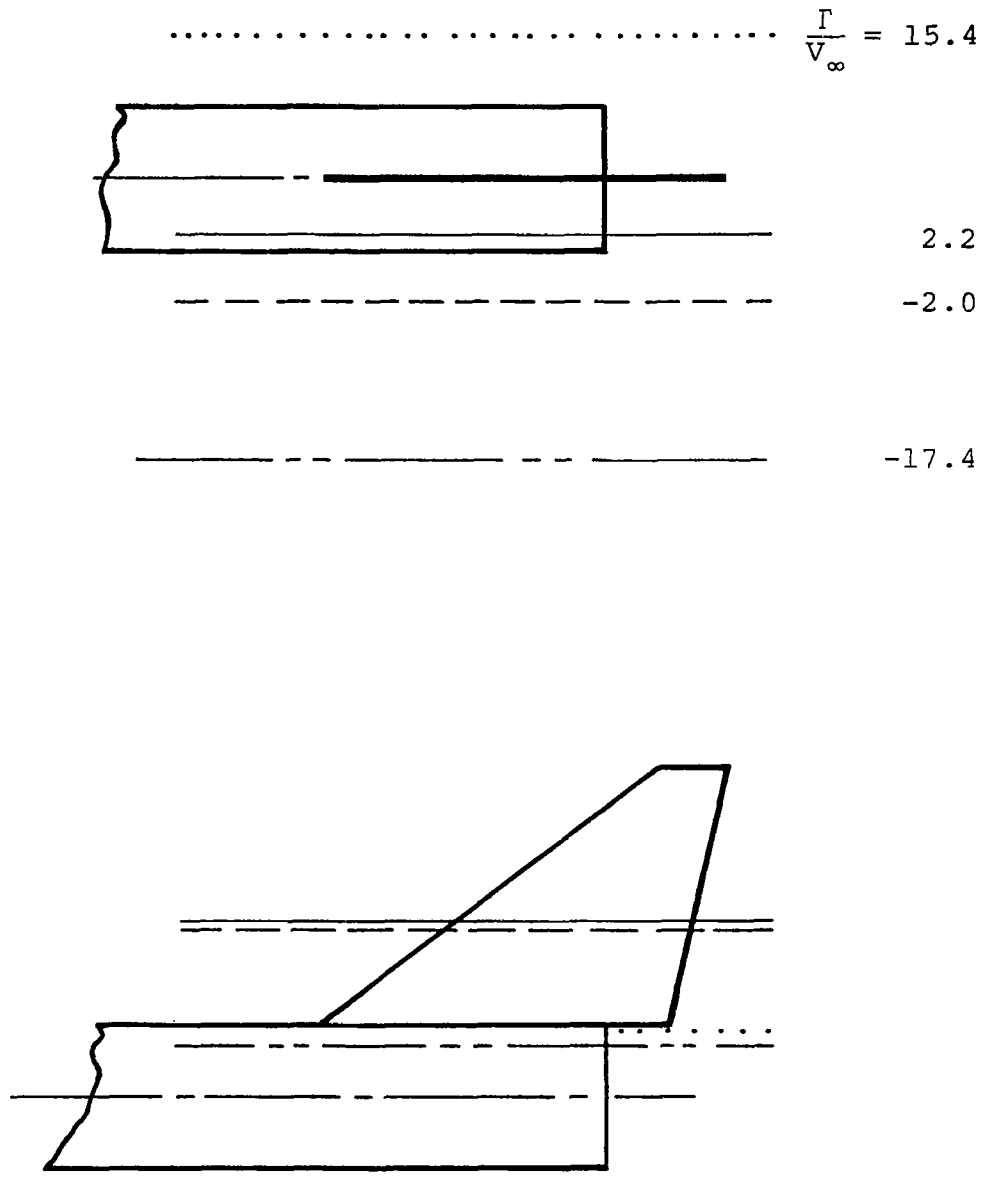

(c) Case 3

Figure 40.- (Continued). For legend, see part (a).

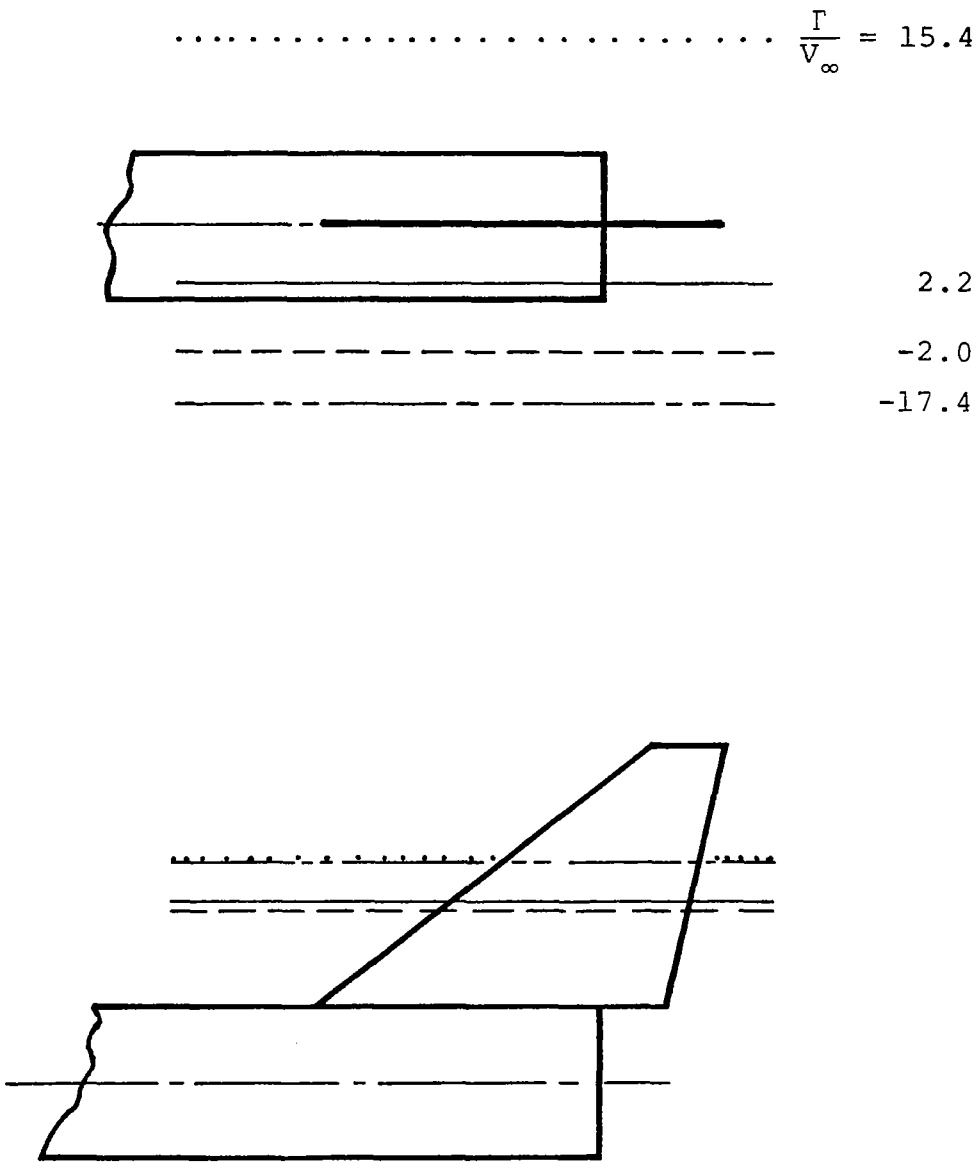

(d) Case 4

Figure 40.- (Continued). For legend, see part (a).

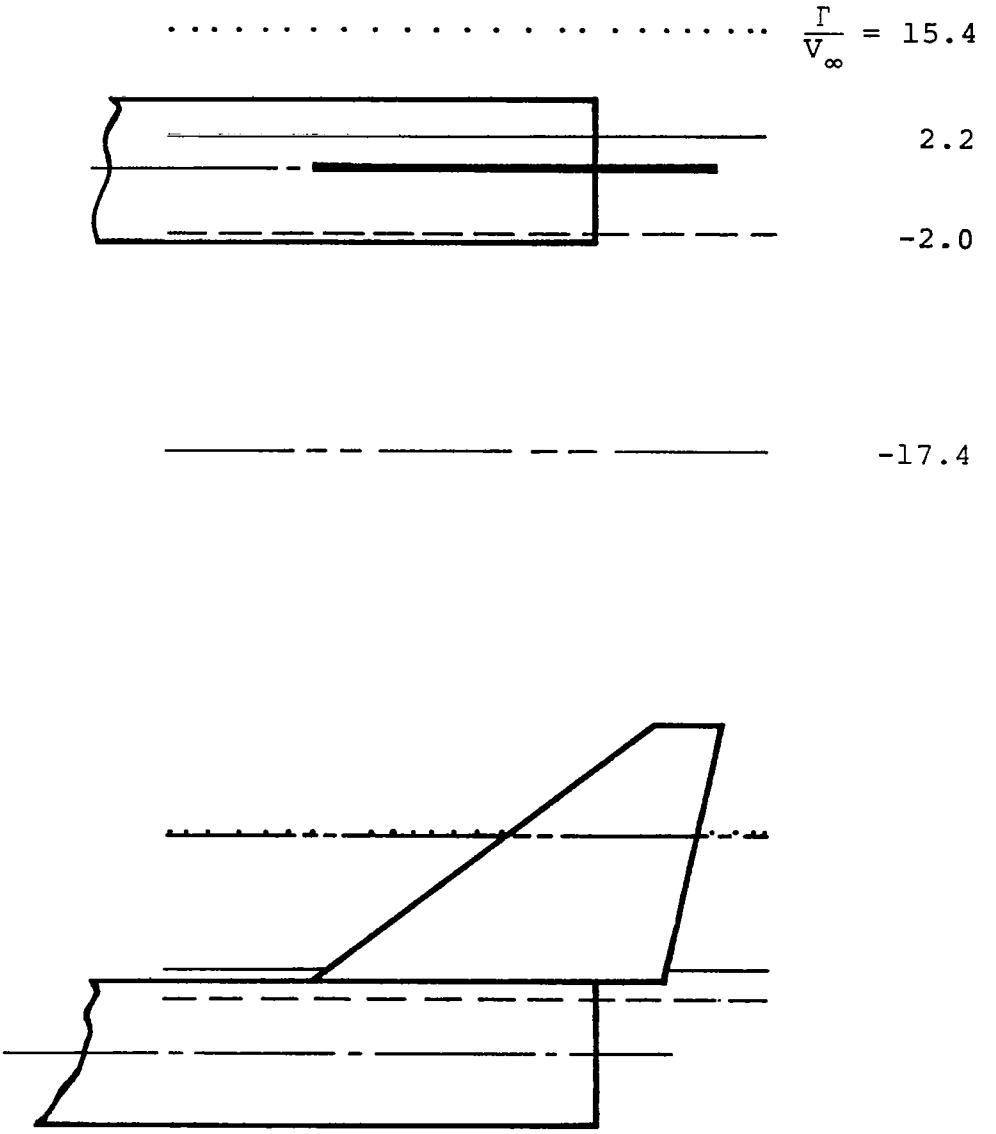

(e) Case 5

Figure 40.- (Continued). For legend, see part (a).

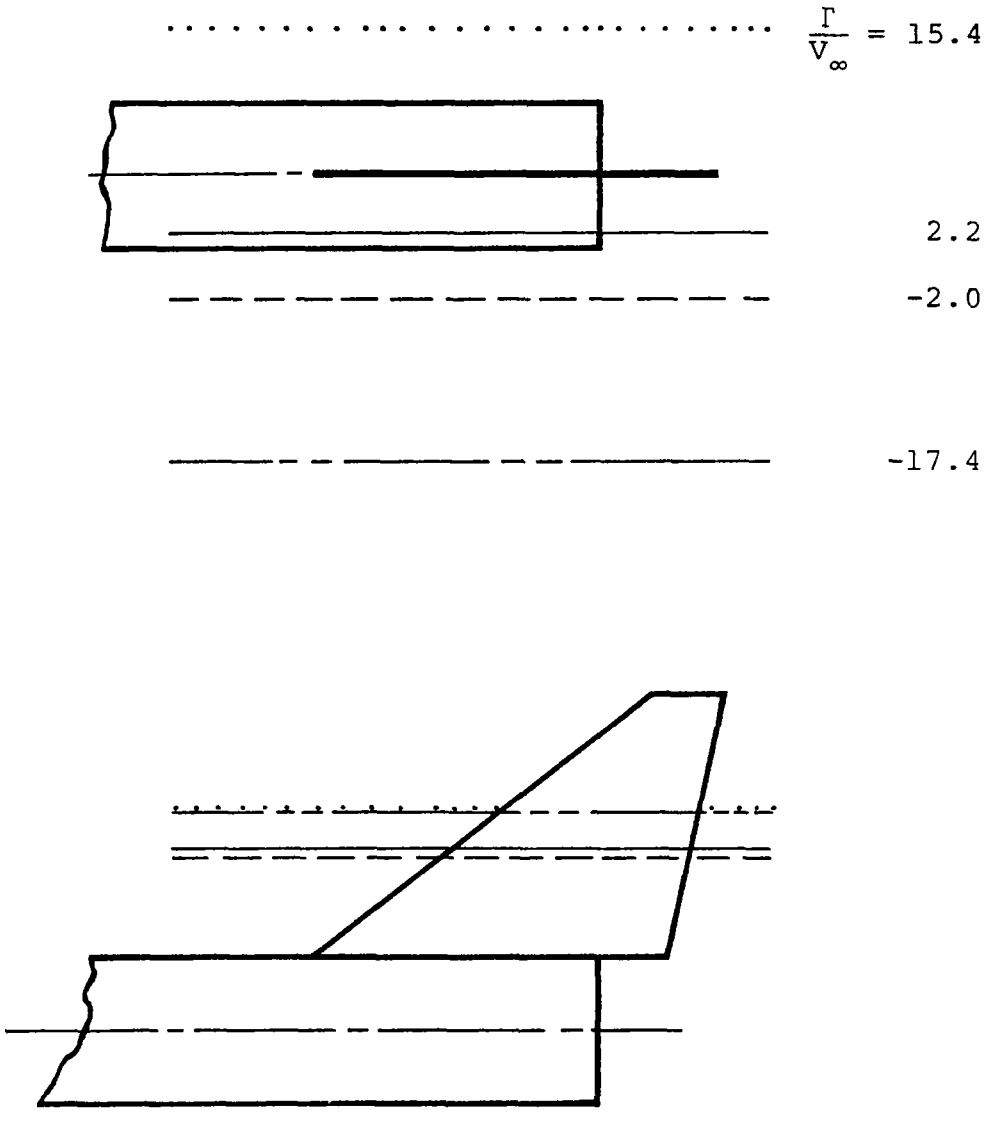

(f) Case 6

Figure 40.- (Concluded). For legend, see part (a).

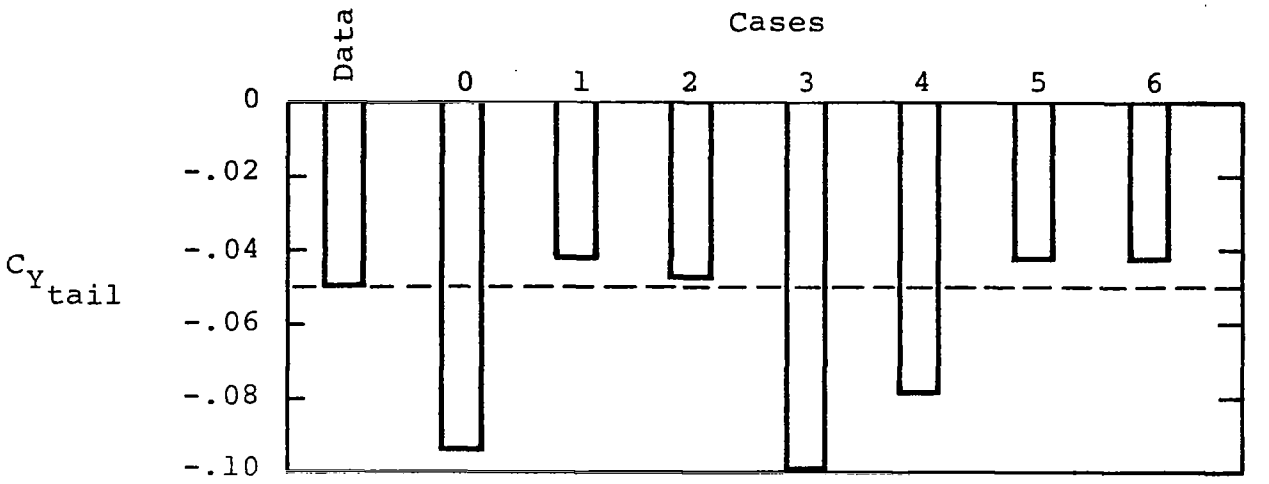

(a) Side force coefficient

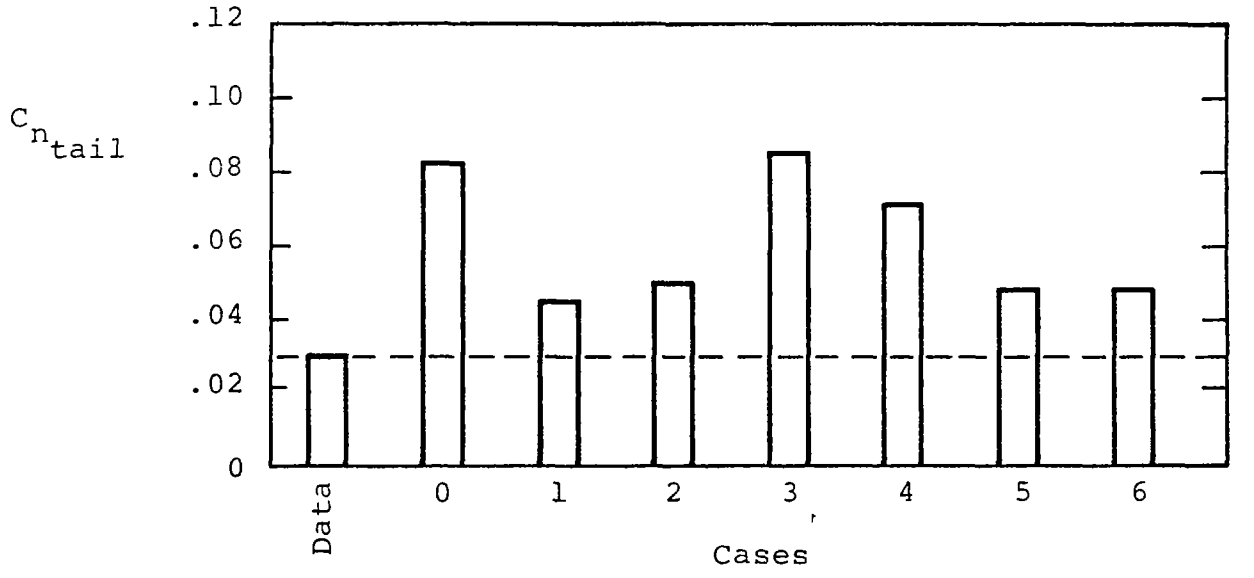

(b) Yawing moment coefficient

Figure 41.- Tail contributions to the lateral-aerodynamic coefficients for the varying vortex trajectories of figure 40, $\beta=5^{o}$.

APPENDIX A

A REVIEW OF PREDICTION METHODS FOR THE LOADS ON A STALLED AIRFOIL

SYMBOLS

c_d	section drag coefficient
c_m	section pitching moment coefficient
U_δ	free-stream velocity at edge of boundary layer, eq. (A-2)
u	streamwise component of velocity in boundary layer
V	velocity
v	transverse component of velocity in boundary layer
x,y	streamwise and normal coordinates, respectively
δ	boundary-layer thickness

Subscripts

i	value integrated over boundary layer, eq. (A-2)

INTRODUCTION

In this appendix, methods are reviewed which allow calculation of the loads on an airfoil experiencing a large region of detached flow. This detached flow may be due to trailing-edge stall or "bursting" of a leading-edge laminar separation bubble. Methods dealing solely with closed laminar separation bubbles are not reviewed. Similarly, methods which require empirical knowledge of section characteristics as a function of

angle of attack (such as the lifting-line analysis of ref. 50) are not included. Finally, although some unsteady methods suitable for application to the dynamic stall problem are discussed, our main interest is in the calculation of the average loads on an airfoil at (constant) high angle of attack.

The existing procedures are, in general, zonal models which combine a line-singularity method with a boundary-layer method for the attached flow and a separated-flow model for the detached region. Although they naturally differ in many (if not most) details, the most important distinction among the methods involves the nature of the treatment of the separated region. For purposes of the present discussion, therefore, it is convenient to group the methods into two broad categories in this respect: (1) the separated flow is modeled by what is equivalent to free vortices shed from the airfoil boundary layers at the separation locations, or (2) the separated flow is treated through some application of the "equivalent inviscid body" concept (defined below).

FREE VORTEX METHODS

In these methods, the free shear layers bounding the separated-wake-flow region are represented by vortex sheets, each point of which is convected by the velocity induced by all the other singularities in the flow, i.e., the other wake vortices and the singularities used to represent the wing surface. The shapes of these shear layers must be determined by iteration or in an unsteady manner. The strength of the wake vorticity is calculated from some criterion based on conditions at the separation locations on the upper and lower airfoil surfaces. In these methods, the pressure in the separated region is

calculated (as opposed to specified, as in some of the methods discussed later) and is used with the pressure calculated on the attached regions to determine the loads on the wing.

The first method of this type to be discussed is the CLMAX method of reference 12. The model used in CLMAX is shown in figure A- (from ref. 12). In this model, the flow is everywhere irrotational except along the vortex sheets representing the airfoil surface and the free-shear layers, the shapes of which are not known a priori. The vortex sheet representing the airfoil surface is broken into discrete panels, in each of which the vorticity varies linearly. The free-shear layers are specified to be of constant and equal vorticity (of opposite sign), the magnitude of which is equal to the vorticity at the trailing edge of the lower surface (the specified lower-surface separation point). The unknown vortex strengths are determined by solving a set of linear equations obtained by imposing boundary and auxiliary conditions as follows: (1) The flow through the airfoil surface in the attached region is the transpiration flow (represented by a piecewise-constant source distribution) calculated from the boundary-layer solution to represent the boundary-layer displacement effect; in the detached region, there is no flow through the surface. (2) The vorticity at the separation point on the upper surface is the same as for the upper free-vortex sheet. (3) The vorticity distribution on the airfoil surface in the separated region must start and end at zero vorticity.

The solution procedure involves two iteration loops. In the outer loop, the pressure distribution from the potential solution is used to derive a boundary-layer solution from which the displacement effects and separation point on the upper surface are determined. In the inner loop, the shapes of the free-vortex sheets are relaxed until they lie along streamlines. The boundary-layer development is calculated using separate integral techniques for laminar and turbulent regions as applicable, with transition automatically accounted for; separation is taken to occur where the local skin-friction coefficient becomes zero. When both iterative cycles are judged to be converged, the pressures on the airfoil are calculated from the Bernoulli equation, accounting for the total pressure loss in the wake.

Numerous examples of the application of CLMAX to calculate the characteristics of airfoils at angles of attack beyond that for the maximum lift coefficient are in the literature (see, for example, refs. 12 and 51). In these applications, it is shown that the constant-strength free-vortex-sheet representation of the separated shear layers is generally quite adequate in terms of the calculated pressure on the airfoil. Downstream however, the lack of accounting for the recompression zone of the separated region makes the model less representative of the actual flow. It is stated that improvement of this particular feature would be required where the wake interacts closely with a downstream component. Also, a weak dependence of the calculated results on the assumed wake

length exists, but a possible correlation for the wake fineness ratio (length/height) in terms of airfoil thickness/chord ratio is given.

A representative example of the application of the CLMAX method to the GA(W)-1 airfoil at high Reynolds number ($Re=6.3x10^6$) is shown in figures A-2 and A-3 (from ref. 12). The agreement with data shown is quite good except at the highest post-stall incidence, where the separation location is seen to be erroneously predicted. The predicted post-stall decrease in lift coefficient at lower Reynolds number is generally not in as good agreement with data as that shown here, probably also due to inadequacies in the predicted separation location.

A second free-vortex method for airfoils is that of reference 52. Because the essential features of this method are similar to those discussed in relation to the three-dimensional method described in the main text (ref. 7), they will not be repeated here.

The final free-vortex method to be discussed is the two-dimensional unsteady method of reference 53. This method is intended for analysis of dynamic stall and combines a discrete doublet-panel representation of the airfoil surface (no flow through the airfoil surface) with unsteady momentum integral boundary-layer methods for the laminar and turbulent regions and a free-vortex representation of the wake (fig. A-4). The boundary-layer methods are used to predict the separation-point location and the strength of the vortex shed at each time step at each separation location using

$$\frac{d\Gamma}{dt} = \int_0^{\delta} \left(\frac{\partial v}{\partial x} - \frac{\partial u}{\partial y}\right) u \, dy \qquad \text{(A-1)}$$

which can be integrated to result in the expression

$$\Gamma_i = \Delta t \, U_\delta^2/2 \qquad \text{(A-2)}$$

if the assumption is made that $\partial v/\partial x = 0$. Boundary-layer displacement effects are apparently not included. The velocity of each discrete vortex during the first time step after it leaves the airfoil surface is based upon average velocities in the boundary layer just prior to separation. Thereafter, the wake vortices are convected by the airfoil/wake induced velocities. The analysis is started with the airfoil at rest and is stepped in time until steady-state results are obtained. This method is at an early state of development, and no results are available at this time.

Equivalent Inviscid Body Methods

Loosely grouped together in this section are a number of methods which use, in one way or another, the idea that the separation streamlines leaving the upper and lower surfaces when combined with the forward unseparated portion of the body define an "equivalent inviscid body." Several of the methods assume the pressure in the separation region within this "body" is

constant and calculates its value using various criteria, while others utilize models of the internal separated flow and calculate the pressure distribution in the separated region.

Included in the former category are several formulations (see, for example, refs. 54-56) of a method which uses sources distributed over the separated region of the actual body. The outflow from these sources combines with the free-stream flow and the singularities representing the unseparated body surface to form the equivalent inviscid body. Reasonably satisfactory results are obtained from these methods once a suitable distribution of blowing is established, but the pressure in the separation region is generally not well predicted in this way.

Another method which does not attempt to calculate the details of the flow within the separation region is the model of reference 57. In this approach, the surface of the equivalent inviscid body is paneled, and the singularity strengths and the shape of this body are iteratively solved for using the following boundary conditions: (1) there is no flow through the unseparated airfoil surface (as modified by the boundary-layer displacement thickness); (2) the velocity is constant along the surface representing the upper edge of the portion of the separated wake over the airfoil and there is no flow through this surface (it is a streamline); and (3) the surfaces representing the trailing wake meet, are streamlines, and at each station downstream of the trailing edge have equal velocity. The pressure in the separated wake over the airfoil is set equal to the pressure at the trailing edge of the bottom surface of the airfoil. Separate momentum-integral boundary-layer methods are used for the regions of laminar and turbulent flow, with laminar leading-edge separation bubbles and transition accounted for. The turbulent separation criterion is that the shape factor (defined as the ratio of displacement thickness to momentum thickness)

be greater than 3. Calculations made using this method but with the separation point known from experiment are compared to measurements for the GA(W)-1 airfoil in figure A-5. These results compare favorably with those for the CLMAX method for the same airfoil shown in figures A-2 and A-3(b); remember, however, that in the CLMAX method, the pressure in the separation region is free to vary and is calculated, as is the separation location. Calculations including the prediction of separation using the method of reference 57 for the GA(W)-1 airfoil are not available, but excellent results including separation prediction are presented for other airfoils in combination with leading and trailing flaps (see, for example, figure A-6).

Another example of a method which assumes constant pressure in the separation region is that of reference 58. This method involves the numerical solution of a Cauchy principal-value integral equation wherein flow properties are computed only along the streamlines which define the equivalent inviscid body, leading to computational economy. A simple wake model is used on these boundaries downstream of the assumed constant-pressure region to provide for the relaxation of the pressure to the free-stream value. In the constant-pressure region, the velocity on the upper bounding streamline is set equal to the value at the upper-surface separation location; on the lower bounding streamline, the velocity is set equal to that at the trailing edge of the airfoil. The position of these streamlines is iteratively adjusted, along with the location of the stagnation point, until a converged solution is obtained. The location of the separation point must be input in the current version of this model. In the application of this model to several airfoils, the (constant) pressures in the separation region were not accurately calculated, perhaps because of the omission of any consideration of boundary-layer displacement effects just prior to detachment.

A final method with the pressure specified to be constant in the separation region within the equivalent inviscid body is that of reference 59. This too is an iterative viscous-inviscid interaction method, but unlike the other methods discussed here, the calculation is not divided into distinct sequential inviscid and viscous steps. Instead, in each iteration cycle, the interaction between an inviscid calculation and a boundary-layer analysis is explicitly modeled by a mathematical expansion retaining linear terms "to account for the complete first-order coupling between the viscous and inviscid equations." The geometry of the displaced streamline, which forms the boundary of the equivalent inviscid body, is perturbed using the results of this expansion, and the procedure continued until convergence is obtained. The inviscid calculation is done using a mixed-boundary-condition potential method. This formulation allows either conventional no-through-flow boundary conditions to be applied at a region of known geometry, or alternatively, the surface velocity can be specified over some region, in which case the bounding streamline is calculated. The boundary-layer analysis is done using integral methods. The physical model of the separated wake assumes constant pressure from the separation point (calculated in the boundary-layer analysis using a shape-factor criterion) to the airfoil trailing edge and a linear decrease in velocity thereafter to the end of the recompression zone.

Examples of the results obtained using this method are shown for the GA(W)-1 airfoil in figures A-7 and A-8. In figure A-7 the integrated loads agree well with data, just as was the case for this airfoil for the CLMAX method (fig. A-2) and the method of reference 57 (fig. A-5). The detailed pressure distribution at one of the incidence angles in figure A-7 is shown to agree very closely with data in figure A-8.

The method of reference 60 relaxes the assumption of constant pressure in the separation region but, like the last method, attempts to deal explicitly with the coupling of the inviscid and separated flow regions. In reference 60, this coupling is accomplished by simultaneously solving a finite-difference equation for the stream function in the inviscid region and an integral boundary-layer equation for the viscous layers, which include the separated flow, in a series of downstream sweeps through the flow field. In each sweep, the solutions are matched at the surface of the airfoil, and convergence is attained when the change between sweeps is within an acceptable tolerance. No explicit modeling is included for the reverse flow in the separated region, and the entire viscous region is assumed thin. The method is presumably limited by its formulation to airfoils with only modest separation, but in one such example where separation occurred at 85 percent chord, good agreement for the pressure distribution and integrated lift coefficient was obtained.

In contrast to the methods just discussed where the idealization inside the inviscid body is not intended to represent the actual flow in that region, several methods exist which contain physically realistic models of the flow region inside the separation streamline, with emphasis on the recompression zone of the separated flow. Two-dimensional methods in this class includes those of refs. 61 and 62. The methods of these authors differ in detail but are conceptually similar, and they both emphasize the importance of including simulation of the recompression zone. As previously stated, this feature of the separated flow is not modeled in the methods which assume constant-vorticity free wakes or constant-pressure recirculation bubbles, although references 57 and 59 include the recompression (but do not calculate flow details in the recompression region). Favorable results have

been shown for the methods which ignore the recompression, but these were all cases where the data showed that recompression was either very small or occurred downstream of the wing. There are measurements (shown later) which indicate that recompression sometimes occurs over the airfoil, and in these cases it would seem to be important to model this process.

In the methods where the recompression process is treated in detail, it is done using a combination of separate zonal models for the free-shear layers and the backflow and rear stagnation regions which interact to cause the pressure rise. The separation streamline which forms a part of the boundary of the equivalent inviscid body is used in these recompression models. It is calculated at each iteration step by a mixed-boundary-condition potential flow procedure, as discussed previously. In the methods of references 61 and 62, an initial pressure distribution in the separated region is assumed, the mixed-boundary-condition potential method is applied resulting in an updated pressure distribution on the unseparated region and a new location for the separation streamline, and the separation streamline is input into the separation model, resulting in an updated pressure distribution in the separated region. This process is repeated (including application of integral boundary-layer methods to model the displacement effects in the attached region and to predict the separation location) until convergence is achieved.

Pressure distributions calculated using the methods of references 61 and 62 are compared to data for the GA(W)-1 airfoil at a Reynolds number of 2.9×10^6 in figure A-9. The predictions from the two methods are quite similar and good agreement with the data is illustrated. Notice that again in this case the recompression process occurs downstream of the trailing edge of the airfoil. In figure A-10(a), however, the

data indicate that a substantial fraction of the recompression occurs over the airfoil (a 63_1-012 section at 15° angle of attack); ironically, the method of reference 62 does not pick this up in this case - it predicts that the recompression occurs downstream. The lift curve predicted by the method of reference 62 for this 63_1 - 012 airfoil is compared to data in figure A-10(b), where it is shown that the predictions are quite irregular at high α and do not have the correct trend as α is increased. A portion of the discrepancy between the measurements and the predictions is attributed in reference 62 to the fact that the potential method used is a chord-line singularity representation, instead of a surface-singularity model. It is unlikely that this is the main difficulty here, however.

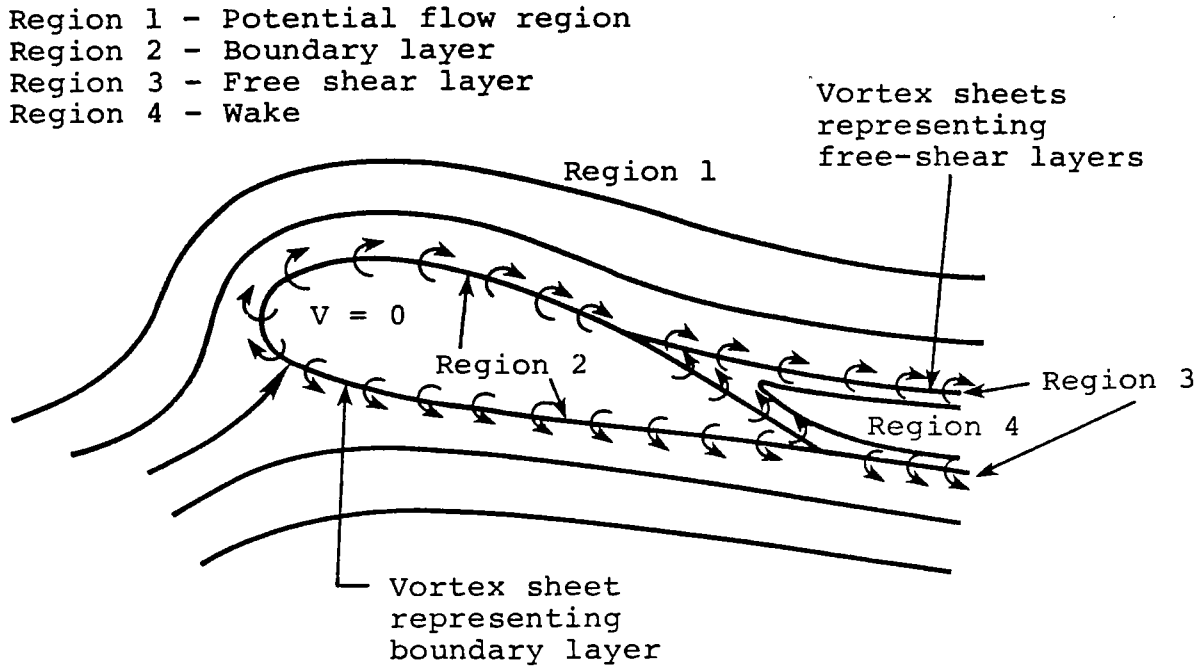

Figure A-1.- CLMAX Flow Model. From reference 12.

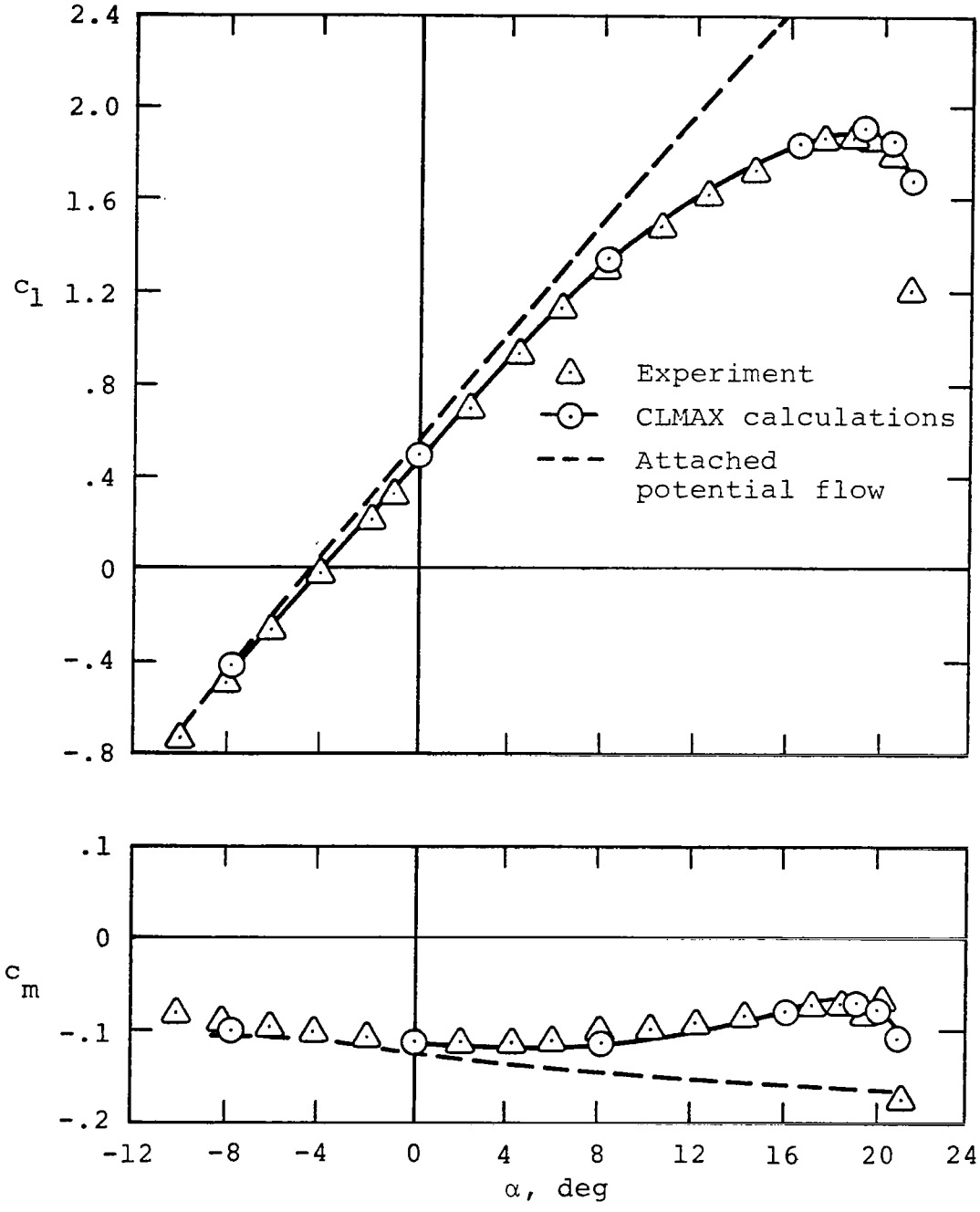

Figure A-2.- Comparison of CLMAX predictions of integrated loads with experiment for the GA(W)-1 airfoil at Re = 6.3×10^6. From reference 12.

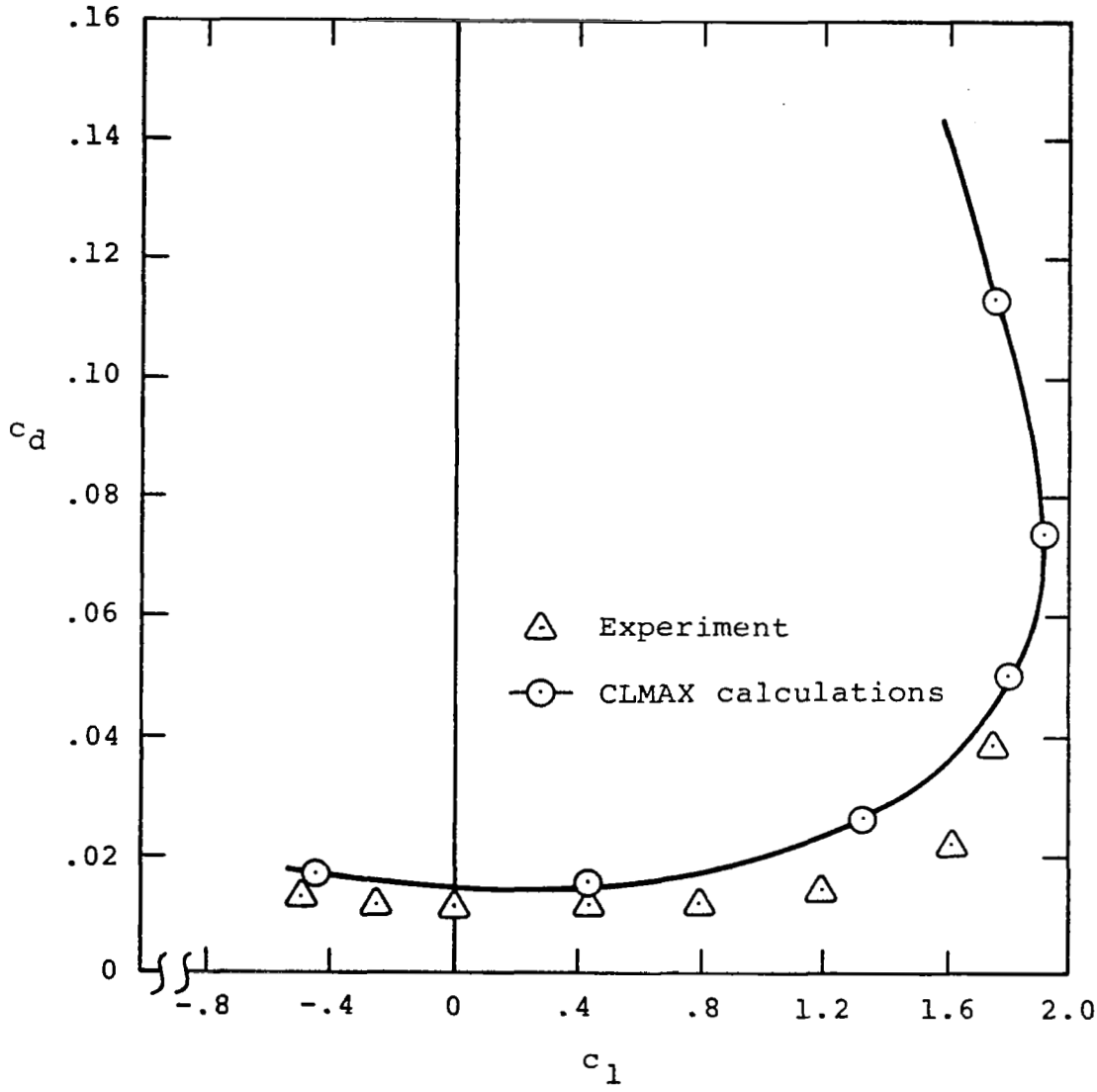

Figure A-2.- (Concluded).

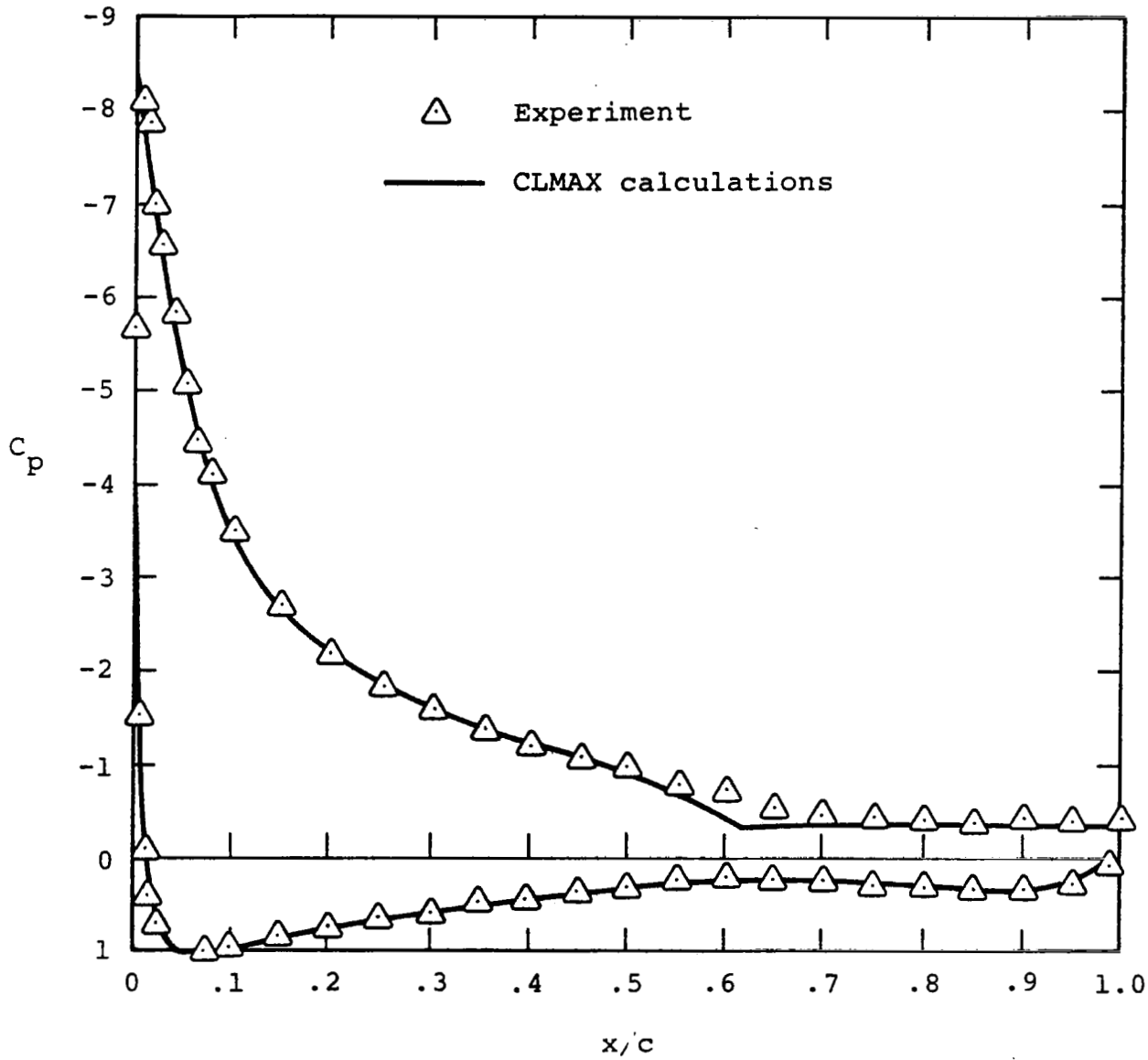

(a) $\alpha = 19.06°$

Figure A-3.- Comparisons of CLMAX predicted pressure distributions with experiment for the GA(W)-1 airfoil at Re = 6.3×10^6. From reference 12.

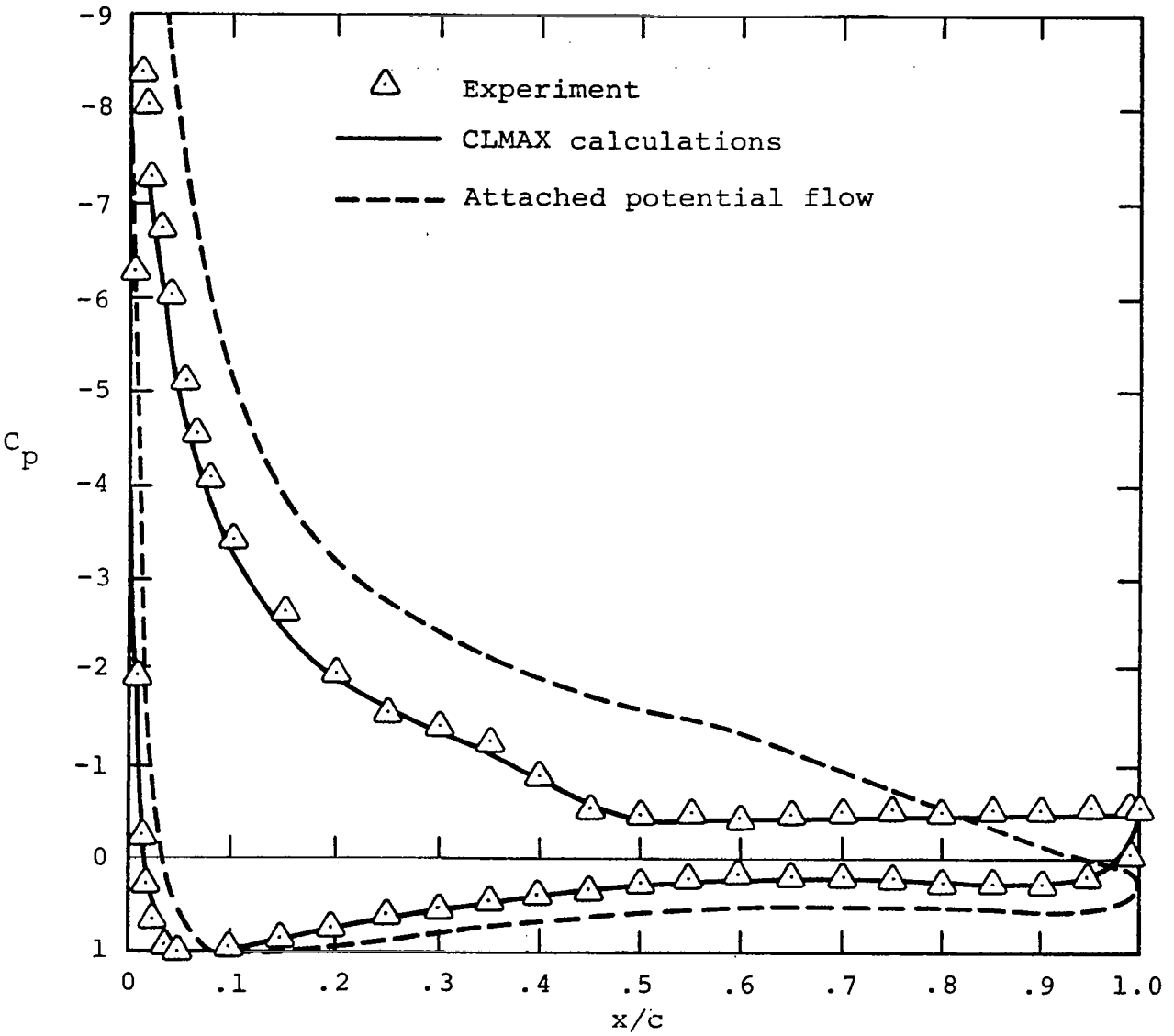

(b) α = 20.05°

Figure A-3.- (Continued).

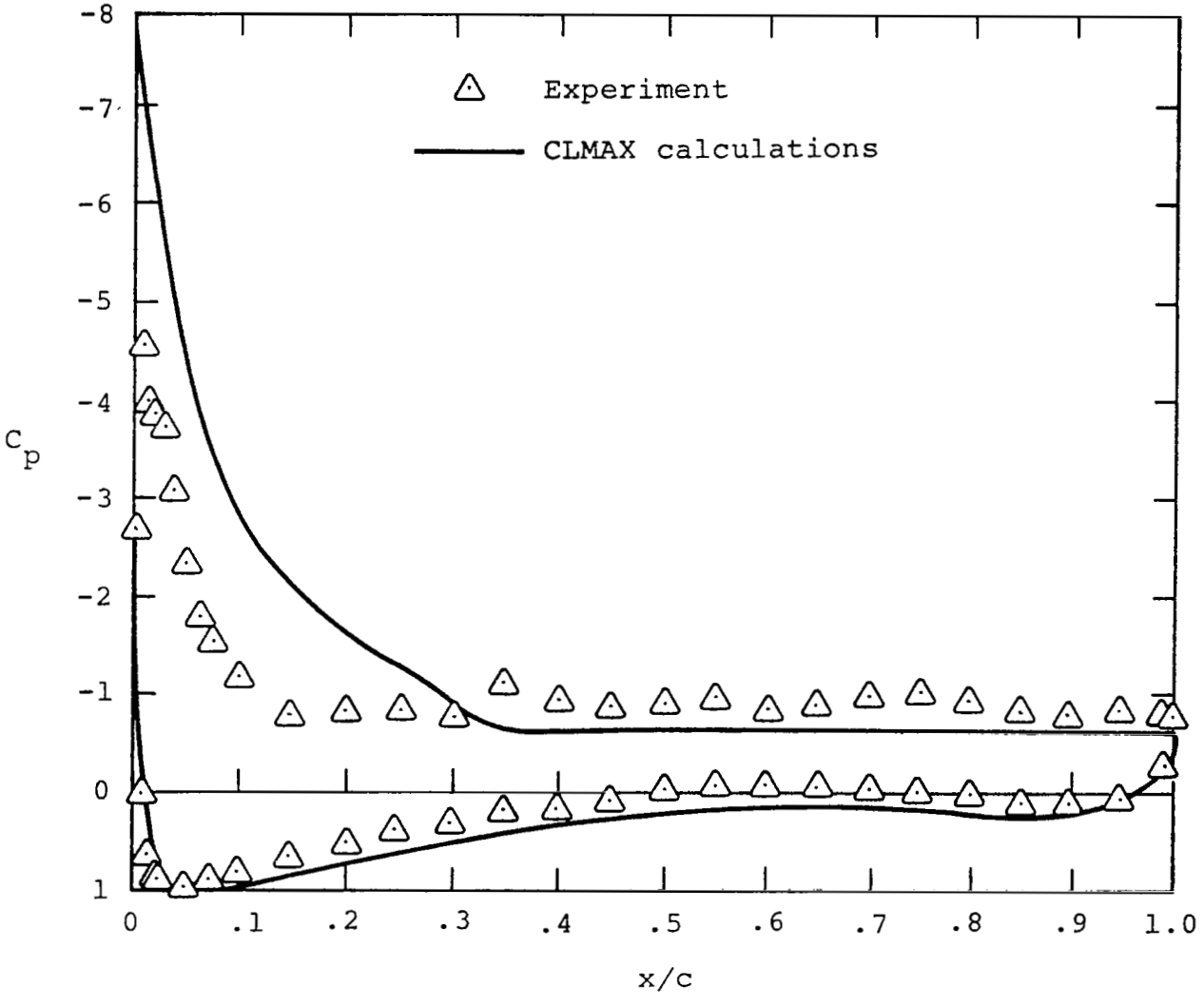

(c) α = 21.14°

Figure A-3.- (Concluded).

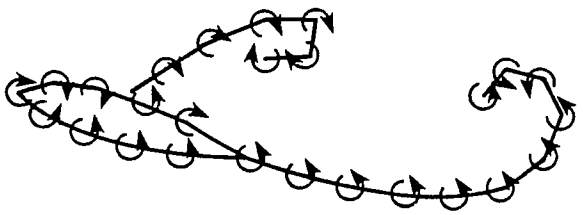

Figure A-4.- Flow model of reference 53.

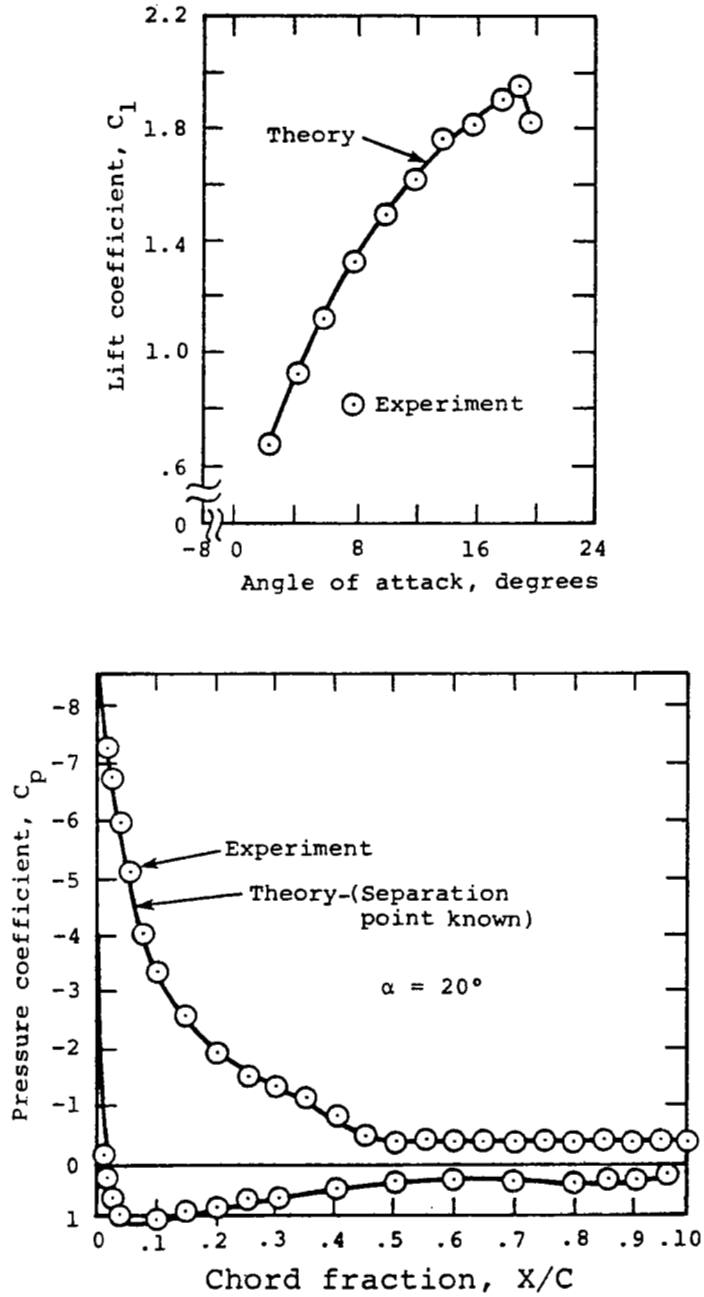

Figure A-5.- Comparisons of predicted lift and pressure distribution for the GA(W)-1 airfoil at Re = 6×10^6. From reference 57.

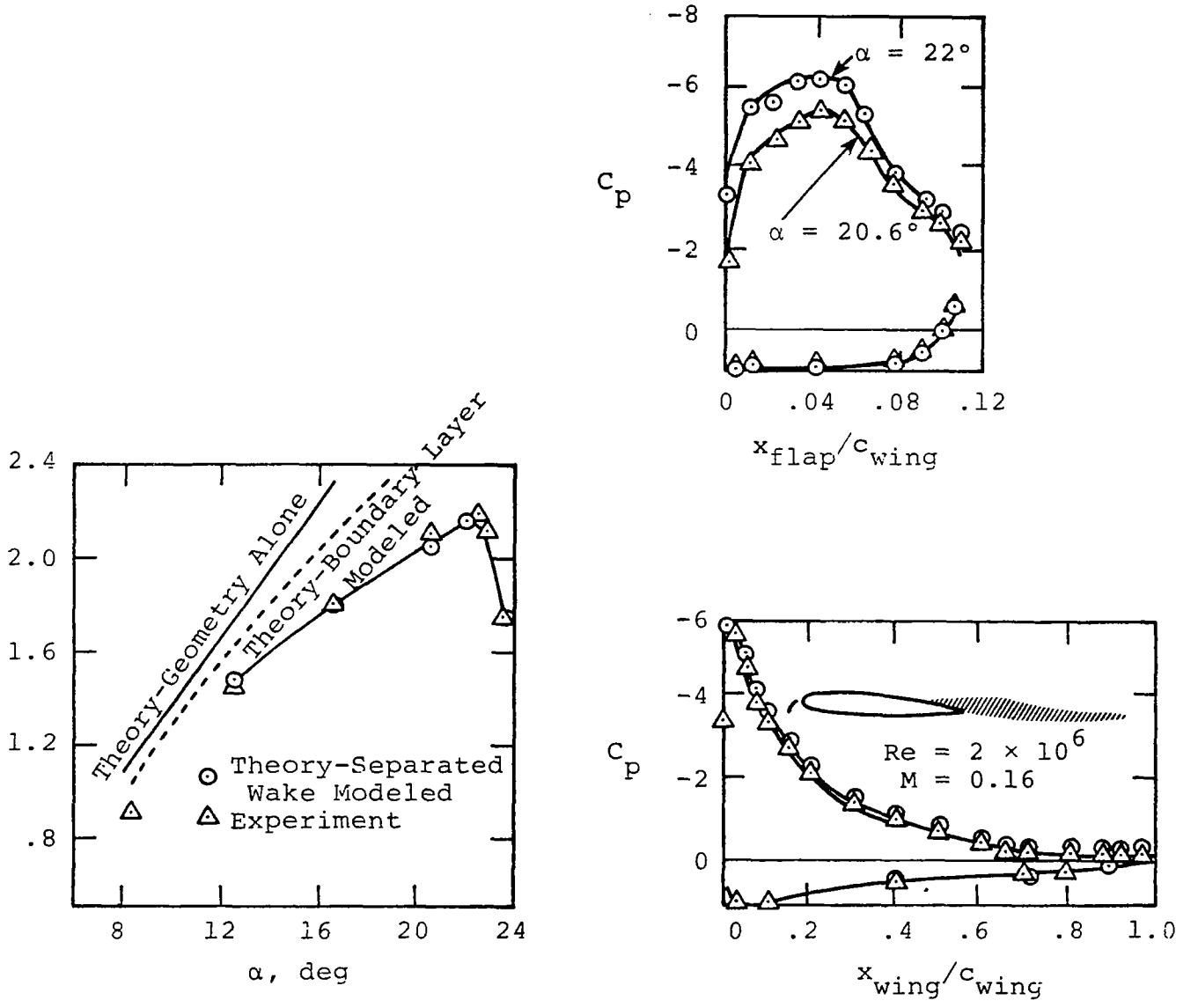

Figure A-6.- Comparisons of predicted and measured airfoil lift and pressure distributions for an airfoil with leading-edge flap. From reference 57.

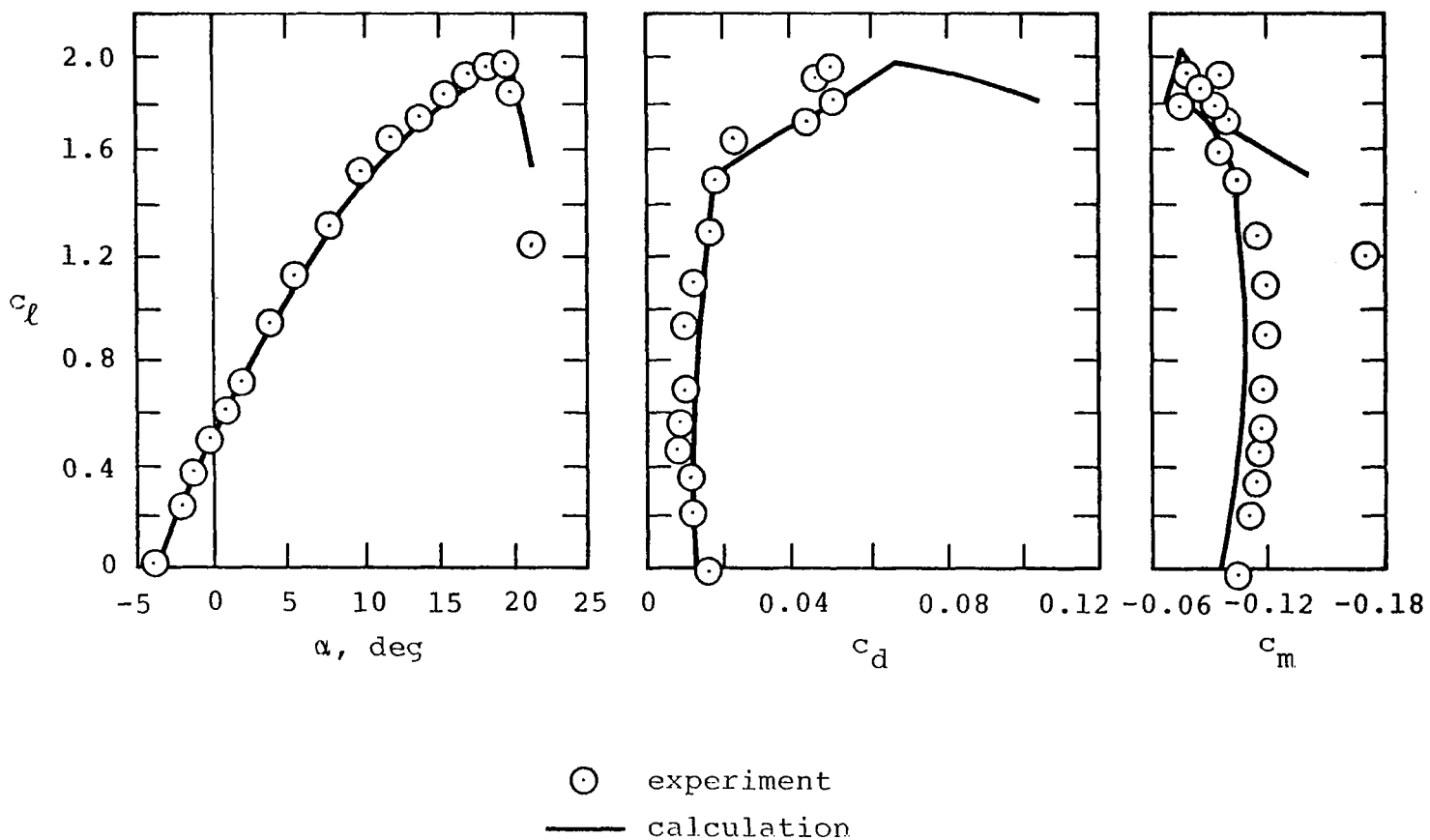

Figure A-7. - Comparison with experiment of integrated loads calculated using the method of ref. 59 for the GA(W)-1 airfoil at Re = 6×10^6.
From reference 59.

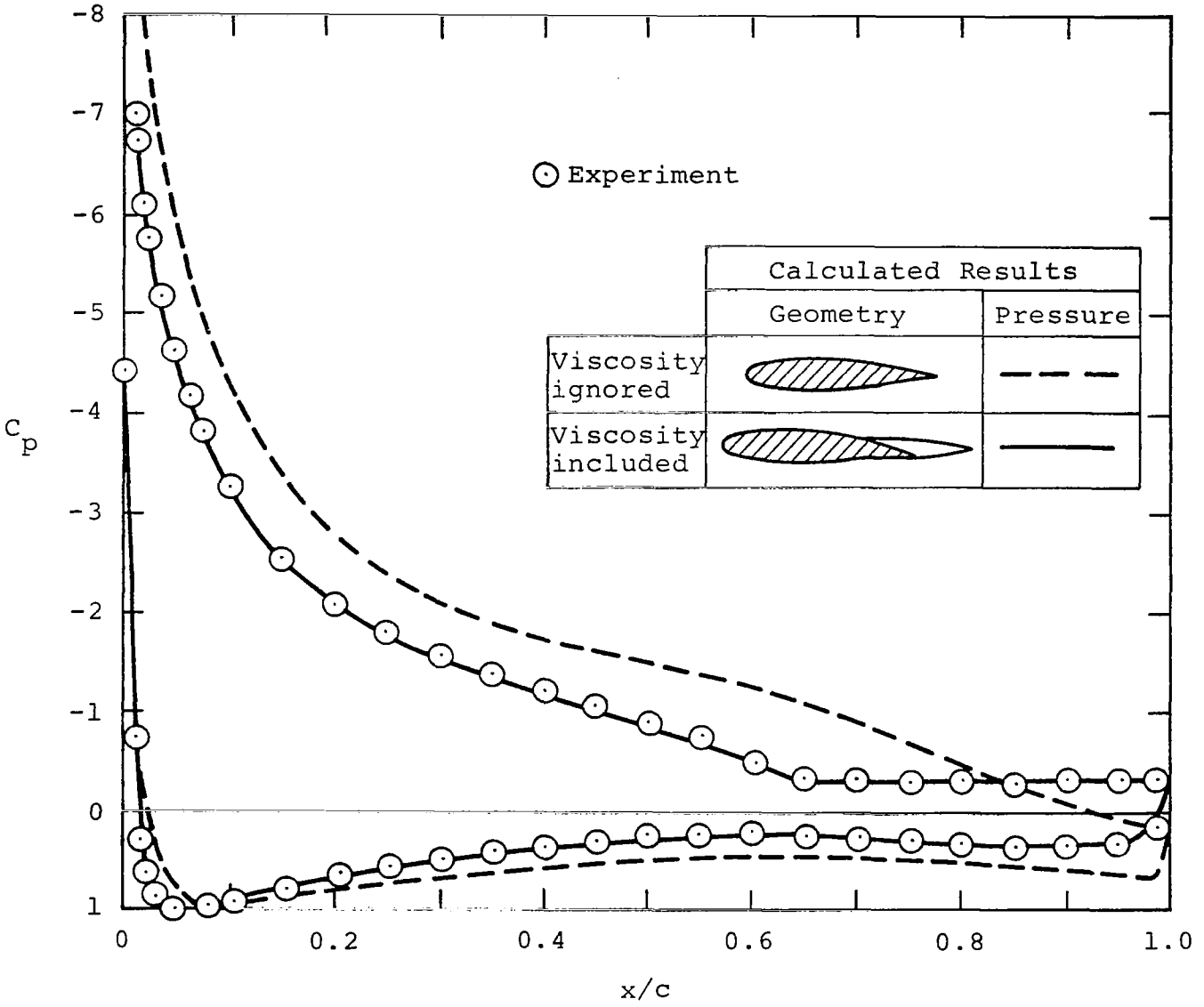

Figure A-8. - Comparison with experiment of the chordwise pressure distribution calculated using the method of ref. 59 for the GA(W)-1 airfoil at $\alpha = 16°$, $Re = 6 \times 10^6$. From ref. 59.

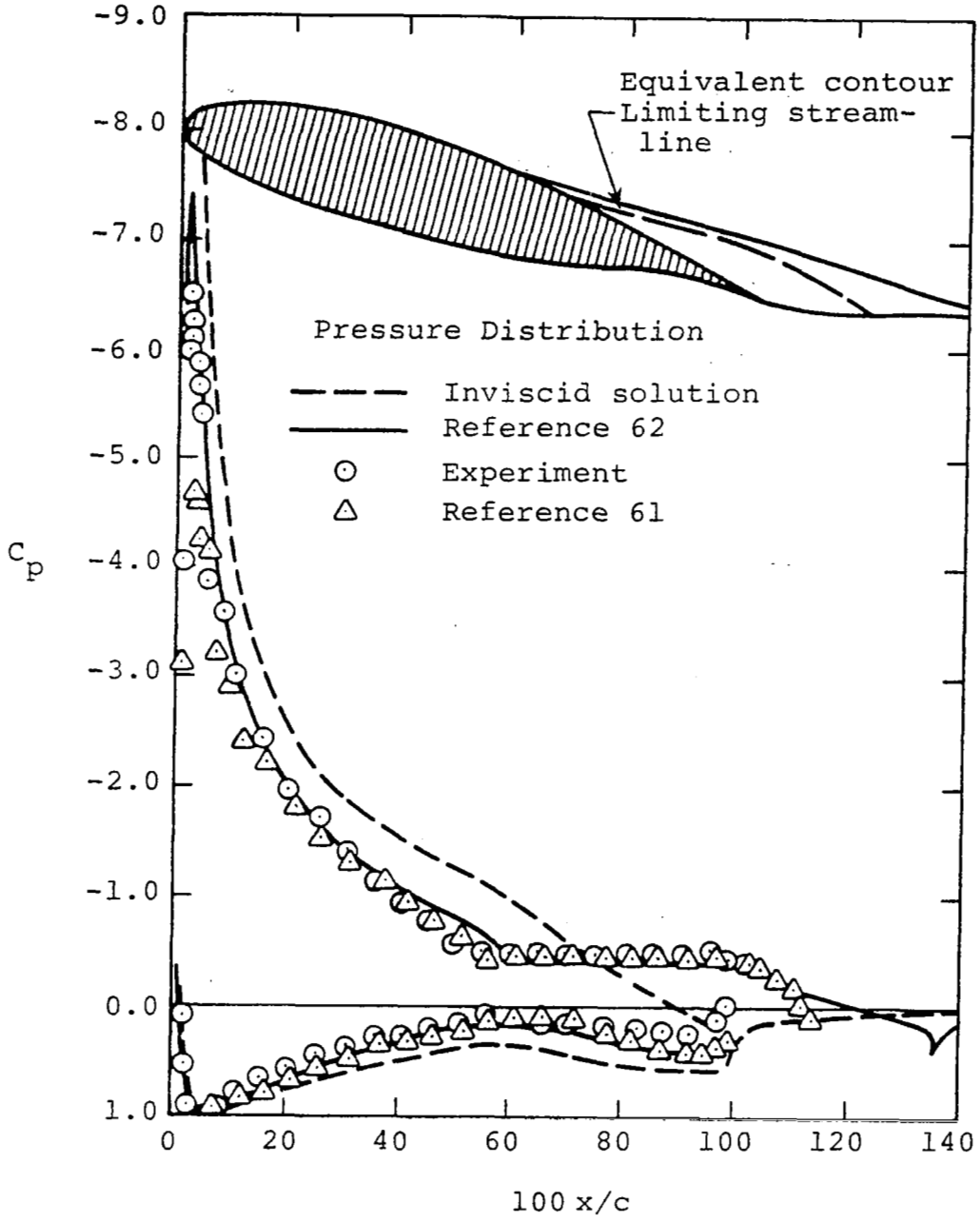

Figure A-9.- Comparison with measurements of predicted pressure distributions on the GA(W)-1 airfoil at $\alpha = 16.4°$ and $Re = 2.9 \times 10^6$ of the methods of refs. 61 and 62. From reference 62.

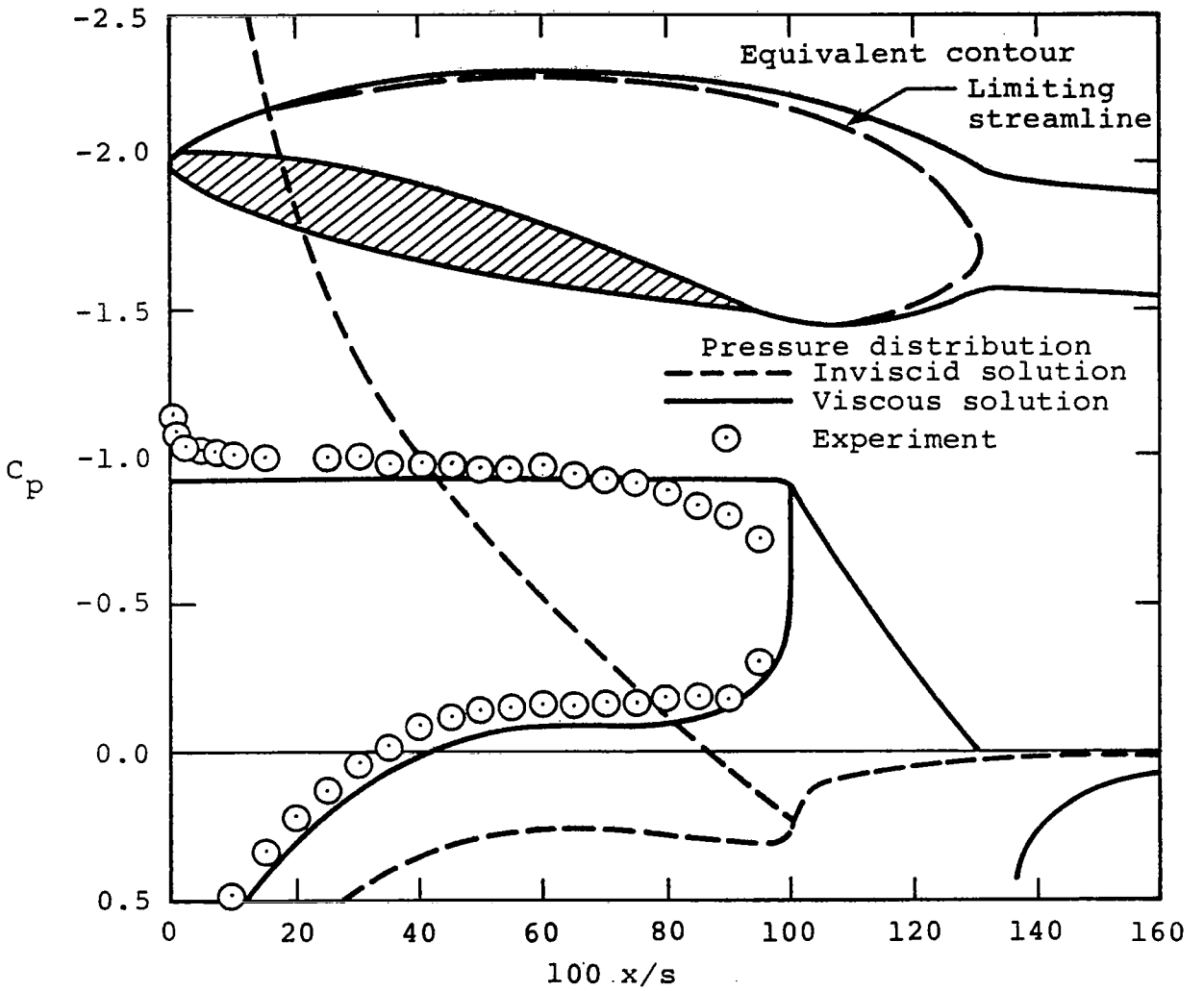

(a) Pressure distribution at $\alpha = 15.01°$

Figure A-10.- Comparisons with measurements of the method of ref. 62 for a 63_1-012 airfoil.
From reference 62.

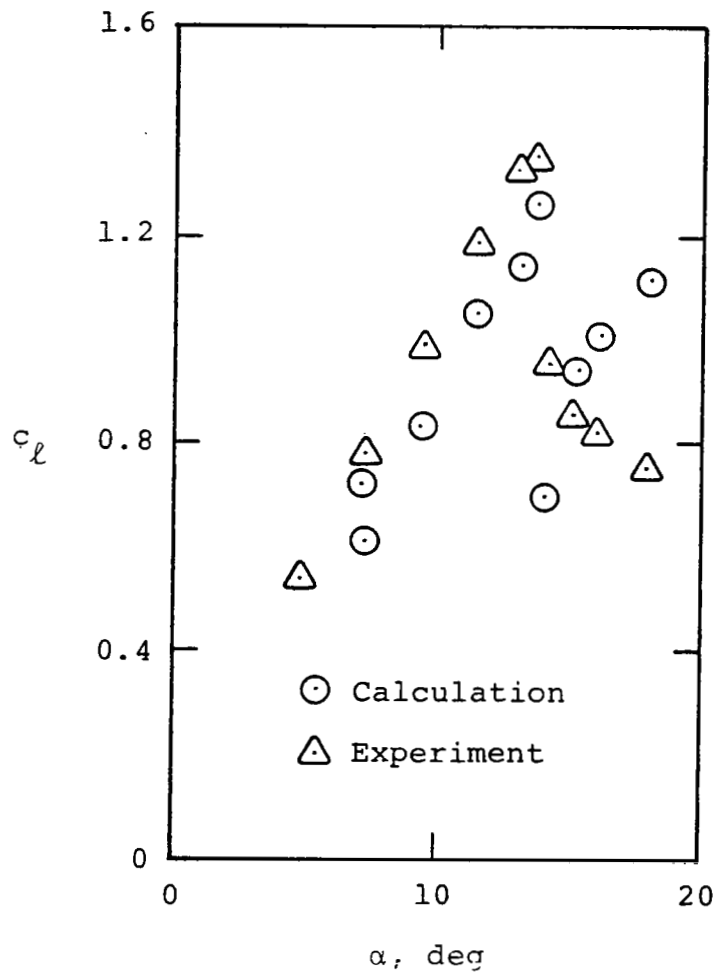

(b) Lift curve

Figure A-10.- (Concluded).

APPENDIX B

CALCULATION PROCEDURE FOR PROGRAM ASYMVL

SYMBOLS

C_x, C_y	total inplane forces in x and y directions, respectively
K_B	carryover factor, eq.(B-1)
K_W	carryover factor, eq.(B-2)
MSW	number of panels on the semispan
$N_{B(W)}$	normal force on the body in the presence of a wing
N_W	normal force on the wing alone
$N_{W(B)}$	normal force on the wing in the presence of the body
N_{total}	total normal force, eq.(B-3)
N_S	normal force from the suction analogy
NCW	number of chordwise panels
U	axial component of free-stream velocity
x,y	wing-fixed coordinates, fig. B-1

INTRODUCTION

Program ASYMVL is a modified version of program RATFLO (ref. 63), which is a rational flow model to predict the nonlinear hydrodynamic characteristics of submersible vehicles undergoing steady motion. In constructing ASYMVL, the subroutines from RATFLO which deal with vortex shedding from and pressure integration on the body were removed, so that only lifting surface and carryover forces and moments are calculated in ASYMVL.

CALCULATION PROCEDURE

The body with its lifting surfaces is broken into a series of regions, in each of which the calculation is done allowing for full mutual interference among the lifting surfaces in that region and the resultant image systems in the fuselage. Each quadrilateral lifting surface (henceforth called a fin) is represented by a chordal-plane vortex lattice. The solution is obtained by calculating the strengths of the lattice singularities so that at each control point in the lattice, the resultant velocity normal to the actual mean surface (i.e., allowing for camber) is zero. Although the slope of the mean surface is thus accounted for, this tangency condition is applied in the plane of the lattice. Nonlinear vortex-lift effects are included through an application of the Polhamus suction analogy. ASYMVL is meant to be used in conjunction with another program, a modified version of VTXCLD (ref. 38), in which the loads on the nose and the associated shed vorticity is calculated. The solution in each region of ASYMVL allows for the existence of external vortices as calculated by this auxiliary program; furthermore, in aft regions, vorticity shed by lifting surfaces in forward regions is accounted for in the calculation. These procedures are discussed further in the following.

The oncoming flow conditions and fuselage geometry are first input by the user. The program requires that in each fin region (wing region or tail region) the fuselage be represented by a circular cylinder of constant radius. A vortex field at the region leading edge may be input by cards or through a local file. (The modified version of VTXCLD writes vortex

field information to the local file required by program ASYMVL.) The trajectories through the region of these impressed vortices are parallel to the fuselage center line, i.e., these vortices are not tracked in a fin region in the current version of the code.

The lifting-surface geometry for the wing region is input. For a fin with a mirror image on the opposite side of the vertical plane of symmetry, such as in the case of a wing, the program requires that geometry information for only the right-hand side fin be input. Note that tails whose leading edges lie ahead of the wing trailing edge should be included in the wing region. The fin may be at any position or incidence angle on the body, but an approximate image system in the fuselage for that fin is constructed as if the fin plane were parallel to the fuselage center line.

The next major procedure in ASYMVL is laying out the horseshoe vortex panels on the lifting surfaces in the wing region. Using the horseshoe vortex-lattice method, a lifting surface is divided into panels, each of which contains a horseshoe vortex with its bound leg on the quarter chord of the panel and its trailing legs along the panel edges. The horseshoe vortices on the lifting surfaces are imaged inside the body and are used to calculate the lift carryover effects. Vortex panels are laid out in the local coordinate system of each fin (figure B-1). Panel side edges are required to be along or emanate from the following locations: (1) the root chord; (2) the tip chord (including those of zero length); and (3) points where there are breaks in leading- or trailing-edge sweep. Panels are formed by dividing the local chord at each of MSW arbitrarily spaced spanwise stations into NCW (number of

chordwise panels) equal parts. Corresponding chordwise divisions of adjacent spanwise stations are connected to form the panels. As an example, the panel layout on a cropped double-delta fin with NCW = 4 and MSW = 5 is shown in figure B-1.

Limitations regarding the panel layout for a given fin and for a fin region are as follows:

- the maximum number of panels on a fin is 100
- the maximum number of spanwise and chordwise panels (MSW and NCW, respectively) on a fin is fourteen (14) for each
- the maximum combined number of panels on all fins in a given region (wing region or tail region) is 300.

After horseshoe vortex panels are laid out on all fins, the influence functions are calculated. Mutual interference exists for all lifting surfaces in a given region. The horseshoe vortices used are considered to consist of three parts: a bound leg and two trailing legs. For purpose of computing the influence function, the trailing legs extend to infinity in the fin chordal plane. The influence coefficients are the perturbation velocity components per unit vortex strength induced at a point (in this case, each control point) by each horseshoe vortex component. At each control point, the sum of all influence coefficients due to all horseshoe vortices and their images is calculated. The component normal to the actual mean surface represented by each panel is used in the lifting-surface boundary condition, which is discussed next.

The tangency boundary condition (zero net velocity normal to the mean fin surface) is satisfied at the midspan of the three-quarter chord of each panel. This boundary condition is implemented as the sum of the normal components of the perturbation velocities due to the lattice and its image system, and the normal components due to the free-stream velocity, the externally imposed vortices, and the cross flow around the fuselage as calculated by a two-dimensional doublet representation. The resulting system of equations is solved by matrix inversion to give the strength of each horseshoe vortex.

The loadings acting on the lifting surfaces are now calculated. The force acting on a vortex filament is given by the Kutta-Joukowski law. Forces are calculated at each bound leg midpoint and at the three-quarter chord position on the side edges of each horseshoe-vortex panel. Note that in program ASYMVL, the contributions to the loads from the free-stream, the impressed vortices and the cross flow around the fuselage are calculated using the velocities calculated at the panel control point; however, the velocities due to the horseshoe vortices are calculated at the actual positions at which forces are determined.

After the individual forces on each panel of a given fin have been calculated, the span load distribution is calculated. Additionally, the inplane forces are used in conjunction with a method to determine an additional nonlinear lift associated with flow separation along leading and side edges. The basis for the vortex lift method is the Polhamus leading-edge suction analogy, which in simple terms states that the vortex lift on a delta

wing is equal in magnitude to the leading-edge suction on the wing. This analogy has been extended to streamwise edges of wings. Furthermore, for delta wings, a procedure to determine the fraction of leading-edge suction converted to normal force has been developed from a correlation of experimental data (ref. 33). This correlation indicates that the fraction of leading-edge suction ($K^*_{v_{le}}$) converted to normal force can vary from 0 to 1 depending on geometric parameters. The correlation is based on equivalent leading-edge sweep angle and is shown as the solid curve in figure B-2.

The leading-edge suction force is obtained by summing the inplane forces on the bound legs over the chord at each spanwise division of the lifting surface. The value of the available leading-edge suction force is given by $(C_x^2 + C_y^2)^{1/2}$, where C_x and C_y are the total inplane forces for a given portion of the span in the x and y directions, respectively. The leading-edge suction force is assumed to act at the bound-leg midpoint of the panel nearest the leading edge. The total available leading-edge suction force on the lifting surface is the sum of the suction distribution over the span. The vortex normal force due to leading-edge suction is the available suction force reduced by $K^*_{v_{le}}$ (for planforms other than deltas, $K^*_{v_{le}} = 1$). The side-edge suction force is obtained by summing spanwise the inplane forces on the trailing legs of each row of panels, i.e., the inplane trailing-edge forces on all the i-th chordwise panels are summed to give the side-edge suction at the i-th panel at the fin's tip. Note that all forces at a body/wing intersection are set to zero. Allowance is made to reduce the suction forces by $K^*_{v_{se}}$ to obtain the total side-edge vortex lift, but $K^*_{v_{se}}$ is usually taken as unity. This lift is assumed to act at the fin side edge at the center of pressure of the side-edge inplane forces. For lifting surfaces which have $K^*_{v_{le}} < 1$, the remainder of the inplane forces not converted to vortex normal force remain as inplane forces.

The span load distribution calculation is also used to obtain the strengths and lateral positions of vortices due to leading- and side-edge suction. These vortices are included in the load calculations in aft regions. Calculation of the separation vortices and their lateral position is described in reference 33. To arrive at the vertical positions of these vortices at the end of the current region, they are assumed to "track" at one-half of the local flow angle obtained from the free-stream flow conditions. This assumed path is based on empirical observations. The separation vortex inboard of a break in leading- edge sweep angle is "tracked" from the axial location of the body-fin intersection to the trailing edge of the region. The vortex outboard of the break in sweep, which is obtained by combining the leading-edge and side-edge vortices, is "tracked" from the axial position of the break to the trailing edge.

The trailing-vortex system from the potential lift for each lifting surface is also available from the loading calculations. The vortex-lattice method results in a trailing-vortex filament from each column of the lattice network, which goes to downstream infinity in the fin chordal plane. The system of trailing vortices for each lifting surface is thus distributed across the span, with the vortices originating in the plane of the lifting surface at the lifting-surface-region trailing edge.

In application of ASYMVL to the GRF, the various vortices were assumed to remain at constant y and z between the wing and tail regions because of the short distance involved. If there were a longer fuselage section, the vortices could have been tracked using VTXCLD. Furthermore, the technology exists (ref. 33) to track vortices within a wing or tail region, and this capability should be added to ASYMVL as discussed in the main text.

The carryover loads acting on the fuselage in the vicinity of each lifting surface are calculated. Consider the following definitions:

$$K_B = \frac{N_{B(W)}}{N_W} \tag{B-1}$$

$$K_W = \frac{N_{W(B)}}{N_W} \tag{B-2}$$

where $N_{B(W)}$ is the normal force on the body in the presence of a wing, $N_{W(B)}$ is the normal force on the wing in the presence of the body, and N_W is the normal force on the wing alone. These normal forces are to be interpreted as calculated using the Kutta-Joukowski law including perturbation velocities. It follows that (in the absence of any normal force from the Polhamus analogy)

$$N_{total} = N_{B(W)} + N_{W(B)} \tag{B-3}$$

and

$$\frac{K_B}{K_W} = \frac{N_{B(W)}}{N_{W(B)}} \tag{B-4}$$

In reference 64, it has been shown that for a delta wing mounted on a cylinder at $\beta = 0°$, K_B/K_W can be computed according to

$$\left.\frac{K_B}{K_W}\right|_{\beta = 0} = \frac{\text{normal force on images due to U}}{N_{W(B)}} \qquad \text{(B-5)}$$

where U is the axial component of the free-stream velocity and $N_{W(B)}$ is calculated using the wing vortex lattice. Extending this to allow for sideslip in the spirit of slender body theory, we obtain

$$\left.\frac{K_B}{K_W}\right|_{\beta \neq 0} = \frac{\text{normal force on images due to U only}}{\frac{1}{2}(N_{W(B)_{left}} + N_{W(B)_{right}})} \qquad \text{(B-6)}$$

where $N_{W(B)_{left}}$ is the lattice-calculated normal force on the left wing panel, $N_{W(B)_{right}}$ that on the right wing panel, again including the effects of perturbation velocities.

Then, assuming that the normal force from the Polhamus analogy N_S is carried over onto the body in the same proportion,

$$\text{Total carryover} = \frac{K_B}{K_W}(N_{W(B)} + N_S) \qquad \text{(B-7)}$$

with K_B/K_W calculated from eq. (B-5) for $\beta = 0$ and eq. (B-6) for $\beta \neq 0$.

As for the carryover of the pitching moment, the carryover of the potential portion is calculated by taking moments on the image system within the body; with respect to the portion from the Polhamus analogy, the center of pressure of the vortex normal force (including both leading- and side-edge

contributions) is computed and the carried over portion ($\frac{K_B}{K_W} N_S$) is assumed to act at the same axial location. It is assumed that there is no carry over of side force, yawing moment or rolling moment.

After the total loads on the lifting surfaces and the total carry over loads are calculated for the wing region, the above procedure is repeated for the tail region. Finally, the component loads are summed to result in values for the complete configuration.

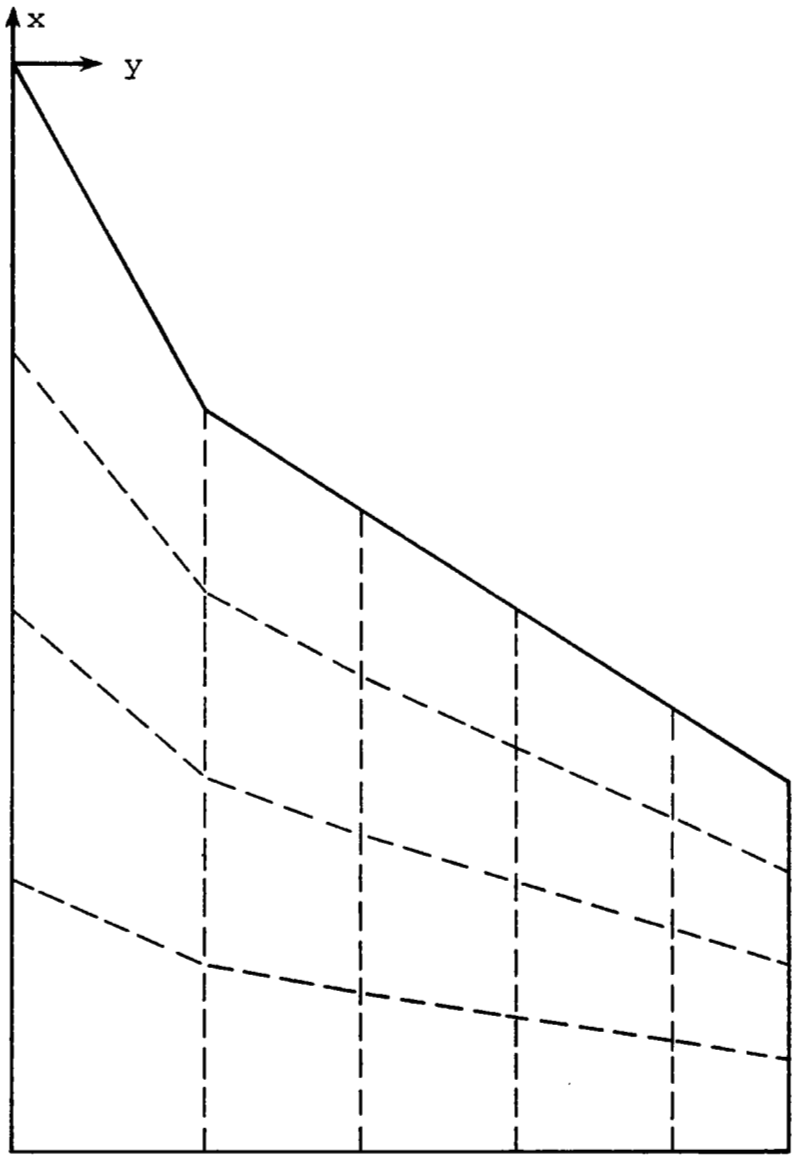

Figure B-1.- Panel layout on a double-delta fin with four chordwise and five spanwise divisions.

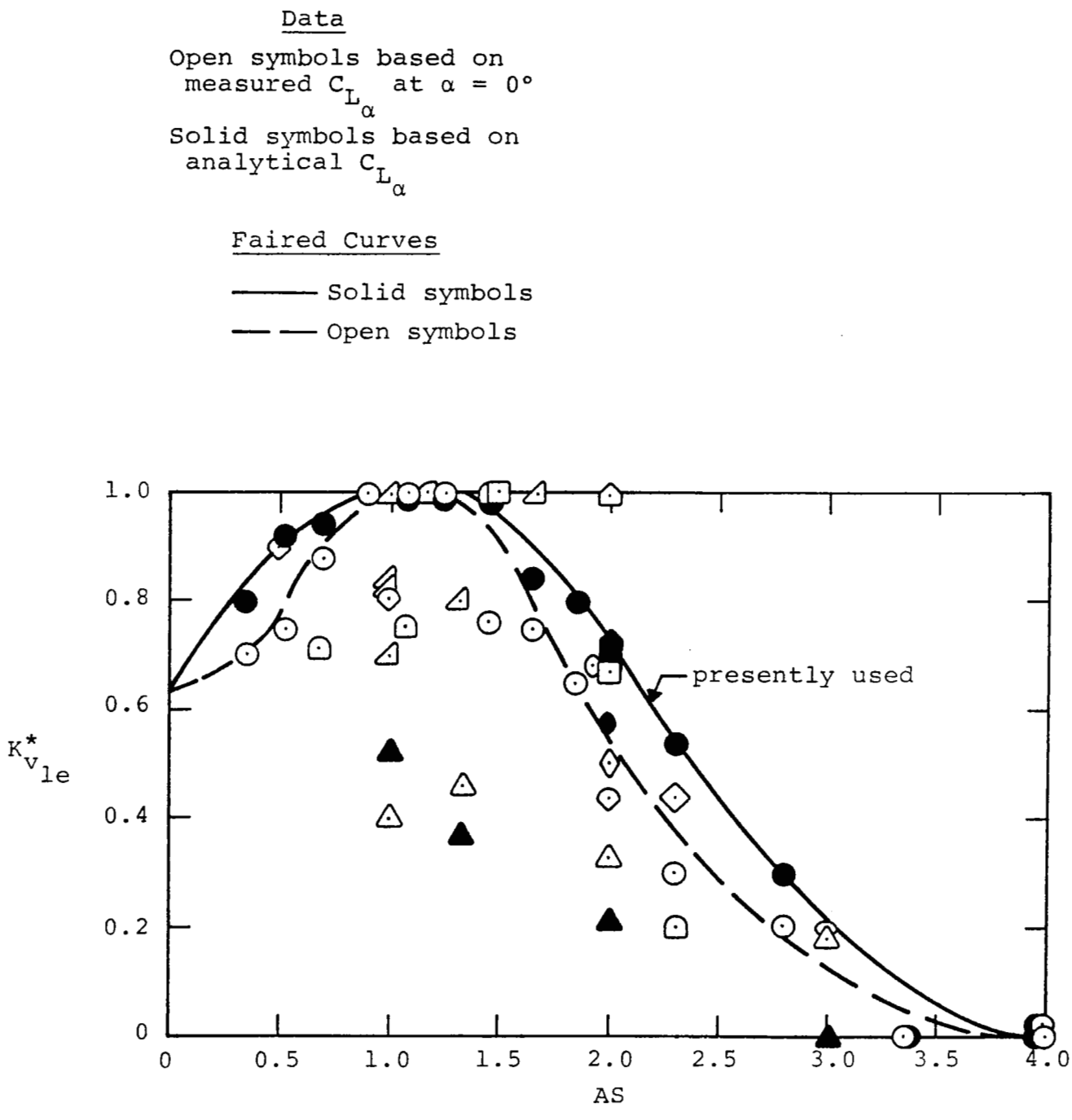

Figure B-2.- Vortex lift on delta wings in incompressible flow (from ref. 33).

REFERENCES

1. Newsom, W. A., Jr., Satran, D. R., and Johnson, J. L., Jr.: Effects of Wing-Leading-Edge Modifications on a Full-Scale, Low-Wing General Aviation Airplane - Wind-Tunnel Investigation of High-Angle-of-Attack Aerodynamic Characteristics. NASA TP-2011, June 1982.

2. Staff of Langley Research Center: Exploratory Study of the Effects of Wing-Leading-Edge Modifications on the Stall/ Spin Behavior of a Light General Aviation Airplane. NASA TP-1589, Dec. 1979.

3. Johnson, J. L., Jr., Newsom, W. A., and Satran, D. R.: Full-Scale Wind-Tunnel Investigation of the Effects of Wing Leading-Edge Modifications on the High Angle-of-Attack Aerodynamic Characteristics of a Low-Wing General Aviation Airplane. AIAA 80-1844, Aug. 1980.

4. DiCarlo, D. J., Stough, H. P., III, and Patton, J. M., Jr.: Effects of Discontinuous Drooped Wing Leading-Edge Modification on the Spinning Characteristics of a Low-Wing General Aviation Airplane. AIAA-80-1843, Aug. 1980.

5. Woodward, F. A., Dvorak, F. A. and Geller, E. W.: A Computer Program for Three-Dimensional Lifting Bodies in Subsonic Inviscid Flow. Report No. USAAMRDL TR-74-18, U.S. Army, Apr. 1974. (AD 782-202)

6. Gross, L. W.: A Prediction Method for the Flow over a Stalled Straight Wing. Vol. I - Theory. McDonnell Douglas Aircraft Co. Report MDC A7056, Apr. 1981.

7. Katz, J.: Large-Scale Vortex-Lattice Model for the Locally Separated Flow over Wings. AIAA-81-1264, June 1981.

8. Maskew, B.: Program VSAERO, A Computer Program for Calculating the Non-Linear Aerodynamic Characteristics of Arbitrary Configurations. User's Manual. NASA CR-166476, Dec. 1982.

9. Maskew, B. and Rao, B. M.: Calculation of Vortex Flows on Complex Configurations. Proc. 13th Congress of the International Council of the Aeronautical Sciences, Seattle, Vol. I, Aug. 1982.

10. Maskew, B., Rao, B. M. and Dvorak, F. A.: Prediction of Aerodynamic Characteristics for Wings with Extensive Separations. AGARD CP-291, Oct. 1980.

11. Maskew, B.: Prediction of Subsonic Aerodynamic Characteristics - A Case for Low-Order Panel Methods. AIAA-81-0252, Jan. 1981.

12. Maskew, B. and Dvorak, F. A.: The Prediction of C_{Lmax} Using a Separated Flow Model. Jour. of Am. Hel. Soc., Vol. 23, No. 2, 1978, pp. 2-8.

13. Winkelmann, A. E. and Tsao, C. P.: An Experimental Study of the Flow Field on a Wing with a Partial Span Drooped Leading Edge. AIAA-82-1369. Aug. 1982.

14. Winkelmann, A. E.: An Experimental Study of Mushroom Shaped Stall Cells. AIAA-82-0942, June 1982.

15. Winkelmann, A. E. and Tsao, C. P.: An Experimental Study of the Flow on a Wing With a Partial Span Drooped Leading Edge. AIAA-81-1665, Aug. 1981.

16. Tobak, M. and Peake, D. J.: Topological Structures of Three Dimensional Separated Flows. AIAA-81-1260, June 1981.

17. Fannel p, T. K. and Krogstad, P. A.: Three-Dimensional Turbulent Boundary Layers in External Flows: A Report on Euromech 60. JFM, Vol. 71, 1975, pp. 815-826.

18. East, L. F.: Computation of Three-Dimensional Turbulent Boundary Layers. TN AE-1211, FFA, Sweden, 1975.

19. Simpson, R. L.: Prediction Methods of Separated Turbulent Shear Flows. VKI Lecture Series 1981-1, Vol. 1, Jan. 1981.

20. Cebeci, T., Mosinskis, G., and Smith, A. M. O.: Calculation of Separation Points in Incompressible Turbulent Flows. Jour. of Aircraft, Vol. 9, No. 9, 1972, pp. 618-624.

21. Gerhart, P. and Bober, L.: Comparison of Several Methods for Predicting Separation in a Compressible Turbulent Boundary Layer. NASA TM X-3102, 1974.

22. Kuhn, G. D.: Computer Program for Calculation of Separated Turbulent Flows on Axisymmetric Afterbodies Including Exhaust Plume Effects. AEDC-TR-79-4, U.S. Air Force, Mar. 1979.

23. Lyrio, A. A., Ferziger, J. H. and Kline, S. J.: An Integral Method for the Computation of Steady and Unsteady Turbulent Boundary Layer Flows, Including the Transitory Stall Regime in Diffusers. Report PD-23, Dept. of Mech. Eng., Stanford University, Stanford, CA, Mar. 1981.

24. Kline, S. J., Bardina, J. G., and Strawn, R. C.: Correlation of the Detachment of Two-Dimensional Turbulent Boundary Layers. AIAA Journal, Vol. 21, Jan. 1983, pp. 68-73.

25. Stratford, B. S.: The Prediction of Separation of the Turbulent Boundary Layer. J. of Fluid Mech., Vol. 5, 1959, pp. 1-16.

26. Smith, J. H. B.: Inviscid Fluid Models, Based on Rolled-Up Vortex Sheets, for Three-Dimensional Separation at High Reynolds Number. AGARD-LS-94, 1978.

27. Lamar, J. E., and Luckring, J. M.: Recent Theoretical Developments and Experimental Studies Pertinent to Vortex Flow Aerodynamics - with a View Towards Design (Review Paper). AGARD-CP-247, 1978.

28. Redelinghuys, C.: Prediction of Wing Side-Edge Suction Forces and Maximum Inviscid Lift. Ph.D. Thesis, University of Stellenbosch, Sep. 1981.

29. Polhamus, E. C.: A Concept of the Vortex Lift of Sharp-Edged Delta Wings Based on a Leading-Edge-Suction Analogy. NASA TN D-3767, 1966.

30. Johnson, F. T., Lu, P., Tinoco, E. N. and Epton, M. A.: An Improved Panel Method for the Solution of Three-Dimensional Leading-Edge Vortex Flows. Volume I - Theory Document. NASA CR-3278, July 1980.

31. Hoeijmakers, H. W. M., Vaatstra, W. and Verhaagen, N. G.: On the Vortex Flow Over Delta and Double-Delta Wings. AIAA-82-0949, June 1982.

32. Lamar, J. E.: Extension of Leading-Edge-Suction Analogy to Wings with Separated Flow Around the Side Edges at Subsonic Speeds. NASA TR R-428, 1974.

33. Mendenhall, M. R. and Nielsen, J. N.: Effect of Symmetrical Vortex Shedding on the Longitudinal Aerodynamic Characteristics of Wing-Body-Tail Combinations. NASA CR-2473, Jan. 1975.

34. Lamar, J. E.: Some Recent Applications of the Suction Analogy to Vortex-Lift Estimates. NASA TM X-72785, 1976.

35. Lamar, J. E.: Strake-Wing Analysis and Design. AIAA-78-1201, July 1978.

36. Luckring, J. M.: Aeodynamics of Strake-Wing Interactions. J. Aircraft, Vol. 16, No. 11, Nov. 1979, pp. 756-762.

37. Lamar, J. E.; Summary of Some Recent Studies of Subsonic Vortex Lift and Parameters Affecting the Leading-Edge Vortex Stability. AIAA-76-414, July 1976.

38. Mendenhall, M. R., Spangler, S. B. and Perkins, S. C., Jr.: Vortex Shedding From Circular and Noncircular Bodies at High Angles of Attack. AIAA-79-0026, Jan. 1979.

39. Campbell, J. F.: Effects of Spanwise Blowing on the Pressure Field and Vortex-Lift Characteristics of a 44^{o} Swept Trapezoidal Wing. NASA TN D-7907, June 1975.

40. Spangler, S. B. and Mendenhall, M. R.: Further Studies of Aerodynamic Loads at Spin Entry. Report ONR-CR212-225-3, U.S. Navy, June 1977. (A 047 952)

41. Fox, C. H., Jr.: Subsonic Longitudinal and Lateral-Directional Static Aerodynamic Characteristics of a General Research Fighter Model Employing a Strake-Wing Concept. NASA TM-74071, 1978.

42. Luckring, J. M.: Subsonic Longitudinal and Lateral Aerodynamic Characteristics for a Systematic Series of Strake-Wing Configurations. NASA TM-78642, Feb. 1979.

43. Luckring, J. M.: Flow Visualization Studies of a General Research Fighter Model Employing a Strake-Wing Concept at Subsonic Speeds. NASA TM-80057, Aug. 1979.

44. Frink, N. T. and Lamar, J. E.: Water-Tunnel and Analytical Investigation of the Effect of Strake Design Variables on Strake Vortex Breakdown Characteristics. NASA TP-1676, Aug. 1980.

45. Lamar, J. E. and Gloss, B. B.: Subsonic Aerodynamic Characteristics of Interacting Lifting Surfaces With Separated Flow Around Sharp Edges Predicted by a Vortex-Lattice Method. NASA TN D-7921, Sept. 1975.

46. Brennenstuhl, U. and Hummel, D.: Vortex Formation over Double-Delta Wings. Proc. 13th Congress of the International Council of the Aeronautical Sciences, Volume 2, Seattle, Aug. 1982.

47. Erickson, G. E.: Flow Studies of Slender Wing Vortices. AIAA-80-1423, July 1980.

48. Moore, W. A., Erickson, G. E., Lorincz, D. J. and Skow, A. M.: Effects of Forebody, Wing and Wing-Body-LEX Flowfields on High Angle of Attack Aerodynamics. SAE 791082, Dec. 1979.

49. Lan, C. E. and Hsu, C. H.: Effects of Vortex Breakdown on Longitudinal and Lateral-Directional Aerodynamics of Slender Wings by the Suction Analogy. AIAA-82-1385, Aug. 1982.

50. Anderson, J. D., Jr., Corda, S. and Van Wie, D. M.: Numerical Lifting Line Theory Applied to Drooped Leading Edge Wings Below and Above Stall. J. Aircraft, Vol. 17, Dec. 1980, pp. 898-904.

51. Dvorak, F. A. and Maskew, B.: Application of the AMI C_{Lmax} Prediction Method to a Number of Airfoils. In NASA CP 2045, Vol. 1, Pt. 1, Mar. 1978.

52. Katz, J.: A Discrete Vortex Method for the Non-Steady Separated Flow over an Airfoil. JFM, Vol. 102, 1981, pp. 315-328.

53. Strickland, J. H., Oler, J. W., Im, B. J. and Smith, T. G.: A Preliminary Dynamic Stall Model Using a Vortex Panel Method. AIAA-81-2584. Dec. 1981.

54. Jacob, K.: Advancement of a Method for Calculating Separated Flows Around Airfoils wth Special Consideration of Profile Drag. DLR-F8-76-36, Translated as ESA-TT-373, Apr. 1977.

55. Jacob, K.: Computation of Subsonic Flow Around Airfoil Systems with Multiple Separation. NASA TM-76930, June 1982.

56. Bhateley, I. C. and Bradley, R. C.: A Simplified Mathematical Model for the Analysis of Multi-Element Airfoils Near Stall. AGARD-CP-102, Nov. 1972.

57. Henderson, M. L.: A Solution to the 2-D Separated Wake Modeling Problem and its Use to Predict C_{Lmax} of Arbitrary Airfoil Sections. AIAA-78-156, Jan. 1978.

58. White, J. M.: A Zone-Interaction Method for the Outer Flow Analysis of a Separated Airfoil. J. Ship Res., Vol. 24, June 1980, pp. 123-127.

59. Gilmer, B. R. and Bristow, D. R.: Analysis of Stalled Airfoils by Simultaneous Perturbations to Viscous and Inviscid Equations. AIAA-81-1239, June 1981.

60. Moses, H. L., Hill, J. M. and Thomason, S. B.: Calculation of the Flow Over a Stalled Airfoil. AIAA-82-1265. June 1982.

61. Zumwalt, G. W. and Naik, S. N.: A New Flow Model for Highly Separated Airfoil Flows at Low Speeds. NASA CP 2045, Vol. 1, Pt. 1, Mar. 1978.

62. Gross, L. W.: The Prediction of Two-Dimensional Airfoil Stall Progression. AIAA-78-155. Jan. 1978.

63. Perkins, S. C., Jr., Mendenhall, M. R. and Young, S. W.: Rational Flow Modeling of Submersible Vehicles. Volume II - RATFLO Program Manual. Nielsen Engineering & Research, Inc. TR 265, Jan. 1982. (Work performed under Naval Coastal Systems Center Contract No. N61331-80-C-0047, period ending 8/24/80.)

64. Dillenius, M. F. E., Mullen, J. and Perkins, S. C., Jr.: A General Method for Determining the Forces and Moments on Components of Finned Sections of Underwater Vehicles. NCSC-TM-319-81, Oct. 1980.

1. Report No.	2. Government Accession No.	3. Recipient's Catalog No.
NASA CR-3764		

4. Title and Subtitle	5. Report Date
A STUDY OF PREDICTION METHODS FOR THE HIGH ANGLE-OF-ATTACK AERODYNAMICS OF STRAIGHT WINGS AND FIGHTER AIRCRAFT	January 1984
	6. Performing Organization Code: 788/C
7. Author(s): O. J. McMillan, M. R. Mendenhall, and S. C. Perkins, Jr.	8. Performing Organization Report No.: TR 296
	10. Work Unit No.
9. Performing Organization Name and Address: Nielsen Engineering & Research, Inc. 510 Clyde Avenue Mountain View, CA 94043	11. Contract or Grant No.: NAS1-17026
	13. Type of Report and Period Covered: Contractor Report 6/82 - 7/83
12. Sponsoring Agency Name and Address: National Aeronautics and Space Administration Washington, DC 20546	14. Sponsoring Agency Code

15. Supplementary Notes

Langley Technical Monitor: William P. Gilbert
Final Report

16. Abstract

Work is described dealing with two areas which are dominated by the nonlinear effects of vortex flows. The first area concerns the stall/spin characteristics of a general aviation wing with a modified leading edge. The second area concerns the high-angle-of-attack characteristics of high performance military aircraft. For each area, the governing phenomena are described as identified with the aid of existing experimental data. Existing analytical methods are reviewed, and the most promising method for each area used to perform some preliminary calculations. Based on these results, the strengths and weaknesses of the methods are defined, and research programs recommended to improve the methods as a result of better understanding of the flow mechanisms involved.

17. Key Words (Suggested by Author(s))	18. Distribution Statement
High angle of attack Separated flow Subsonic flow Prediction methods General Aviation Wings Fighter Aircraft Configurations	Unclassified - Unlimited Subject Category 02

19. Security Classif. (of this report)	20. Security Classif. (of this page)	21. No. of Pages	22. Price
Unclassified	Unclassified	204	A10

For sale by the National Technical Information Service, Springfield, Virginia 22161

☆U.S. GOVERNMENT PRINTING OFFICE:1984 -739 -010/ 51